A UNIFORM PRESSURE ELECTROMAGNETIC ACTUATOR FOR FORMING FLAT SHEETS

DISSERTATION

Presented in Partial Fulfillment of the Requirements for

the Degree Doctor of Philosophy in the Graduate

School of The Ohio State University

By

Manish Kamal, M.S.

*****

The Ohio State University

2005

Dissertation Committee:

Dr. Glenn S. Daehn, Adviser

Dr. David A. Rigney

Dr. Yogeshwar Sahai

Approved by

_____

Adviser

Graduate Program in Materials Science and Engineering

ABSTRACT

Electromagnetic forming can lead to better formability along with additional benefits. The spatial distribution of forming pressure in electromagnetic forming can be controlled by the configuration of the actuator. A new type of actuator is discussed which gives a uniform pressure distribution in forming. It also provides a mechanically robust design and has a high efficiency for flat sheet forming. An analysis of the coil is presented that allows a systematic design process. Examples of uses of the coil are then presented, specifically with regards to forming a depression, embossing and cutting. Some practical challenges in the design of the coil are also addressed. This work emphasizes the approaches and engineering calculations required to effectively use this actuator.

TO MY PARENTS

ACKNOWLEDGMENTS

With a deep sense of gratitude and indebtedness, I wish to record the relentless, timely and untiring guidance I received from Dr. Glenn Daehn. His energy and vast pool of ideas has been a source of constant inspiration. With thought provoking discussions and personal help made available by Dr. Daehn on this fascinating subject in general and the problem of the present investigation in particular, it has become possible for me to complete this dissertation. I especially appreciate your ability to encourage free-thinking amongst your students.

I would like to thank General Motors, BMW Germany, EWI, MIRDC Taiwan and American Trim for sponsoring this research work. Helpful advice from John Bradley, Steve Hatkevich, Peihui Zhang and Haiping Shao is greatly appreciated.

My thanks are due to the technical staff in the Materials Science, Chemistry and Industrial Engineering departments, who have helped me at all stages in my research. I would like to extend a special note of thanks to Eric Winnard, Ken Kushner, Mary Hartzler and Larry Antal for helping me with the coil, die and experimental setup.

I am also thankful to Vincent Vohnout for his advice and suggestions. I wish to acknowledge my heartfelt and deep sense of appreciation to my research group members Mala Seth, Jianhui Shang, Eduardo Del Rio, Kinga Unocic, Edurne Iriondo and Inaki Eguia. I would like to thank my friends Arunesh, Soumya and Dhriti for being there for me during trying times.

I would not be where I am, without the foresight, constant support and love of my parents, brother and my sister. I dedicate this thesis to them. You have been patient with me for long when I have shied away from family responsibilities. I would not have had the strength to go on, if I did not have you to fall back and count on. Thank you, I love you all.

I would also like to thank Arpita for all the support. During my graduate study at OSU, her patience, understanding, encouragement and love helped me go through every obstacle and make my life here enjoyable and productive. Being with you has inculcated in me a sense of looking at the "big picture".

VITA

December 23, 1974	Born – Jamshedpur, India
1999	B.E., Metallurgical Engineering
	Indian Institute of Technology, Roorkee, India
1999 - 2000	Senior Officer, Scientific Services Department
	Tata Iron and Steel Company, Jamshedpur, India
2000 - present	Graduate Teaching and Research Associate
	The Ohio State University, Columbus, Ohio

PUBLICATIONS

1. Manish Kamal and Yogeshwar Sahai, “Modeling of Melt Flow and Surface Standing Waves in a Continuous Casting Mold", Steel Research Int., 76, No. 1, 2005.

2. Manish Kamal and Yogeshwar Sahai, “Fluid Flow, Heat Transfer, and Solidification in a Continuous Casting Mold: A Modeling Study”, AISTech 2004 Conference, Nashville, TN, USA, September, 2004.

FIELDS OF STUDY

Major Field: Materials Science and Engineering

TABLE OF CONTENTS

LIST OF TABLES

LIST OF FIGURES

CHAPTER 1

INTRODUCTION

Electromagnetic forming (EMF) is a non-contact forming technique where large forces can be imparted to a conductive metallic work piece by pure electromagnetic interaction [1]. When properly applied, this can accelerate the sheet to velocities on the order of 200 m/s over a distance of a few millimeters. This high velocity forming can be quite beneficial. It can provide: improved formability, improved strain distribution, reduction in wrinkling, active control of springback and the possibility of local coining and embossing [1, 2].

If one is to use conventional electromagnetic forming coils to form directly, it is important that the EM pressure distribution is appropriate for the part that one would wish to form. It has been found that the velocity distribution within the sheet metal during forming significantly influences the result [3]. Risch *et al.* [3] have shown that puckers can form when the launch velocity is not uniform.

The spatial distribution of forming pressure can be controlled by the configuration of the actuator [4-6]. Traditionally EM coils have been used to form axisymmetric parts as in tube expansion, tube compression and by using flat spirals as shown in Fig. 1.1. One issue with spiral coils of any configuration is that the pressure distribution is not uniform. Figure 1.2 shows the typical example where a flat spiral coil was used to accelerate a circular disk. Here the pressure is zero at the center of the part and the edges and reaches a maximum midway between them. The flat spiral coil is shown in Fig. 1.3.

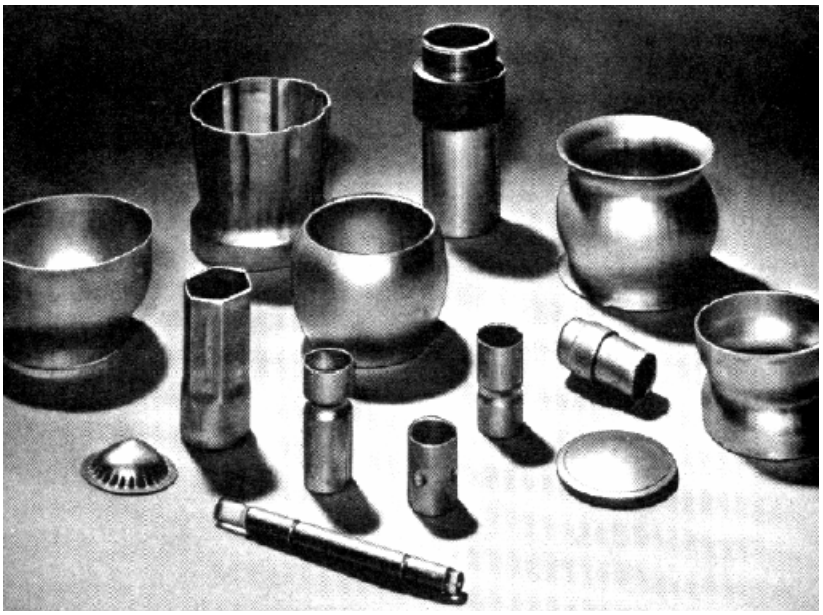

Figure 1.1: Typical parts made by electromagnetic forming [7].

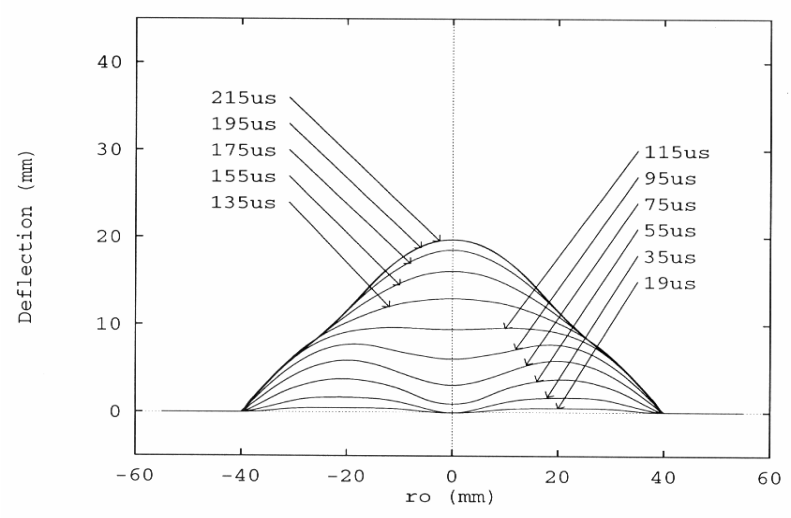

Figure 1.2: CALE calculated profiles of Takatsu disk [8] during deformation with a flat spiral coil [9]. The sheet is secured at its circumference.

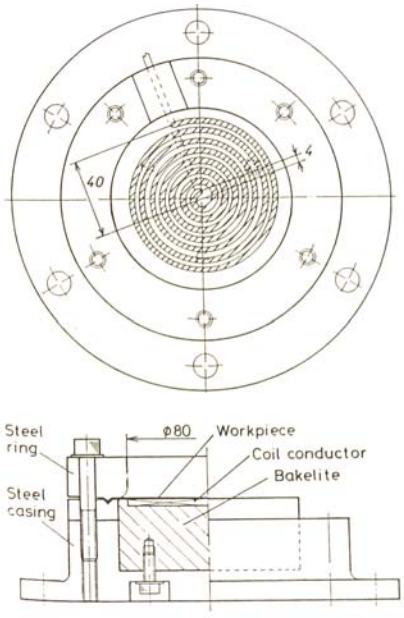

Figure 1.3: Flat spiral coil from Takatsu [8].

The early literature (from the first wave of electromagnetic forming research) seems to have only one reference to a non-axisymmetric coil [6]. It consists of an elongated actuator, and that work also discusses the non-uniform pressure distribution developed. Work on actuators for flat forming of sheet, has been limited and an actuator that gives a uniform pressure distribution is not available until now.

Uniform pressures can be developed if the current in the coil and sheet are both uniform and the gap between them is constant. It can be achieved in two ways: (i) a section along one perimeter of a flat spiral coil (which might be elongated). Although the pressure varies along the radius of the coil, if one takes a small section, the pressure distribution at that section is close to uniform. (ii) Use a linear actuator, like taking a section in the three bar coil. Along any particular bar the pressure is close to being uniform so long as the sheet to coil gap is small relative to the bar width.

Process efficiency is also of paramount importance. The cost of electrical energy in EMF is rather trivial, but if one is to use especially large energies or charging voltages, these cause problems with electrical interconnects, insulation and this puts large mechanical forces on the coils that can damage the electromagnetic coils. The approaches mentioned above can create a uniform pressure distribution *but*, the efficiency of such systems is poor.

This dissertation presents a new approach, which offers a uniform pressure distribution as well as high efficiency for flat sheet forming. The dissertation begins with the basics on

high velocity forming and the approaches used for coil design in Chapter 2. The details of the new coil approach; construction of the actuators and the experimental procedure is outlined in Chapter 3. Chapter 4 deals with the basic behavior of the uniform pressure actuator. A simplified analysis of the coil is presented in Chapter 5 that helps in the design of the system. Commercial codes that can be used in the design of the actuator are also discussed. Examples are then presented in Chapter 6 about varied applications of the coil specifically in three different areas: embossing, forming depressions and cutting. Some practical challenges in the design of the coil are discussed in Chapter 7. Chapter 8 summarizes the work on the new actuator and Chapter 9 describes the avenues for further investigation.

CHAPTER 2

HIGH RATE METHODS

Dynamic behavior of materials can differ significantly as compared to the behavior under static or quasi-static loading conditions. A simple illustration is the sand bag which is used by soldiers to stop bullets. Soft free flowing sand is effective against impact of velocity on the order of 1600 m/ s (30.06- caliber bullet speed) [9]. On the other hand a simple knife can defeat the bag. Also, consider a solid steel or wood plate not excessively thick. A bullet can possibly penetrate that but not a knife. Another example is the classic Harold Edgerton image shown in Fig. 2.1 [10].

Physics is very different in dynamic conditions and inertia can affect behavior significantly. The issue is if we can take advantage of dynamic effects? Our focus here is on using dynamic effects in metal forming. Typically inertia is ignored in metal forming. This is acceptable since the inertial effects are small and the velocity seldom exceeds 5 m/s. High velocity techniques can be practically used in metal forming and this adds process flexibility. Though new opportunities are apparent, basic understanding and creative thinking are needed [1].

Figure 2.1: Edgerton high speed image of a bullet cutting through a card [10]

2.1 High Velocity Methods

High velocity forming operations are considered to be operations where the workpiece velocities typically exceed 100 m/s [1]. These methods include techniques such as explosive forming and electromagnetic forming. These techniques are distinct from most other metal forming methods in that the workpiece is accelerated to a high velocity by the chemical or electrical force, and the kinetic energy of the workpiece is significant. The sheet metal workpiece then changes shape either as it strikes a die or is decelerated by plastic deformation. The physics that determines the launched profiles of the workpiece is different in different forming methods.

An important difference to be noted about dynamic processes is that in quasi-static deformation, we have, at any time, a situation of static equilibrium. This means that at any time, any element on the body has the summation of forces acting on it close to zero. At high rates one part of the body maybe stressed, whereas the other portion has not seen the stresses yet. In other words stress (and its associated deformation in terms of strain) travels in the bodies in the form of waves of a specified velocity. Thus dynamic deformation involves wave propagation whereas quasi-static deformation can be considered as a sequence of states of equilibrium that can be treated by the well known equations of mechanics [10].

High velocity techniques generally provide robust methods of performing metal forming operations that are quite difficult conventionally. Although these methods have been known for over 100 years and saw significant development (particularly in the 1960's), these methods have not been developed or documented so they can be routinely used to their potential [1]. However, because these methods work well on even hard to form materials, and because manufacturing systems are generally much simpler and can be established quickly, there is a recent resurgence in interest in these methods. There are a number of methods for HVF mainly based on the source of energy used for obtaining high velocities. The common ones are explosive forming, electrohydraulic forming (which uses an electric arc discharge to convert electrical energy to mechanical energy) and electromagnetic forming (EMF). Figure 2.2 shows a schematic of the different impulsive methods commonly used.

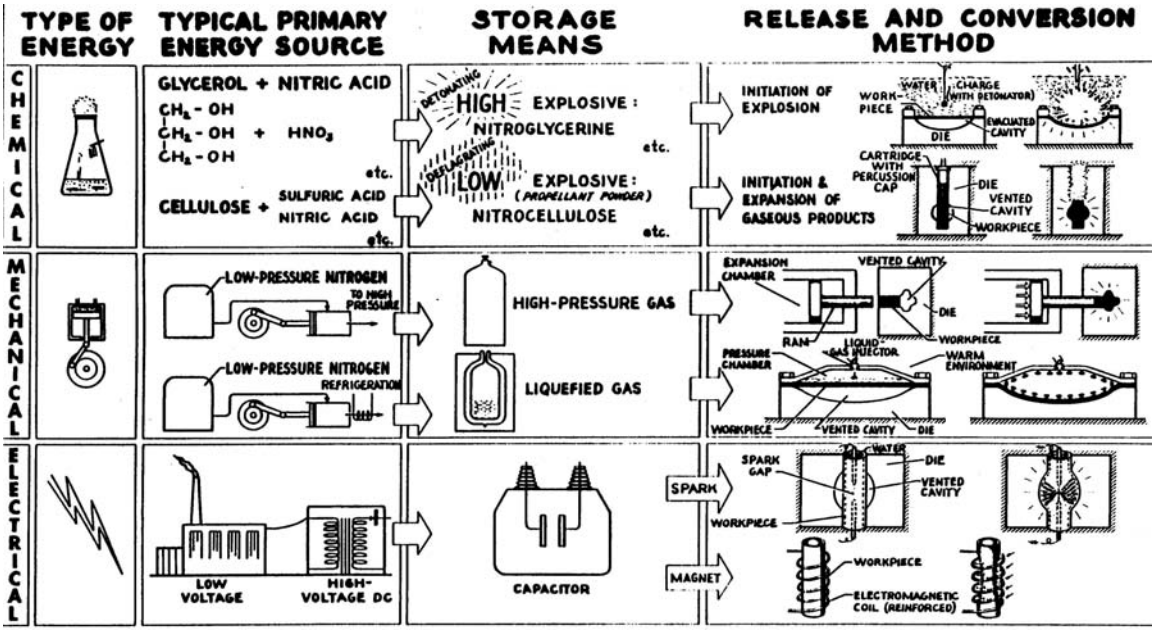

Figure 2.2: Impulsive methods available [12]

2.1.1 Explosive Forming

In this process the energy liberated due to the detonation of an explosive is used to form the desired configuration. The charge used is very small, but is capable of exerting tremendous forces on the workpiece. The U.S. Defense Advanced Projects Agency (DARPA) cites explosive forming as “a cost effective process for forming a variety of metals and alloys that results in remarkably high reproducibility (~0.5%) for complex, large metal structures. Used extensively in DoD projects, the applications include afterburner rings for the SR-71, jet engine diffusers, Titan “manhole” covers, rocket engine seals, P-3 Orion aircraft skin, tactical missile domes, jet engine sound suppressors, and heat shields for turbine engines” [1, 13].

Explosive metalworking can be quite inexpensive. High explosives have detonation velocities in the order of 3,500 to 8,000 m/s and energies on the order of 1 MJ/Kg [1]. A few cents worth of explosives can carry out the biggest of the forming experiments. However, both the transportation, storage and the working with explosives is severely controlled by the government. Table 2.1 gives a list of some common explosives and the energy associated with them [1].

Explosive	**Form of charge**	**Deformation Velocity (m/s)**	**Energy (Joules/ gram)**	**Storage Life**	**Pressure (GPa)**
TNT	Cast	7,010.4	780	Moderate	16.536
RDN	Pressure granules	8,382	1265	Very good	23.426
PETN	Pressure granules	8,290.56	1300	Excellent	22.048
Pentolite (50/50)	Cast	7,620	945	Good	19.92
Smokeless Powder	Powder	<1 m/s	300	Excellent	0.35

Table 2.1: Common explosives and their typical properties [1].

There are two typical ways in which explosives are generally used [1, 14, and 15]. One is the standoff operation where the explosive is set at a distance from the workpiece and detonated. This is the more common method used in sheet metal forming. Here a medium, typically water, is used to couple the explosive and the workpiece. In cases

where high pressures or velocities are desired, like in solid state impact welding, a contact method is used. In this case the explosive is detonated at a close proximity to the workpiece. Figure 2.3 shows some examples of applications of explosive forming. Figure 2.4 shows schematics of some common ways in which explosives are used.

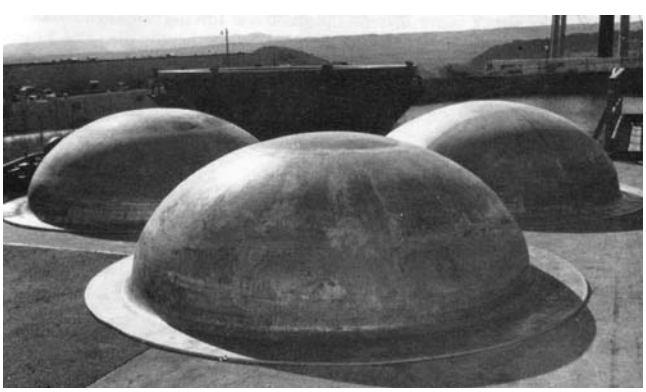

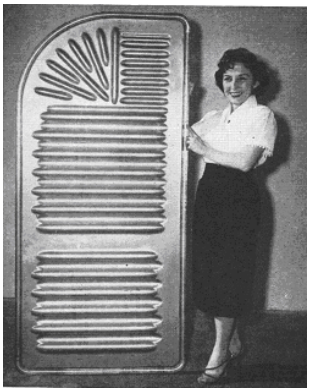

Figure 2.3: Applications of explosive forming, (a) 10-foot diameter domes formed explosively from 2014-0 aluminum [1, 14], (b) 321 stainless steel aircraft panel formed in a single operation with a kirksite die [15].

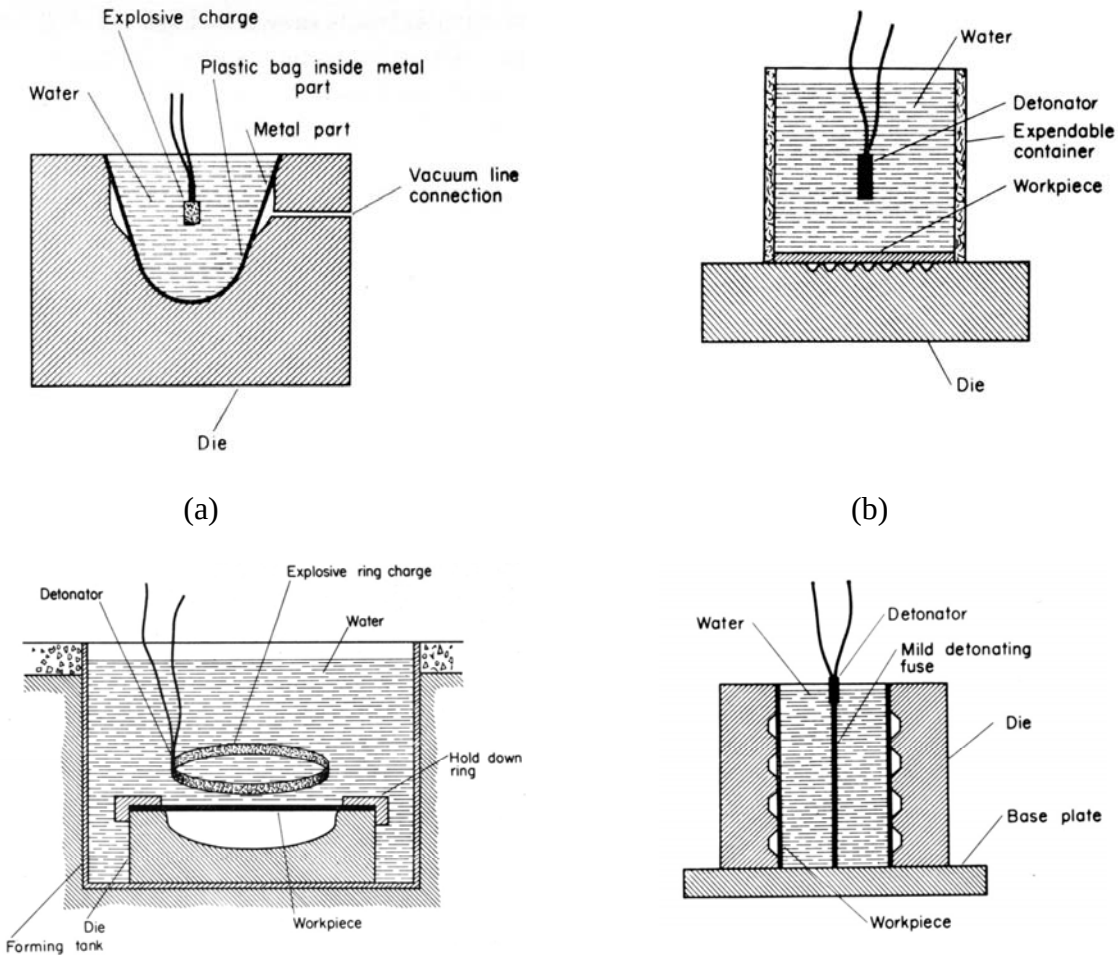

Figure 2.4: Schematics of typical explosive forming operations, (a) sizing with a water filled die cavity, (b) method forming a flat panel, (c) use of detonation cord to prescribe the pressure distribution in an open forming system, (d) use of detonation cord to form a cylinder. Open or closed die systems can be used [1, 15].

2.1.2 Electromagnetic Forming

In principle, an electromagnetic forming system consists of a capacitor bank, a conductive actuator and the metallic workpiece to be deformed [16-18]. The basic experimental scheme for electromagnetic tube expansion is shown in Fig. 2.5 [1]. The capacitor bank is connected to the actuator, which is near the workpiece. When the main switch is closed, the large current through the actuator produces a transient magnetic field that induces eddy currents in the nearby metallic workpiece. The currents in the actuator and metallic workpiece travel in opposite directions, according to Lenz's Law. The electromagnetic repulsion between the oppositely flowing currents, governed by the Lorentz force, provides the deformation force to the workpiece.

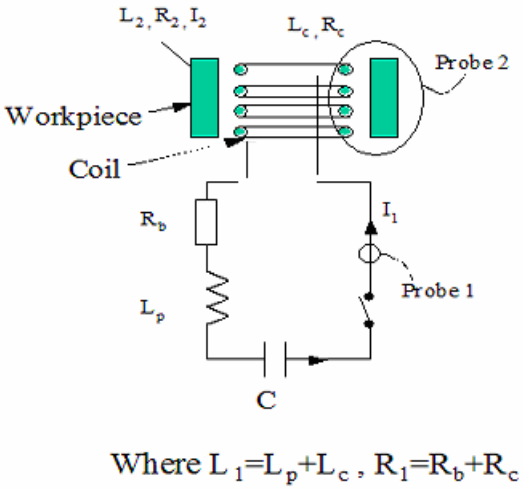

Figure 2.5: Schematic illustration of an electromagnetic forming operation [1].

This process is governed by the classical coupled differential equations [1, 19],

$$\frac{d}{dt}(L_1 I_1 + M I_2) + R_1 I_1 + \frac{Q_1}{C_1} = 0 \qquad \text{..... (2.1)}$$

$$\frac{d}{dt}(L_2 I_2 + M I_1) + R_2 I_2 = 0 \qquad \text{..... (2.2)}$$

where L_1, R_1 and C_1 are the inductance, resistance and capacitance of the bank and actuator. L_2 and R_2 are the inductance and resistance of the workpiece. M is the mutual inductance between the actuator and workpiece. Q_1 is the stored charge in the bank. I_1 and I_2 are currents in actuator and workpiece. R_b and R_c are the bank and coil resistances. L_c is the coil inductance and L_p is the parasitic bank inductance. Detailed calculations are complex because many aspects are coupled and vary with the motion of the workpiece [20-24]. The electromagnetic pressure distributions may take on complex configurations with advanced actuator designs. The electromagnetic force per unit length that acts between the actuator and workpiece can be approximated as [23],

$$\frac{F}{l} = \frac{\mu_0 I_1 I_2}{2\pi d} \qquad \text{..... (2.3)}$$

where d is the distance between the workpiece and the actuator and μ_0 is the magnetic permeability of free space. Required pressures can be easily obtained to exceed the plastic yielding of metal sheets and provide material acceleration to high velocity, by adjusting the stored charge in the bank.

An important feature of electromagnetic forming is that the workpiece must be conductive enough to get induced eddy currents. The efficiency of electromagnetic forming is directly related to the resistance of the workpiece materials. Materials with poor conductivity can only be effectively formed if an auxiliary driver sheet with high conductivity is used to push the workpiece [1].

2.2 Why High Velocity Methods?

The high velocity methods have had a recent resurgence in interest due to the need for greater use of aluminum alloys in the automotive industry. The weight saving of up to 50% and gains in fuel efficiency is largely responsible for this interest. Additionally, the superior recycle characteristic of aluminum is recognized as becoming of increasing importance as the total life cycle cost of automobiles becomes an issue [25-27].

The press forming of aluminum alloys has problems in comparison to steel principally due to very low strain rate hardening, low r (strain ratio) value and high galling tendency [25, 28 and 29]. Steels have significant strain rate sensitivity which is identifiable by a long arching stress-strain curve. Figure 2.6 graphically illustrates this point with a side by side comparison of two automobile door-inner panels from the same stamping die [25]. Panel A is a fully formed panel of specified production steel sheet that was produced after set-up trials indicated satisfactory tool performance. Panel B is a 6111-T4 aluminum panel of the same thickness as the steel and was processed directly after the steel panel. The wrinkling and large splits in the aluminum panel occurred within the first 25% of the

tool stroke and were not unexpected [25]. High velocity methods allow the forming of Aluminum alloys in a better way [1, 25].

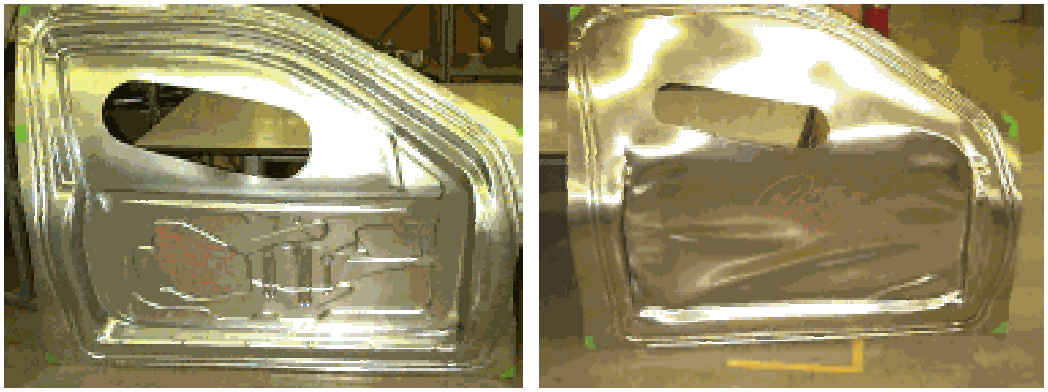

Panel A, production steel Panel B, 6111-T4 aluminum

Figure 2.6: Automotive door-inner panels, forming demonstration [25].

The focus in this section will be on the benefits of electromagnetic forming, though some of these are generic to high velocity methods. The issues that electromagnetic forming can address include improved formability, improved strain distribution, reduction in wrinkling, active control of springback and the possibility of local coining and embossing [30]. Some of these issues will be reviewed here.

2.2.1 Enhanced Formability

Electromagnetic forming provides a technique where the formability is not limited by the traditional flow limit diagram (FLD). Traditionally, the main application of electromagnetic forming is to improve the formability of metals [14, 17 and 18]. Electromagnetic forming usually is used to accelerate the metal sheet at velocities which are 100 to 1000 times greater than the deformation rates of conventional quasi-static forming such as the sheet metal stamping (~0.1 m/s to ~100 m/s) [25]. High deformation velocity makes these two kinds of forming processes quite different. It is well known that high deformation velocity (over about 50 m/s) can significantly increase the limit strains by several times, compared with those obtained in conventional forming. Many of the commercial metals including aluminum alloys have demonstrated increases in formability of 100% or more in comparison to the elongation obtained at low, quasi-static rates [14, 17, 18, 25, 31 and 32]. Figure 2.7 shows the results of some experiments in high velocity forming of aluminum alloys presented in FLD data format [31].

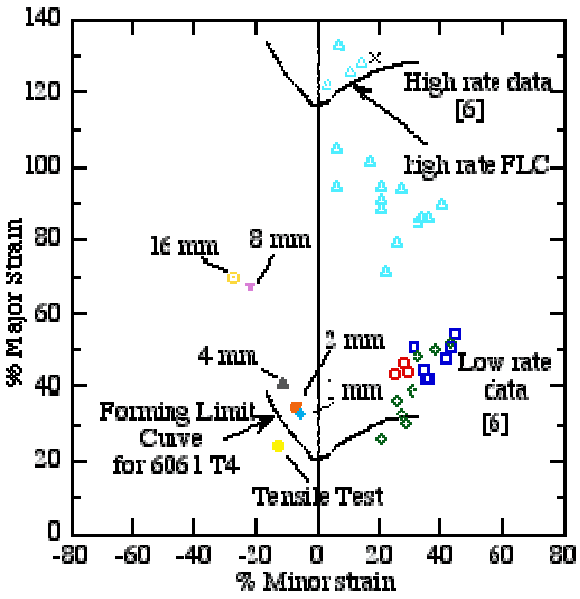

Figure 2.7: Forming limit diagram (FLD) with high velocity forming data [31].

Some of the important factors that affect the high velocity formability are:

(a) Inertial stabilization of necks. The effect of inertia on a neck is the most important factor that explains the improved formability in high velocity forming. Several researchers have shown that failure in a tensile sample is delayed when inertial forces are relatively large [33-38]. Hu and Daehn [33] analyzed this effect by a one-dimensional finite element model, and believed that this inertial stabilization of necking is a first-order effect in high velocity formability. During uniform deformation, the local velocity of any location of the sample will vary with its position along the sample. If necking is to ensue, a sharp velocity gradient will be developed over the region of the neck. In order to

accommodate the velocity gradient, the material in the necking region must experience an increasingly large acceleration, which produces non-uniform inertial forces. The inertial forces tend to produce additional tensile stresses outside the neck, and then additional extension can be obtained. This effect is always present, but only significant at high deformation velocity.

(b) Inertial ironing. Ironing is used traditionally to generate very large deformation. Large through-thickness stresses are generated between tools to extend the sheet materials by squeezing the sheet in the through-thickness direction. In high velocity forming, the impact with the die and the rapid deceleration produces a large through-thickness compressive stress that can also produce lateral extension of the material. This is presently termed inertial ironing [18]. The through-thickness pressure can easily become on the order of the materials flow stress in electromagnetic forming, and then should be able to affect the deformation characteristics in forming.

There are other effects that may be important for formability in high velocity forming [1, 30-33].

2.2.2 Benefits due to impact

The very large pressures available from impact or directly from explosives make possible several things that are difficult or impossible with conventional forming. First, by producing a sufficiently high impact velocity, large pressures can be developed over a large surface. High velocity forming techniques offer the ability to perform coining-like

operations over large areas. An example and more details of this effect are discussed in Chapter 6.

Also the impact of sheet metal with the tool at high velocities generates large compressive impact stresses. This can reduce springback, improve surface finish and enhance formability. The large impact pressure causes sheet metal to closely conform to the shape of the die. One of the primary reasons for this is that upon impact with a rigid tool, a plastic wave front will propagate through the sheet thickness, this will cause the residual elastic strains in the sheet to be minimized (these elastic strains cause distortion and springback). Second, upon impact the large pressures will cause the struck surface to displace and the rebound wave will tend to lock produce interference fit between the sheet component and the die [1, 18].

2.2.3 Wrinkling is suppressed

Wrinkling is caused by compressive stresses and usually necessitates a change in direction of the material flow. When a sheet is launched with a particular velocity profile, each part of the sheet would like to travel along its launch path. At high velocity wrinkling is inhibited my material momentum [1]. As an example, one can reduce the diameter of slender rings with an electromagnetic impulse by a 2:1 ratio or more [30]. Another example is shown in Fig. 2.8.

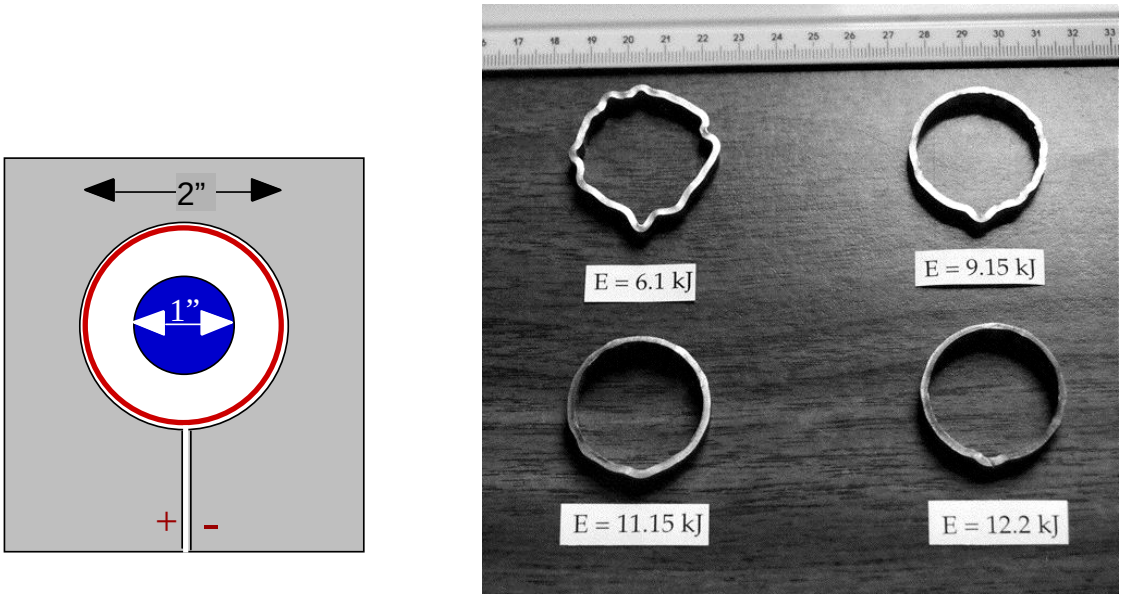

(a) (b)

Figure 2.8: Example of electromagnetic high velocity crimping of thin aluminum tube onto a mandrel; (a) Schematic of the coil made from a 1.32 cm thick 6061-T6 plate, (b) Behavior of initial 1.651 mm thick, 5.08 cm OD 6061 T6 rings compressed onto a 3.175 cm diameter mandrel at varied indicated launch energies [1, 39].

2.3 Techniques for Design of Coils

There are several different philosophies on how electromagnetic forming actuators can be fabricated. Most of the work to date has been with solenoidal or spiral coils [1, 6]. There are a number of ways in which actuators can be distinguished. Belyy *et. al.* [4] have used the application based approach to distinguish actuators. They have distinguished actuators as compression coils (as in tube reduction), expansion coils (e.g. for assembly,

flanging, punching holes in the cylinder) and flat forming coils (as in flanging, cutting and recessing). Another approach is to distinguish coils based on the design of the coil [1] and is discussed below. Each of these actuators has a different approach and correspondingly different optimal capacitor bank system characteristics associated with it.

2.3.1 Single Turn and Machined Actuators

These are the simplest of all the actuators in construction. Consider an electromagnetic compression coil in Fig. 2.8 (a). The coil is made by simply cutting a slot and hole in a conductive plate. High material conductivity will improve system efficiency and high material yield strength provides a strong, robust, long-life coil. High strength aluminum alloys, copper-beryllium alloys, brasses, and oxide dispersion strengthened materials such as Glidcop® are all good candidate coil materials [1].

This basic approach of machining coils from relatively thick flat plate can also be used to form effective actuators for the different forming configurations. Figure 2.9 shows an example of an intuitive design for forming flat sheets [1]. Here the electromagnetic field intensity is intentionally varied from place to place by varying the spacing between the conductors. As discussed previously, the shape of the coil determines the pressure distribution and launch velocity distribution for the sheet. Here a higher magnetic pressure is developed in the bottom half of the coil than in the top. The effect of varying the distance between the conductors has been discussed in detail in Chapter 7.

Figure 2.9: Example of a coil designed for forming flat sheet using high strength Al [1].

2.3.2 Multi Turn Actuators

These types of actuators are the most common and are the kind used in this study. They may be constructed by coiling a conductive wire (often common copper magnet wire) over a strong non conductive mandrel such as grade G-10 laminated phenolic composite (or a single-use coil can be created by only using the wire itself). Reinforced epoxy or urethane is often used as a structural and insulating over layer. Compression, expansion or flat coils can all be made following this same general approach [1]. According to Daehn [1], there are two important limitations of this type of coil. First, the coil is usually limited to pressures on the order of 7,000 psi, if they are to be used for many operations. The coil materials determine the pressure the coil can withstand since the forces on the workpiece and coil are equal and opposite. Second, it is usually difficult to use a very fine winding pitch to increase local field intensity due to insulation needs.

This also limits the local pressures that can be generated from this kind of coil. Both these issues can be partly treated in short-run production by using inexpensive coils that are essentially disposable [1].

2.3.3 Field Shaper

In general, the highest electromagnetic pressures can be generated when the working surface of the coil is made from a monolithic block of a high strength (and high conductivity) metal [1]. Hence, large pressures can often be created with single turn coils, but because single turn coils typically have quite low inductance, they are often quite inefficient. Field shaper based coils can be used to develop high electromagnetic pressure while being able to increase and tailor the inductance of the coil. The operation of a field shaper coil is illustrated in Fig. 2.10. A typical multi-turn coil is still used to create a magnetic field. This is coupled to a secondary inductor or field shaper. As schematically described in Fig. 2.10, if properly designed, essentially the entire current flux (amp•turns) that is created in the primary current can be transferred to the bore of the shaper. Belyy *et al.* [4] provide some good design guidelines for these actuators. The coil is able to concentrate large magnetic pressures in a desired area but is less efficient than a well-designed single-stage coil.

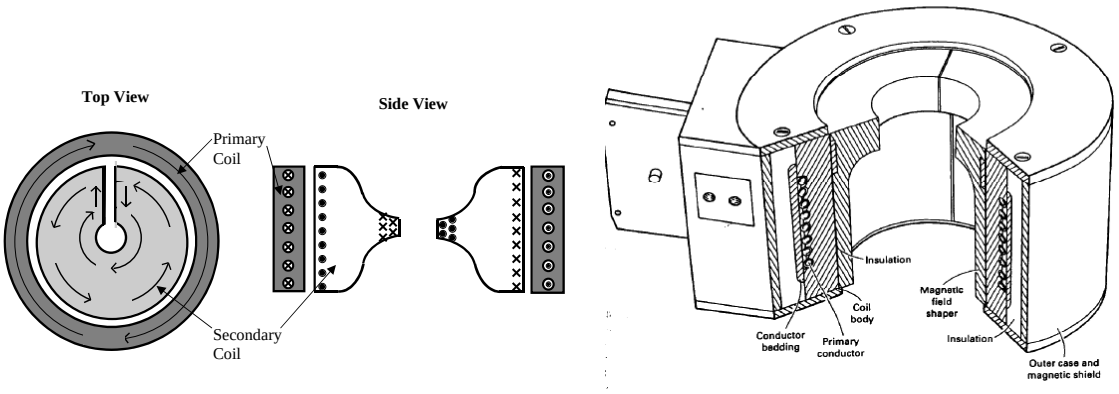

(a) (b) (c)

Figure 2.10: Field shaper (a) shows the behavior of a field-shaper based coil looking at the coil cross section. The many turns of the primary coil induce a current in the shaper; (b) shows the situation looking down the axis of the shaper. A slot in the coil forces the current to the bore of the coil, concentrating current there. (c) shows the practical construction of a field-shaper based coil [1].

2.4 Applications of Electromagnetic Forming

Electromagnetic forming is a process that has been applied since the 1960's, but is still not used very extensively. Its common application is in assembly operations to form axisymmetric parts, using compression or expansion solenoid type forming coils. Most of the applications are for the swaging of tubular components onto coaxial mating parts for assembly. The method is also used, though not commonly in forming of shallow shells from flat sheets using flat spiral coils [40-42]. Figures 2.11(a)–(c) show schematics of the

general classes of electromagnetic forming coils and workpieces. A recent hybrid approach of incorporating coils in the press is shown in Fig. 2.11 (d).

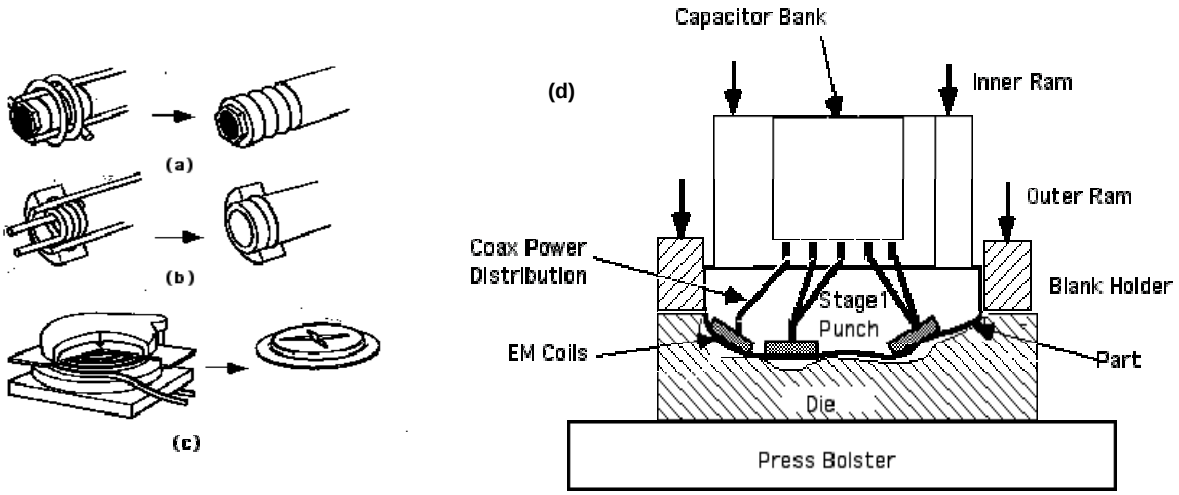

Figure 2.11: Electromagnetic forming application:(a) tube compression [42]; (b) tube expansion [42]; (c) sheet or pan forming [42]; (d) Matched tool-electromagnetic hybrid sheet forming [25]

A recent industrial application of electromagnetic forming is shown in Fig. 2.12. High-lift wing panels in the 777 (and retrofit in other Boeing aircraft) are manufactured with EM forming. These have shown lifetime fatigue resistance and are manufactured with permanent coils [1].

Figure 2.12: Torque tubes used in Boeing 777 showing the behavior of a tube subjected to torque overload testing. Failure is outside the joint region. [1].

2.5 Summary

Electromagnetic forming is a well studied subject with a lot of published research dating back to the 1960's, but the application of this approach is still very limited in industry. The work to date has primarily focused on assembly operations using axisymmetric coils. Flat forming using this approach has seen limited use. Axisymmetric coils have a non uniform pressure distribution. The principal goal of this project is to exploit the advantages of electromagnetic sheet metal forming using a uniform pressure actuator. Our previous work has proven the feasibility of electromagnetic forming. The current work aims at extending the capabilities of this process.

The limited information on flat forming using electromagnetic forces brings some difficulties into the study. Even electromagnetic forming on the whole is still in its early stages of development and the more immediate need now is to show the enormous

capabilities of the process. Also there is a need to have a predictive capability and good engineering tools for the design of the process. The key to success in improving the reliability and efficiency of the process is in getting better with each step along the learning curve.

CHAPTER 3

EXPERIMENTAL PROCEDURE

By design this dissertation is written in a tutorial manner to describe the theory, engineering calculations and applications of the rather novel uniform pressure actuator. As a result of this, several experiments are briefly described and the results reported. Some of the experimental procedures and the equipment details that are general to all the experiments follow.

3.1 Capacitor Banks

Two commercial Maxwell Magneform capacitor banks were used for experimentation. Figure 3.1 shows the first bank which has a maximum stored energy of 16 kJ. The energy is stored in 8 capacitors, each with a capacitance of 53.25 μF. The system has maximum working voltage of 8.66 kV. Both the number of capacitors and charging voltage can be changed to control the discharged energy and voltage. The second bank has a maximum stored energy of 48 kJ with a maximum working voltage of 10 kV (Fig. 3.2). The energy is stored in 8 capacitors, each with a capacitance of 125 μF. The bank is charged using a

460 V single phase AC line. The peak line current is 35 A and the average line current is 10 A to 16 A [39]. The capacitor usually takes a few seconds to charge at maximum energy. The inductance and resistance values for the 48 kJ bank are given in Appendix A.

Figure 3.1: Photograph of the 48 kJ Maxwell Magneform capacitor bank.

Figure 3.2: Photograph of the 16 kJ Maxwell Magneform capacitor bank.

3.2 Concept of the Uniform Pressure Actuator

A novel concept of an electromagnetic actuator which develops uniform forming pressure was developed at the Ohio State University by Dr. Glenn Daehn. Figure 3.3 shows a schematic of a section through the uniform pressure coil. When the capacitor bank is discharged, the primary current flows through the primary coil. The primary coil is well insulated from the outer conductive channel. The outer channel and the sheet metal form a closed circuit and the induced current flows through it. Repulsive Lorentz forces develop between the opposed primary and induced currents, causing sheet metal to be thrown at the die with high velocities. Since the induced current path completely encircles the coil, there is little loss of the magnetic flux energy and hence better

efficiency. Also, since the primary coil repels from both the sheet and channel, it is forced onto a mandrel and this can provide a robust coil design.

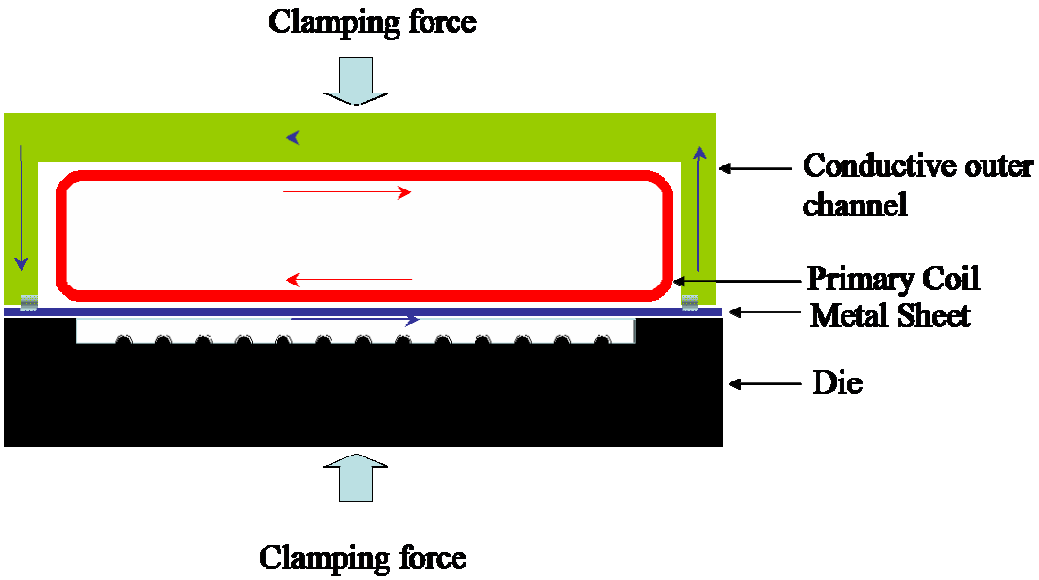

Figure 3.3: Schematic of a uniform pressure coil. The primary coil has many turns going into the depth of the paper.

Figure 3.4 shows the first attempt at a UP actuator. Insulated copper wires were wound on a G-10 (phenolic laminated composite) insulative core. A cut tube was used as an outer channel. The coil was potted in urethane to provide electrical insulation and

mechanical support. Encouraging results from this actuator were used to develop the concept further.

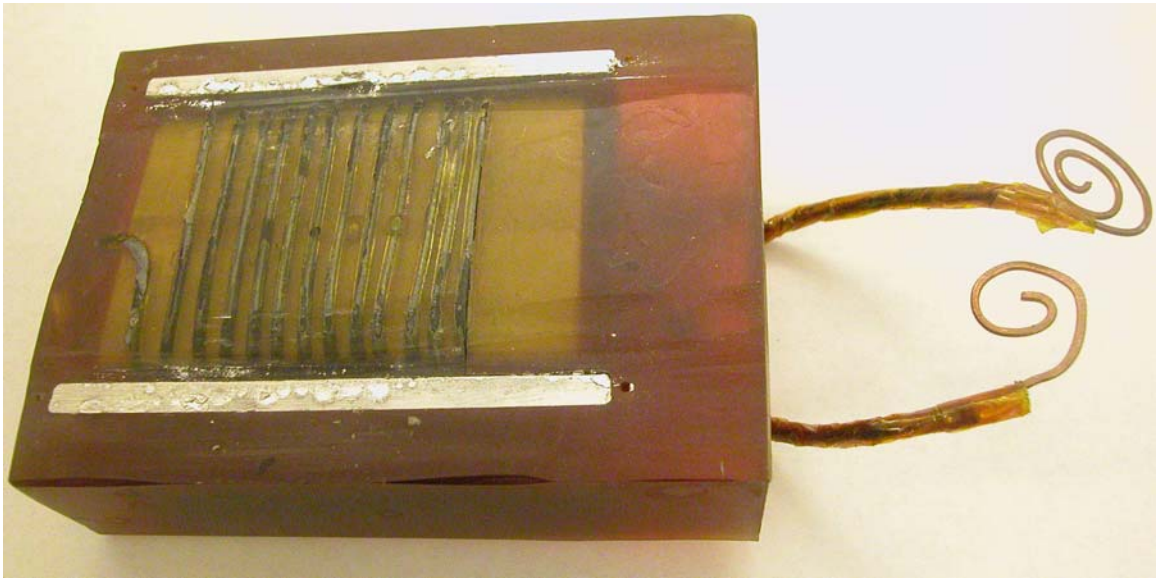

Figure 3.4: An actuator designed to evaluate the concept of the uniform pressure actuator.

3.3 First Generation Actuators

These were among the first actuators designed. The detailed construction of Actuator 1 is shown in Fig. 3.5. It shows a coil of 15 turns. A G-10 laminated phenolic composite block was machined to provide grooves to incorporate the required number of turns of a copper magnet wire (cross-sectional area of 9.0 mm^2). The G-10 block was then placed inside an Al 6061-T6 channel (7.5 x 2.5 x 9.375 cm and 0.3125 cm thick) which has

Kapton® insulation on its interior. Urethane potting was then used to provide insulation and structural support. A Mylar® sheet is placed in-between the metal sheet and the coil for insulation. The aluminum channel is placed on top of the coil. The coil with the metal sheet is then clamped using an arrangement of eight nuts and bolts. The system is then connected to the 16 kJ capacitor bank for forming operation.

G-10 block with 15 turns Cu

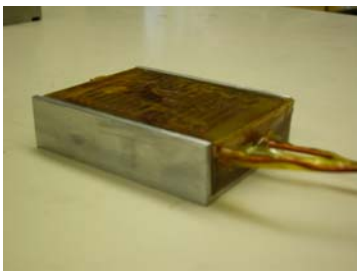

Coil in epoxy with Al c-channel

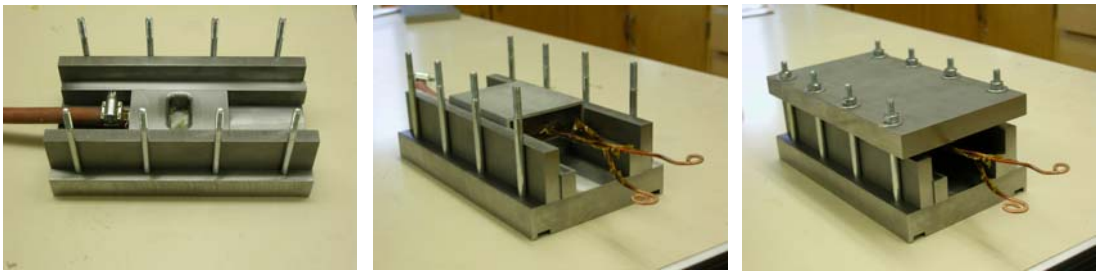

Stages in the assembly of the setup ⟶

Figure 3.5: Construction of the 1st generation 15-turn uniform pressure actuator.

3.4 Second Generation Actuators

The second generation actuators, use a better contoured outer channel in which the coil is fixed. This gives the actuator better mechanical and electrical integrity.

3.4.1 Second generation with aluminum outer channel

The CAD file of a 2nd generation actuator (referred to later as Actuator 2) is shown in Fig. 3.6. The outer channel was specially designed to provide two distinct contact surfaces with the sheet metal.

Figure 3.7 shows the 2nd generation actuator, a coil of 23 turns with an Al outer channel (15 x 15 x 5 cm). Based on earlier experiences, a G-10 block was machined to provide grooves to incorporate the required number of turns of copper wire (cross sectional area of 11.5 mm^2).

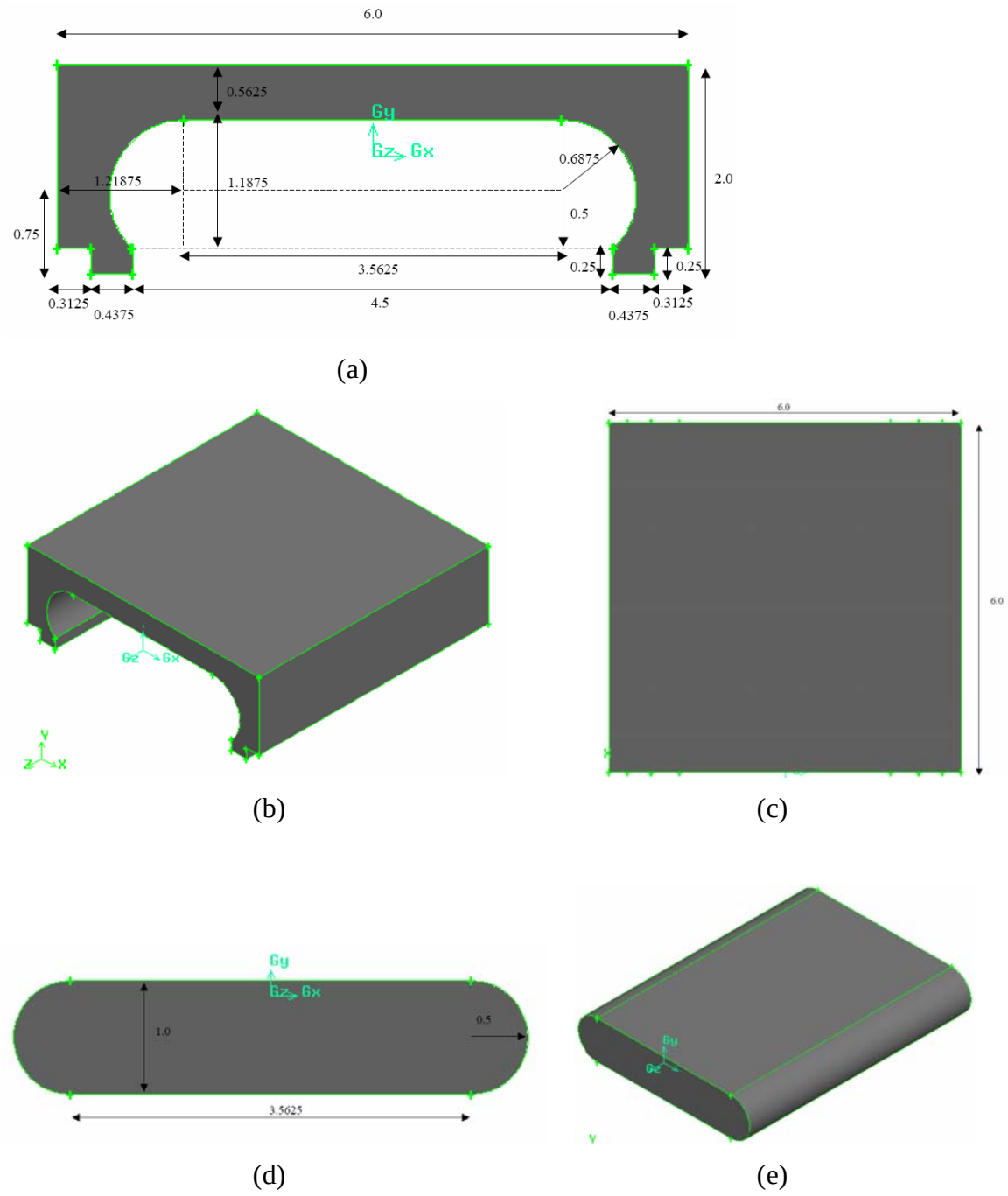

Figure 3.6: Design for Actuator 2; (a) front view of the outer channel, (b) isometric view of the outer channel, and (c) top view of the outer channel, (d) front view of the un-machined inner mandrel, and (e) isometric view of the un-machined inner mandrel. All dimensions in inches.

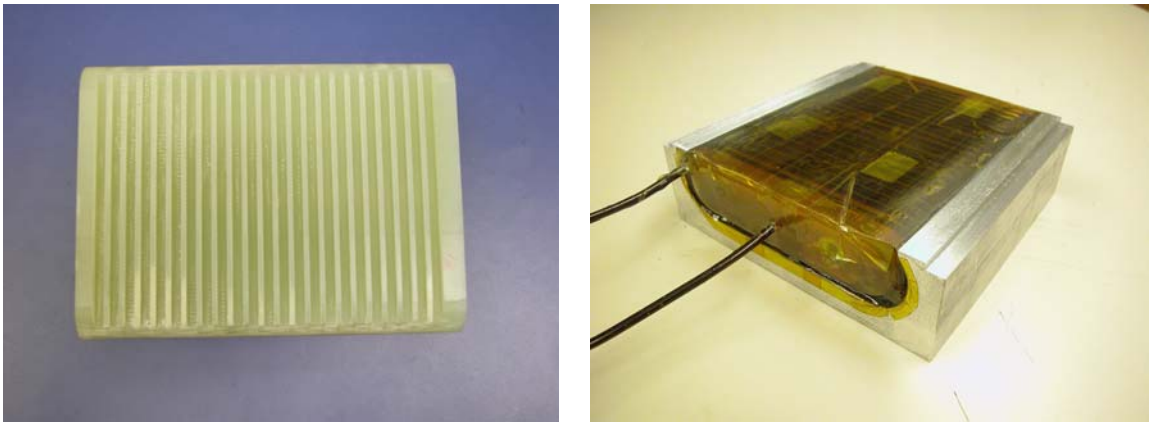

(a) (b)

Figure 3.7: A 2nd generation uniform pressure coil, Actuator 2; (a) Machined G-10 block for the mandrel, (b) A 23 turn coil with a fixed outer Al channel.

The setup designed for this actuator is shown in Fig. 3.8. The assembly uses the same concept as the earlier generation of an arrangement of eight nuts and bolts.

(a)

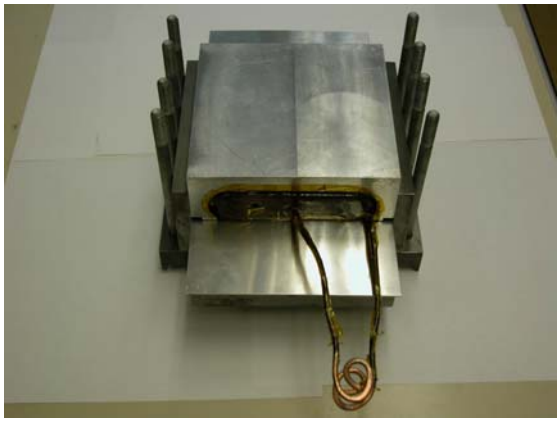

(b)

(c)

Figure 3.8: Experimental setup for Actuator 3; (a) lower part of the assembly with a removable die, (b) lower assembly with the sheet on top of the die and the actuator covering it, and (c) The clamped assembly with the two leads that connect to the capacitor bank.

3.4.2 Second generation with copper outer channel

This actuator (later referred to as Actuator 3) uses a contoured outer channel. In this case however the outer channel was made from Alloy 110 copper. Copper is soft, has higher conductivity, more conducting oxides and higher melting point than aluminum. This is beneficial for the electrical contact between the sheet metal and the outer channel (discussed in detail later under electrical contacts in Chapter 7). Successful results from the smaller setup were used to scale the design for forming bigger panels in this case (discussed later in Chapter 5). The in-house code was used to predict the design parameters like the forming pressure required, peak currents, number of turns, etc.

The CAD file of the 2nd generation actuator with Cu outer channel is shown in Fig. 3.9. This is the largest actuator that was designed in the current study. Rectangular sectioned copper wires (2 mm x 6 mm) were used for the 15 turn coil.

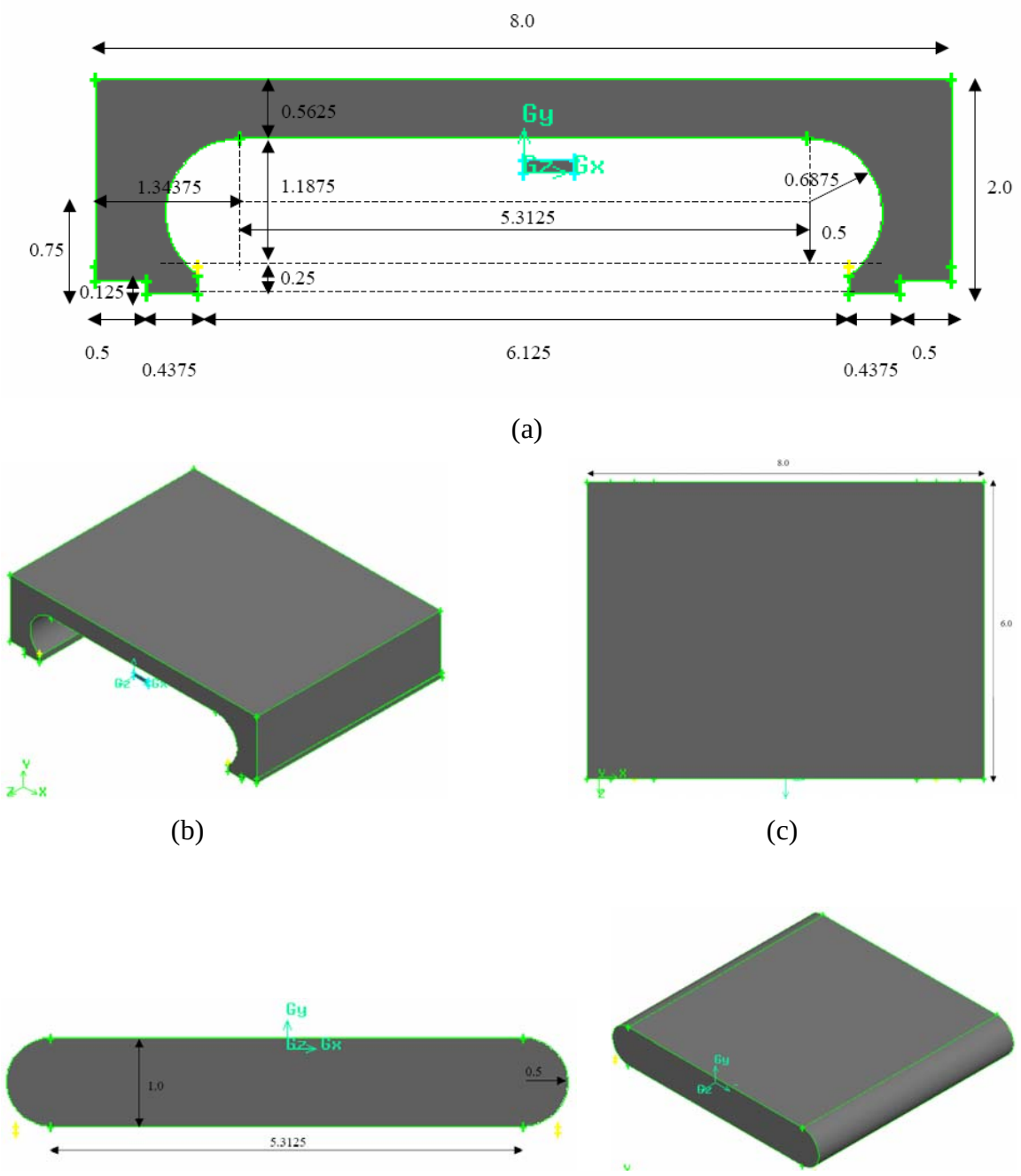

Figure 3.9: Design for Actuator 3; (a) front view of the outer channel, (b) isometric view of the outer channel, and (c) top view of the outer channel, (d) front view of the un-machined inner mandrel, and (e) isometric view of the un-machined inner mandrel. All dimensions in inches.

This actuator was used for multiple-step forming. A single coil covering the entire width of the feature would be high in inductance with a low forming efficiency (discussed in Chapter 5). The forming was carried out as a three step process with the die with the sheet metal being stationary and the actuator was moved over the die. A schematic is shown in Fig. 3.10. The coil construction has been shown in Fig. 3.11.

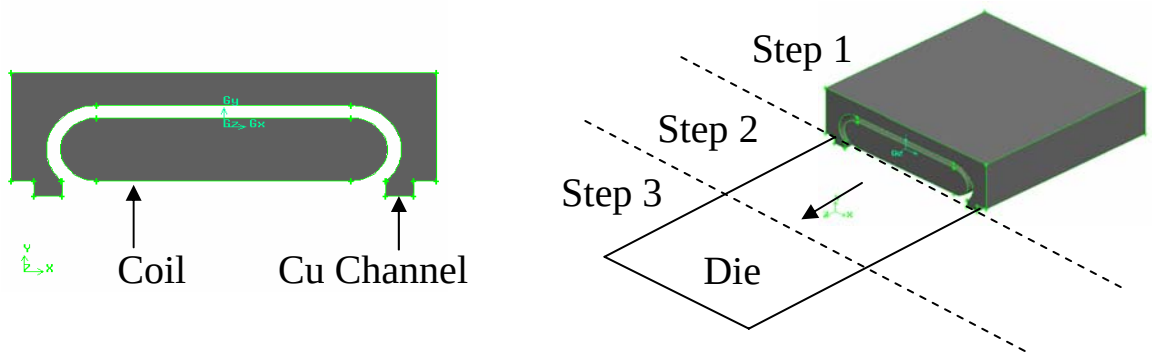

Figure 3.10: Schematic of the multiple step operation using Actuator 3.

Copper channel

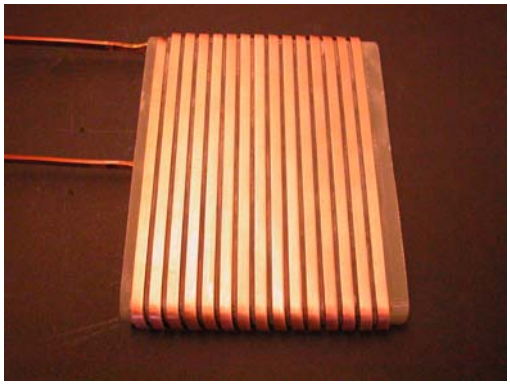

G-10 mandrel with 15 turns of Cu wire

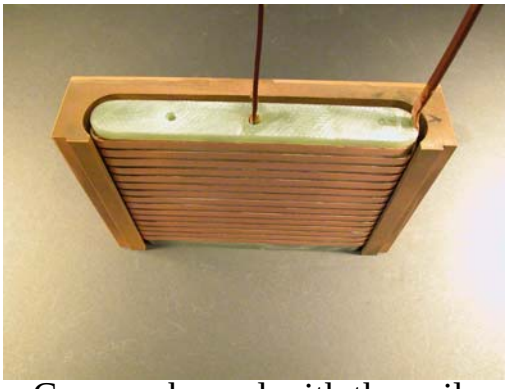

Copper channel with the coil

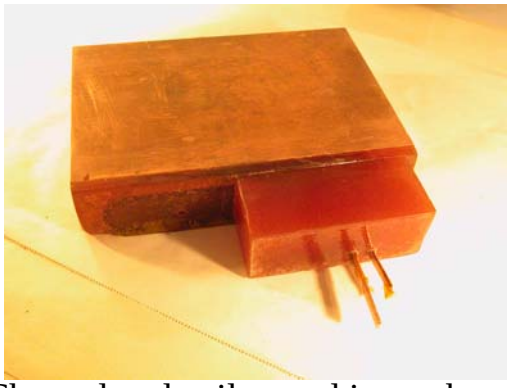

Channel and coil potted in urethane

Figure 3.11: Steps in the construction of Actuator 3, 2nd generation actuator with Cu outer channel.

A 100,000 lbs press was used instead of the nut and bolt arrangement. This simulates the actual industrial operation of EM forming and adds the capability of applying higher, uniform and precisely controlled loads. The setup for the press has been shown in Fig. 3.12. A G-10 insulative base was used to isolate the electrical path of the coil. The rubber pad is helpful in distributing the clamp load evenly onto the coil surface even if the surfaces are not entirely flat. It also acts as an electrical isolator.

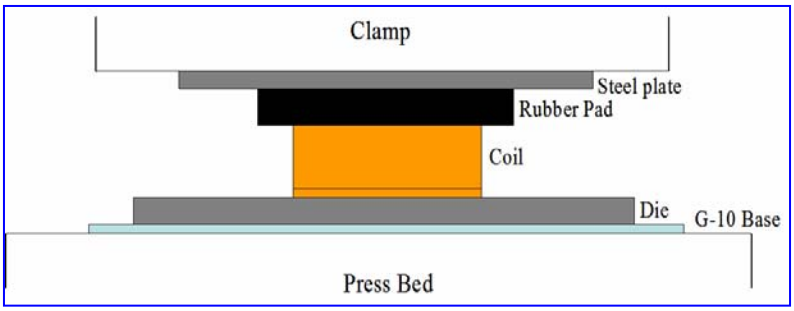

(a)

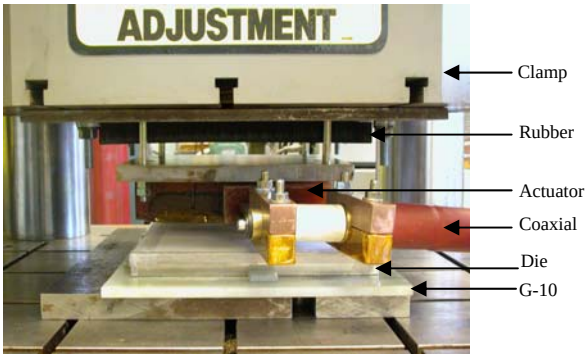

(b)

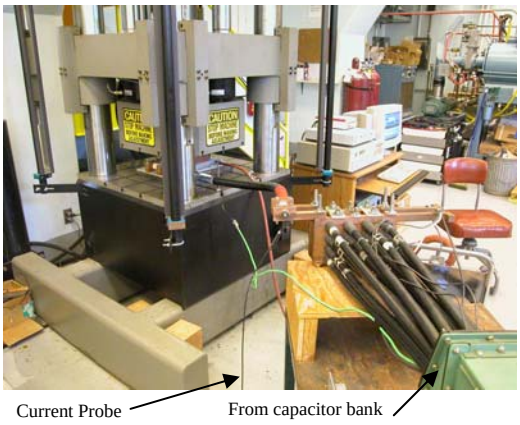

(c)

Figure 3.12: The actuator setup in the press for Actuator 3; (a) schematic of the setup in the press, (b) actual setup showing the press with the coil and (c) connection of the actuator to the capacitor bank.

3.5 Third Generation Actuators

This generation marks the next stage of a more formal design process for both the coil and setup design and manufacturing. Conceptual sketches were converted into CAD files with the help of Axxiss Engineering, Canton, Georgia. The coil and its setup were manufactured at American Trim, Lima, Ohio. Figure 3.13 shows the CAD file of the coil setup.

Robust coils were manufactured using machined ASTM B16 Brass and Cu 110 as shown in Fig. 3.14 Contoured copper/brass outer channel were made to evaluate the effect of material on actuator performance.

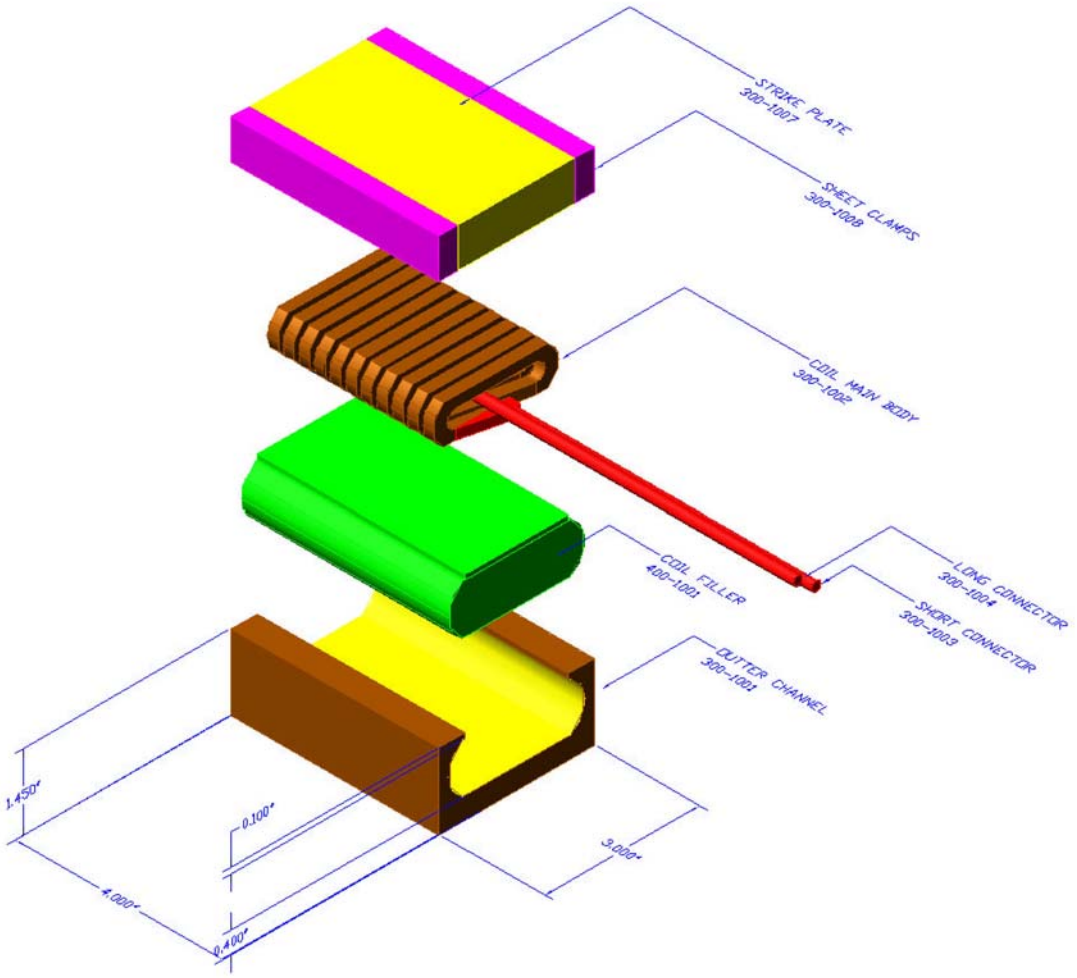

Figure 3.13: CAD image of the machined coil setup in the outer channel with the die (dimensions in inches).

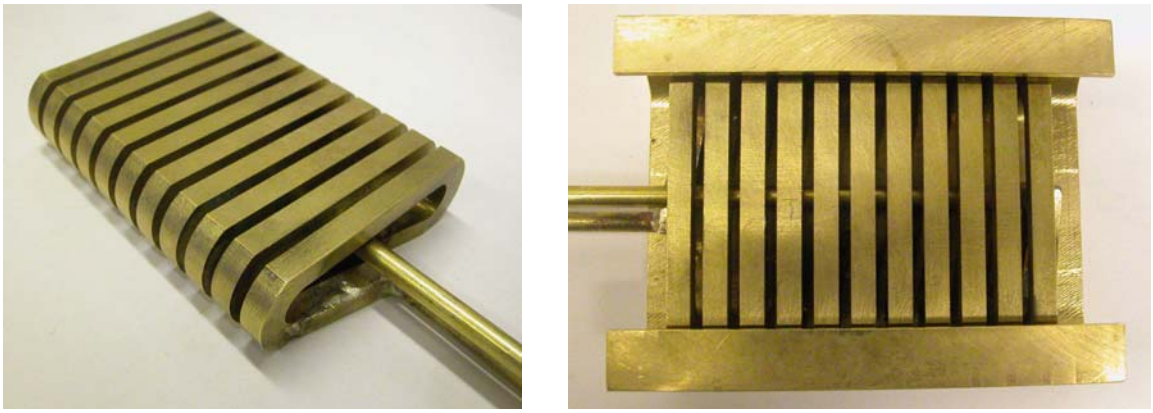

(a) (b)

Figure 3.14: Third generation actuators; (a) Machined brass coil and (b) unpotted machined brass coil in a brass outer channel.

Figure 3.15 shows the CAD file of the vacuum chamber designed to study the effect of vacuum level on embossing. The setup has the ability to study the effect of standoff between the sheet metal and the die.

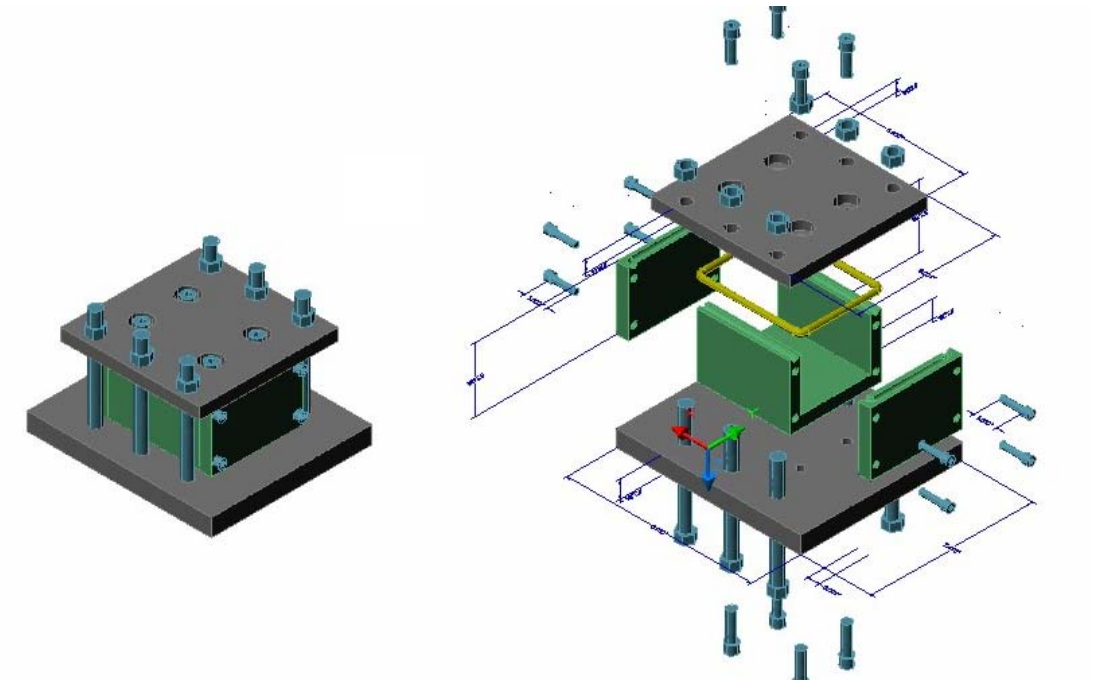

Figure 3.15: Vacuum chamber design for the 3rd generation actuators. The color coding is as follows: green- G10, gray- mild steel and blue- fasteners.

3.6 Dies

A number of dies were used for evaluating the forming characteristics of the uniform pressure actuator. The details of the dies are summarized below.

3.6.1 Free Forming Dies

Four dies were used here. Die FF1 is a free forming mild steel die with a rectangular opening. The die is shown in Fig. 3.16 (a). The free forming die was filled with urethane to give a fixed end (25 x 19 x 89 mm with 12.7 x 38.1 x 4.76 mm recess with 4.76 mm

fillet along the recess). This was used for studying the basic behavior of the uniform pressure actuator. The die was provided with a 4.76 mm hose barb connection for vacuum in the die and was designed for use with Actuator 1.

(a) (b)

Figure 3.16: Die FF1, (a) free forming die and (b) urethane potting on the same die to get a fixed end.

Die FF2 is also a free forming mild steel die and was used for experiments on forming into a rectangular cavity. The die dimensions were based on BMW die for car door pockets. The geometry was chosen to simplify the earlier trials of forming car door pockets. A schematic and the die are shown in Fig. 3.17. A vacuum port was provided in the die.

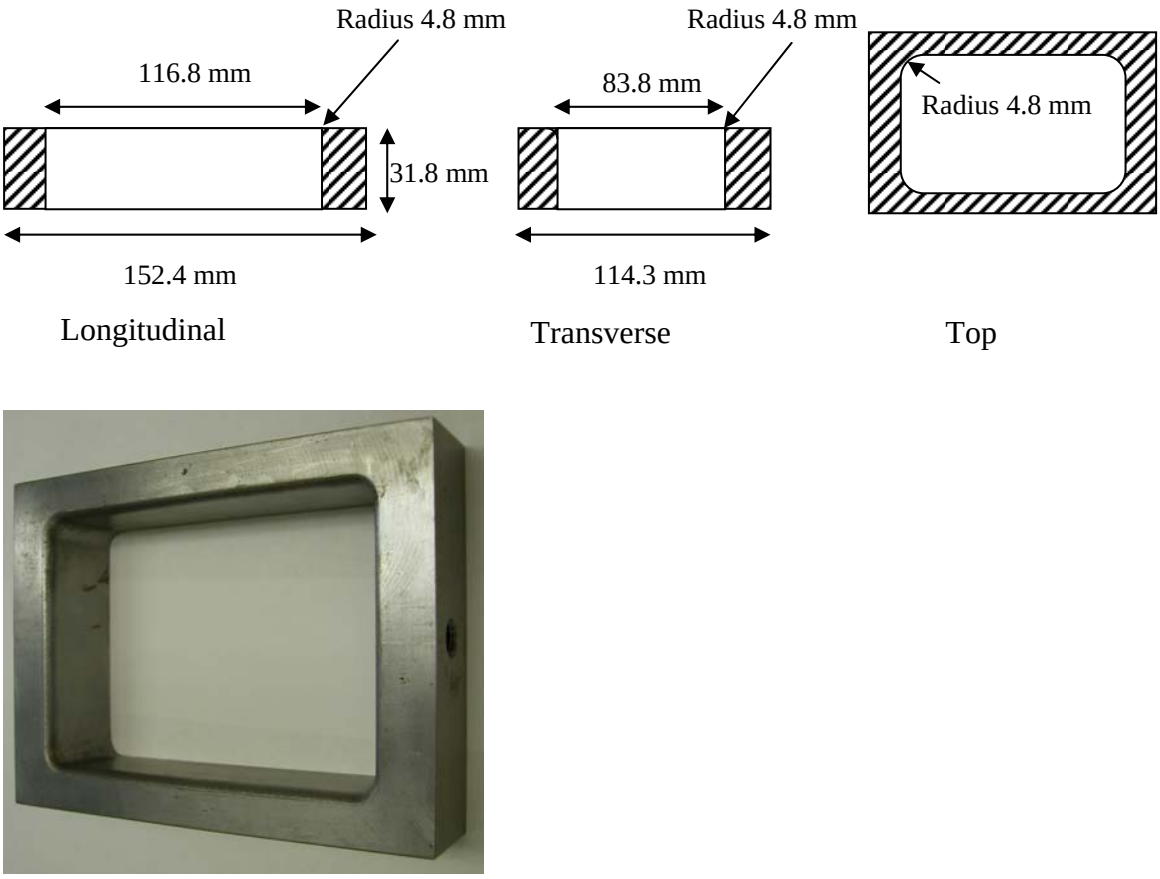

Figure 3.17: Die FF2, used for forming into a rectangular cavity.

Die FF3 was also used for car door pockets project. As compared to Die FF2, the entry radius was increased and the open area was decreased to control draw-in. A schematic and the actual die are shown in Fig. 3.18. Both Die FF2 and FF3 were designed for use with Actuator 2.

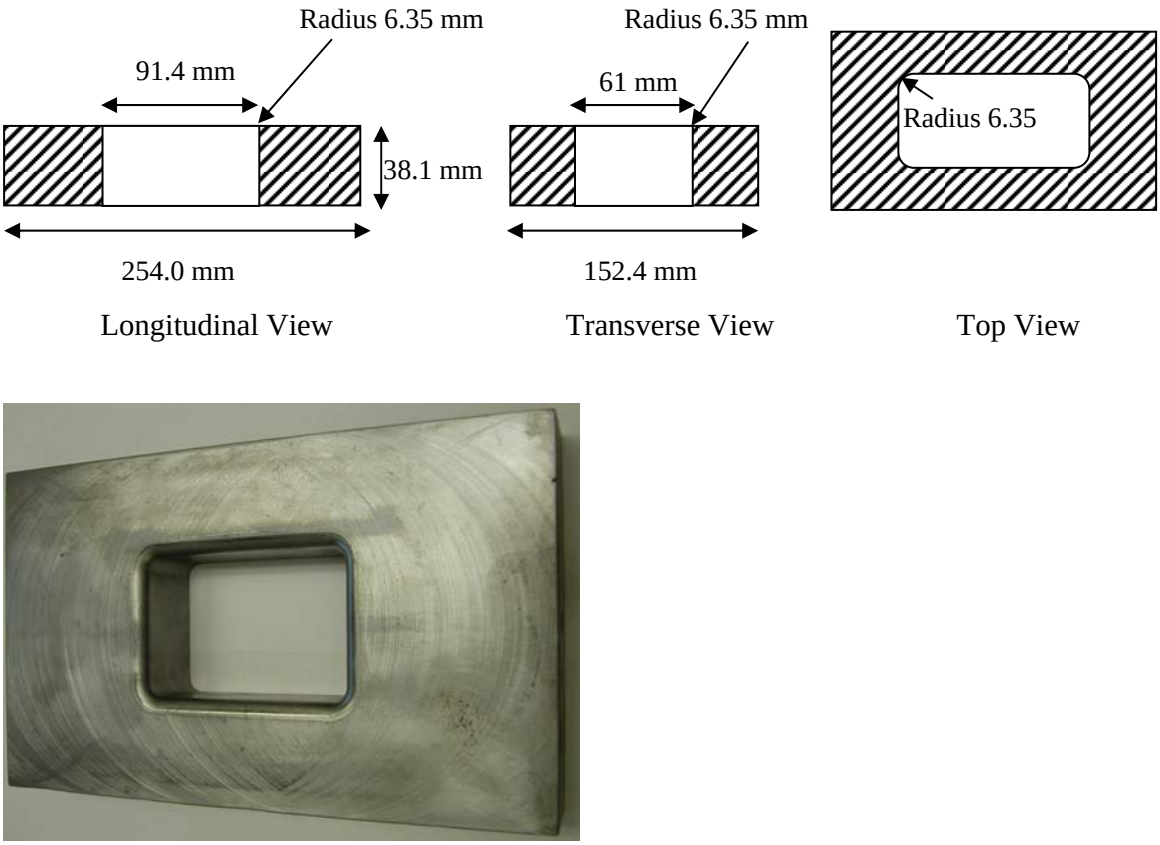

Figure 3.18: Die FF3, a variation of Die FF2 used for forming into a rectangular cavity.

Die FF4 is a mild steel die with a variable entrance radius, designed for Actuator 1. The die is shown in Fig. 3.19. The die measures 114 x 76 x 19 mm. Three through holes of diameter 15.88 mm each were made. Each hole had a different entry radius. The radius was chosen to be a multiple of the maximum sheet thickness (0.5 mm in this case) for which the data were required. The radii used were: 1.19 (labeled A), 1.98 (labeled B) and 3.97 mm (labeled C). A vacuum port was provided in the die.

Figure 3.19: Die FF4 with the three holes and vacuum port.

3.6.2 Embossing Dies

Features with crisp outlines can be formed better with EM process and very fine details can be achieved. Die E1, shown in Fig. 3.20, was designed for the preliminary investigations in embossing. A 0.6 mm surface roughness gauge (to get different textures, made from metal-plated plastic) was glued to a mild steel bottom to serve as a die. The die was used with Actuator 1.

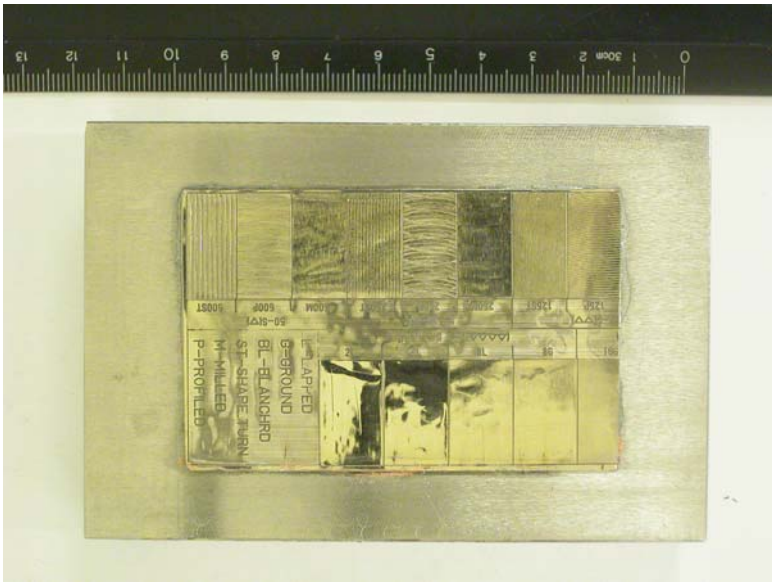

Figure 3.20: Die E1 used for embossing (metal coated plastic roughness gauge glued to a steel backing).

Die E2 is a partially finished GM fuel cell die made of SS 316 alloy. It was designed for use with Actuator 1. However the setup described for Actuator 1 was not used. Here a section of the die was chosen along which the sheet metal was to be formed. Based on earlier concepts, a four nut and bolt arrangement was made with the die as a base. The setup is shown in Fig. 3.21.

Die E3 is the fully finished GM die which was used for the forming of full sized fuel cell plates. The face of the die, made from SS 316, measures 250.4 mm by 355.6 mm. Actuator 3 and its setup in the press were designed around Die E3. The die is shown in Fig. 3.22.

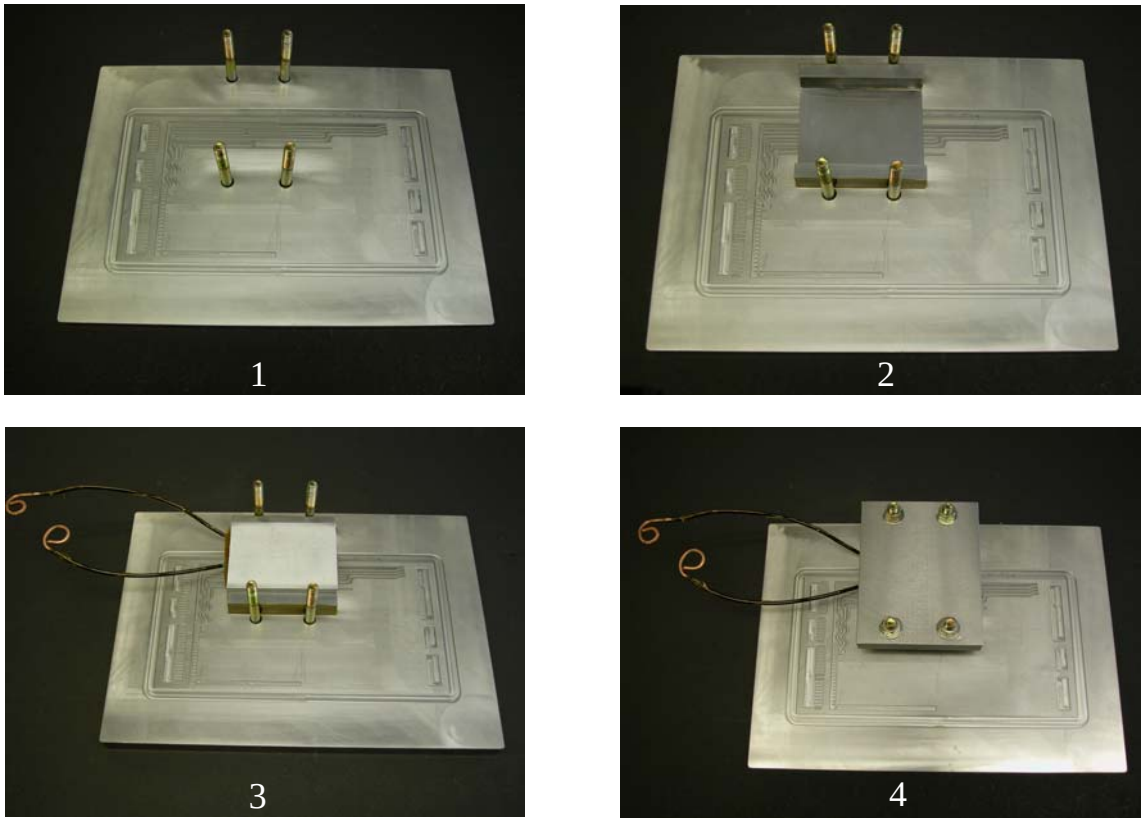

Figure 3.21: Die E2, used for fuel cell plates forming. The numbers indicate the stages in the setup of the actuator for forming. The two leads in 4 are connected to the capacitor bank.

Die E4 is a die to evaluate hologram embossing. A 0.5 mm thick, commercially available hologram (electroless nickel plated) from MIRDC was taped onto a stainless steel block to serve as a die. The basic design is shown in Fig. 3.23. The die was designed for use with Actuator 1.

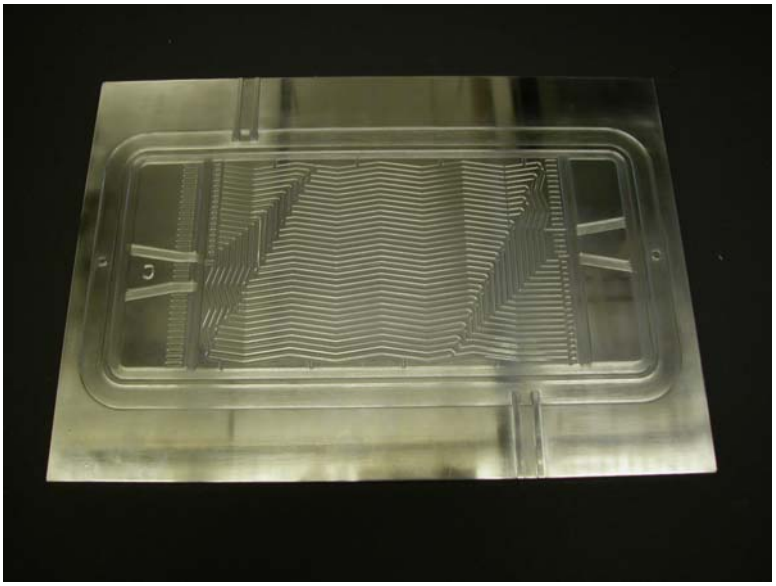

Figure 3.22: Die E3, used for forming full length fuel cell plates with Actuator 3.

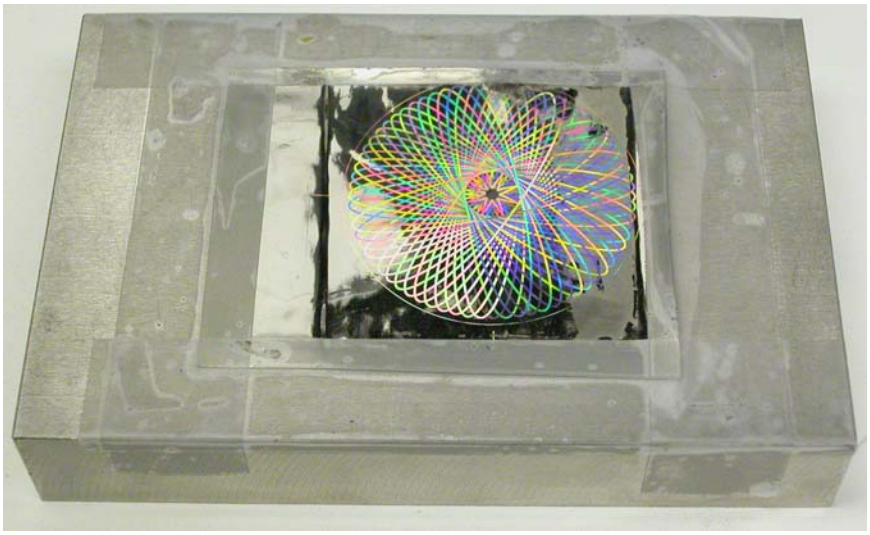

Figure 3.23: Die E4, used for evaluating hologram embossing with the uniform pressure actuator.

3.6.3 Die to Form Depressions

The stainless steel die provided by MIRDC, Taiwan, was used for the trials for forming cellphone cases. The idea was to achieve case depth and surface details in one operation. The die D1 is shown in Fig. 3.24. Vacuum was created in the die with the help of a vacuum port connection.

Figure 3.24: Die D1, used for cellphone case forming. The figures on the top are the CAD images of the sheet when formed into the die and lower picture shows the actual stainless steel die. It shows the fine details required on the surface and the depth of the case required.

3.7 Measurement Tools

The basic tools used in all the experiments are described in this section.

Primary and induced currents are measured by Rogowski flexible coils from Rocoil [43]. Rogowski probes can be used to measure the primary and induced currents as mentioned earlier. The schematic for the probe setup for measuring primary and induced currents is shown in Fig. 3.25. Here probe 1 measures the primary current. Probe 2 measures the current that passes through its loop which is the sum of (*n* x primary) plus the induced currents. Probes 600 mm long with a peak range of 150, 000 amperes/volt were used.

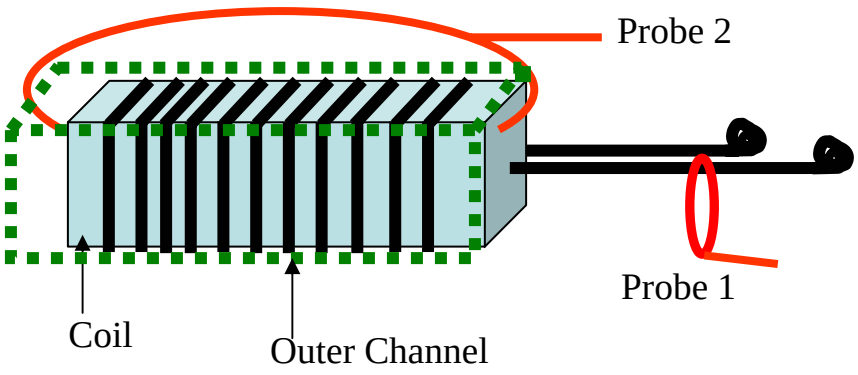

Figure 3.25: Schematic of the usage of Rogowski probes.

The current and voltage probes depicted in Figure 3.25 were used in conjunction with the two-channel digital storage scope (Fluke Scopemeter 99 Series II) to capture the coil

current and voltage traces. The scopemeter can follow input signals from 15 Hz to 50 MHz with record length of 256 or 512 samples and a rise time of less than 7 ns. Inductance of the coils was measured using a LCR bridge. The frequency can be varied in the bridge using a variable input.

Formability of materials was evaluated using circle gridding technique. By this method a circular grid pattern was etched on the sheet surface. A Lectrotech grid-marking unit was used for etching grid patterns on the surface of the sheet. As the sheet metal is deformed, the circles are deformed too. The possible ways in which the circles can deform is shown in Fig. 3.26. If the sheet is stretched in uniaxial tension, the grid circles elongate in one direction and contract in the other. If the sheet deforms under plane strain condition, the circles elongate in one direction and remain unchanged in the perpendicular direction. Under biaxial tension, the circles elongate in both directions, i.e. they become larger circles. Comparison of the grids before and after elongation gives the stress state under which the sheet had deformed at different locations on the sheet surface. The diameter of the grids along the major and minor axes was measured to determine the major and minor strains. The major and minor strains are used as a measure of formability.

3.8 Sheet and Die Materials

The materials used for the forming experiments have been listed in Table 3.1. They include both the materials used as sheets as well as that for the outer channel. Typically rectangular sheet samples were cut for the appropriate setup. They were circle gridded if required for formability studies.

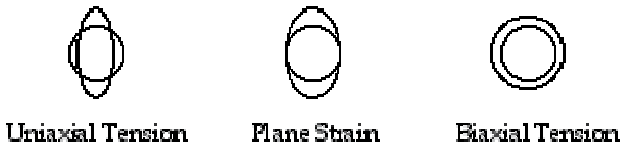

Figure 3.26: Possible types of deformation of the grid circles [39].

3.9 Typical Experimental Procedure

The following general procedure was used for the experiments:

1. Sheet is placed on top of the die. Standoff if any between the die and the sheet is incorporated.
2. The actuator is placed over the sheet with the outer channel contacting the sheet.
3. The setup is bolted or a load is applied from a press to provide a contact load between the sheet metal and the outer channel.
4. The leads from the actuator are connected to the capacitor bank.
5. Vacuum, if needed, is created by the use of a vacuum pump.
6. Rogowski probes are attached to the scopemeter and calibrated to record the current and voltage trace from the coil and the outer channel.
7. The capacitor bank is charged to a specified energy and voltage and then discharged over the actuator.

Alloy	Yield Strength / UTS (MPa)	% Elong.	Resistivity (μΩcm)	Density (g/cm^3)	Thickness (mm)	Application
Al 5052-H32	193/ 228	12	4.99	2.68	0.25	Sheet
Al 2219-O	76/ 172	18	3.99	2.84	0.80	Sheet
Al 5083-H18	228/ 317	16	5.9	2.66	1.1	Sheet
Mg AZ31B-H24	220/ 290	15	9.2	1.77	0.5	Sheet
Ti grade 2	345/483	27	170	4.52	0.3	Sheet
Autograde Steel	305/475	38	17.4	7.87	0.85	Sheet
Cu 110 ETP	195/ 250	30	1.71	8.89	0.13	Sheet and Driver, Outer channel
OFHC Cu	69/221 varies with H/T	55	1.71	8.89	0.40	Sheet and driver
SS 301	276/1034	18	69.5	7.88	0.13, 1.1	Sheet
SS 316	290/579	50	74.0	7.99	-	Die
Mild-Steel 1018	275/475	38	15.9	7.87	-	Die and setup
ASTM B-16 Brass	124/338	53	6.6	8.49	-	Outer channel and coil
G-10	262 cross 310 leng.	-	-/31.5 kV/mm	1.8	-	Insulator, coil mandrel etc.
Kapton	69/ 221	75	-/276 kV/mm	1.42	-	Insulation

Table 3.1: Summary of the materials used for experiments [137].

CHAPTER 4

BASIC BEHAVIOR

This chapter will deal with the basic behavior of the uniform pressure actuator. Important parameters that affect the performance of the actuator will also be discussed.

4.1 Pressure Distribution

The dimpling method [6], using a die with a regular array of holes, was used to evaluate the pressure distribution of various coils. By this method the pressure is directly proportional to depth of the dimple formed [6] and is given as:

$$\bar{h} = \frac{p_o \bar{f}(s)}{(4t_0 Y / 3a^2) + \rho t_0 s^2} \qquad \text{..... (4.1)}$$

where h is the height of the dimple, s is the Laplace operator, p_0 is the peak pressure, Y is the material flow stress, t_0 is the material thickness, a is the blank radius and ρ is the density. As the time function of each dimple is the same, equation 4.1 indicates that the height of the dimple is directly proportional to the pressure at that point. Details of the derivation may be found elsewhere [6].

Figure 4.1 shows a comparison of the pressure distribution achieved by three coils at energy of 0.8 kJ, with 0.13 mm, alloy 110 copper. The three coils are shown in Fig. 4.2.

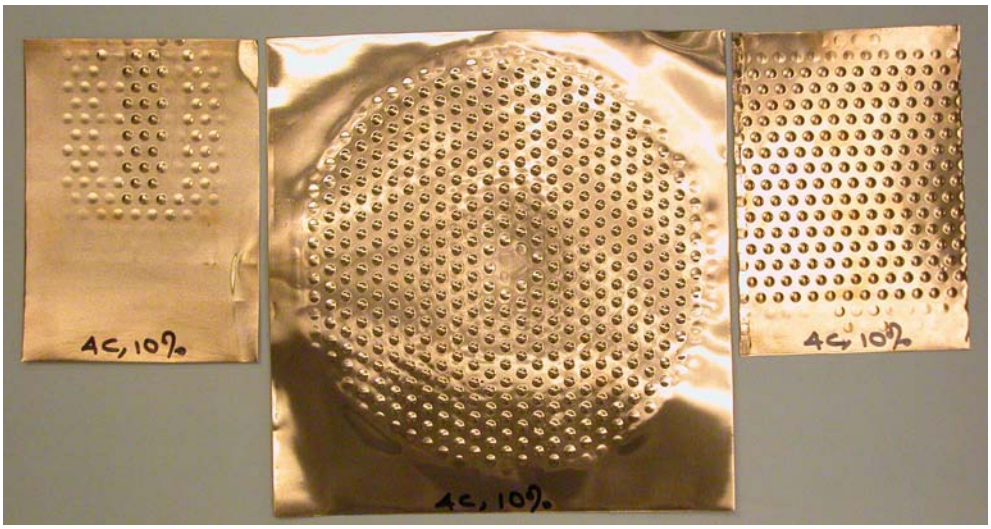

Figure 4.1: Pressure distribution due to the different coils (3-bar coil, pancake coil and the uniform pressure coil, from left to right) at 0.8 kJ (4 Capacitors, 10% energy) on 0.13 mm Cu.

Figure 4.2: 3-bar coil, pancake coil and the uniform pressure coil (arrows indicate current direction).

Figure 4.3 shows the variation of peak depths obtained by the coils along the width. In the case of the UP actuator, the peak depths are almost uniform along the width indicating that the actuator indeed develops uniform pressure. In the case of the 3-bar coil the magnetic pressure is four times higher at the central bar as compared to the two peripheral ones as it carries twice the current density compared to them. The relationship between currents and magnetic pressure is discussed later in Chapter 5. In the case of the 14 turn pancake coil, the pressure is maximum midway between the center and the edge of the coil. The peak currents observed were 38 kA for the 3-bar coil, 18 kA for the UP coil and 12 kA for the pancake coil. This is related to the inductance of the coils

discussed later. The pancake coil had lower wire spacing (~ 0.25 mm) as compared to the UP actuator (2.54 mm) giving it a higher efficiency in this case.

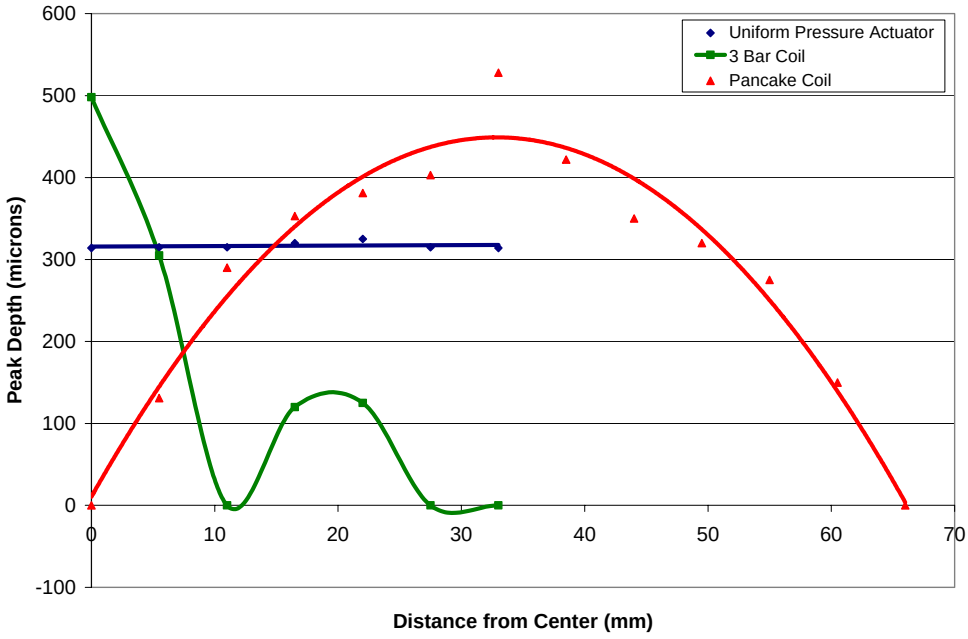

Figure 4.3: Comparison of the peak depth obtained at 0.8 kJ (4 Capacitors, 10% energy) by a uniform pressure (Actuator 1), pancake and 3-bar coils. A peak depth of 600 μm corresponds to 19.2 MPa of magnetic pressure.

The Takatsu disk and the uniform pressure actuator were studied using 2D simulations in Maxwell 2D®. Similar geometries were compared for both the cases, i.e., the wire section, sheet spacing, wires spacing and the current. Thirteen circular (1.7 mm radius)

wires, all 9 mm^2 in area were used. Each wire carried a current of 50 kA at 5 kHz, typical of our system. A spacing of 2 mm between the wire edges was chosen for our simulations (this is a typical practical gap governed by our insulation needs). A 1 mm thick Al sheet was placed at 2 mm below the coil (again typical of our system). The current density was measured and compared along the width of the sheet, at a thickness of 0.2 mm below the surface, as shown in the schematic in Fig. 4.4. In the case of the Takatsu disk, the left vertical plane was considered as an axis of symmetry.

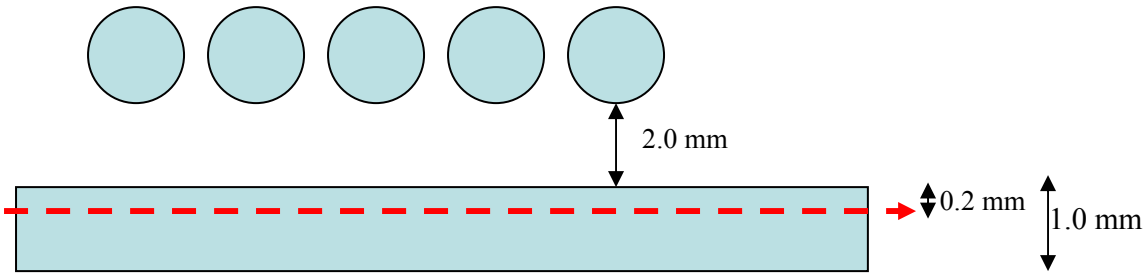

Figure 4.4: Schematic of the simulation in Maxwell 2D for comparison between Takatsu disk and uniform pressure actuator.

The current density plots are shown in Fig. 4.5. In the case of the Takatsu disk, the leftmost wire has the peak current density location turned away from the sheet and towards the axis of symmetry. The current distributes like this to lower the inductance of the system, since there is an equal and opposite current flowing on the other side of the

plane of symmetry. As the effect of the other side of the plane of symmetry reduces, the current distributes to lower the inductance between the sheet metal and the coil. This leads to a peak in the pressure, approximately midway along the coil. This current distribution is the reason for the pressure variation observed in the Takatsu disk. In the case of the uniform pressure actuator there is no such effect and the current distributes to lower the inductance between the sheet and the coil. Therefore the current distributes in a more uniform fashion with the peak oriented towards the sheet, barring the edge effects. This leads to a uniform pressure distribution along the width of the coil.

Figure 4.6 shows the actual current density distribution observed along the width of the sheet at a depth of 0.2 mm. It enforces the uniform pressure distribution of the new actuator and non uniform distribution of the Takatsu disk.

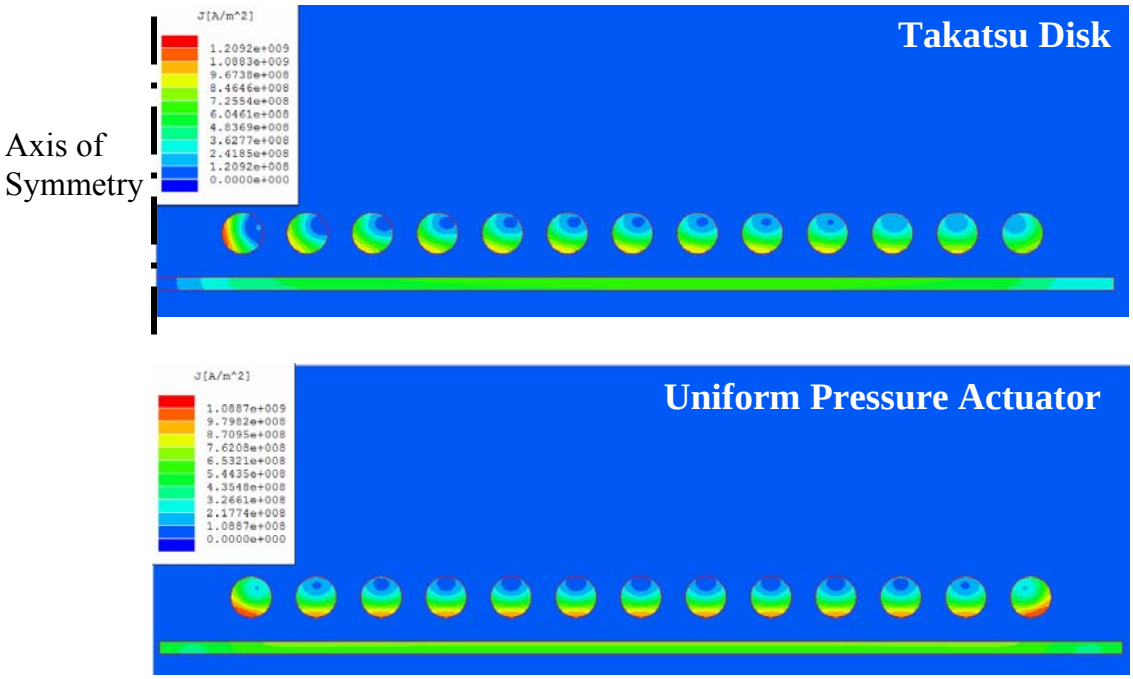

Figure 4.5: Current density plots for the Takatsu disk and uniform pressure actuator using Maxwell 2D.

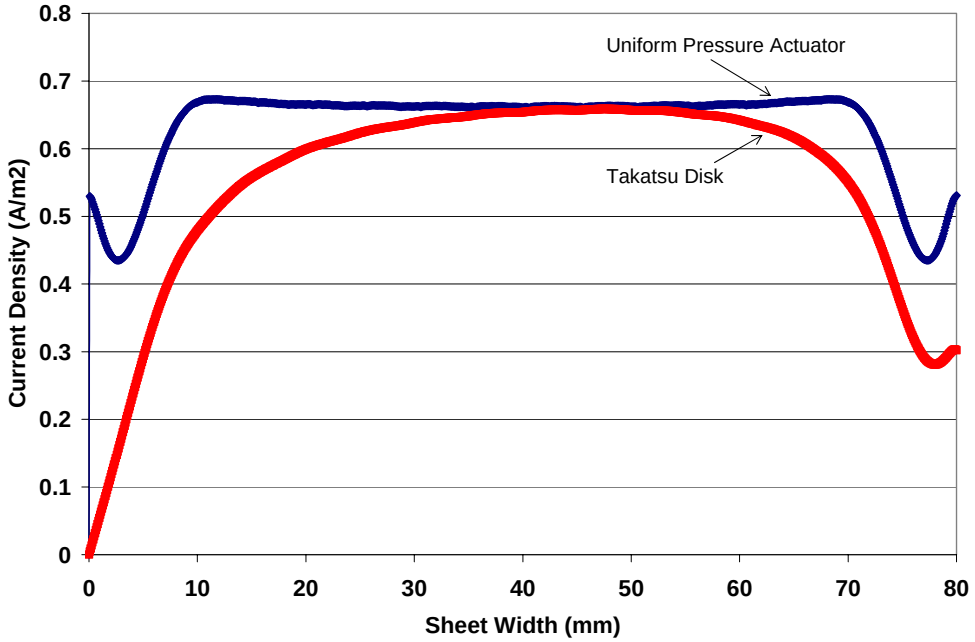

Figure 4.6: Current density distribution at 0.2 mm depth

4.2 Importance of Providing a Return Path

One of the major innovative features of the uniform pressure actuator is the presence of the outer return path for the induced current. Such a path adds difficulties to the actuator design, like a proper contact design at the interface of the sheet metal and the outer channel. We wish to demonstrate the effect of the return path. Al 5052-H32 alloy, 0. 25 mm thick, was formed into a free forming die with a rectangular opening (Die FF1, Fig. 3.14 (a)). The effect of the return path on the efficiency can be seen in Fig. 4.7. Part (a) shows the normal case with the return channel in place. In part (b), the outer channel was insulated so that the current path between the sheet and outer channel was broken. In the

last case, i.e. part (c), the outer channel was removed. All the experiments were carried out at energy of 0.8 kJ (4 capacitors, 10% energy) using Actuator 1 and the peak depth was noted in each case. The efficiency is the highest in the case where a return path is provided. The return path allows for better coupling with a lower inductance and is more efficient.

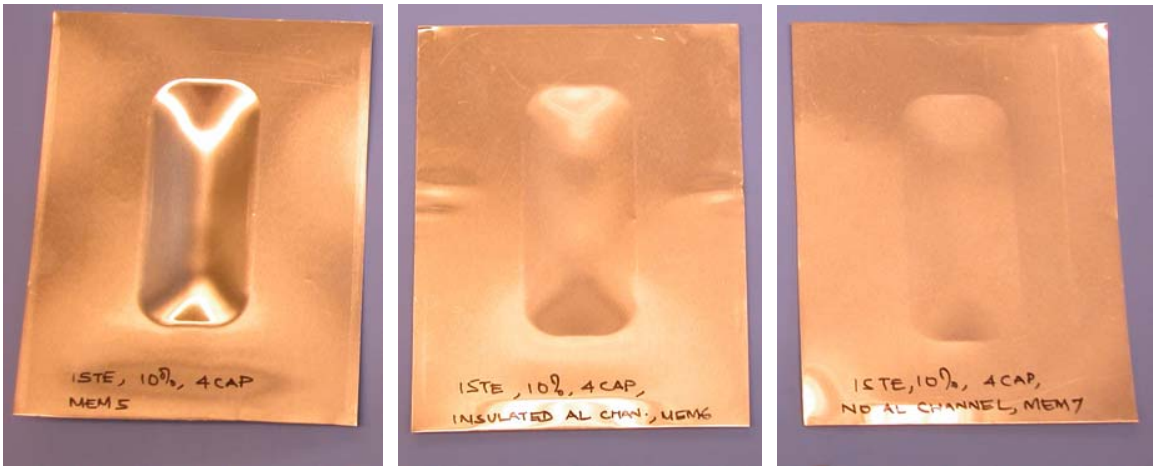

(a) (b) (c)

Figure 4.7: Importance of return path for induced current: (a) normal case, peak depth 5.36 mm, (b) insulated Al channel, peak depth 1.24 mm, (c) no Al channel, peak depth 0.40 mm.

4.3 Effect of Important Parameters

Some parameters are critical in deciding the efficiency of the process and they are described below.

4.3.1 Material Conductivity

The effect of sheet conductivity on process efficiency was studied in a series of experiments. Materials were EM formed using Actuator 2 at energy of 4 kJ (4 Cap. and 50% energy) into a free forming die with a rectangular opening (Die FF2, Fig. 3.15). These were OFHC copper, 5083-H18 Al, auto grade steel and stainless steel SS301. For each the primary and induced currents were plotted and the peak currents and rise times were recorded.

High deformation is observed in the Cu sheet. The sheet hits the bottom of the setup at high velocity and then rebounds. This is due to the low strength, small thickness and high conductivity of Copper. None of the other materials are deformed to this extent. Stainless steel was the least deformed, by far. A summary of the peak currents, etc., is shown in the Table 4.1.

Characteristic	**OFHC Copper**	**Al 5083-H18**	**Auto-grade Steel**	**SS 301**
Peak Primary Current (kA)	33	34	32	26
Peak Induced Current (kA)	503	538	476	332
Rise Time, Primary (μs)	59	62	68	74
Loss (%)	33.72	31	35.3	44.48
Thickness (mm)	0.40	1.1	0.85	1.1
Resistivity (μΩ-cm)	1.7	5.9	17.4	69.5
Yield Strength (MPa)	69	228	305	276
Max. Deformation depth (mm)	>31.8	12.4	9.3	1.0

Table 4.1: Comparison of EM forming characteristics with different sheet materials at 4 kJ (4 Cap. and 50% energy).

Induced currents in stainless steel are the lowest and are the highest in Al as expected. Based on simple ideas, Copper should have the highest induced currents and lower rise time as compared to Al due to its higher conductivity. Although the rise time of Cu is lower as expected its peak current is also lower than that of Al. This is probably due to the fact that in the case of copper, the sheet is thrown at a much higher velocity than Al, and hence, it essentially moves away before the current is fully developed, increasing inductance. This decreases the induced current in Cu as opposed to Al. The relatively small deformation in stainless steel can be explained because the primary and induced currents are the smallest in this case, and it is one of the thicker and stronger materials. The formed parts are shown in Fig. 4.8 for comparison.

(a) (b)

Figure 4.8: Effect of material on forming efficiency (a) 5083 Al deformed at 4 kJ; (b) SS 301 deformed at 4 kJ ((4 Cap. and 50% energy)

Similar experiments were done with Actuator 1. Here Mg AZ31B-H24 and Al 2219-O alloy were compared for the induced currents generated at the same energy using Die FF4, as shown in Fig. 4.9. This Mg alloy is around 2.5 times more resistive than the Al alloy (Table 3.1) and therefore has lower induced currents at the same energy.

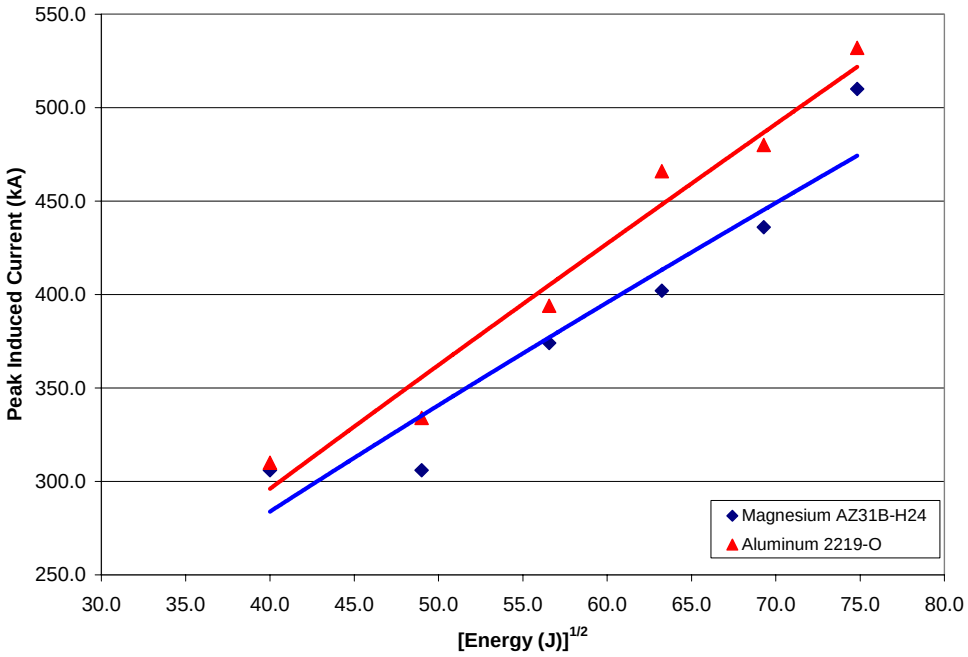

Figure 4.9: Variation of induced current of two sheet materials with energy for Actuator 1.

The effect of sheet material was also simulated with Maxwell 2D (details in Chapter 5). Thirteen solid circular sectioned copper wires in vacuum were simulated. The wires had a radius of 1.7 mm (area 9 mm^2). A spacing of 5.4 mm between wire centers, i.e., 2 mm between ends of two wires was used as shown in a schematic in Fig. 4.10. The wires carried a current of 50 kA at 5 kHz, typical of our system. A 1 mm thick metal sheet was placed 5 mm below the coil. The sheet material was varied and the primary and induced currents were measured along the line shown in Fig. 4.10. The sheet metals used, with their properties, are shown in Table 4.2.

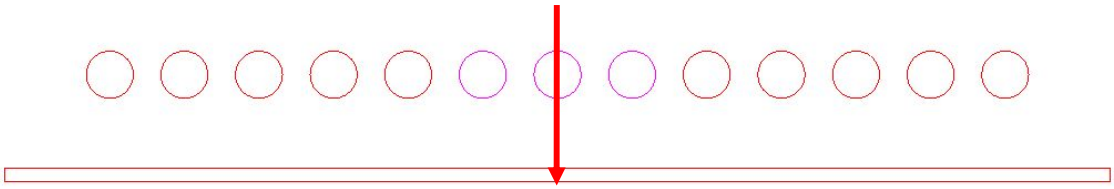

Figure 4.10: Schematic of the model in Maxwell 2D to evaluate the effect of sheet materials on actuator performance.

Material	**Conductivity (Siemens/m)**
Copper	5.8 e7
Al	3.8 e7
Steel (1010)	0.2 e7
Stainless Steel	0.11 e7

Table 4.2: Sheet metal properties of the materials used in the Maxwell 2D to evaluate the effect of sheet materials on actuator performance.

Figure 4.11 shows the variation of the primary and induced currents with different sheet materials. Higher primary and induced current are observed when the sheet metal has higher conductivity. Since the magnetic pressure developed is a product of the primary and induced currents, higher conductivity sheet metals increase process efficiency.

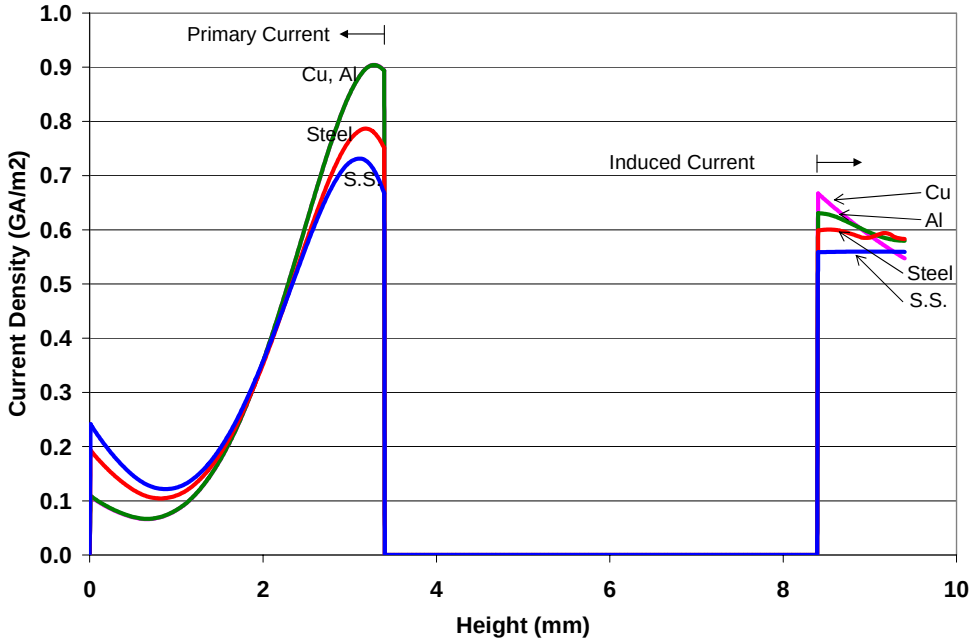

Figure 4.11: Variation of current density with sheet materials using Maxwell 2D.

Sheets with a lower conductivity can still be formed by using a driver sheet. In this case a sheet of higher conductivity is placed close to the actuator and the lower conductivity sheet is placed over the die. The higher conductivity sheet is then used to push the lower conductivity sheet into the die. Since the higher conductivity sheet is in contact with the actuator the process efficiency is high. An example of this effect is shown in Fig. 4.12. Here a 0.3 mm, Ti grade 2 was formed at an energy of 3.2 kJ (4 Cap., 40%), with vacuum onto Die D1. Ti sheets have low conductivity (~ 1% IACS) and cannot develop significant induced currents for EM forming. However with the help of an expendable Cu driver sheet, the lower conductivity material may still be formed.

No driver With 0.32 mm Cu driver

Figure 4.12: Effect of a driver sheet in forming lower conductivity materials (Ti) by EM forming.

4.3.2 Number of Turns in the Actuator

At a fixed primary circuit current, the magnetic pressure (electromagnetic field intensity) is increased by increasing the number of windings in the forming coil or solenoid, but this will increase the inductance of the system. This in turn reduces the peak current. The result is that for any situation, there is an optimum number of coil windings. As a general rule for efficient forming most of the total system inductance should reside in the forming coil. There is an engineering trade-off, however as the number of turns increases, the inductance of the system rises, reducing ringing frequency. This reduces the peak current

and will allow more flux to leak through the workpiece. An optimum number of turns can be decided based on the modeling approach described in Chapter 5.

4.3.3 Changes in Voltage and Capacitance

Developing a relatively high system ringing frequency is often quite important. If the electrical oscillation frequency is too low, intense eddy currents are not induced in the workpiece, and the force developed is low. The ringing frequency is directly related to the circuit LRC characteristics and low capacitance and low inductance favor a high ringing frequency. Materials of lower conductivity demand higher ringing frequency for effective forming.

Low capacitance is required for high system ringing frequency, which leads to intense eddy currents in the workpiece, and hence higher forming force. Lower charging voltages are desired to avoid problems with electrical interconnects, insulation and longer coil life. However this means using a higher capacitance for the same energy. An optimization approach will be discussed in Chapter 5.

4.3.4 Putting Windings in Parallel vs. Series

This will depend on how the inductance in the system has to be balanced based on considerations of system frequency and peak current as described earlier. Parallel windings are better for high inductance coils as they lower the inductance.

4.3.5 Need for Vacuum

Vacuum, between the sheet metal and the die, may be important in high velocity metal forming. The whole forming process is very fast and the process finishes in less than 0.1 seconds. The sheet strikes the die at velocities ranging from 50- 200 m/s. The air present in the die does not have enough time to leave the die and may cause problems with the shape fidelity.

An example of the effect of vacuum has been shown in Fig. 4.13. The figure shows two Al 5052-H32 0.25 mm samples that were formed using 4 capacitors at 15% energy (1.2 kJ). This was done using Actuator 1 and Die FF1 (Fig. 3.14 (b)). The die was initially used with no vacuum assembly attached to it. The result shows the formation of a prominent ridge due to air entrapment in the no vacuum case. Using a vacuum assembly lowers/ eliminates the problem. Another approach is to use small multiple impacts where the sheet gradually moves with each shot and takes the shape of the die cavity. This is discussed in detail later in Chapter 6.

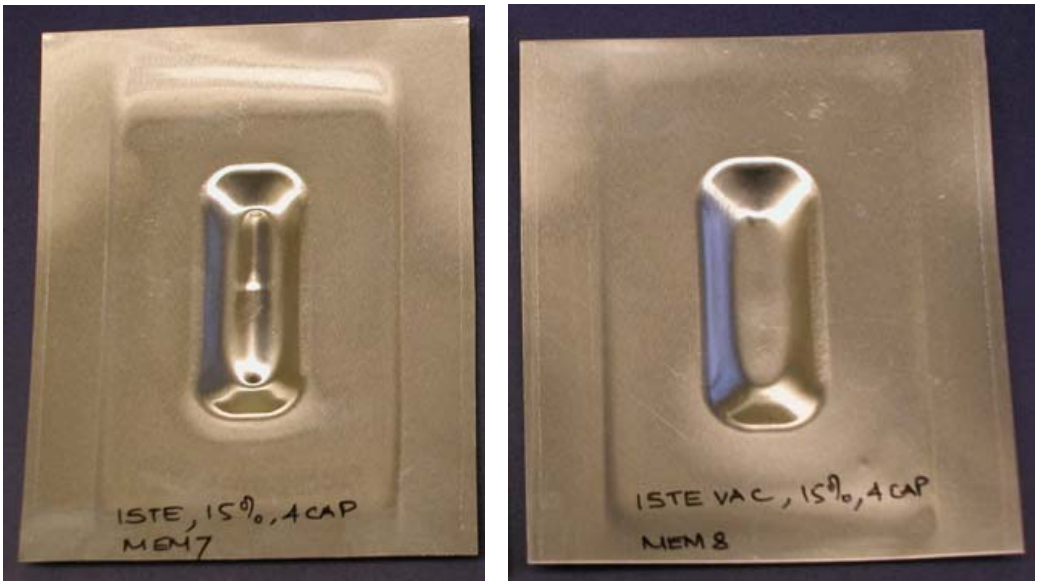

(a) (b)

Figure 4.13: Effect of vacuum in the die assembly, (a) Al sheet formed with no vacuum, and (b) the sheet formed with vacuum between the sheet and die at 1.2 kJ.

CHAPTER 5

ACTUATOR DESIGN AND SIMULATION

This chapter summarizes the approach for an engineering design of the uniform pressure actuator. It also deals with the tools that can be used to simulate high velocity metal forming and electromagnetic fields and how these can be used in designing the forming methodology.

The design approach is shown in Fig. 5.1. An analytical model can be used to create a rough coil design. Simulations of eddy currents and electromagnetic fields in MAXWELL 2D can be used to fine tune the actuator design. Simulation of high velocity deformation in AUTODYN 2D can be used to predict the process parameters including the sheet velocity at which a desired shape can be formed. The analytical model along with MAXWELL and AUTODYN can provide a comprehensive tool set for the design and successful application of the uniform pressure actuator.

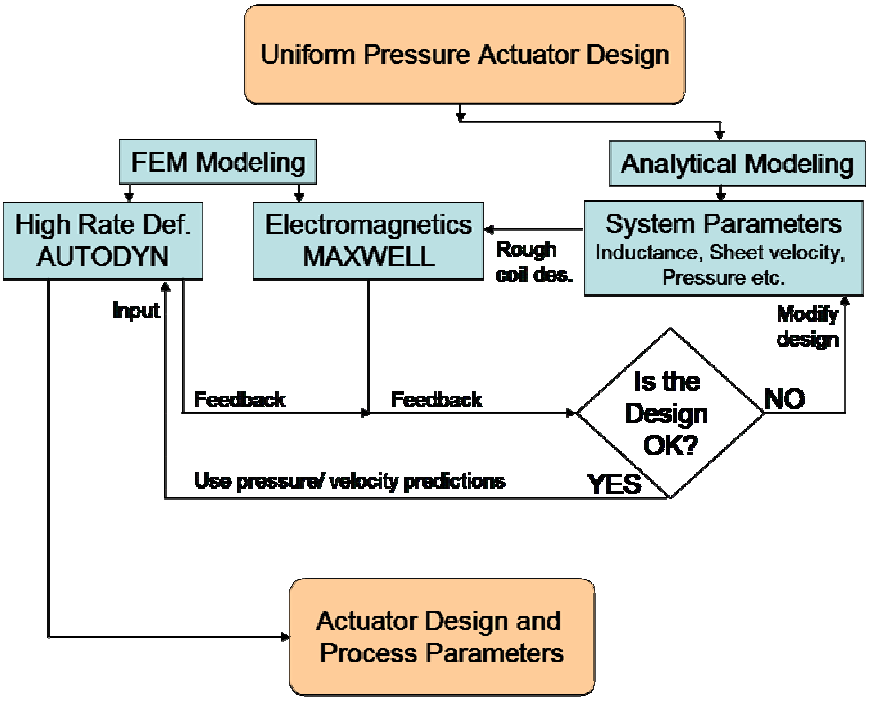

Figure 5.1: Design approach for the uniform pressure actuator.

5.1 Engineering Design of the Uniform Pressure Actuator

The basic electromagnetic repulsion between the coil and sheet can be modeled, to a good approximation, as the repulsion between two uniform planar sheets of electrical current of a given density. Currents can be estimated by standard inductance, resistance and capacitance (LRC) analyses. In the limit of an ideally-coupled transformer the current in the sheet is equal to n times the current in the primary coil, where n is the number of turns in the primary coil.

The differential equation of an LRC system can be expressed as:

$$\frac{d^2 I(t)}{dt^2} + 2\xi\omega\frac{dI(t)}{dt} + \omega^2 I(t) = 0 \qquad \text{.... (5.1)}$$

Here I is the current, ω is the frequency, ξ is the damping factor and t is the time. The solution to this equation is discussed in detail later.

Both the first and second generation actuators are discussed. Experiments with Actuator 1 consisted of using a three hole free forming die (Die FF4, Fig. 3.17) with 0.80 mm Al 2219-O and 0.5 mm Mg AZ31B-H24. Experiments with Actuator 2 consisted of free forming on to a die with rectangular opening (Die FF3) with 1.1 mm Al 5083-H18. The materials and their properties are listed in Table 5.1.

Characteristic	**Al 2219-O**	**Al 5083-H18**	**Mg AZ31B-H24**
Thickness (mm)	0.80	1.1	0.50
Resistivity (μohm-cm)	3.99	5.9	9.2
Density (g/cm^3)	2.84	2.66	1.77
Yield Strength (MPa)	75.8	228	220

Table 5.1: Comparison of sheet materials used for the analysis.

5.1.1 Estimating Inductances

The first task in the analysis is to estimate the effective inductance of the system. This can be done as is typically done in coupled LRC circuits. The simplest way to go about this is to consider the effective inductance of the system, including the primary coil, find the current in the primary coil and then assume that the same current density runs in the secondary as exists in the primary. Later we will correct this simple analysis. We can create two limiting estimates of the effective circuit inductance. In the low-frequency limit we assume that the magnetic field of the primary fully bleeds through the workpiece and return path completely. In this case the effective inductance of the primary coil is estimated as that for a section of an infinitely long solenoid as:

$$L_s^{low} = \frac{\mu_0 A_s n^2}{l_s} \qquad \text{.... (5.2)}$$

where A_s is the area inside the solenoid. Its length is l_s, n is the number of turns and μ_0 is the magnetic permeability of free space. There are some corrections that can be made for wire diameter and aspect ratio [1], but these will be ignored for now.

In the high frequency limit, the magnetic field is confined to the volume defined between the coil, the inside of the return path structure and the workpiece. To describe this area we define the term A_{gap}, which is the area of the gap between the coil and structure. A_{gap} can be estimated as the product of the outer perimeter of the coil and the insulation gap between coil and the surrounding structure (one can also consider small corrections due to the skin depth of the conductors). We can define the high frequency limit of the coil inductance as [12]:

$$L_s^{low} = \frac{\mu_0 A_{gap} n^2}{l_s} \qquad \text{..... (5.3)}$$

Using this effective inductance the system can be analyzed as a simple LRC circuit. The total circuit effective inductance is the sum of the effective coil inductance and the system inductance. Likewise the total circuit resistance is the sum of the coil and system resistance. However in these actuators the coil inductance far exceeds the bank inductance due to the high number of turns. Hence the system inductance is given as a close approximation by the actuator inductance.

Given an actuator, the system inductance (L_{sys}) can be estimated from the rise time from the current probes. Taking the system capacitance as the known bank capacitance, the system inductance can be estimated from experiment as:

$$L_{sys} = 4t_{rise}^2 / \pi^2 C \qquad \text{..... (5.4)}$$

where t_{rise} is the rise time (time to peak current) and C is the system capacitance. This equation assumes that the resistance in the system is low, a reasonable approximation, as shown later.

The inductance of the actuator can also be determined by the use of an LCR bridge. An example of the inductance measured for Actuator 2 is shown in Fig. 5.2. Here variable frequency input was used in the LCR bridge to measure the inductance, with varied sheet metals completing the return circuit. The conductivities of the sheet metals used are reported in Table 3.1.

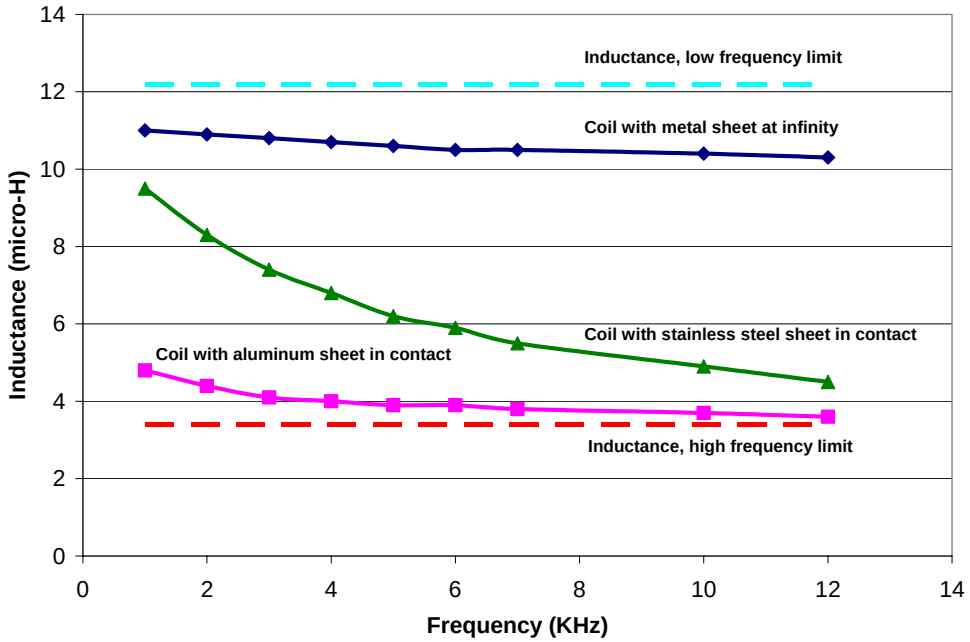

Figure 5.2: Variation of coil inductance with frequency, measured with LCR Bridge (Actuator 2).

It is seen that the inductance of the actuator system decreases when sheet metal completes the circuit. As the sheet metal is removed away from the coil (which occurs during the forming process), the area between the coil and return path increases, and the inductance of the system increases. This reduces the current and increases the rise time.

Inductance is also lower with the use of higher conductivity sheets. Therefore higher peak currents and higher efficiency are expected for them as compared to lower conductivity materials. Experimental calculations using Eqn. (5.4) yield similar results. For example,

at 5.68 KHz, the predicted high frequency limit inductance is 3.68 μH, which is very close to the value of 3.90 μH as measured by an LCR bridge with a highly conductive sheet on the actuator.

5.1.2 Estimating Currents

The solution of Eqn. (5.1) yields the variation of current *I(t)*, with time *t*, and can be expressed as:

$$I(t) = \frac{V_o \sqrt{C/L_{sys}}}{\sqrt{1-\xi^2}} e^{-\xi\omega t} \sin(\omega t) \qquad \text{..... (5.5)}$$

Here V_0 is the system voltage and the damping factor, $\xi = \frac{1}{2} R_{sys} \sqrt{C/L_{sys}}$. Also R_{sys} is the resistance of the system. Thus the current has a damped sinusoidal waveform.

In the absence of large resistive losses, the maximum primary current (I_{max}) can be estimated as:

$$I_{\max} = f_1 V_o \sqrt{C/L_{sys}} = f_1 \sqrt{2E/L_{sys}} \qquad \text{..... (5.6)}$$

Here E is the energy stored and f_1 is assumed to be a constant that is a function of the resistance of the system and workpiece. In an ideal system without resistance, f_1 would be 1.00. The variation in f_1 with energy for the two actuators has been shown in Fig. 5.3. Generally for our system a good approximation for f_1 is about 0.75. Note that as shown in Fig. 5.2, inductance can be a function of frequency.

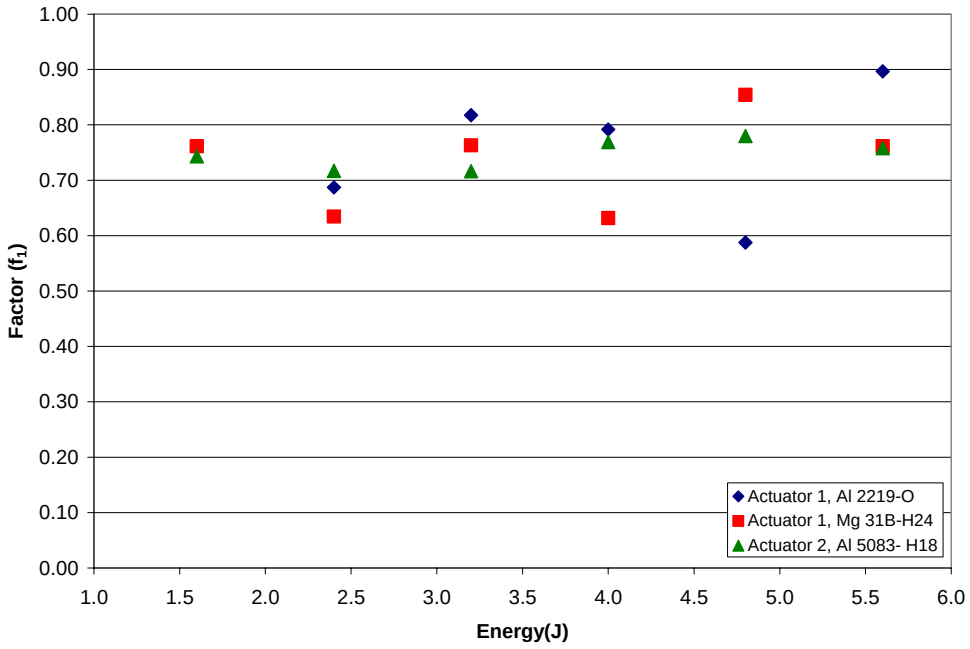

Figure 5.3: Variation in f_1 with energy for different actuators and workpiece combinations.

Rogowski probes can be used to measure the primary and induced currents as mentioned earlier (Chapter 3). Figure 5.4 shows a typical plot of the measured primary and calculated (from measurement) induced current.

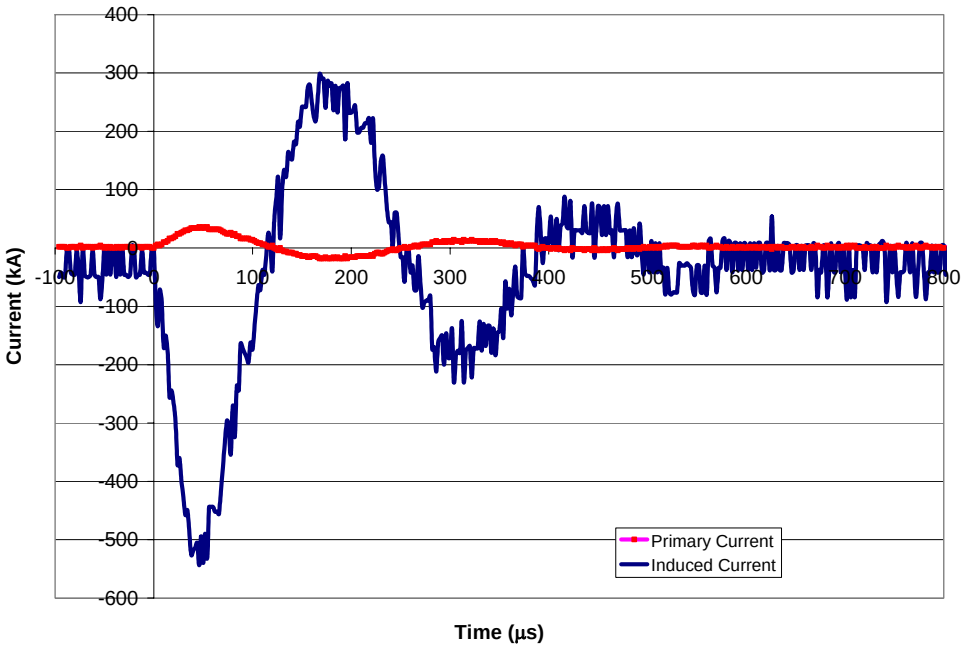

Figure 5.4: Primary and induced current plots in Al 5083-H18, using Actuator 2, at 4 kJ (4 Cap., 50% energy). Because the coil has 23 turns, the induced current greatly exceeds the primary.

Eqn. (5.6) is supported by the plot shown in Fig. 5.5. The peak current is shown for Actuator 1 and 2 for a range of energies to vary linearly with the root of the energy.

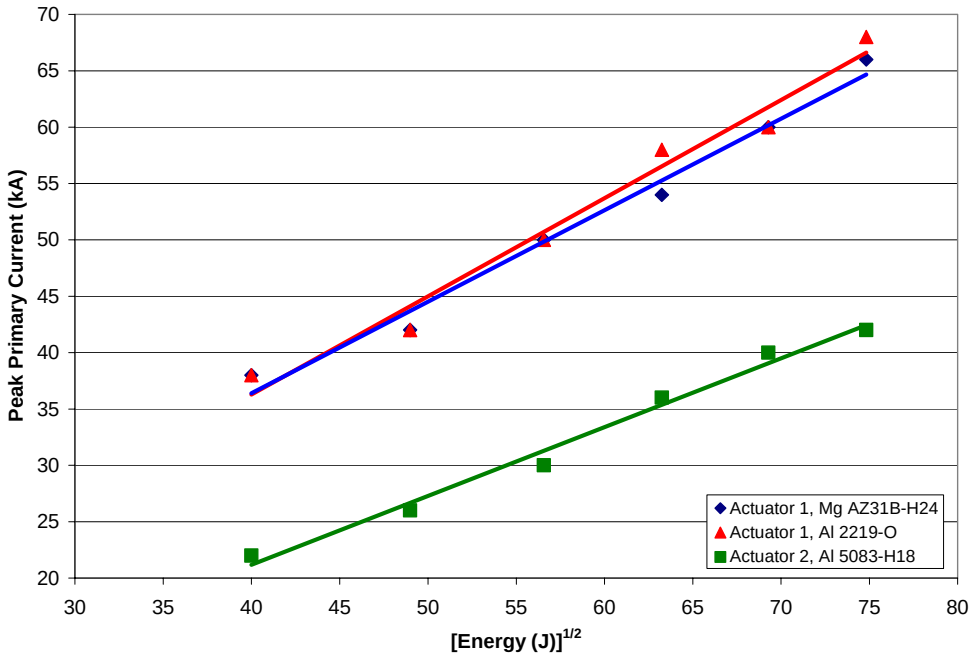

Figure 5.5: The variation of peak current with root of energy in Actuators 1 and 2 with varied workpiece materials.

The variation of current with time may also be predicted by estimating the damping factor (ξ). This factor can be calculated from any measured current pulse from the actuator. Typical values from Actuators 1 and 2 are given in Table 5.2. Using the damping factor, the current waveform can be predicted at any energy. Figure 5.6 shows an example of the predicted current waveform for Actuator 2 for an Al 5083-H18 sheet formed at 4 kJ (4 Cap., 50% energy). Comparisons between the predicted and measured waveforms will be shown later.

Material	Damping Factor (ξ)	System Resistance (R_s) Ω
Actuator 1		
Al 5052-H32	0.136	0.022
Mg AZ31B-H24	0.148	0.026
Actuator 2		
Cu 110	0.129	0.045
Al 5083-H18	0.198	0.052
Autograde Steel	0.263	0.107

Table 5.2: Variation of damping factor and system resistance with sheet material for Actuators 1 and 2.

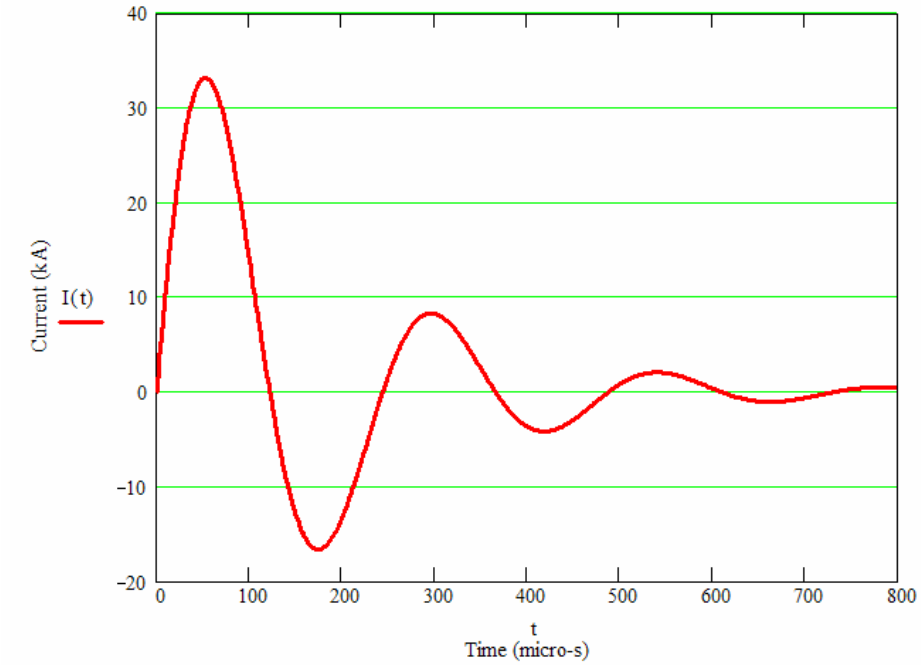

Figure 5.6: Predicted current waveform for an Al 5083-H18 sheet formed at 4 kJ (4 Cap., 50% energy) using Actuator 2.

Suppose the actuator consists of a coil of n turns and I_p and I_i denote the primary and induced currents respectively, then for the more general case of imperfect coupling, we can define a second coupling factor, f_2:

$$f_2 = \frac{I_i}{nI_p} \qquad \text{..... (5.7)}$$

Using a series of experiments the coupling factor f_2 can be determined. Experiments with Actuator 2 show that the factor f_2 is 0.70 for Al sheet and 0.55 for stainless steel (SS 301) sheets for our 16 kJ bank system. The factor increases with increasing conductivity of the sheet material. The specifics of the experiment have been discussed earlier (Chapter 4) under material conductivity.

5.1.3 Estimating the Ringing Frequency

Assuming negligible resistance, the ringing frequency for the bank, ω, is given by:

$$\omega = \sqrt{\frac{1}{LC}} \qquad \text{..... (5.8)}$$

In most EM forming systems as frequency decreases, the magnetic field will bleed through and skin depth must be important. If the electrical oscillation frequency is too low, intense eddy currents are not induced in the workpiece, and the force developed is low. The ringing frequency is directly related to the circuit LRC characteristics and low capacitance and low inductance favors a high ringing frequency. Materials of lower conductivity demand higher ringing frequency for effective forming. Unlike most coils used in electromagnetic forming, the ringing frequency is not of primary importance. Because the return path acts much like a transformer, so long as significant currents are

developed in the return path, a repulsive force will be developed. This can be seen from the significant currents that are generated in a stainless steel sheet (Table 4.1) although it is low in conductivity. However, the system will generally become more efficient as frequency increases. The primary reason for this is that we will approach the high frequency limit of inductance as frequency rises. Figure 5.7 shows the variation in the ringing frequency with capacitance for Actuator 2. The results follow the behavior predicted by Eqn. (5.8).

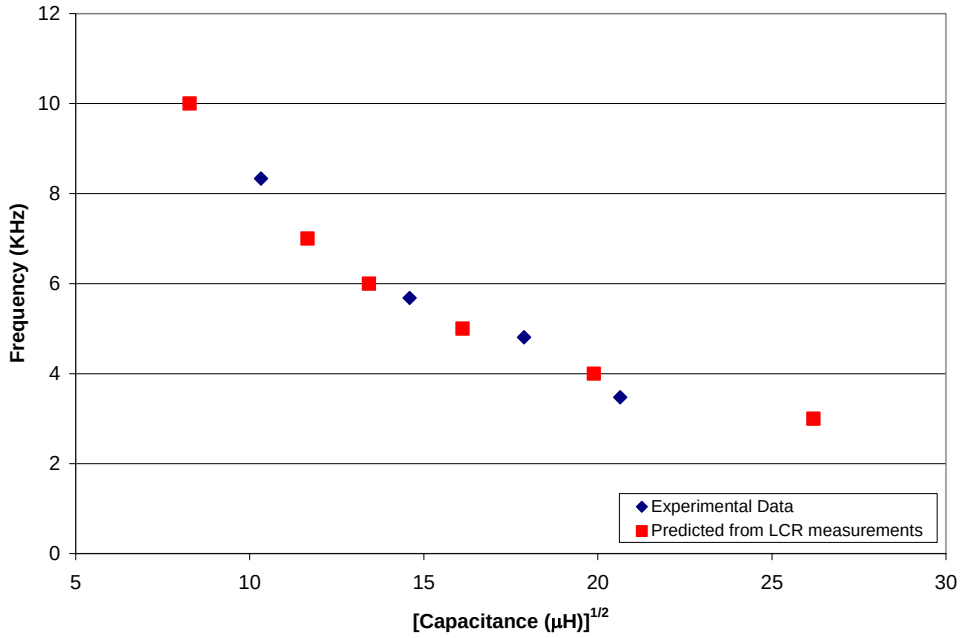

Figure 5.7: Variation in frequency with capacitance for Actuator 2 and Al 5083-H18. Two, four, six and eight capacitors of the 16 kJ bank used respectively to vary the capacitance.

5.1.4 Important Metrics- Maximum Pressure or Maximum Speed

There are two approaches one may use as a design criterion for forming the workpiece. If one wants to primarily form into shallow features which are close to the initial workpiece position, the maximum pressure may be the main figure of merit used in designing a forming process. However, magnetic pressure can also be used to accelerate the sheet to a desired velocity and forming will take place by impact with the tool. Very large impact pressures can be developed by modest strike velocities. Thus this can be very effective for embossing. In the latter case having some acceleration distance available to 'push' the sheet is imperative and Newton's second law of motion can be used to estimate velocity with time. In either case we need estimates of magnetic pressure.

5.1.5 Estimating Magnetic Pressure

We can calculate the field from the solenoid assuming the sheet metal is made of a dense array of wires each carrying a current. Maxwell's equations [1, 19-22] can be put into a more useful form which gives estimate of the magnetic forces:

$$P_m = \frac{\mu_o H_p H_i}{2} \qquad \text{..... (5.9)}$$

Here P_m is magnetic pressure, and H_p and H_i respectively represent the current densities expressed in amperes per width, in the primary and induced circuits, respectively. The peak current density in Eqn. (5.9) is simply the value from Eqn. (5.6) multiplied by the number of turns per unit length. For example, the variation of peak pressure calculated by the above approach using data from Actuators 1 and 2 is shown in Fig. 5.8. It can be seen

that the generated pressures are modest. It is the impact with the die which generally generates the high pressure that results in forming. This is discussed in detail later under embossing.

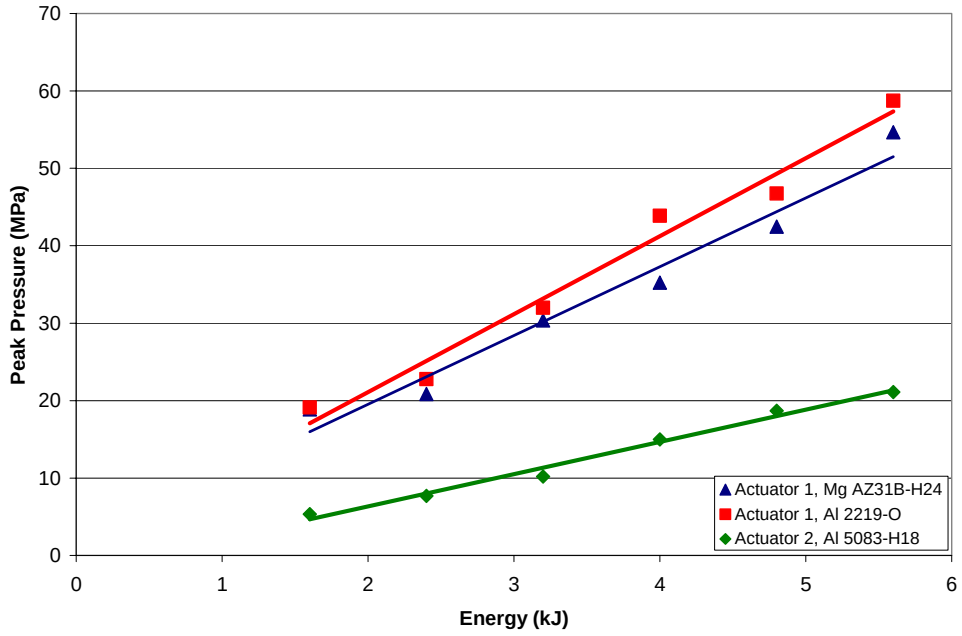

Figure 5.8: Variation of peak pressure with energy for Actuators 1 and 2, calculated from Eqn. (5.9).

The variation of pressure can be expressed as:

$$P(t) = \frac{\mu_0 f_2 n^2}{2 l_s^2} I^2(t) \qquad \text{..... (5.10)}$$

A typical pressure pulse is shown in Fig. 5.9 for Actuator 2 for an Al 5083-H18 sheet formed at 4 kJ (4 Cap., 50% energy). Clearly the pressure pulse from the first half cycle of the current pulse is more significant than the later parts.

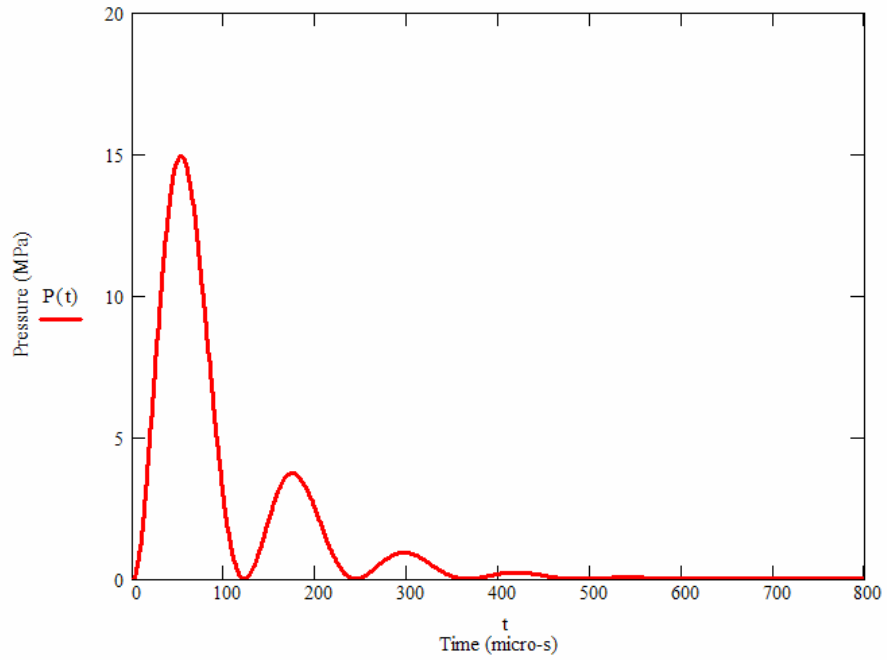

Figure 5.9: Predicted magnetic pressure pulse for an Al 5083-H18 sheet formed at 4 kJ (4 Cap., 50% energy) with Actuator 2.

5.1.6 Estimating Velocity

The primary and induced currents are damped sinusoidal waveforms as discussed earlier. At any time *t*, the acceleration of the sheet, *a*, can be given by

$$a = \frac{P(t)A}{m} = \frac{P(t)}{\rho t_h} \qquad \text{..... (5.11)}$$

Here A is the forming area, m is the mass of the sheet, ρ is the density of the sheet and t_h is the thickness of the sheet.

The velocity of the sheet, v, at a particular time t, is then given by:

$$v(t) = \int_0^t a\,dt = \left(\frac{\mu_0 f_2 n^2}{2 l_s^2 \rho t_h}\right) \int_0^t I^2(t)\,dt \qquad \text{..... (5.12)}$$

Figure 5.10 shows the variation of velocity with time for Actuator 2 for an Al 5083-H18 sheet formed at 4 kJ (4 Cap., 50% energy). Clearly the gain from the first half cycle of the current pulse is more significant than the later parts. Thus, to a good approximation, the forming event occurs during the first half cycle of the current pulse, i.e., at $t = \pi/\omega$. After this time, currents are reduced and coupling is diminished. The peak sheet velocity, v_{max}, can therefore be approximated as,

$$v_{\max} = \left(\frac{\mu_0 \pi}{4\omega}\right)\left(\frac{f_1^2 f_2 n^2}{l_s^2 \rho t_h}\right)\left(\frac{E}{L_{sys}}\right) \qquad \text{..... (5.13)}$$

The variation in sheet velocity with energy is shown in Fig. 5.11. It varies linearly with energy as predicted by Eqn. (5.13). A linear variation of sheet velocity with capacitor bank energy in electromagnetic forming has also been predicted in ring expansion [44, 45].

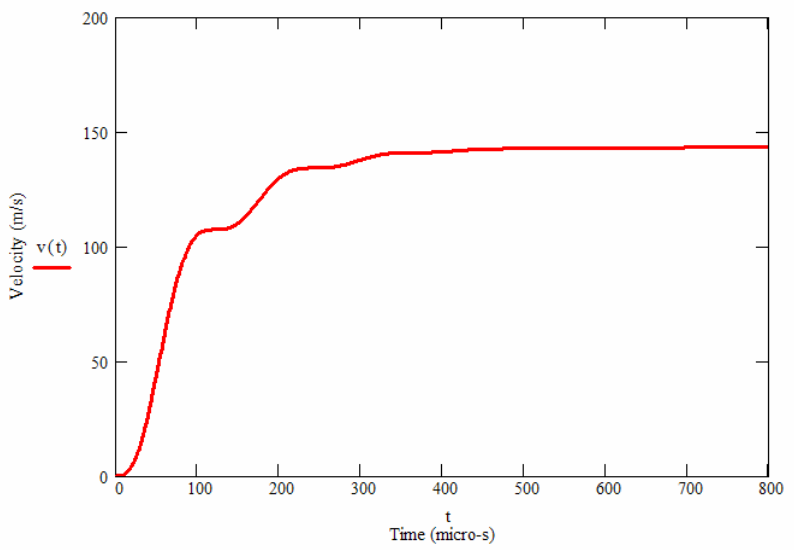

Figure 5.10: Predicted current waveform for an Al 5083-H18 sheet formed at 4 kJ (4 Cap., 50% energy) using Actuator 2.

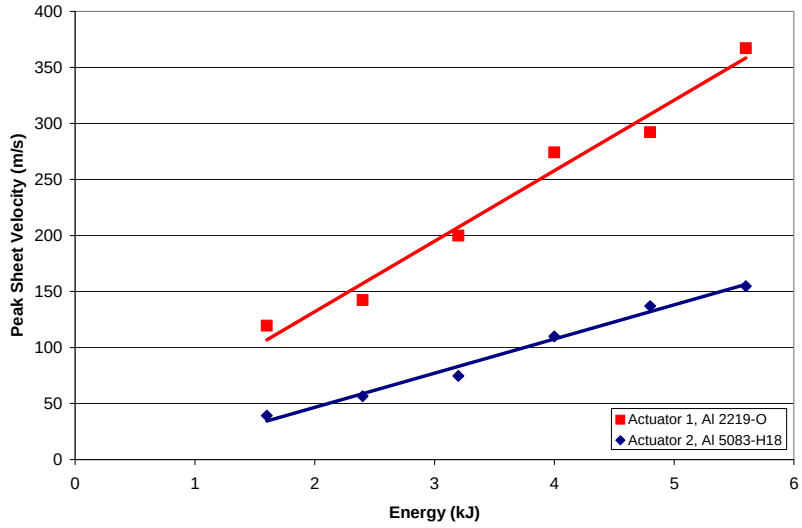

Figure 5.11: Predicted variation of peak sheet velocity with energy with Actuators 1 and 2.

It is clear from above that a standoff between the sheet metal and the die may be important in achieving the highest impact velocity. A good estimate of the required standoff can be generated by assuming, that the sheet accelerates until the first half cycle of the current. Hence,

$$s_{opt} = (\frac{\mu_0 \pi^2}{8\omega^2})(\frac{f_1^2 f_2 n^2}{l_s^2 \rho t_h})(\frac{E}{L_{sys}}) \qquad \text{..... (5.14)}$$

where s_{opt} is the standoff required for peak sheet velocity. The optimal standoff required to achieve highest velocities of sheet impact with the die can be estimated from the above equation. The optimal standoff for a range of energies is shown in Fig. 5.12 for Actuators 1 and 2. It is clear that generally a few millimeters are required to reach peak velocity.

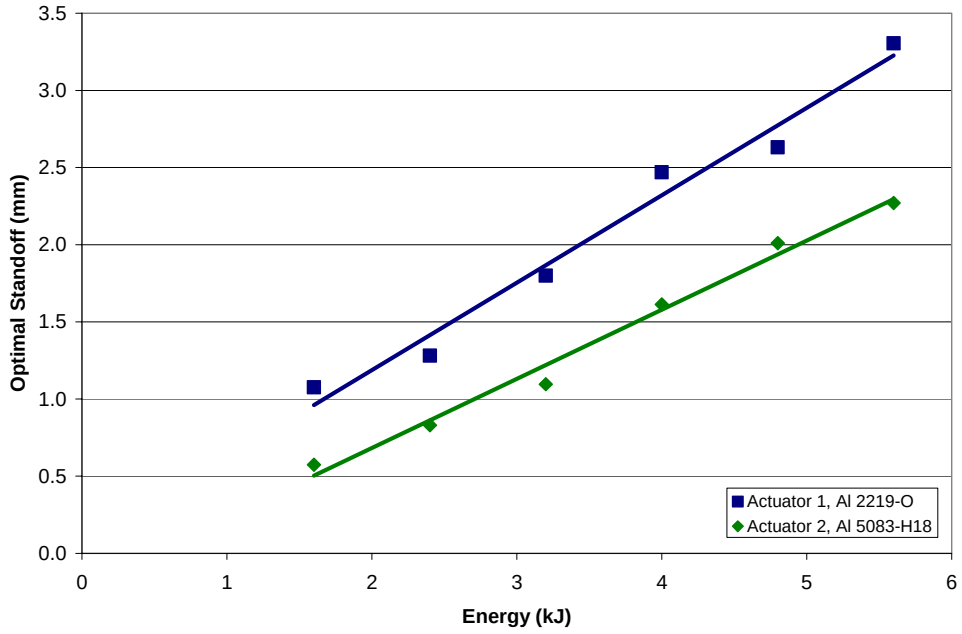

Figure 5.12: Variation of optimal standoff with root of energy for Actuators 1 and 2.

5.1.7 Estimating Number of Turns

The coil can be tailored to give a maximum pressure at a given energy. In this case an optimization can be carried out for the number of turns. An approach is described over here.

The inductance of a coil (L_{Act}) can be further defined as,

$$L_{Act} = f_3 \frac{\mu_0 A_{gap} n^2}{l_s} \qquad \text{..... (5.15)}$$

where f_3 is a frequency dependent factor based on the leakage of flux. Here f_3 accounts for the transition between high and low frequency limits. For low number of turns, say 2, the frequency is high enough so we are at the high frequency limit. In this case the value of f_3 is close to 1. With higher number of turns we start deviating from the Eqn. (5.3) and f_3 is higher.

As an example, consider Actuator 2. The variation of inductance with frequency is shown in Fig. 5.2. Here f_3 varies from 1 to 4. Also let us assume a 2, 6 and 20 turn coils and try to compare them. We assume energy of 10 kJ, f_1 of 1, 10 cm length of the coil and a bank inductance of 0.25 μH. The system inductance is the sum of the bank inductance and coil inductance. The summary of the currents and peak pressures with the variation of number of turns is shown in Table 5.2. The variation of pressure with the number of turns is shown in Fig. 5.13. It shows that there is a peak in the pressure with the number of turns.

The approach shows that the number of turns of the coil can be optimized. The term f_3 can be determined experimentally with a series of coils with different number of turns. Another way (and much simpler) is to determine this parameter from a model in an electromagnetics code like Maxwell 2D.

No. of Turns n	$\mathbf{f_3}$	$\mathbf{L_{Act}}$ From eqn. (5.15) μH	$\mathbf{L_{sys}}$	$\mathbf{I_{max}}$ From eqn. (5.6) kA	**Peak Pressure** From eqn. (5.9) MPa
2	1	Assume 1	1.25	126.5	4.023
6	1.2	10.8	11.05	42.5	4.087
20	4	400	400.25	7.1	1.267

Table 5.3: Summary of calculations for optimizing the number of turns in a coil.

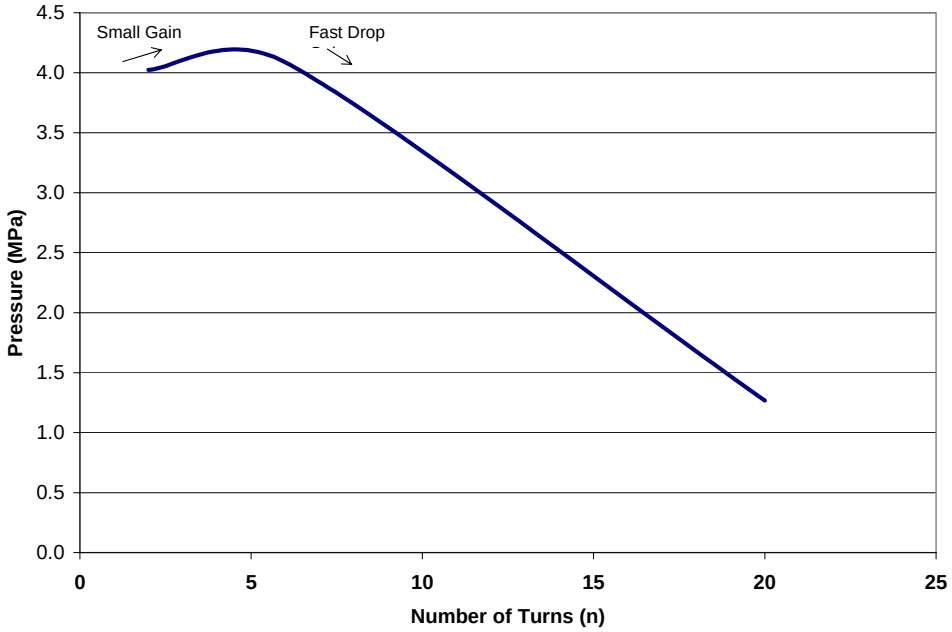

Figure 5.13: Variation of pressure with number of turns in the coil.

5.1.8 Summary

The analysis described above gives a decent method of predicting parameters in the electromagnetic forming process. An example for predicting the current profile has been shown for Actuator 2 in Fig. 5.14. Figure 5.15 shows the prediction capability for Actuator 1. The plots show a good correlation between the experimental and predicted data. The prediction is off after the first peak as the model assumes a constant frequency. The frequency decreases with time in the actual forming process. However, to a good approximation, the forming occurs within the first current pulse and therefore the model can be very useful.

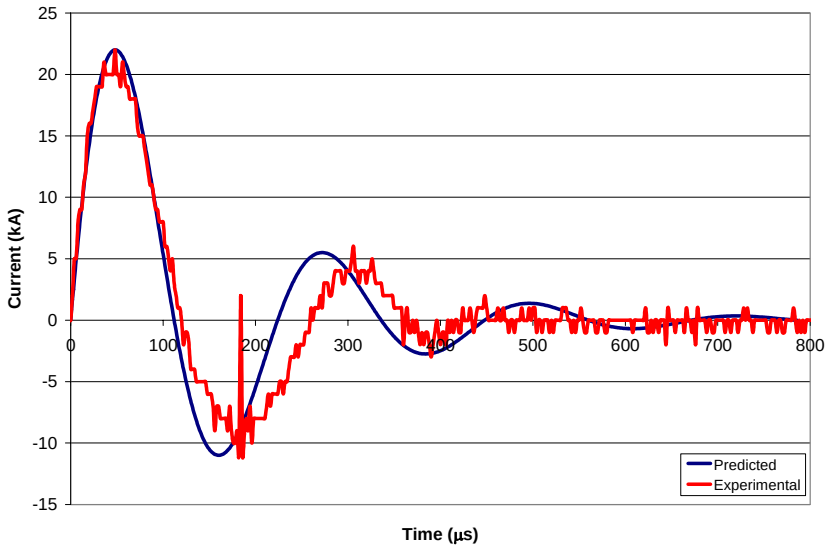

Energy of 1.6 kJ (4 Cap. and 20% energy)

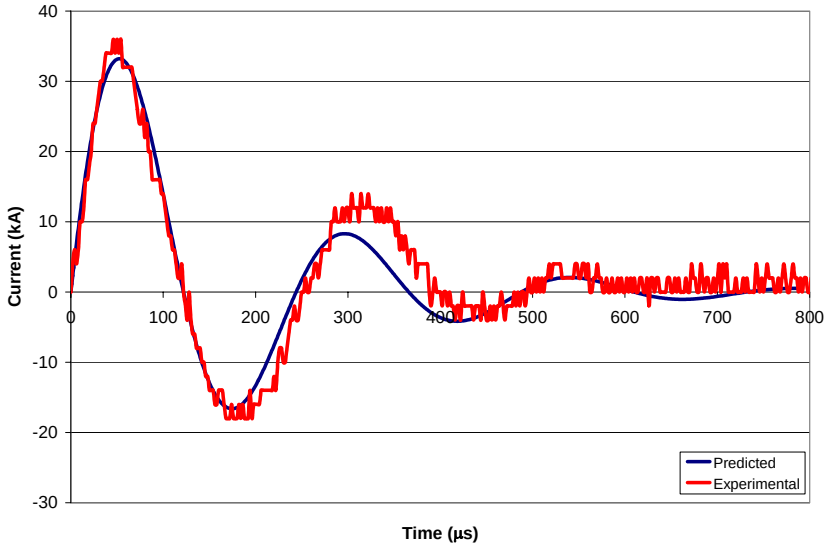

Energy of 4 kJ (4 Cap. and 50% energy)

Figure 5.14: Comparison between predicted and experimental values of the current for Al 5083-H18 using Actuator 2.

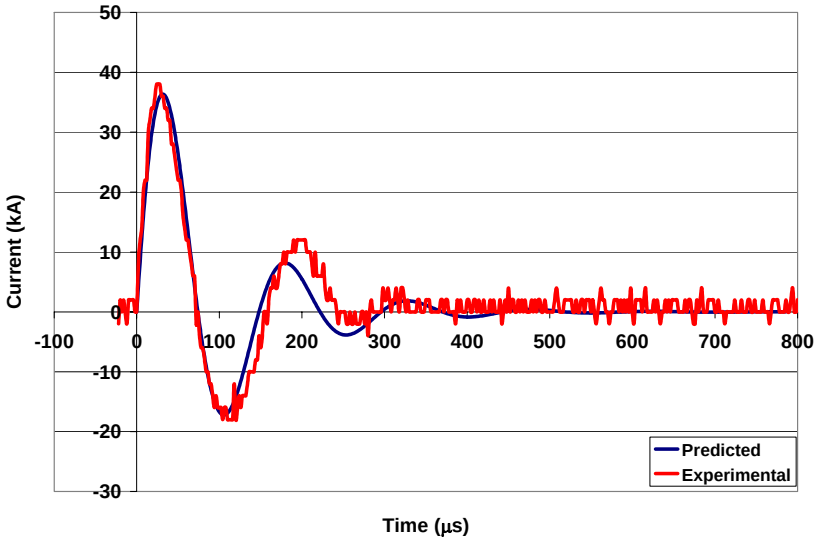

Energy of 1.6 kJ (4 Cap. and 20% energy)

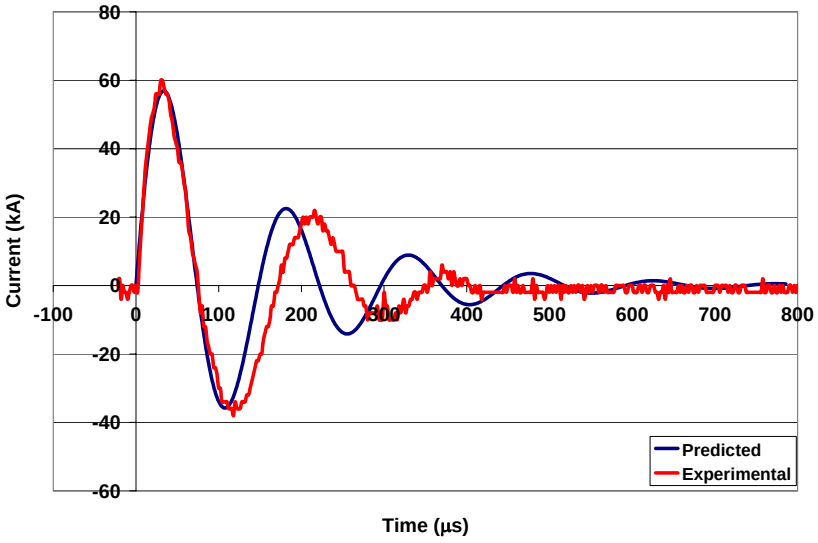

Energy of 4.8 kJ (4 Cap. and 60% energy)

Figure 5.15: Comparison between predicted and experimental values of the current for Mg AZ31B-H24 using Actuator 1.

5.2 Simulating High Velocity Metal Deformation

Electromagnetic forming is a complex process involving plastic deformation of solids coupled with electromagnetic field interactions. Dynamic behavior of materials along with heating by eddy currents complicates the analysis. The approach in designing the actuator as described above can greatly benefit from a numerical tool. Such a code can help in understanding what initial velocity or forming pressure distribution (as calculated from the Section 5.1) is required to completely form a desired shape. This would speed up the process of design of coils and the other forming system components.

Several commercial codes can deal with nonlinear dynamic problems however few standard codes integrate electromagnetic field interaction and material deformation. The High Rate Forming group at OSU has shown the applicability of three commercial codes: AUTODYN, ABAQUS/STANDARD and ABAQUS/EXPLICIT, and MP*one* [46] to study electromagnetic forming. AUTODYN and ABAQUS don't have the ability to model electromagnetic field interactions. MP*one* has both the ability to model dynamic mechanical deformation and electromagnetic field interactions. These two abilities are also coupled within the code. However the code is still in its infancy. AUTODYN was used in this study to study high rate forming.

5.2.1 AUTODYN

AUTODYN, developed by Century Dynamics (now a part of ANSYS) is a commercial general purpose hydro code designed for transient nonlinear dynamics in 2D and 3D. The capability of AUTODYN includes solving problems in nonlinear dynamics, fluid and gas

dynamics, large strain and large deformation, explosion, shock and blast waves, impact and penetration, and contact problems [47]. It includes multiple analysis techniques such as Lagrange, Euler, Arbitrary Lagrange Euler (ALE), SPH (smooth particle hydrodynamics), and shells. All these techniques can be coupled both in time and space to allow a variety of application problems. The non-linearities in AUTODYN include geometry and material non-linearities, extreme deformations and complex material behavior, contact opening and closing. One of the greatest advantages of this code is the ability to modify a problem during analysis, deletion and addition of materials and interactions and remeshing of highly distorted elements. AUTODYN provides an extensive material library for user's selection. A variety of explosives, liquids, polymers, minerals and metals with different strength models are available. The strength models of those materials include twelve different types of equation of state, sixteen strength models including Johnson-Cook, and a variety of failure criteria. AUTODYN also provides user subroutine interface for materials and boundary conditions.

In AUTODYN, Lagrangian, Eulerian and SPH (Smooth Particle Hydrodynamics) techniques are available to describe material movement. In this dissertation only the Lagrangian scheme has been used. In the Lagrangian technique the material moves with the mesh, whereas in the Eulerian technique the material is transported between elements. The governing equations in AUTODYN are the conservation of mass, momentum and energy. To complete the description of the continuum, two further relations describing the material behavior are required (besides the load and boundary conditions): first the equation of state, and secondly a constitutive model. As in any numerical code, the

governing equations need to be discretized both in time and space. The temporal discretization is the same for different analysis techniques in AUTODYN. Explicit time integration is used for computing required variables. The spatial discretization is different for different processors as noted before. Further details on the governing equations, material models and failure models can be found in [47].

5.2.2 Validation

The first step in using AUTODYN was to simulate a simple problem to study the ability of the code in simulating impact problems. Peihui Zhang [46] has looked at Hopkinson Bars using AUTODYN and found the results agreeable. Here a Taylor impact problem was chosen for the simulations [1, 10]. The approach of Wilkins and Guinan on Taylor impact was used for the study [49].

A 2-dimensional model with axial symmetry was made. An Al bar with a radius of 3 cm and 10 cm in length was made to impact a stainless steel wall. The Al bar had a uniform mesh of 12 x 30 elements. The mesh is shown in Fig. 5.16. The Al bar was assigned a Von Mises strength model, a shock equation of state with no failure model. This is similar to what was simulated by Wilkins and Guinan [49]. They used a shock equation of state, an elastic plastic strength model and no failure criteria in their model. The bar was given an initial velocity and made to impact on the steel wall. The die was constrained to have a general 2D velocity of zero. The range of velocities from 0 m/s to 200 m/s was investigated. Al 2024-T351 bars were also simulated using the Johnson-Cook strength model with and without a failure criterion. The failure was based on a

principal tensile stress. The descriptions of the Johnson-Cook model and the shock equation of state can be found elsewhere [47, 50]. The material properties used in the simulation are given in Table 5.4. The materials were chosen because of the availability of the Johnson-Cook and shock parameters for those materials in AUTODYN library. According to the analysis of Wilkins and Guinan [49], the behavior of the materials does not differ significantly in Taylor impact experiments in certain parameters evaluated in the study.

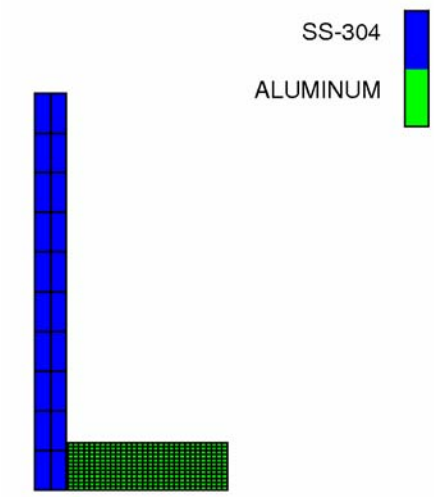

Figure 5.16: Mesh used in the Taylor impact problem simulation with AUTODYN.

Equation of State	**Shock**
Reference density	2.71000E+03
Gruneisen coefficient	2.10000E+00 (none)
Parameter C1	5.38000E+03 (m/s)
Parameter S1	1.33700E+00 (none)
Strength	**von Mises**
Shear Modulus	2.69000E+10 (Pa)
Yield Stress	2.90000E+08 (Pa)

(a) Parameters used in Al impact on steel die for Al.

Equation of State	**Shock**
Reference density	2.78500E+03
Gruneisen coefficient	2.00000E+00 (none)
Parameter C1	5.32800E+03 (m/s)
Parameter S1	1.33800E+00 (none)
Reference Temperature	3.00000E+02 (K)
Specific Heat	8.75000E+02 (J/kgK)
Strength	**Johnson Cook** $Y = [A + B\varepsilon_p^n][1 + C\log\varepsilon_p^*][1 - T_H^*]$
Shear Modulus	2.76000E+10 (Pa)
Yield Stress (A)	2.65000E+08 (Pa)
Hardening Constant (B)	4.26000E+08 (Pa)
Hardening Exponent (n)	3.40000E-01 (none)
Strain Rate Constant (C)	1.50000E-02 (none)
Thermal Softening Exponent (m)	1.00000E+00 (none)
Melting Temperature	7.75000E+02 (K)

(b) Parameters used in Al Impact with steel die for Al 2024-T351.

Table 5.4: Important material properties for Taylor impact simulation in AUTODYN 2D.

The deformation of the bar after impact with the wall is shown in Fig. 5.17. With increasing velocity the impacted end deforms significantly. The shape is close to that predicted by Taylor impacts. For a quantitative analysis, the results were compared to the results from Wilkins and Guinan [47]. These results are plotted in Fig. 5.18. Here the Y axis is the negative natural logarithm of the ratio of the final length of the bar (L_f) to its initial length (L_0). The X axis is the given ratio where ρ is the density of the bar material, U is the velocity and Y_0 the yield strength of the bar.

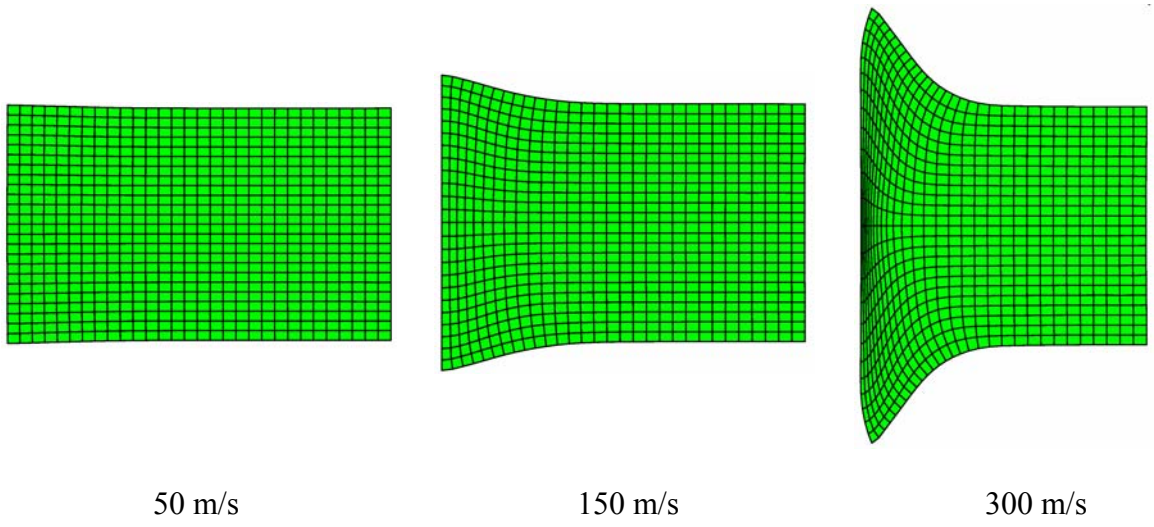

Figure 5.17: Final bar shape after impact with the steel wall using AUTODYN.

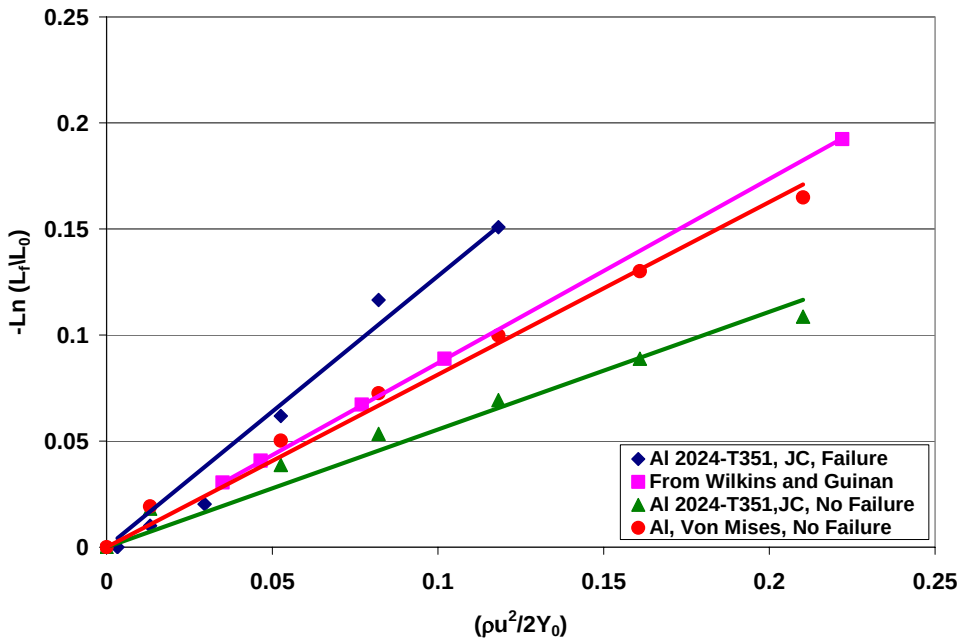

Figure 5.18: Taylor impact simulation with AUTODYN, quantitative comparison.

The results are close when the AUTODYN simulation used models used by Wilkins and Guinan. A failure model is not appropriate to model this as no failure is observed in actual experimentation in this velocity range [48, 49].

AUTODYN-2D simulations of the Taylor impact process show promising results for modeling impact problems.

5.2.3 Using AUTODYN with the Analytical Model

Velocity from the analytical solution may be used as an input in AUTODYN. The model in AUTODYN may then be used to estimate the velocity needed to fully form a given geometry. Experiments with Actuator 1 using a three-hole free forming die (Die FF4, Fig. 3.17) with 0.80 mm Al 2219-O will be discussed over here.

A 2-dimensional model with planar symmetry was made to simulate the impact of Al sheet into the hole with the largest entry radius (4 mm). The Al sheet had a uniform mesh of 16 x 50 elements. The Al sheet was assigned a Von Mises strength model, a shock equation of state with no failure model. The sheet was given an initial velocity and made to impact on the steel wall. The die was constrained to have a general 2D velocity of zero. A range of velocities from 0 m/s to 200 m/s was investigated.

Figure 5.19 shows the case with sheet velocity of 200 m/s. A comparison is also shown with a sheet formed at 6 kJ. The predicted shape is very close.

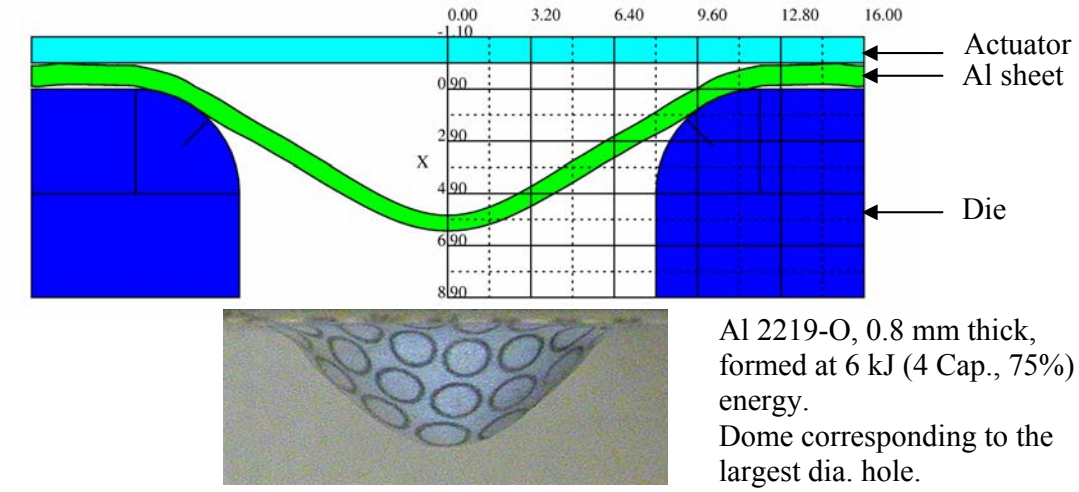

Figure 5.19: Comparison between an AUTODYN simulation of 0.8 mm Al sheet impacting a die at 200 m/s and the same geometry formed using Actuator 1 at 6 kJ.

Peak dome depths were obtained from experiments at different capacitor bank energies. AUTODYN was then used to predict the velocities at which these dome depths can be formed. The peak sheet velocities that can be obtained at the same energy by allowing the sheet to accelerate over a distance were then obtained by the analytical model. A comparison between the two velocities is shown in Fig. 5.20. This velocity is higher than that predicted by AUTODYN as expected.

The analytical model along with simulation of high velocity deformation in AUTODYN gives a decent method of predicting parameters in the electromagnetic forming process.

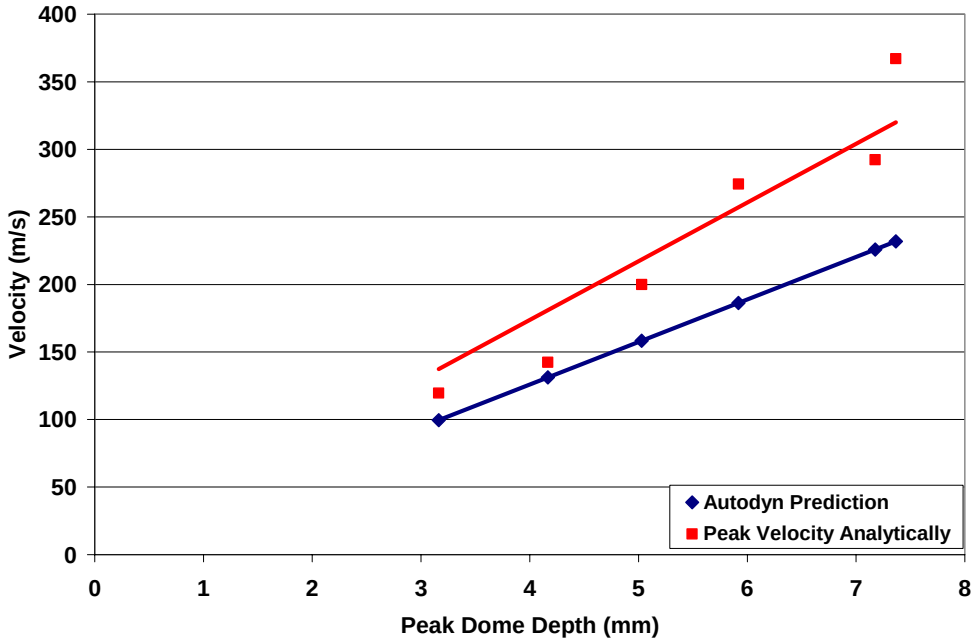

Figure 5.20: Comparison between velocities predicted by AUTODYN for dome depths measured experimentally to the maximum velocities achievable using the analytical model.

5.3 Simulating Electromagnetic Fields

Simulating the deformation of the material provides a solution to one facet of the design. Further design enhancement can be achieved with the help of codes that can simulate the electromagnetic fields and eddy currents. This can help tremendously in the design of the actuator by providing basic guidelines and eliminating costly reruns. MAXWELL 2D was used in this study to simulate the electromagnetic fields and eddy currents. In the present study, the use of this tool is primarily for qualitative results.

Maxwell2D is a powerful simulation software for electromagnetic, electrothermal, and electromechanical analysis. Maxwell 2D can be used to quickly and accurately develop virtual prototypes of electric machines, actuators, transformers, sensors and other electromagnetic devices that can be modeled in two-dimensions [51]. It can simulate frequency and time domain electromagnetic fields, steady-state thermal fields, strongly-coupled electromagnetic circuits and equivalent circuit model.

It is a finite element based field solver and uses automatic, adaptive meshing. Up to eight different solvers may be selected based on the problem to be simulated. The solvers include ac conduction, dc conduction, electrostatics, transient and thermal analysis. In the current study only the eddy current solver has been used.

The eddy current solver can simulate the effects of time varying currents. Designers may use the solver in frequency ranges from 0 Hz through several hundred MHz. The solver automatically calculates power loss, core loss, impedance for frequency, force, torque, inductance, and stored energy. However the calculations are steady state and variation of frequency with time cannot be simulated. Additionally, plots of flux lines, B and H fields, current distribution, and energy densities over the entire phase cycle are available. Power and core loss can be exported and used for thermal simulations [51].

Conductors may be placed in series or parallel, and termination may be included. Each conductor may have a current with different amplitude and phase lead or lag. The eddy current solver assumes that all currents are sinusoids oscillating at the same frequency.

A number of boundary conditions exist in the code. Two are important in the current study. Balloon boundaries model the region outside the drawing space as being nearly "infinitely large". This effectively isolates the model from any other sources of current or magnetic fields. The magnetic vector potential goes to zero at infinity. The other boundary condition used in the simulations is the eddy current source. Here the total current in the conductor is constrained to the value specified by the user.

The eddy current field simulator solves for time harmonic electromagnetic fields governed by Maxwell's equations:

$$\nabla \times H = J + \frac{\partial D}{\partial t} \qquad \text{..... (5.16)}$$

$$\nabla \times E = -\frac{\partial B}{\partial t} \qquad \text{..... (5.17)}$$

$$\nabla \bullet D = \rho \qquad \text{..... (5.18)}$$

$$\nabla \bullet B = 0 \qquad \text{..... (5.19)}$$

Where E is the electric field, D is the electric displacement (εE), B is the magnetic flux density, H is the magnetic field intensity (B/μ), J is the current density (σE) and ρ is the charge density. The quantity that the eddy current field simulator actually solves for is the magnetic vector potential.

CHAPTER 6

APPLICATIONS

While electromagnetic force can be used in very general and creative ways to form conductive sheet metal, to date it has been almost exclusively used to form crimped assemblies from round tubes [1]. The uniform pressure actuator gives several added degrees of freedom to the designer and the manufacturing engineer in conceptualizing and producing a part. In this chapter we will talk about examples of using the actuator. The application areas have been divided into three different categories: forming depressions, embossing and shearing. Figure 6.1 shows the summary of the applications that have been shown in the current work.

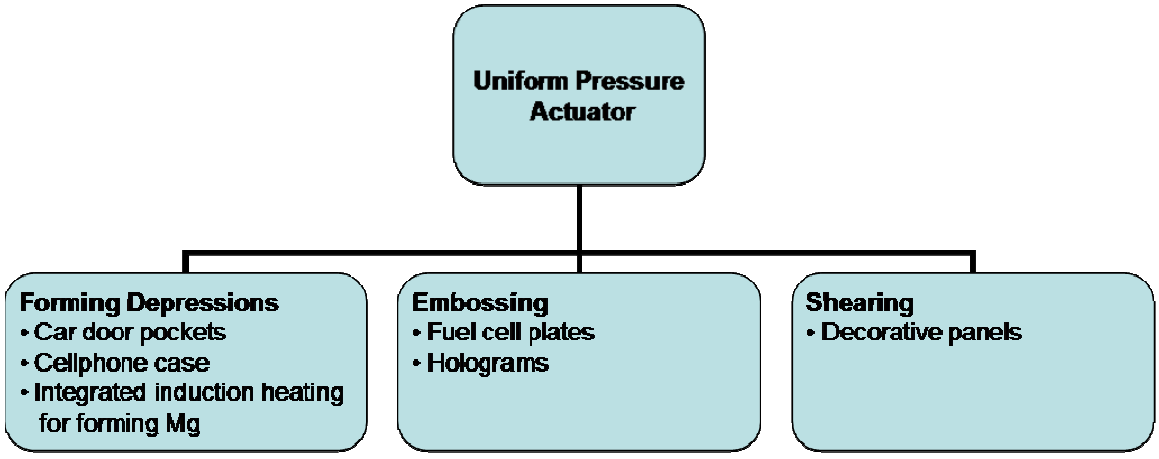

Figure 6.1: Summary of applications of the uniform pressure actuator.

6.1 Forming a Depression

Impulsive and quasi-static forming are fundamentally different. Dynamic forming methods are not bounded by the restrictions of a traditional Flow Limit Diagram (FLD). Instead, if launch and boundary conditions are properly chosen, ductility far beyond typical quasi-static ductility can be achieved.

Since the metal sheet comes in contact with a tool only on one side, single sided tooling can be used. Since tooling costs can be quite significant, EM forming can reduce costs in this aspect. This also means that coated sheets can be formed without the concern of contact with the tool. The lower press cost by this process is an added advantage.

The technique can also be joined with embossing to yield depth and surface features at the same time, e.g., cell phone cases. The impact gives good dimensional tolerance in the workpiece and the process is amenable to easy integration and complete automation.

6.1.1 Forming Rectangular Pockets

Deep drawing is a metal forming process in which a sheet of material is formed using a punch and a die [28, 29]. The shapes can vary from simple axisymmetric cups to complex automotive panels. Deep drawing processes for noncircular components are used in many industrial areas, such as construction, automobile manufacturing, aerospace technology, and electrical power engineering [52]. Our focus here is on forming into rectangular recesses which is of particular importance in forming car door pockets.

Deep drawing into rectangular or square pockets is an issue due to material flow leading to the formation of mouse-ear type defects. The idea is shown in Fig. 6.2. This is the strain distribution observed in a square cup drawing process as modeled using PAM-STAMP2G. The chosen simulation is a deep drawing of a square cup, a benchmark problem of the Numisheet'93 conference. Here a 111 mm square Al sheet, 0.81 mm thick is formed into a square cup at 19.6 kN blankholder force. The sheet is modeled using a Belytschko-Tsay (BT) shell element. Away from the formed geometry, there are no strains along the corners. Correspondingly the sheet around this location is thicker. Along the edges the strains are higher and the sheet therefore gets thinner. Also the draw in at the edges is more than three times that compared to the draw in at the corners. The non-uniform geometry leads to non-uniform metal flow. In such geometry, there is no

material flow at the corners [52]. This leads to the formation of mouse-ear type defects at the corners. These defects stand out on painted sheets as ears or areas of differential pattern around the corner of the pockets.

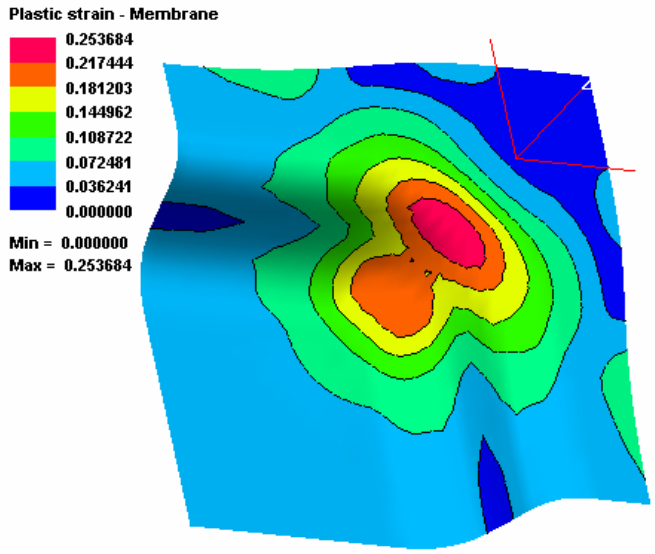

Figure 6.2: Plastic strain distribution within a square cup forming of aluminum based on Numisheet'93 conference.

While the demand for such cups is increasing, the technology of their design and manufacturing still needs to be improved. The problems are eliminated by using a multistage deep drawing process [53-55], optimizing the blank design [56-58], control over drawbeads, lubricants and variable blankholder force [59, 60]. In particular aluminum is more difficult to draw than steel because of its anisotropy. Current initiatives

in automotive industry are driving a need for stronger and lighter automotive panels. With the great push by the automakers for the usage Al in car bodies, there is a lot of interest in studying the deep drawability of Al [59].

In sheet metal stamping, there are two basic deformation modes, deep drawing and stretching. For deep drawing, one of the principal strains in the plane of the sheet is positive and the other is negative, and the change of thickness is small. For stretching, two of the principal strains are tensile, and thinning is required [28, 29]. In stamping, stretching may predominate in one region while drawing prevails in another. The relative amounts of drawing and stretching vary in different stamping processes. The uniform pressure actuator can help to solve the problem of mouse-ear type defects by controlling the amounts of stretching and drawing. By design the uniform pressure actuator can be used to form rectangular pockets where the deformation mode is only stretching with minimal drawing, reducing the mouse-ear type defects.

The objective of the study in this section is to develop an EMF process that will allow the creation of form in drawn in panels. The idea is to show an EMF process and its constituent elements that can be transferred to a full hybrid tool of a car body panel. To achieve this goal we wish to demonstrate the reduction of mouse-ear type defects in rectangular cup forming with the possibility of extending the technology for the forming of car door pockets.

6.1.1.1 Experimental Procedure

Al 5083-H18, 1.1 mm thick was formed into dies FF2 and FF3. Both are free forming dies with a rectangular opening. Actuator 2 was used for the experiments. The draw in was observed and circle gridding was used to measure the strain distributions. The strain distributions were used to evaluate the deformation mode, i.e., stretching or drawing.

6.1.1.2 Material Flow

Draw-in can be controlled by the area fraction of the open and non-open regions in the die under the uniform pressure actuator. Material flow from the flange into the formed area was observed. There is some flow, but we believe it is much reduced. Predominantly pure material stretching in the formed area occurs during the EM-forming.

An example is shown in Fig. 6.3. It shows an Al 5083-H18 alloy formed into die FF3. The material flow in the longitudinal direction is negligible. There is some flow in the transverse direction which can be quantified by the draw-in. The peak depth is 13.17 mm with a draw in of 1.69 mm in transverse direction. Sheet is 15 cm in the transverse direction. Table 6.1 lists the draw in for Al 5083 at different energy configurations.

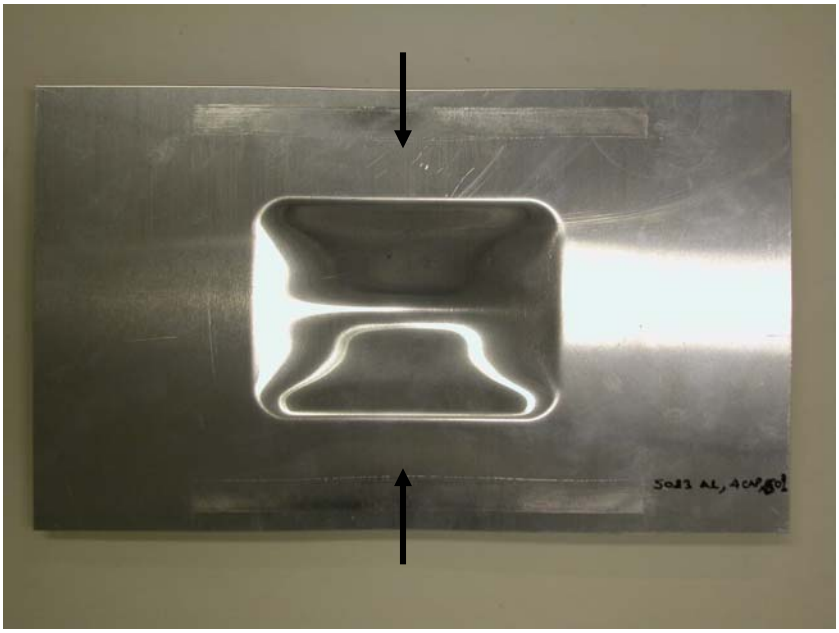

Figure 6.3: Al 5083-H18, 1.1 mm thick formed at 4.8 kJ (4 Cap., 60%) into die FF3 using Actuator 2. Arrows indicate the draw in direction.

The marks from the clamps are visible (parallel to the longer edge). The clamping of the sheet is not to restrain flow but to apply a sufficient pressure to resist arcing at the contacts. Downward force is required for this reason. Draw-in will reduce once the sheet size approaches that of a car door. Thus mouse-ear is reduced due to controlled draw-in.

Energy Cycle	Energy (kJ)	Max. depth in sheet metal specimen (mm)	Total draw-in along the longer side (mm)
4 Cap, 50%	4.0	11.91	0.88
4 Cap, 60%	4.8	13.17	1.69
6 Cap, 40%	4.8	14.22	1.82
6 Cap, 50%	6.0	17.42	4.03
6 Cap, 40% + 6 Cap, 20%	4.8 + 2.4	14.86	2.70

Table 6.1: Comparison of the maximum deformed depths and draw-in obtained in Al 5083 at energy different configurations.

6.1.1.3 Grid Analysis

Circle gridding was done on the formed parts. The goal here was to analyze the material flow, not to show extended formability. Figure 6.4 shows an Al alloy which was formed into die FF2 using Actuator 2. Here at the energy of 4.8 kJ tearing takes place on the sheet, corresponding to the smaller edge entry radius. No major strains of over 10 % were reported. However it is clear that stretching predominates which is good for reducing mouse-ears.

Changing entry radius will change effective formability. Die FF3 was designed after studies with die FF2 to take this into account. In Fig. 6.4, the sheet cracks along the shorter edge at 4.8 kJ. This is due to the sharp fillet radius (4.76 mm) for the current die

dimensions and higher energy. Another problem was realized with the die FF2. As there is an interface between the die and the outer block, the sheet takes that shape when it hits it at high velocities. Our purpose was to eliminate this and we did this by making a die that covers the entire area. Die FF3 was designed to incorporate these changes with a higher fillet radius (6.35 mm) and with the die extending all the way up to the outer structure as shown in Fig. 6.5.

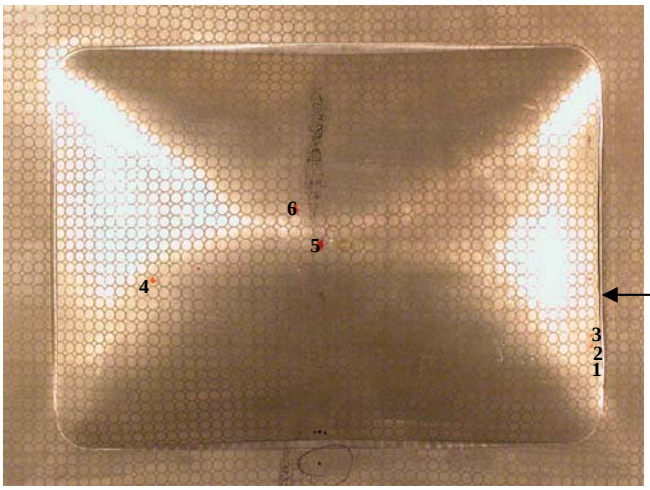

Points	1	2	3	4	5	6
Major Strain	4.61	4.87	0.66	0.83	8.86	5.92
Minor Strain	3.42	3.38	-0.95	0.48	4.43	2.11

Figure 6.4: Al 5083-H18, 1.1 mm thick formed at 4.8 kJ (4 Cap., 60% energy) using Actuator 2 and die FF2.

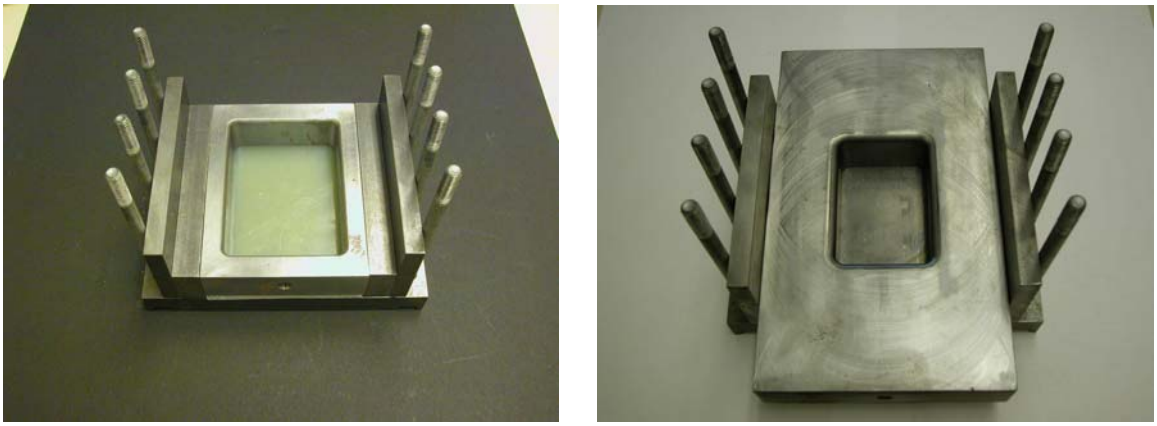

(a) (b)

Figure 6.5: (a) Die FF2 in the setup for Actuator 2 and (b) Die FF3 in the same setup.

6.1.1.4 Multiple Capacitor Discharges

The above experiments were carried out with free forming dies where vacuum is not an issue. In the case of forming into a closed end die, multiple capacitor discharges of lower energies can provide a useful forming operation. Significant deformation depth increase is not noted with increase in the number of shots; however the deformed shape may change. As an example, consider free forming into a FF2 die using an auto grade steel and Actuator 2 to form a rectangular pocket. The effect was very promising with the deformed contour becoming more rounded. With a single shot of 4 kJ in auto grade steel, the four lines connecting the edges of the die are visible. However three more shots give a more uniform rounded contour. Figure 6.6 compares the depth achieved with one shot and multiple shots. The formed parts are shown in Fig. 6.7. The depths were measured along the lines bisecting the edges of the die cavity. Although no significant increase in depths are obtained as the sheet is far away from the coil and the coupling is poor, a more

rounded profile is obtained. This may also be helpful in relaxing the need for vacuum in EM forming. Vacuum is typically used in forming details as the entrapped air creates a problem in getting the details. With multiple shots and progressive movement of the sheet metal to fill the die cavity, the air is progressively removed and hence vacuum may not be required.

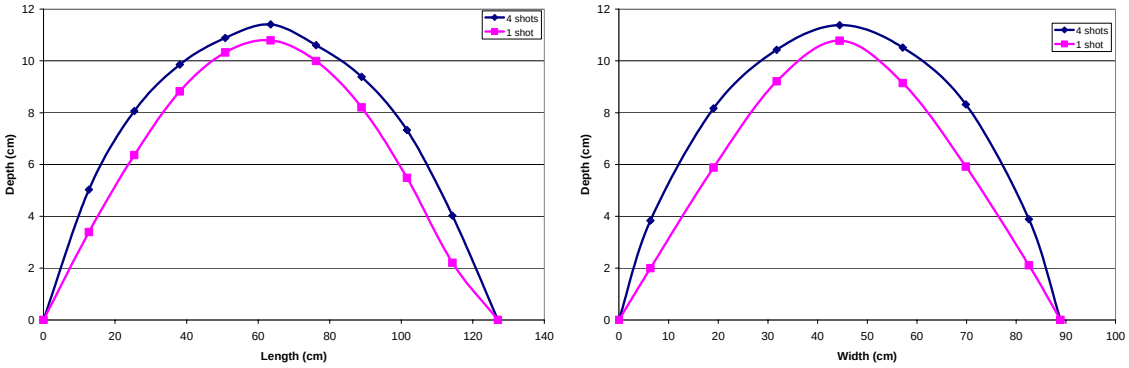

(a) (b)

Figure 6.6: (a) Depth contour along length of cavity; (b) Depth contour along the width of the cavity at 4 kJ (4 Cap. and 50% energy).

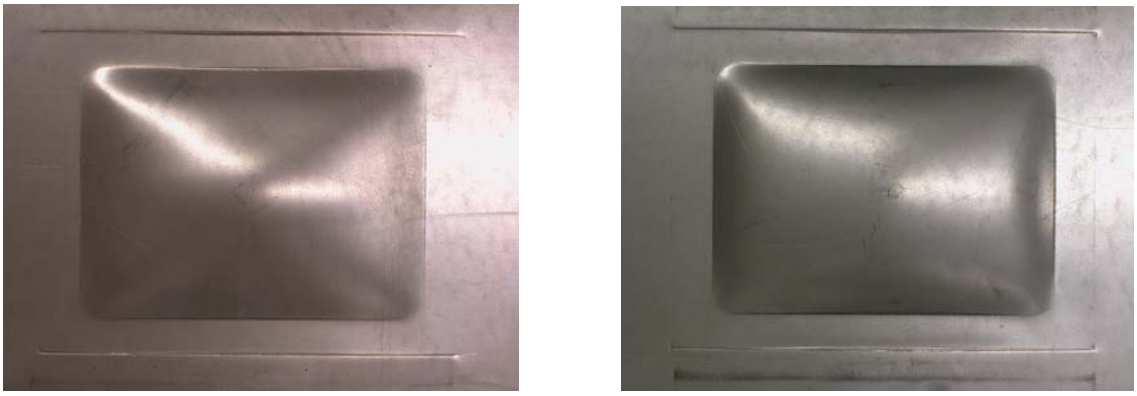

(a) (b)

Figure 6.7: (a) Auto grade steel, one-shot of 4.0 kJ (4 Cap. at 50% energy); (b) Auto grade steel, four shots of 4.0 kJ each (4 Cap. at 50% energy).

6.1.1.5 Defects

The only defect we see is a bit of oil-canning when putting the depressions in flat sheets. We believe this would totally disappear if we were to form on curved (versus flat) sheets. No wrinkles or other unusual deformation was observed in the sheets formed.

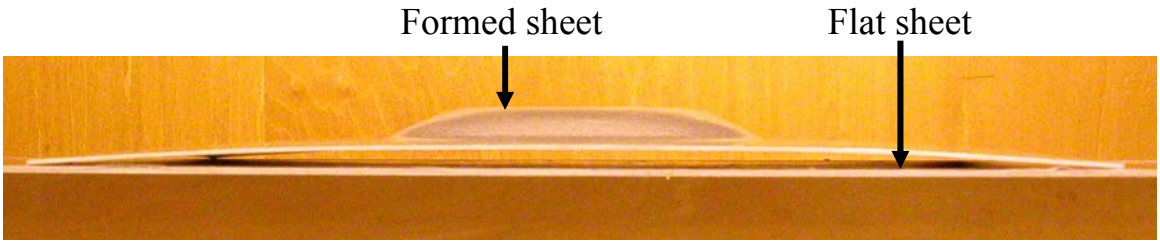

Figure 6.8: Al 5083-H18, 1.1 mm thick formed at 5.6 kJ (4 Cap. and 70% energy).

6.1.1.6 Arcing Issue

The arcing issue and the method used to tackle the same is described in detail in Chapter 7. Uniform contact load is required to control arcing. If this technique is used to form car door pockets or other products where the top surface quality is critical, arcing is a special concern. In this setup an Al-Al contact occurs between the sheet metal and the outer conductive channel. Thin strips of copper of the same dimensions as the contact areas were placed between the contacts. It was seen that the contact surface after forming has a better appearance with the usage of copper. Only very slight scuffing results from the current path. Copper reduces the contact resistance due to its higher conductivity. It can be seen in Fig. 6.9 (a) that there is no indication of any sparks in the sample. Later designs of the actuator (Actuator 3) incorporate a copper outer channel for better contacts. The samples were spray painted to check the effect of contact surfaces on aesthetic appearance (Fig. 6.9 (b)). It is believed that after painting these surfaces will be indistinguishable from the rest.

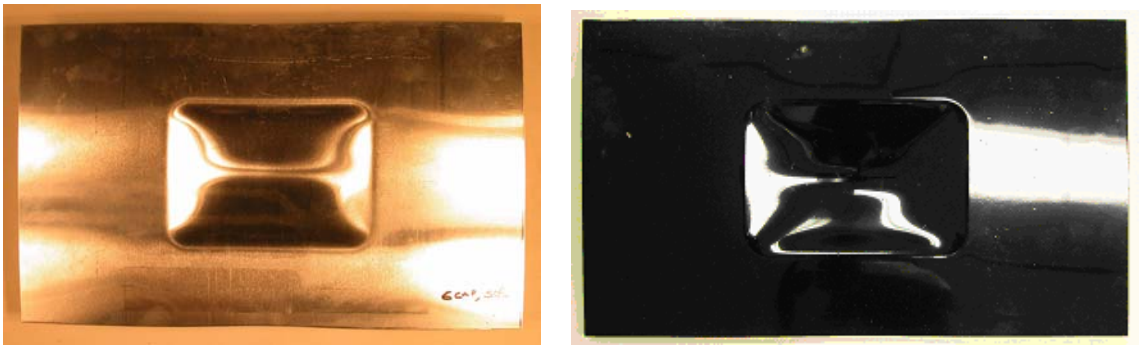

(a) (b)

Figure 6.9: (a) Al 5083 at 6 kJ (4 Cap. and 50% energy) showing a flat surface (die FF3) with no indications of sparks and (b) Painted Al 5083 formed at 4kJ (4 Cap. and 50% energy) using die FF3.

6.1.1.7 Summary

Overall this study shows the promising results of controlling mouse-ear type defects by using a uniform pressure actuator. The mouse-ears are controlled by predominant stretching in the formed rectangular cavity as opposed to predominant draw-in in typical deep drawing process.

6.1.2 Forming Cellphone Cases

Forming a depression can be joined with embossing techniques to yield depth and surface features in a single operation. This is particularly appealing for portable electronic devices like PDA covers and cell phone cases. Typically cellphone cases for the mass market are manufactured from plastics. However, there is a niche, high-end market for

metallic cases. Aluminum and magnesium are the top contenders for the spot because of their light weight. The objective in this study is to demonstrate that an appropriate combination of technologies including electromagnetic forming plus traditional forming either before or afterwards can effectively form cellphone cases. We will demonstrate the technology with aluminum.

6.1.2.1 Experimental Procedure

A cellphone die (die D1) was provided by MIRDC, Taiwan (shown in Fig. 3.24). Al 2129- O, 0.8 mm thick was used for the forming trials. Evaluation was carried over a range of launch energies. Vacuum was created between the sheet metal and the die. Industrial grease was used to promote drawing by applying a layer on the die till the entry radius.

6.1.2.2 Formability

The sheet metal was formed at launch energies from 1.6 kJ to 5.6 kJ. With increasing energy the sheet has a higher velocity of impact with the die and therefore has sharper features. An example is shown in Fig. 6.10. Until 3.2 kJ there are no signs of any failure. Above this energy the sheet starts to crack along the die edges. Teflon was also used at the die edges to promote drawing but it does not have a significant benefit.

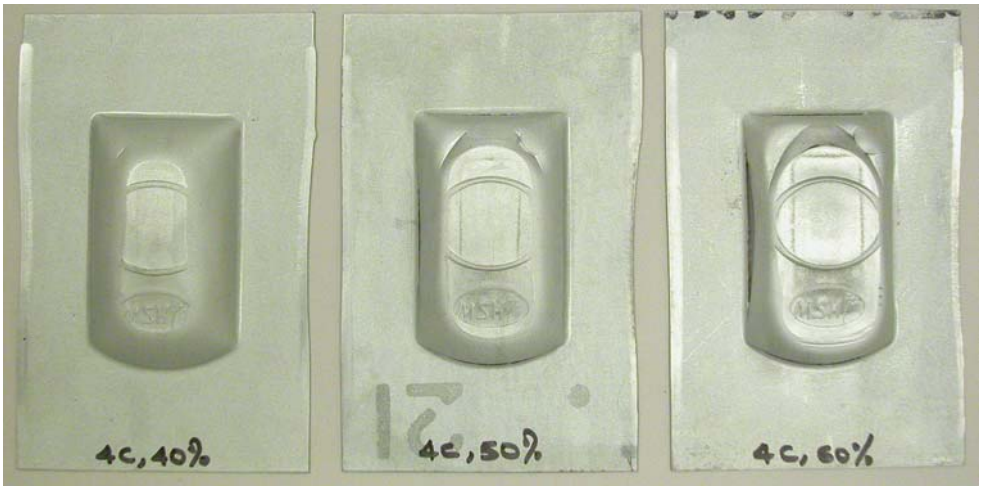

Figure 6.10: Comparison of the cellphone cases formed at 3.2 kJ (4 Cap., 40%), 4.0 kJ (4 Cap., 50%) and 4.8 kJ (4 Cap., 40%), left to right, using die D1 and Actuator 1.

Figure 6.11 shows the case formed at 5.6 kJ. It shows cracks along the long and short edges. It shows that although cracks are present, surface details have a good resolution. The logo of "MSK" along with the flower pattern is very clear. It demonstrates the ability of EM forming to form the part. However the die/process needs some modifications to make the part successfully.

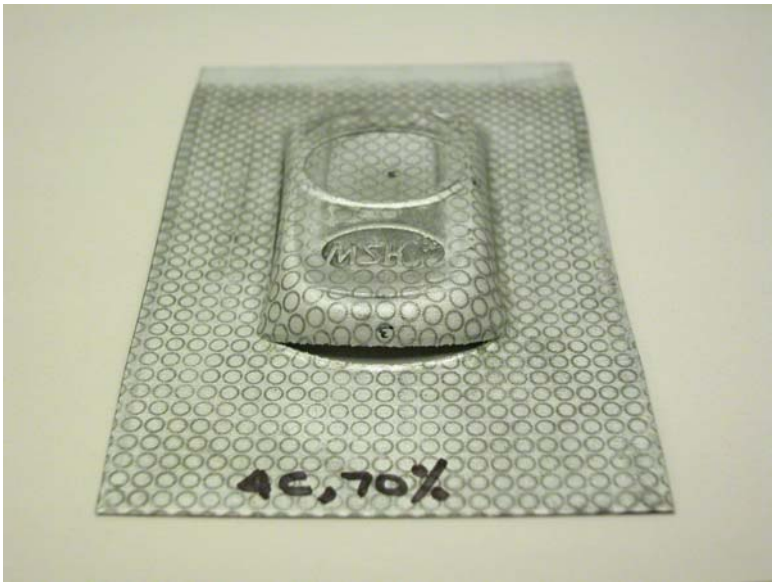

Figure 6.11: Cellphone case formed at 5.6 kJ (4 Cap., 70% energy) showing the tears along the edges.

Circle gridded samples as shown in the figure above were used to evaluate the formability. Five regions as shown in Fig. 6.12 were selected to check the strain distribution. The circle with the maximum elongation in a particular region was selected for the strain distribution calculations.

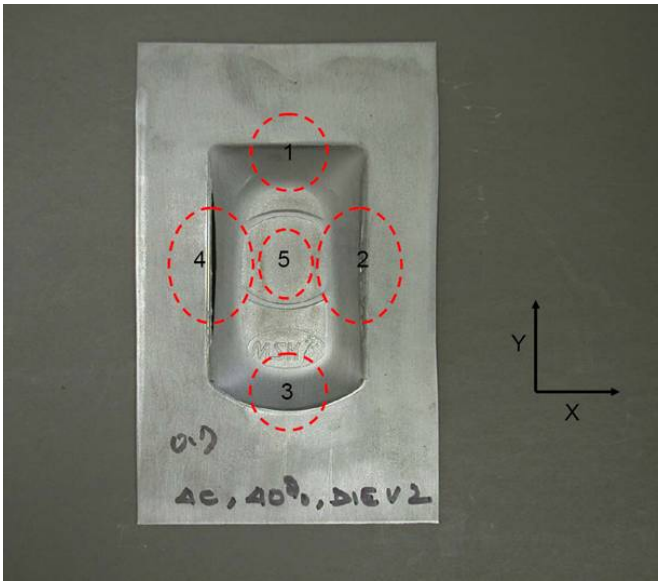

Figure 6.12: Formed cellphone case showing the areas for strain distribution measurements.

Figure 6.13 shows the plot for the strain distribution. The plot also shows comparative data for Al 2219-T31, 0.813 mm thick from Hursman [61]. Maximum strain of 26% was observed in one sample which is higher than what is predicted by the FLD of a similar alloy. However for most cases the maximum strain was in the range of 8 to 16%. Al 2219-O has 18% ductility at break in uniaxial tension.

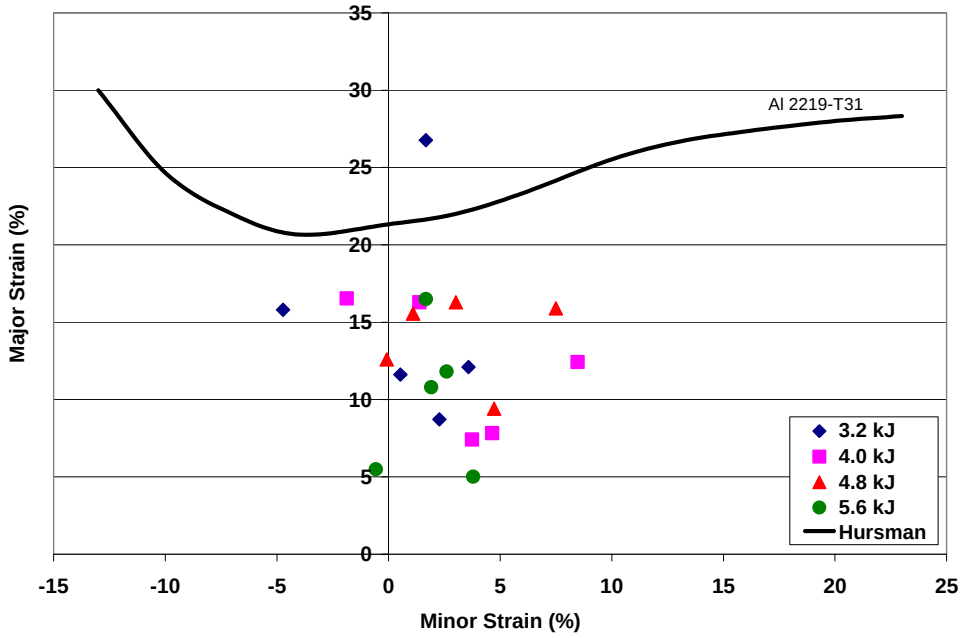

Figure 6.13: Strain distribution at varying launch energies for cell phone case forming.

Although the setup was not designed to evaluate formability, EM forming is able to achieve much higher strains than that predicted by the FLD. The strains by location and axes are shown in Table 6.2.

3.2 kJ			4.0 kJ		
Location	**Strain x**	**Strain y**	**Location**	**Strain x**	**Strain y**
1	2.28	8.72	1	7.41	3.75
2	15.80	-4.73	2	7.82	4.64
3	26.76	1.67	3	-1.87	16.54
4	11.61	0.53	4	16.29	1.38
5	12.10	3.58	5	12.42	8.47
4.8 kJ			**5.6 kJ**		
Location	**Strain x**	**Strain y**	**Location**	**Strain x**	**Strain y**
1	3.01	16.29	1	5.01	3.79
2	15.56	1.10	2	16.50	1.67
3	9.41	4.73	3	11.81	2.61
4	12.59	-0.08	4	10.79	1.91
5	15.89	7.49	5	5.50	-0.57

Table 6.2: Strain distribution at specified locations and varying launch energies for cellphone case forming.

6.1.2.3 Effect of Vacuum

As discussed in Chapter 4, if air is present in the die, it does not have enough time to escape and is entrapped. This leads to prominent ridges of air bubbles reflecting on the formed parts. A vacuum in the system for forming cellphone cases is therefore important. An example of the effect is shown in Fig. 6.14.

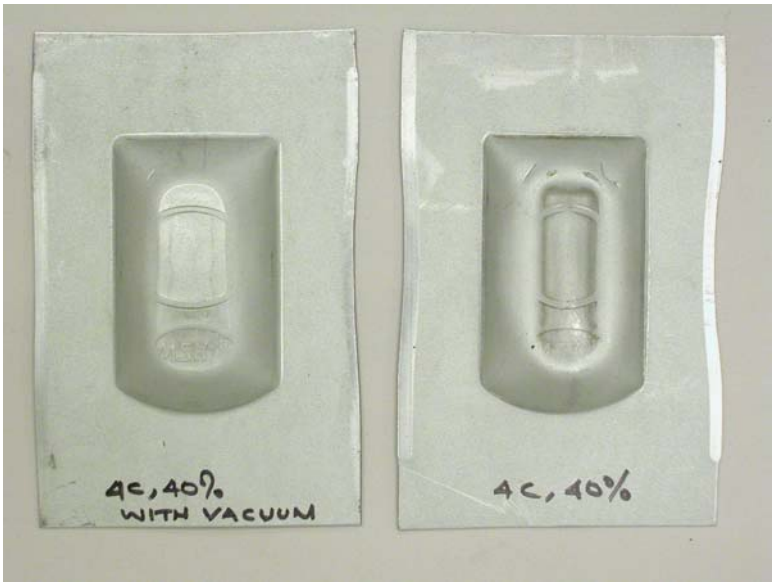

Figure 6.14: The effect of vacuum on Al alloy formed at 3.2 kJ (4 Cap., 40% energy) using die D1 and Actuator 1.

6.1.2.4 Alternate Methods of Forming

The approach to form the metal using a single step and achieving the depth and corners appropriately is an aggressive solution for the given geometry. As shown in Fig. 6.11, the metal sheet is able to achieve the depth and the surface details. However, the resolution at the corners is not as desired. Also the part tears along the edges. Alternate methods may provide a solution in forming the part as desired.

An example of alternate methods is demonstrated in Fig. 6.15. Al 2219-O alloy was first formed at energy of 3.2 kJ. Copper sheets (0.4 mm thick) were then used as drivers to push the Al further. The Cu sheets were used for two shots at 5.6 kJ each. The result is a

formed part with good surface details, no shock lines and no imminent signs of failure. Exceptional surface detail is captured in the part. The Cu was not as effective as there was an air problem now between the Cu sheet and Al sheet. Removal of air by a vacuum setup will increase the efficiency.

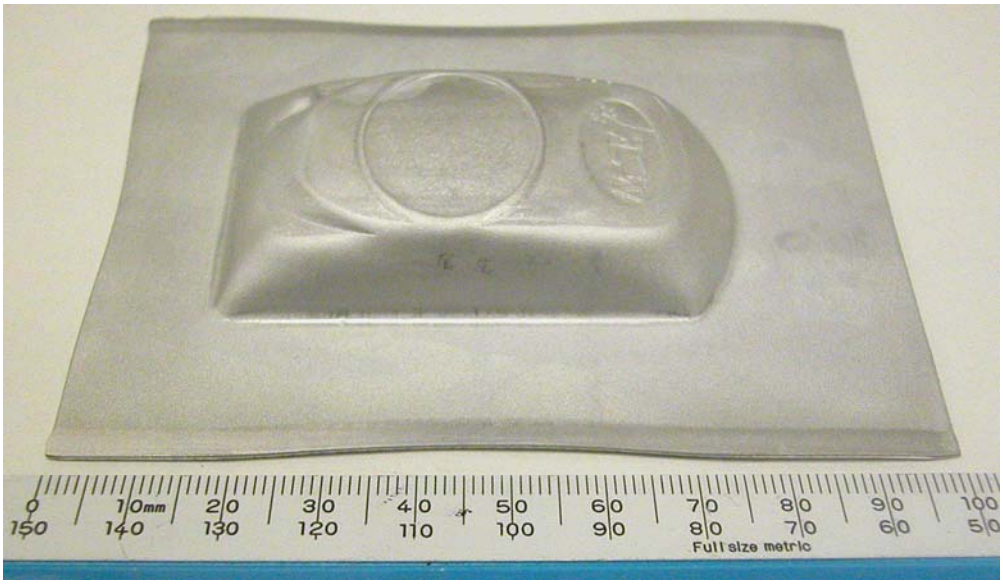

Figure 6.15: Forming a cellphone case with 0.8 mm Al alloy using multi-step impact forming.

6.1.2.7 Summary

There are a few decent conclusions that can be drawn from the experiments. The uniform pressure actuator works well in forming features where exceptional surface details are required along with case depth. Forming the cellphone case in a single step may not be

the best approach and alternate approaches like the one described above may help. However the study does show the immense capability of the new actuator design.

A fully formed part with the above specifications needs die and process modifications. A possible hybrid forming approach has been shown in Fig. 6.16. These process figures have been provided by OSU group (Glenn Daehn and Jianhui Shang) in consultation with the MIRDC, Taiwan. Here embossing is carried out into a die with shallow features and high entry radius using the uniform pressure actuator. A coil in then used in step 2 to flange the edges and give the sharp corners.

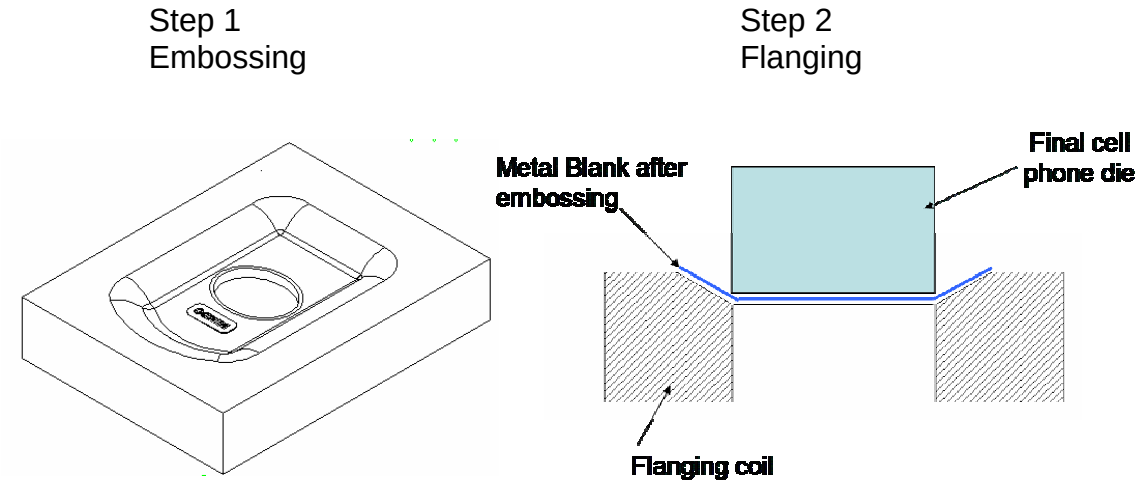

Figure 6.16: Hybrid approach to form cellphone cases. Process figures from Jianhui Shang and MIRDC, Taiwan.

6.1.3 Integrating Induction Heating

The new coil develops a uniform pressure over the entire sheet metal surface and is more energy efficient than conventional electromagnetic forming coils and processes [62, 63]. This technique offers significant opportunities in forming ductile metals (aluminum, steel, copper, etc.) beyond conventional forming. At present this method must be applied to nominally ductile materials, but there are very significant opportunities in the forming of materials that are rather brittle at room temperature. Magnesium is one such example. Above about 200º C, magnesium has exceptional formability, but it is quite brittle at room temperature as shown in Fig. 6.17 [64, 65].

Here induction heating will be added to this unconventional forming technique and this will enable the fabrication of very complex nominally flat magnesium components (such as personal electronics cases). Uhlmann and Hahn [66] have demonstrated a tool using the hybrid approach for Magnesium. The infrastructure developed here can be easily applied to joining of materials at elevated temperatures in subsequent programs.

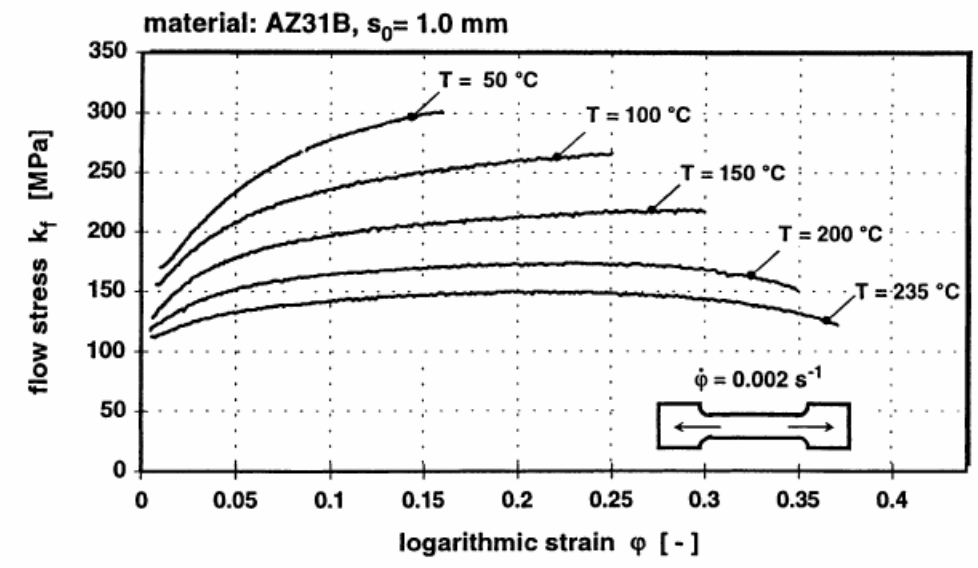

Figure 6.17: Temperature dependent flow curves of AZ31B (s_0= 1.0 mm) determined in the uniaxial tension test [64].

The objectives in this part of the study are:

1) To further demonstrate the capability of the uniform pressure distribution coil in fabricating nominally flat components such as cell phones, PDA covers, decorative housings and medical devices such as microfluidic enclosures.

2) To extend this capability to low ductility materials such as Mg sheet by integrating induction heating with the forming tooling system.

6.1.3.1 Experimental Procedure

The 16 kJ Maxwell Magneform capacitor bank was used in this study along with Actuator 1. A mild steel die with a variable entry radius, Die FF4 was used. The entry radii were chosen in multiples of the sheet thickness to be used. A 0.5 mm thick AZ31B-H24 Mg alloy was used for the study. Al 2219-O, 0.8 mm thick was also used for comparison with the Mg alloy. Parts were launched by the uniform pressure coil into the above die. Evaluation was carried out over a range of launch energies from 1.6 kJ to 5.6 kJ at increments of 0.8 kJ. Samples were circle gridded to see the formability at a particular energy. Formability was observed specifically at the dome tips of the formed sheets and near the entry radius.

6.1.3.2 Integration of Induction Heater with the Capacitor Bank

The approach here was to use the forming coil as an induction heating coil also. A 2.5 kW Lepel induction heater was used for the integration with the capacitor bank. The heater is shown in Fig. 6.18. The induction heater was connected with the coil as shown in the schematic in Fig. 6.19. A coaxial cable was used to connect the induction heater to the circuit breaker and the circuit breaker to the forming coil. A circuit breaker with a peak capacity of 100 A at 230 V was used and it was placed in between the forming coil and the induction heater. This would help in isolating the induction heater when the capacitor bank is switched. For simplicity no switch was placed in between the capacitor bank and the coil.

Figure 6.18: The 2.5 kW Lepel induction heater used in integrating induction heating with EM forming.

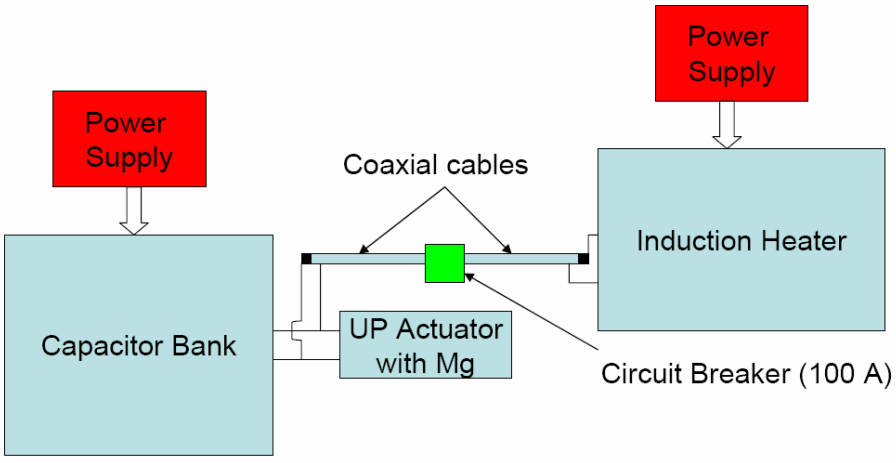

Figure 6.19: Schematic of the connection between induction heater and the capacitor bank.

(a)

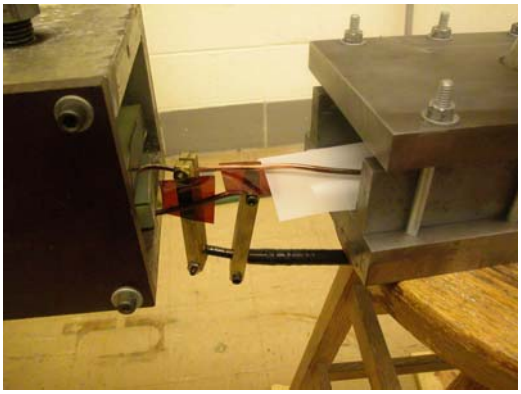

(b)

(c)

Figure 6.20: Setup of the induction heater with the capacitor bank; (a) the induction heater with the circuit breaker and coaxial connections, (b) the actuator connections to the capacitor bank and the coaxial, (c) overall setup showing the manual switching.

The actual setup is shown in Fig. 6.20. Manual switching was used here for simplicity. The cooling water in the induction heater was bypassed using a rubber hose. The time gap between the charge and discharge from the capacitor bank was evaluated. This ranges

from 1 second for 4 Cap., 10% energy (0.8 kJ) to 4 seconds for 4 Cap., 60% energy (4.8 kJ). The following sequence of steps was used:

(i) Switch on the capacitor bank, and put it in activate mode.

(ii) Switch on the induction heater with a timer for 10 seconds.

(iii) After the heating switch off the circuit breaker and push the start on the capacitor bank simultaneously.

6.1.3.3 Basic Analysis

A basic analysis was done to predict the temperature rise in various parts of the system. The coil has an inductance of 3.45 μH with no sheet metal in contact as measured by a digital LCR bridge (SE 280). The sheet metal is assumed to be an Mg alloy which needs to be heated to 200ºC. The coil is to be used with the induction heater to heat the Mg sheet and then the same coil is to be used for electromagnetic forming of the sheet. A simplified analysis of the problem is presented below:

The time durations of the heating is assumed to be short so that the heat transfer by conduction is negligible. Therefore heat transfer is governed by:

$$mC\Delta T = \int_0^t i^2 R dt \qquad \text{..... (6.1)}$$

Here m is the mass, C is the heat capacity, R is the resistance, t is the time and i is the time varying current.

$$\int_0^t i^2 R dt = \frac{I^2 R}{\omega}[\omega t - \sin \omega t \cos \omega t / 2] \qquad \text{….. (6.2)}$$

where ω is the frequency.

Taking R.H.S. of expression (2) as $I_m^2 Rt$ where I_m is a constant dependent on the current. The calculations for the different components in the system are summarized in Tables 6.3, 6.4 and 6.5.

Property	***Value***
Thickness	0.5 mm
Mass (m)	6.879 g
Resistance (R)	1.39 x 10^{-4} Ω
Heat Capacity (C)	1 J/g-ºC
Temp. rise (ΔT)	200ºC, given
Time reqd. to get to 200ºC (t)	(9.898x10^6/I_m^2) using eqn. (6.1) and (6.2)

Table 6.3: Heating calculations for 0.5 mm thick AZ31B-H24 Magnesium alloy.

Property	***Value***
Length (l)	12.5 cm
Area (A)	3.27 cm^2
Resistivity (ρ)	3.7 x 10^{-6} Ω cm
Mass (m)	110.363 g
Resistance (R)	1.414 x 10^{-5} Ω
Heat Capacity (C)	0.896 J/g-ºC
Time of heating (t)	($9.898x10^6/I_m^2$), same as Mg, with the same current flowing
Temp. rise (ΔT)	1.415ºC, using eqn. (6.1) and (6.2)

Table 6.4: Heating calculations for 6061-T8 Aluminum alloy.

The copper coil is a 15 turn coil. The material considered for calculations is OFHC Copper C10200. Assuming perfect coupling,

$$I_{cu} = I_m / 15 \qquad \text{….. (6.3)}$$

Using our experimental data with the given coil

$$I_{cu} = I_m / 10.5 \qquad \text{….. (6.4)}$$

Property	***Value***
Length (l)	285.4 cm
Area (A)	5.515 cm^2
Resistivity (ρ)	1.69 x 10^{-6} Ω cm
Mass (m)	140.9 g
Resistance (R)	8.75 x 10^{-3} Ω
Heat Capacity (C)	0.385 J/g-ºC
Time of heating (t)	($9.898x10^6/I_m^2$), or ($4.399x10^4/I_{cu}^2$) using eqns. (6.3) and (6.4) , same as Mg
Temp. rise (ΔT)	7.14ºC (perfect coupling)/ 14.57ºC (non-perfect)

Table 6.5: Heating calculations for OFHC Copper C10200 alloy.

Issues

1. Epoxy: Might be a concern here. We are using the product Conathane Tu-971 from Cytec Industries. The product has a heat distortion temperature of 98ºC (at 60ºC curing temperature). The Mg in contact with the Kapton tape and the epoxy has to be heated to a temperature of 200ºC. Since this is a thin sheet, low in mass, the heat loss will be fast. However, this is still a matter of concern. The solution may be using high temperature resistant epoxies, but all our present coils are made from Tu-971.
2. Kapton: The Kapton tape covers the epoxy surface and is the surface that is directly in contact with the sheet metal which is at 200ºC. The heating here is due to conduction with the heated metal sheet and not due to any induced currents.

Most Kaptons are rated to continuous service at 220-240ºC. The maximum service temperature is 400ºC.

3. Copper coil: The heating here is Joule heating due to the passage of current. Assuming perfect coupling between the copper coil and the metal sheet the typical rise in temperature is estimated to be 7ºC. Taking the coupling factors seen experimentally in our system the estimated temperature rise in the copper coil is 15ºC. This temperature rise is OK and can be dissipated very fast since copper is a good conductor.
4. Al Channel: Joule heating due to the passage of induced currents is applicable here also. The estimated temperature rise is approximately 2ºC which should not be a problem for the operation.

6.1.3.4 Room Temperature High Velocity Formability of Mg

The experiments were designed to study the room temperature formability of the Mg alloy and then compare that with results at higher temperatures. Die FF4 was used to make simple shallow cup shape parts using the uniform pressure actuator.

Magnesium has poor room temperature formability and this is clear from Table 6.6 which summarizes the peak dome depth achieved at each energy level.

Energy (kJ)	Configuration	Depth (in mm)		
		A 1.19 mm	**B** 1.98 mm	**C** 3.97 mm
1.6	4 Cap., 20%	0.84	0.97	1.61
2.4	4 Cap., 30%	1.54, slight crack at edges	1.75, slight crack at edges	2.3
3.2	4 Cap., 40%	2.65, partial cut at edges	2.72, partial cut at edges	3.15
4.0	4 Cap., 50%	Cut	Partial Cut	3.42
4.8	4 Cap., 60%	Cut	Cut	4.25
5.6	4 Cap., 70%	Cut	Cut	Dome tip failure

Table 6.6: Summary of the effect of energy on the formability of Mg alloy.

At the lowest energy of 1.6 kJ there are no signs of any cracks in the material. At 2.4 kJ the material starts to crack along the edges of the sharper radius hole, i.e., along A and then along B. With increasing energy and higher impact velocity of the sheet with the die, the damage along the edges is greater until the case of 4.0 kJ where the sheet shears along the hole edges. With higher energies the higher radius hole also gives way and the sheet tears along the edges. In the case of 5.6 kJ, the peak energy tried in this case, the entry radius does not have an effect and the dome tip failure results. The sheets formed at different energies are shown in Fig. 6.21. The 5.6 kJ case is shown in Fig. 6.22.

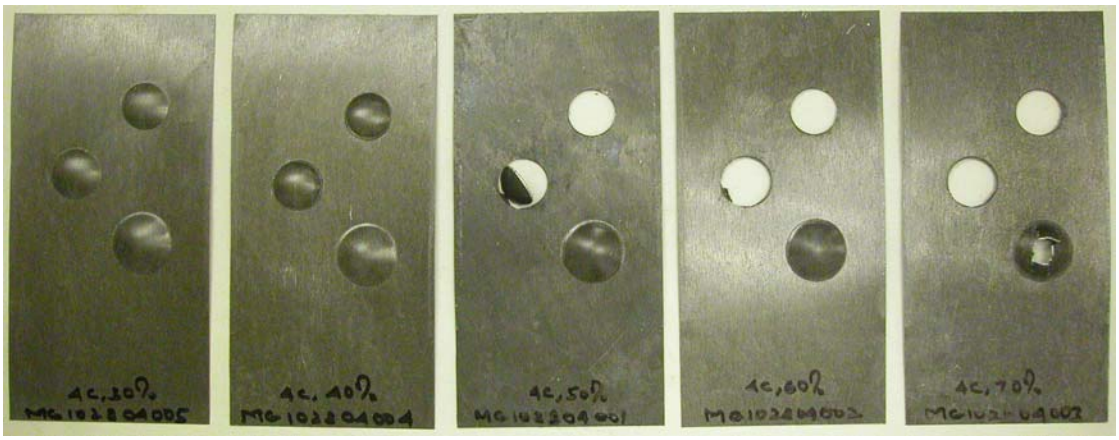

Figure 6.21: Mg alloy formed at different energies from 2.4 kJ to 5.6 kJ at 0.8 kJ intervals (increasing in energy from left to right).

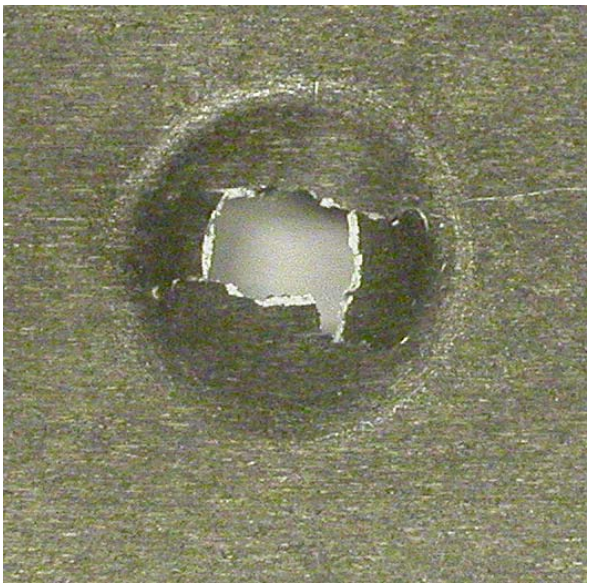

Figure 6.22: Dome corresponding to the biggest entry radius (hole C) at 5.6 kJ (4 Cap., 70% energy).

The peak dome depth is dependent on the energy as well as the entry radius. The results are shown in Fig. 6.23 following from Table 6.6. With increasing energy the peak dome depth increases as the sheet has more velocity and energy. At a particular energy the depth is higher in the case of higher entry radius hole.

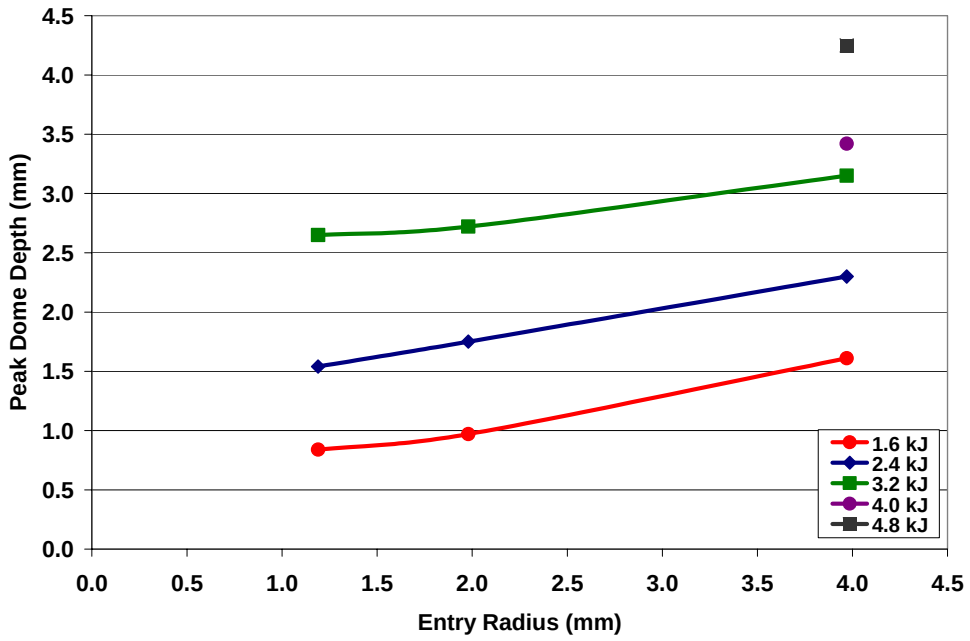

Figure 6.23: Variation of peak dome depth with entry radius, Mg alloy AZ31B-H24.

The variation of the peak dome depth with energy is shown in Fig. 6.24. It shows a linear variation as predicted by Johnson [7].

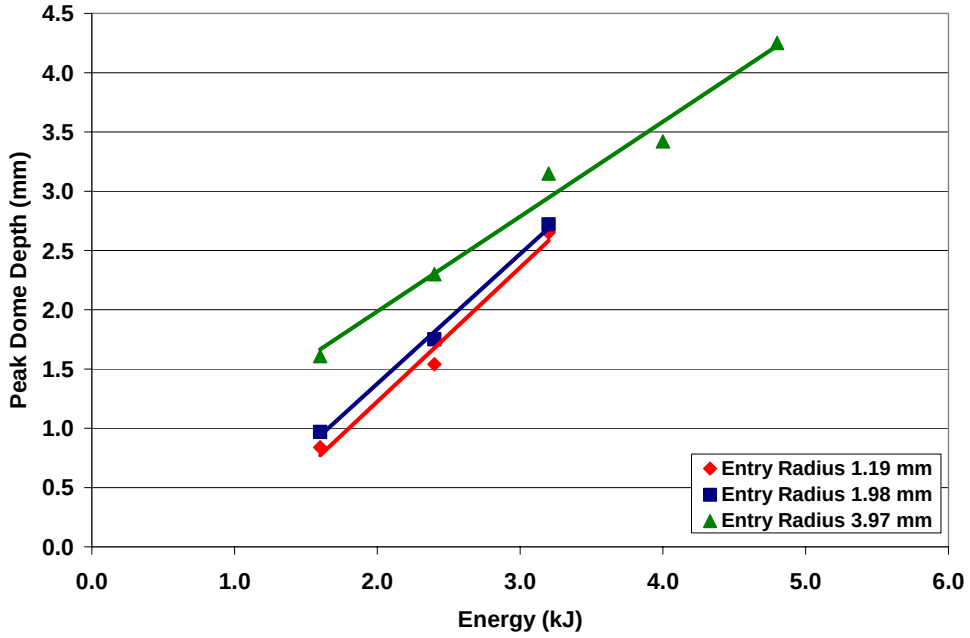

Figure 6.24: Variation of peak dome depth with energy, Mg alloy AZ31B-H24.

The Mg alloy was also circle gridded to evaluate the formability. With the presence of an oxide layer on the top surface, reading the grids is difficult in magnesium. Circle gridding results are shown in Fig. 6.25 in terms of the major and minor strains observed in samples at three energy levels. For comparison an FLD for AZ31B alloy formed at higher temperatures is also shown. It is clear that high velocity forming leads to strains that can be much higher than that predicted by the traditional FLD.

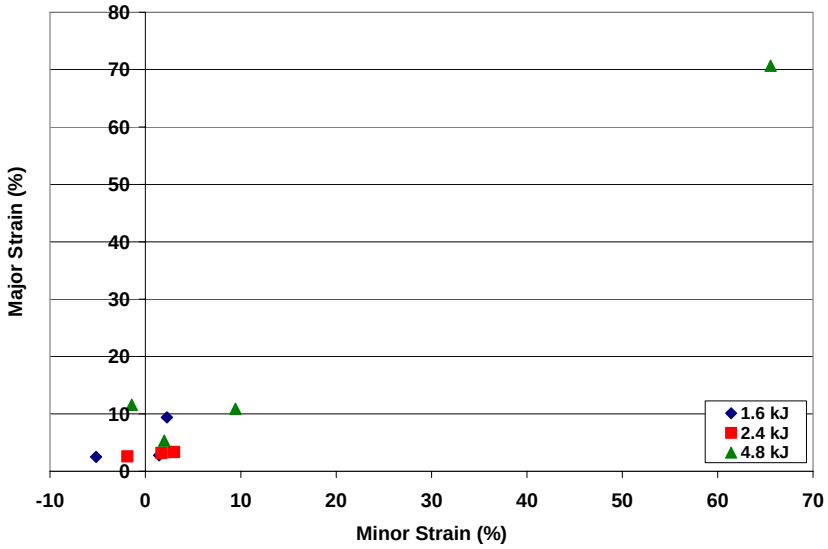

(a)

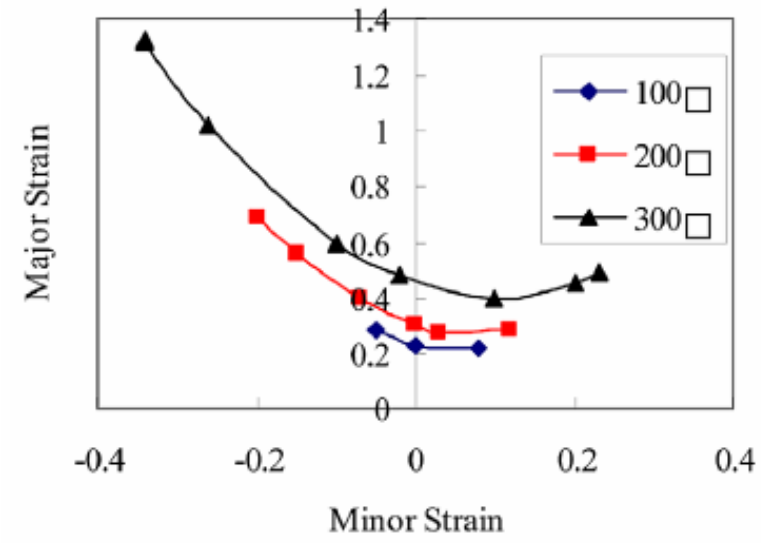

(b)

Figure 6.25: Mg Alloy AZ31B-H24 formability, (a) Room temperature EM formability, and (b) High temperature formability data for Mg AZ31B alloy [65].

Figure 6.25 shows that the dome tip fails in the case of 5.6 kJ because the Mg alloy has reached its high velocity formability. The dome tip already has a biaxial strain of more than 65%. This is huge considering that the uniaxial ductility of this alloy at room temperature is just 15%.

6.1.3.5 Room Temperature High Velocity Formability of Al

Aluminum alloy 2219- O was used for evaluating the formability in the same way as with Mg alloys for comparison. The sheet was launched into the die at increasing energies from 1.2 kJ to 6.4 kJ, generally in increments of 0.8 kJ. Figure 6.26 shows some of the parts formed.

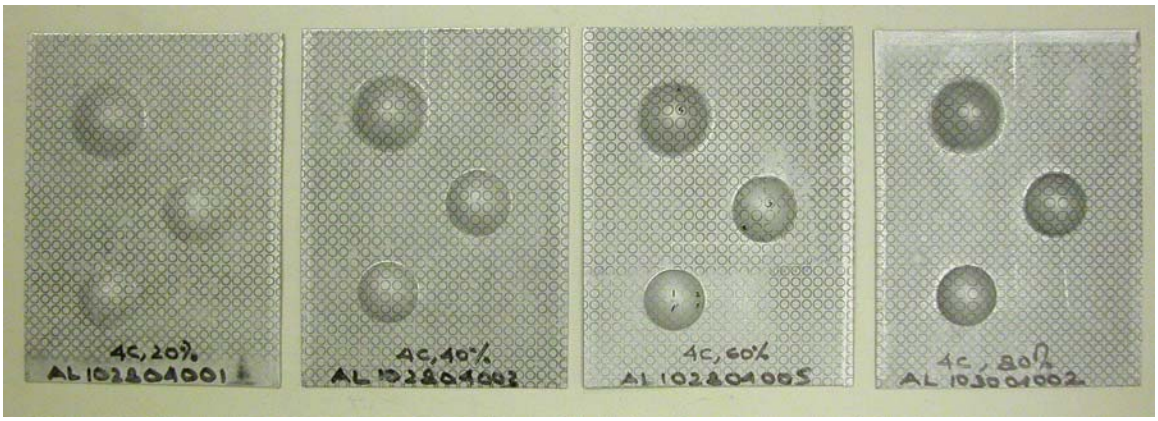

Figure 6.26: Al alloy formed at increasing energies from 1.6 kJ to 6.4 kJ at 1.6 kJ increments, all using 4 capacitors.

The increase in dome depth with energy is clearly visible in the figure above. The increase in the peak dome depth for the holes is plotted with energy in Fig. 6.27. The plots show the same variation as in the case of Mg alloy. Peak dome depth increases with energy and also with the increase in entry radius. Cracks along edges were observed in 5.6 kJ along hole A. The peak depth obtained in forming is linearly related to the energy as in the case of Mg, shown in Fig. 6.28.

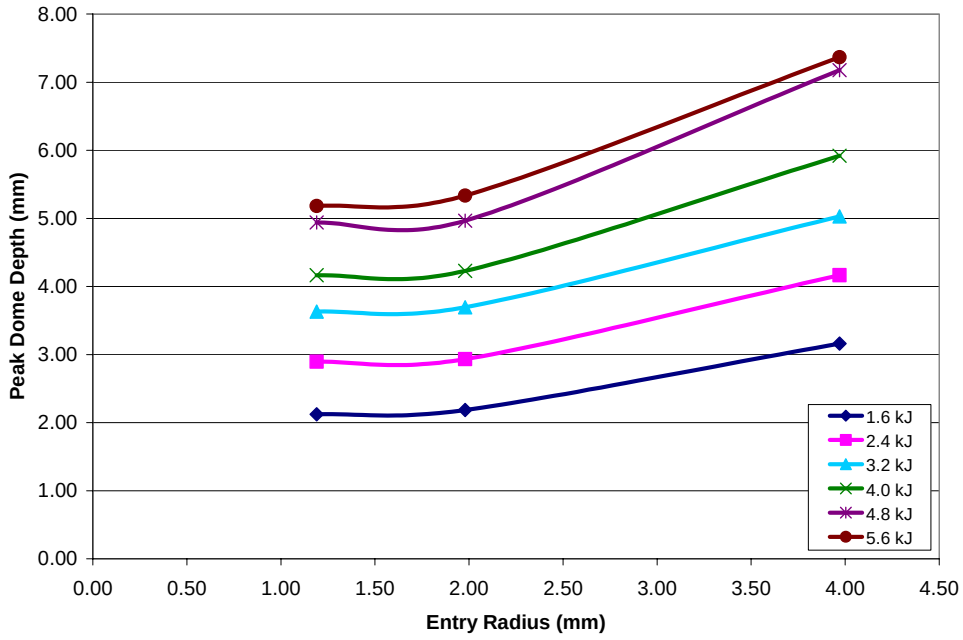

Figure 6.27: Effect of energy and entry radius on the peak dome depth for Al 2219-O.

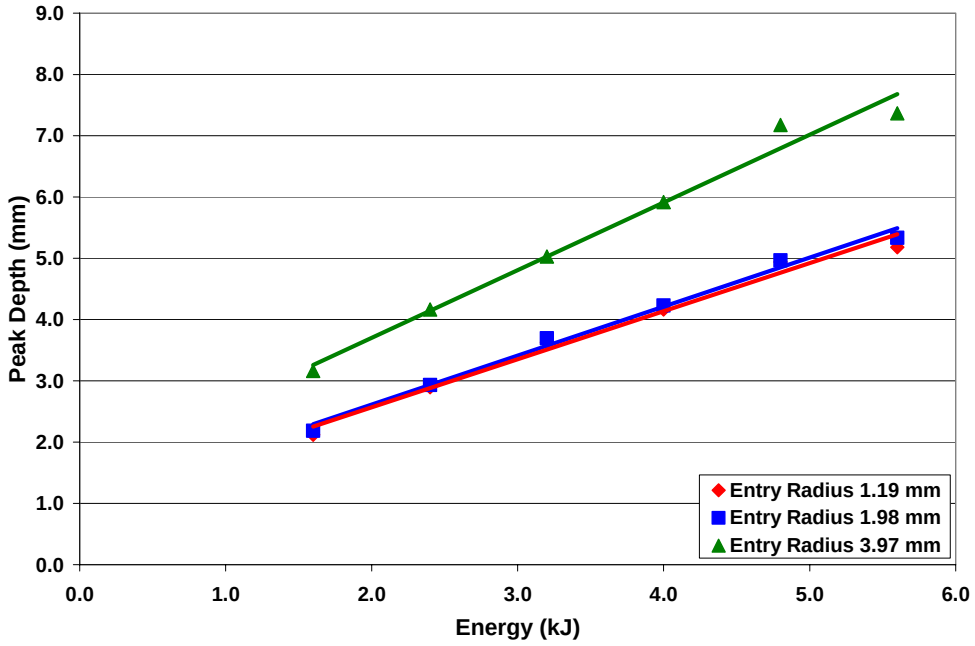

Figure 6.28: Variation of peak dome depth with energy for Al 2219-O using Actuator 1 (all using 4 capacitors).

The samples were also circle gridded to evaluate the formability of the material. Six spots were chosen for each sample, with two per dome. One point was at the dome peak which corresponds to a biaxial strain and one near the dome base which corresponds more to a plain strain or uniaxial strain condition. Figure 6.29 shows the plot of strain distributions at a few energies and is compared with the FLD for Al 2219-T31 [61]. Some strains are higher than that predicted by the traditional FLD. However, the Al sheets were still a long way from failure and still higher strains could be achieved from them.

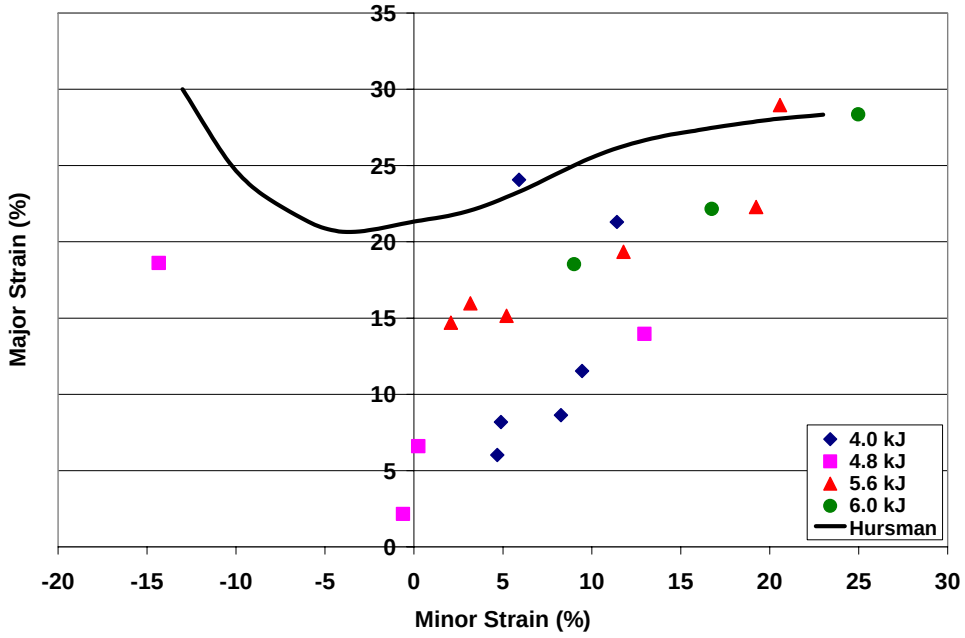

Figure 6.29: Strain distributions for free forming of Al 2219- O using die FF4 and Actuator 1.

6.1.3.6 Effect of Standoff

As discussed in Chapter 4, a distance of few millimeters between the sheet metal and the die, i.e., the standoff, is very important. Since high impact pressures can be developed, higher velocities can be beneficial. This effect was studied by comparing standoff of 0 mm, 1.40 mm and 1.91 mm. The results are shown in Fig. 6.30. With 0 mm standoff, the sheet shows cracks along the edges corresponding to hole A. With 1.40 mm standoff, the edges corresponding to holes A and B are partially cut. With still higher standoff of 1.91 mm, the sheet metal is sheared along the edges corresponding to A and C and partially

cut along B. There is an upper limit to the standoff for an increased efficiency and it can be predicted by our in-house code as described in Chapter 4.

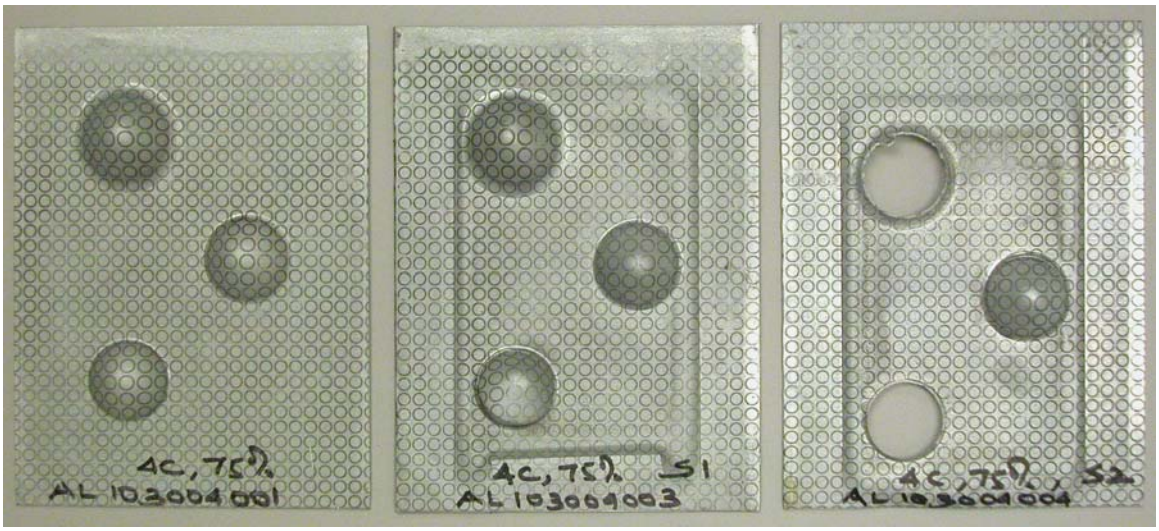

Figure 6.30: Al 2219-O sheets formed at standoff of 0, 1.40 and 1.91 mm respectively, left to right on die FF4 using Actuator 1.

6.1.3.7 Room Temperature Embossing on Mg

The Mg alloy was also used to do embossing at room temperature. Figure 6.31 shows an embossed Mg alloy. The embossed features are clear with no signs of cracking.

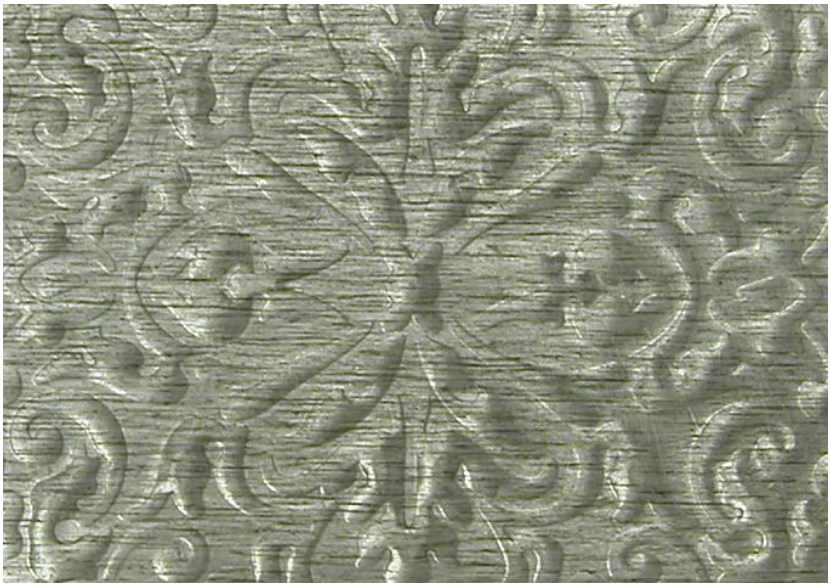

Figure 6.31: Mg AZ31B-H24 embossed at 2.4 kJ (4 Cap., 30%) with 2 mm, standoff and 0.4 mm Cu sheet as driver. No cracks observed in the formed sheet.

The Mg alloy was also used to form into deep features. A cell phone case die (die D1), with a peak depth of 1.2 cm was used and Mg was formed into it. Figure 6.32 compares the sheets formed at different energies. The sheet starts cracking along the die edges at 1.2 kJ itself before the sheet has any die features.

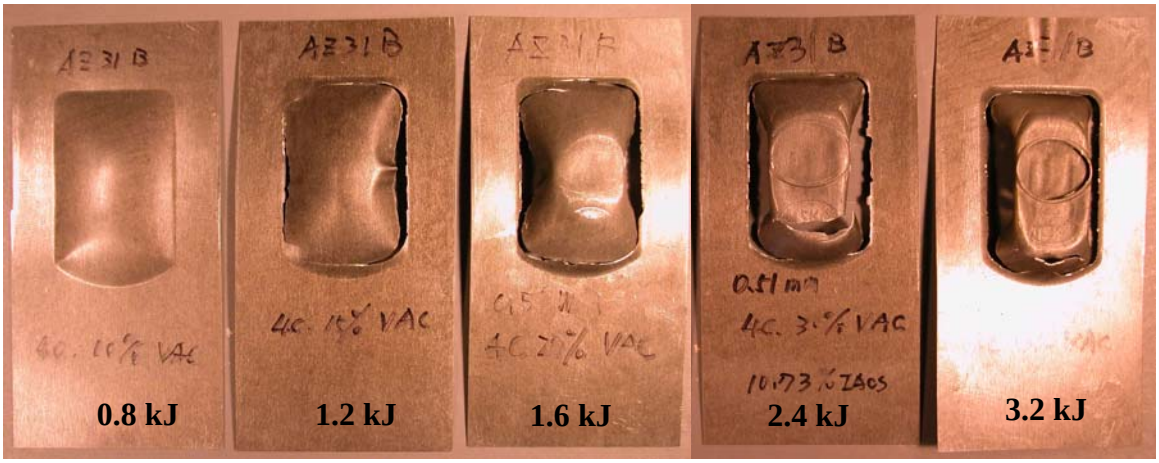

Figure 6.32: Mg alloy formed into a cellphone case die at increasing energies using Actuator 1. Above 0.8 kJ Mg starts cracking along the die edges.

6.1.3.8 High Velocity High Temperature Formability of Mg AZ31B

The induction heater was integrated with the capacitor bank in this set of experiments as described before.

i) Effect of die contact with sheet

An Ameritherm 100 kJ solid state induction heating system at EWI was used to investigate this effect. The die was placed in contact below the sheet. The part of the Mg sheet that projected beyond the die was used to measure the temperature of the Mg sheet. Non-uniform heating of the Mg sheet occurs due to the die contact. Severe temperature gradients exist as the Mg sheet above the cavity is not able to conduct the heat, whereas the part in contact does. Thus the part above the cavity melts due to intense localized

heating even before the rest of the sheet temperature reaches 65ºC. Figure 6.33 shows one such experiment where the sheet has melted above the die cavity.

Figure 6.33: Localization of induction heating due to die contact with sheet metal.

Therefore die insulation from the sheet metal is essential. For later runs the die was placed at a standoff from the sheet metal. A schematic for the same is shown in Fig. 6.34 where a 3.175 mm G-10 strip was used. This standoff is also good to provide the sheet with higher velocities while striking the die.

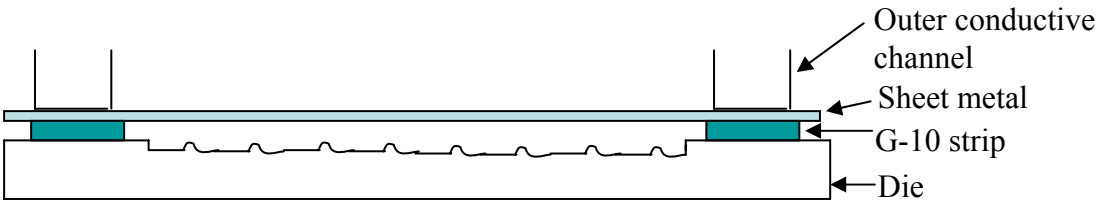

Figure 6.34: Schematic of the die insulation from sheet metal for induction heating integration.

ii) Variation of sheet temperature with time

The sheet temperature variation with time was measured after the induction heater was used to heat the sheet for a certain amount of time. As mentioned earlier, the capacitor bank takes between 1 to 4 seconds in the charge to discharge cycle. It is important to note the drop in temperature of the sheet in this forming window.

A typical current in the coil from the induction heater was 150 A at 12.5 V. Three circuit breakers of 30A, 50A and 100A were used. Even with a 100 A circuit breaker the power from the induction heating is cutoff at approximately 15 seconds due to the high frequency (450 KHz) effect of the induction heater. Therefore two heating times of 10 s and 15 s were selected and the variation in temperature with time was recorded. This variation is shown in Fig. 6.35. The sheet temperature falls very rapidly. Although the sheet is not in contact with the die, it is still in contact with the coil which acts as a heat

sink. The gap between the coil and sheet cannot be increased as it reduces the efficiency of the system by increasing the inductance.

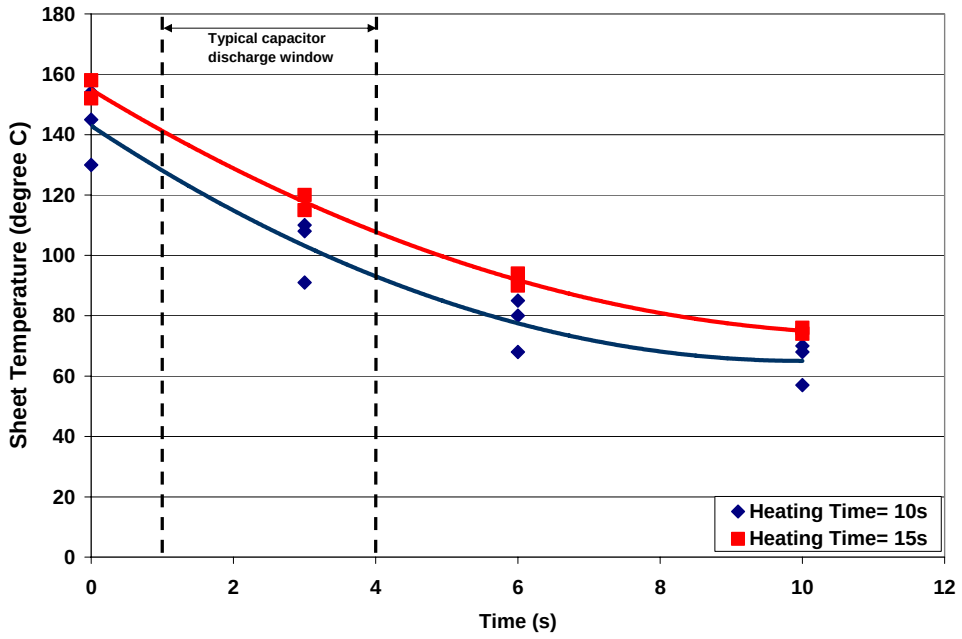

Figure 6.35: The variation in sheet temperature with time after the completion of heating by the induction heater.

The drop in temperature can be further reduced by using heated tooling. A hand held heater was used to see the effect.

iii) Effect of sheet temperature on the formability of Mg Alloy

The sheet was heated for 10 s with the induction heater and formed into the three hole die (die FF4). In another case the tooling was heated to 70ºC using a hand held gun, before applying the induction heat for 10 s. A comparison between the sheet formed at room temperature and the one at elevated temperature is shown in Fig. 6.36.

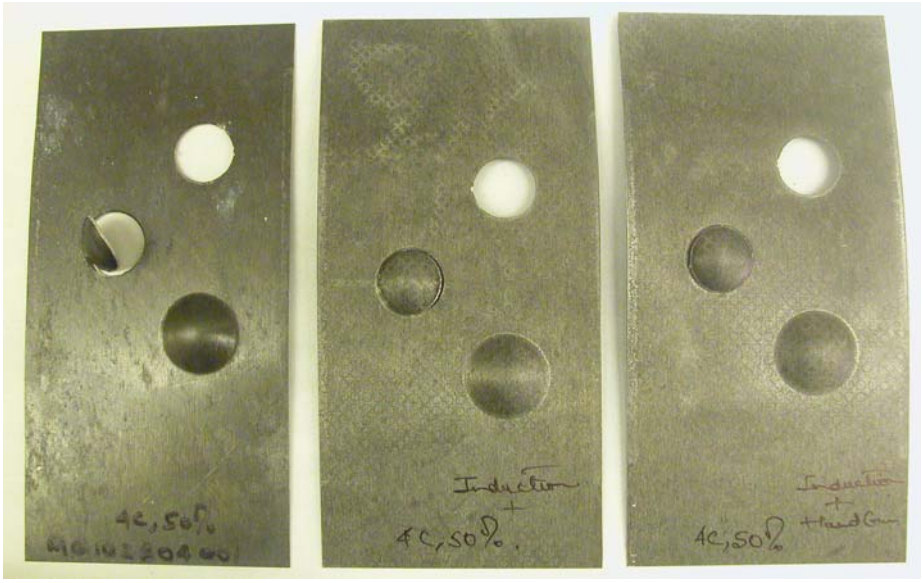

Figure 6.36: The effect of sheet temperature in Mg alloy forming, (a) sheet formed at room temperature, (b) sheet formed after induction heating for 10 s, (c) sheet formed after preheating tools to 70ºC and then induction heating for 10 s.

The variation of peak dome depth with temperature is shown in Fig. 6.37. By Fig. 6.36 and 6.37 we see marginal improvements in the formability of the Mg sheet with increase

in temperature. Significant improvements could not be seen as the sheet is losing a lot of heat during the capacitor charge-discharge cycle.

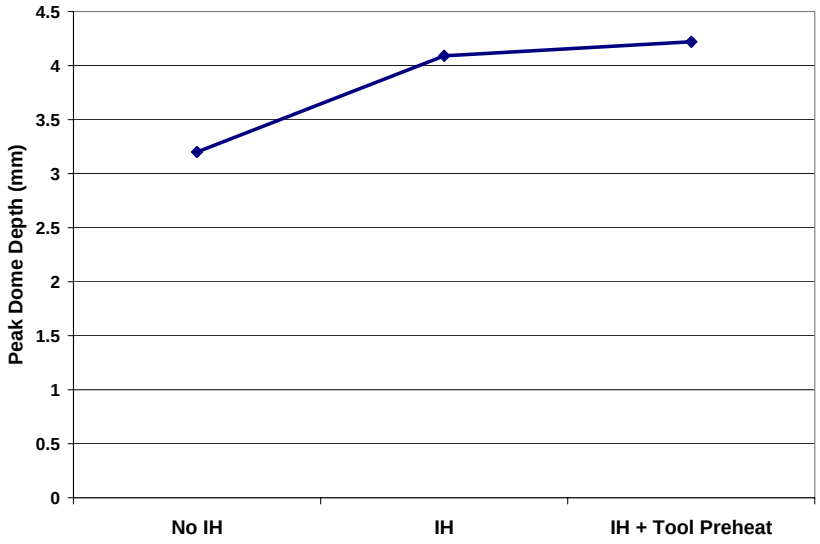

Figure 6.37: Variation in peak dome depth in Mg alloy corresponding to hole C with varying sheet temperature.

6.1.3.9 Summary

The following can be concluded form the above set of experiments:

1. Mg shows higher formability with high velocity forming.
2. Embossing large areas are made possible by EM forming. It can capture fine details on Mg even at room temperature.
3. Higher sheet temperatures improve the forming ability of Mg.

4. Capacitor charge-discharge time needs to be synchronized with the induction heating for maximum efficiency. Ideally there should be a minimum time gap between the end of induction heating and the capacitor discharge.

As discussed before, Uhlmann and Hahn [5] have demonstrated a tool using the hybrid approach for Magnesium. The work also discusses a switch that can handle the high induction heater currents used in conjunction with a Maxwell capacitor bank. The above work with the uniform pressure coil shows the immense capabilities of the hybrid forming process. However, an approach similar to Uhlmann and Hahn [5], may be viable for the current system.

Properly controlling the time lag between the end of the heating cycle and the capacitor discharge is essential. It is difficult to control the time lag by manual control. A microprocessor based control is required to reduce the time lag. A schematic of the proposed approach is shown in Fig. 6.38.

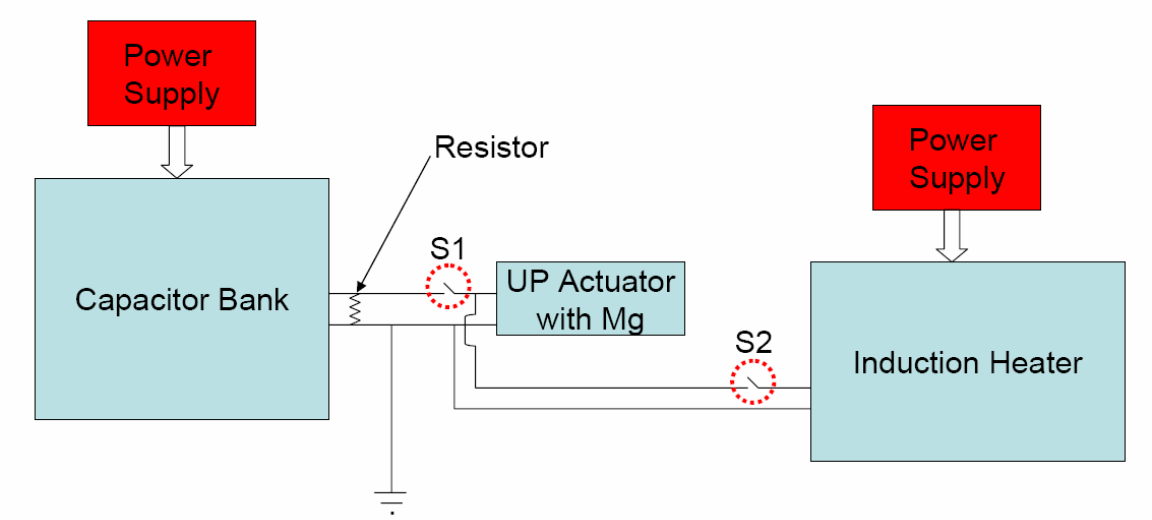

Figure 6.38: Schematic of the proposed design approach for integrating induction heating with EM forming.

The approach can be summarized as:

- Single point ground for the whole system
- Two switches
- Need for automated sequence in the following order

  - Induction heater energized

  - Capacitor bank energized

  - Switch 2 (S2) is closed and heating is initiated

  - 5 seconds before target temperature, capacitor bank is charged through the resistor. This time is based on the experimentally calibrated time.

  - 1 second before the discharge, open S1 and close S2. Fire capacitor bank.

6.2 Embossing

The large pressures available from impact make several things possible that are difficult or impossible with conventional forming. First, by producing a sufficiently high impact velocity, large pressures can be developed. Usually the high-pressure forging process known as coining is used to capture fine surface detail in a metal surface. Coining pressures usually operate only on small areas (like coins). High velocity forming techniques offer the ability to perform coining-like operations over large areas.

The impact pressure, P_{impact}, that is developed when two semi-infinite elastic bodies labeled 1 and 2 collide at an impact velocity V_i is given as [1]:

$$P_{impact} = \frac{\rho_1 \rho_2 C_1 C_2}{\rho_1 C_1 + \rho_2 C_2} V_i \qquad \text{..... (6.5)}$$

Here for each material ρ represents density and C is the longitudinal wave speed. Longitudinal wave speeds are on the order of about 7,000 m/s for most structural metals. Equation (6.5) shows that for aluminum-steel and steel-steel couple's impact pressures of 500 MPa and 1.4 GPa are generated for a 50 m/s impact [1]. As shown earlier, it is very easy to obtain velocities over 100 m/s with this actuator. This analysis further point out that it is very easy to develop pressures large enough to produce significant plastic deformation at the interface.

A plot from the Taylor impact analysis, discussed in Chapter 5, is shown in Fig. 6.39. Here the peak pressure is plotted with the impact velocity. The peak pressure was evaluated at a point in the rod at a depth of 2 mm from the point of impact. The elastic equation (6.5) seems to work well at low velocities (<150 m/s). Also the analysis shows that very high pressures can be developed by impact.

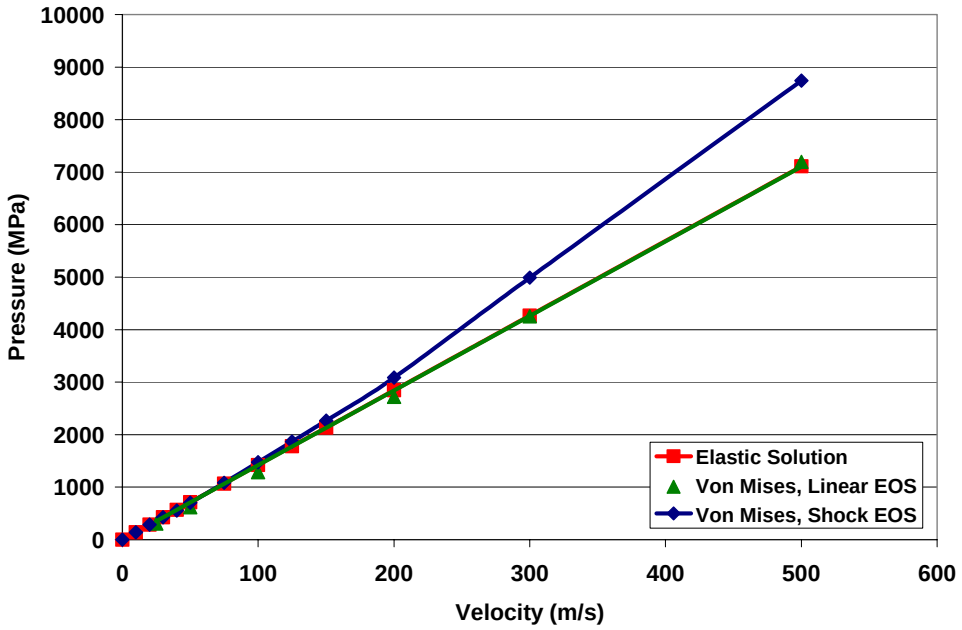

Figure 6.39: Variation of peak impact pressure with velocity using Taylor impact simulations in AUTODYN.

Therefore, features with crisp outlines can be formed better with EM process and very fine details can be achieved. As an example, consider forming into a die E1 shown in Fig. 3.20. A 0.6 mm surface roughness gauge (to get different textures, made from metal-plated plastic) was glued to a mild steel bottom to serve as a die. A comparison between the die and formed 0.25 mm, Al 5052-H32 at 4 kJ (4 Capacitors and 50% energy) is shown in Fig. 6.40. The die has very fine features but the Al sheet is able to capture the details well. This performance is achieved with a simple die. A commercially manufactured die to achieve the same would obviously make better formed sheets. Note also that there are problems with entrapped air here.

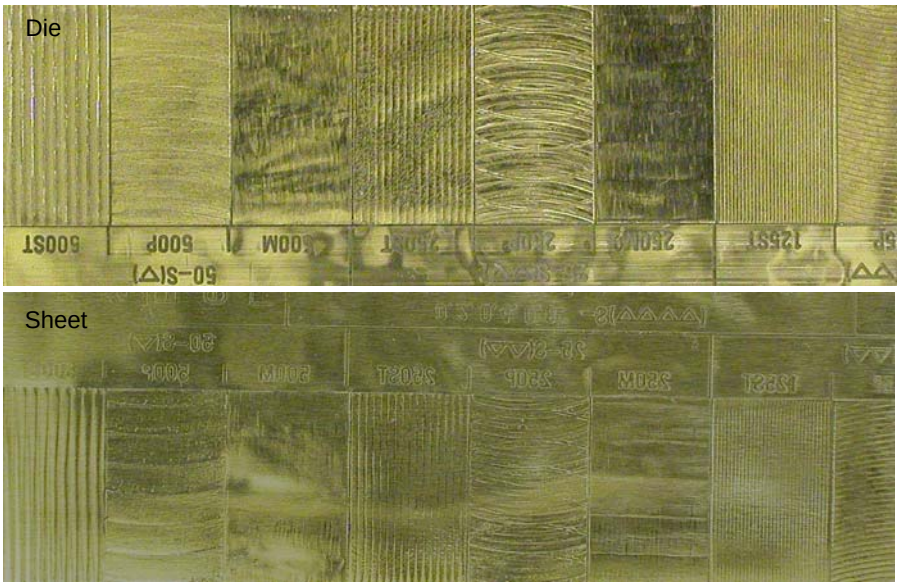

Figure 6.40: Formed Al 5052-H32, 0.25 mm thick at 4.0 kJ (4 Cap. and 50% energy), with the die in background, using Actuator 1, 2 mm standoff between sheet and die and no vacuum.

6.2.1 Estimating Velocities to Form a Feature

The velocities required to form a feature may be estimated from AUTODYN. In this section the effect of sheet thickness on sheet feature size (compared to that of the die) at a given sheet velocity is investigated.

A 2-dimensional model with planar symmetry was made to simulate the impact of Al sheet onto a die with circular features. Four Al sheet thicknesses of 1, 5, 10 and 30 mm at a constant width of 10 mm were used. The Al sheet had a higher mesh density at the side of impact. Typically a mesh of 20 x 60 elements was used for the 1 mm sheet and 20 x 150 for the 30 mm sheet. The Al sheet was assigned a Von Mises strength model and a shock equation of state with no failure model. The sheet was given an initial velocity and made to impact on the steel wall. The die was constrained to have a general 2D velocity of zero. A range of velocities from 0 m/s to 400 m/s were investigated. The die had three semi circular features, 1 mm in radius and 1 mm apart. The peak feature depth was measured in each case after the sheet rebounds from the die. The sheet feature depth was estimated by measuring the difference in the peak depth of the central circular feature and that corresponding to the mid region between the central and corner features.

Figure 6.42 shows a 1 mm and 30 mm thick sheet impacting the die at 200 m/s. The effect of inertia is clearly evident as the 30 mm sheet is able to take the features of the die whereas the 1 mm sheet does not. Figure 6.43 shows the effect of mesh variation on the peak depth obtained in the 1 mm thick sheet. It shows the mesh used for the simulation was appropriate.

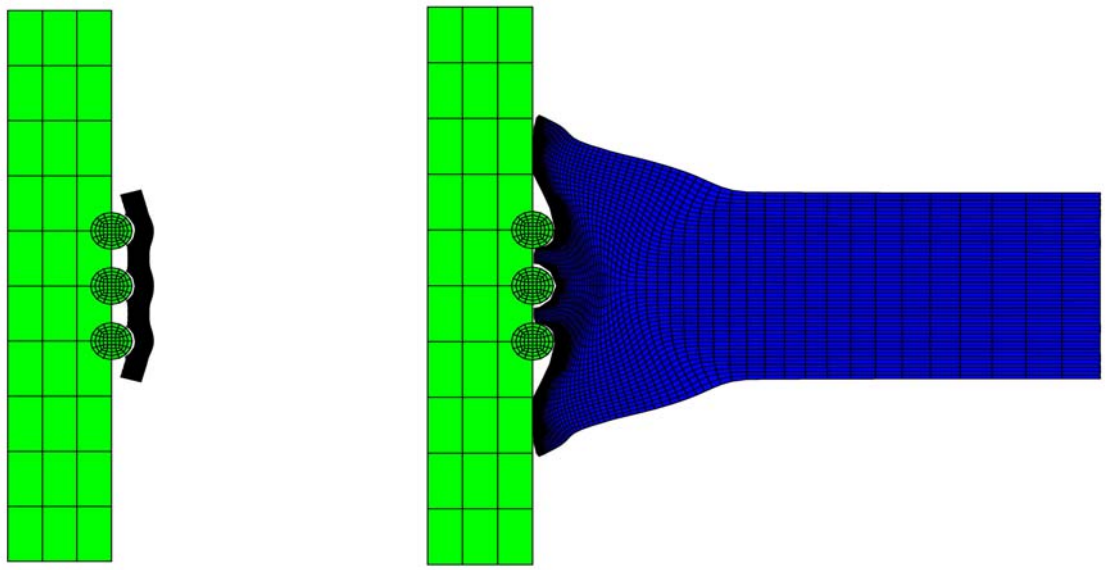

1 mm thick Al 30 mm thick Al

Figure 6.41: The effect of sheet thickness on the ability to take a feature size at 200 m/s.

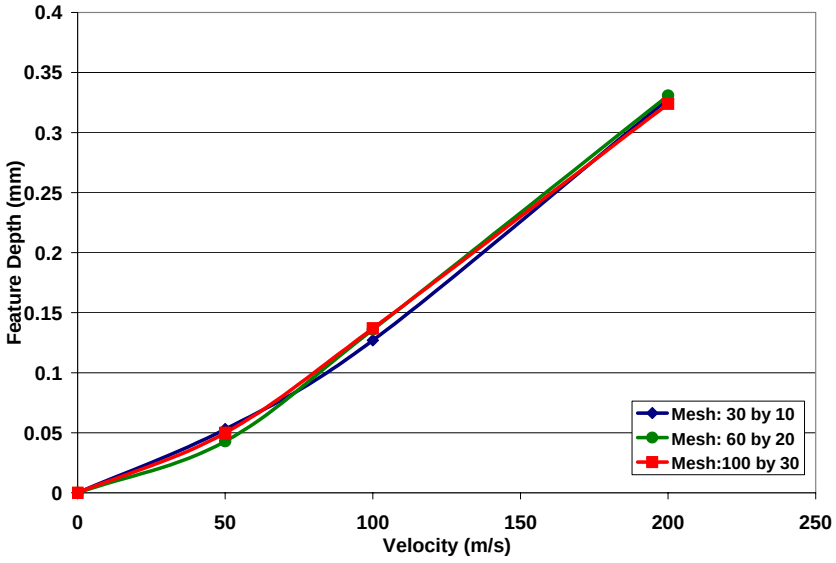

Figure 6.42: Effect of mesh variation on the feature depth in 1mm thick Al sheet.

Figure 6.43 shows the comparison between the feature depths obtained at different sheet thicknesses. After a sheet achieves the peak feature size, increasing velocities do not help any further. Dimensionless parameters were also used to compare the data. Dimensionless energy per unit length was defined as,

$$Energy^* = \frac{\rho t u^2}{2Y_0} \qquad \text{..... (6.6)}$$

where ρ is the density, t is the thickness, u is the velocity and Y_0 the yield strength. Dimensionless feature size can be defined as,

$$FeatureSize^* = \frac{Peak\_Depth\_in\_Sheet}{Peak\_Depth\_in\_Die} \qquad \text{..... (6.7)}$$

Figure 6.44 shows the effect of sheet thickness on the feature size obtained in terms of the dimensionless parameters. All the sheet thicknesses show a similar line showing that the feature size obtained is linearly related to the initial kinetic energy of the sheet. This may be used to predict the velocities required to form a give feature size.

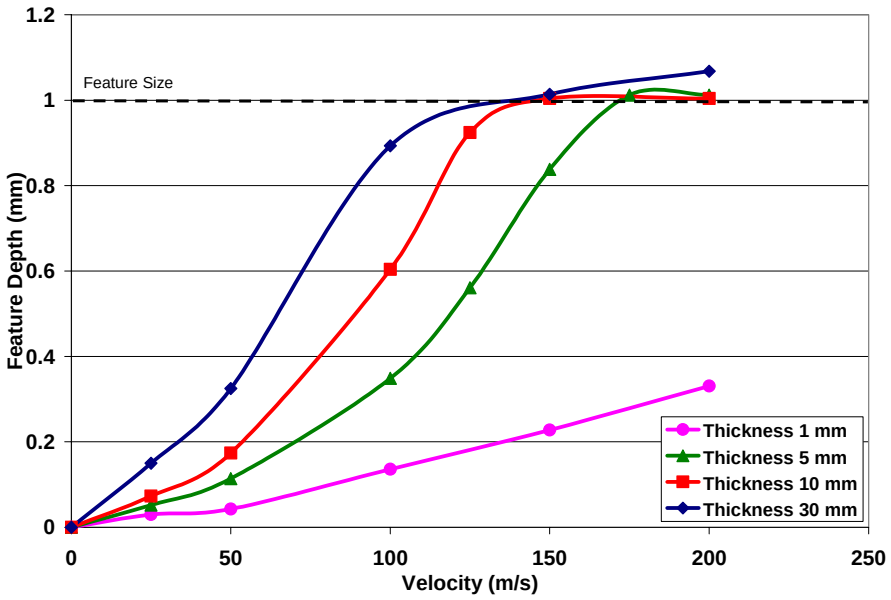

Figure 6.43: Effect of sheet thickness on the feature depth at different velocities.

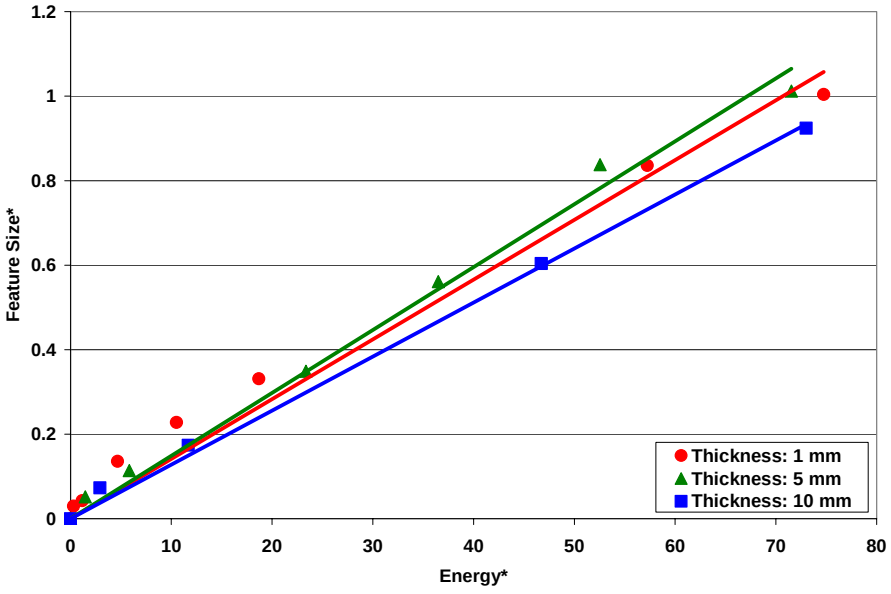

Figure 6.44: Variation of dimensionless energy with dimensionless feature size.

6.2.1 Forming Bipolar Fuel Cell Plates

The embossing capabilities of this actuator were demonstrated in forming bipolar fuel cell plates. The objective in this part of the study was to show the utilization of the uniform pressure actuator to form fuel cell bipolar plates. This process is especially appealing to forming fuel cell plates because of the following reasons:

- Only single sided contact with tooling is required for forming. This may be beneficial for forming coated sheets.
- The process has the capability of combining the forming and trimming operations, which provides good cost savings.
- Dimensional accuracy is good with reduction in springback.
- The process has the flexibility to form and evaluate a variety of flow field geometries, materials, surface treatments and coatings.

6.2.1.1 Forming a Small Section of Bipolar Fuel Cell Plates

The first part of this project was to form a section of the fuel cell plates and see the capability of the process. An unfinished GM die (die E2) was used along with Actuator 1. Evaluation was carried over a range of launch energies. No vacuum was created in the system as there was an outlet for the air through the channels in the die.

The actuator was able to make the 7.5 x 10.0 cm^2 sections very well. An example has been shown in Fig. 6.45. This shows that EM forming can be applied effectively to form the fuel cell plates.

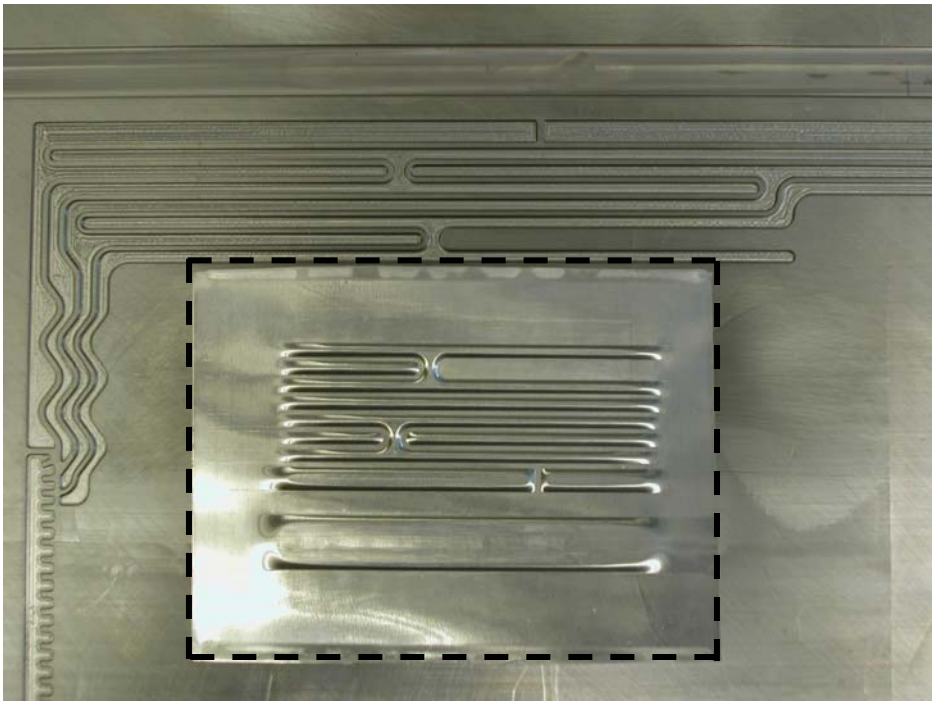

Figure 6.45: Formed Al sheet, 0.4 mm thick, 7.5 x 10 cm^2 at 6.6 kJ with the die E2 in the background for comparison.

6.2.1.2 Forming a Full Bipolar Fuel Cell Plate

The focus on this part of the project was on scaling the smaller coil (7.5 x 10 cm^2) into a bigger coil to form a full 22.5 x 35 cm^2 fuel cell plate. An analysis based on the approach in Chapter 4 was used to predict the design in the new setup. The coupled differential equation model described in Chapter 4 was also used to predict parameters in EM forming.

The pressure requirement from the successful part shown in Fig. 6.45 was used. For this a bigger actuator (15 x 22.5 cm^2) was made. A single actuator encompassing the entire area of the die would be high in inductance. The actuator accordingly was designed so that the full plate can be formed in three horizontal motions of the actuator as shown in Fig. 3.10. Over 2.5 cm of overlap in area was used between successive shots. Die E3 was used for this as shown in Fig. 3.22. To simulate the actual industrial application of this actuator and for better control of the load, a 100,000 lbs hydraulic press was used. A design criterion to avoid arcing was developed (discussed in Chapter 7). Vacuum was created between the sheet and the die.

Stronger coils were designed so that higher energies could be used. One of the ways to do this is to use thicker section copper wires which have higher current carrying capacity. Actuator 3 used in this setup was manufactured using rectangular section copper wires (2 x 6 mm). The in-house code was used to predict the number of turns.

6.2.1.2.1 Scaling to a bigger geometry

The variation of the peak primary currents with energy is shown in Fig. 6.46 for Actuator 3 and Die E3.

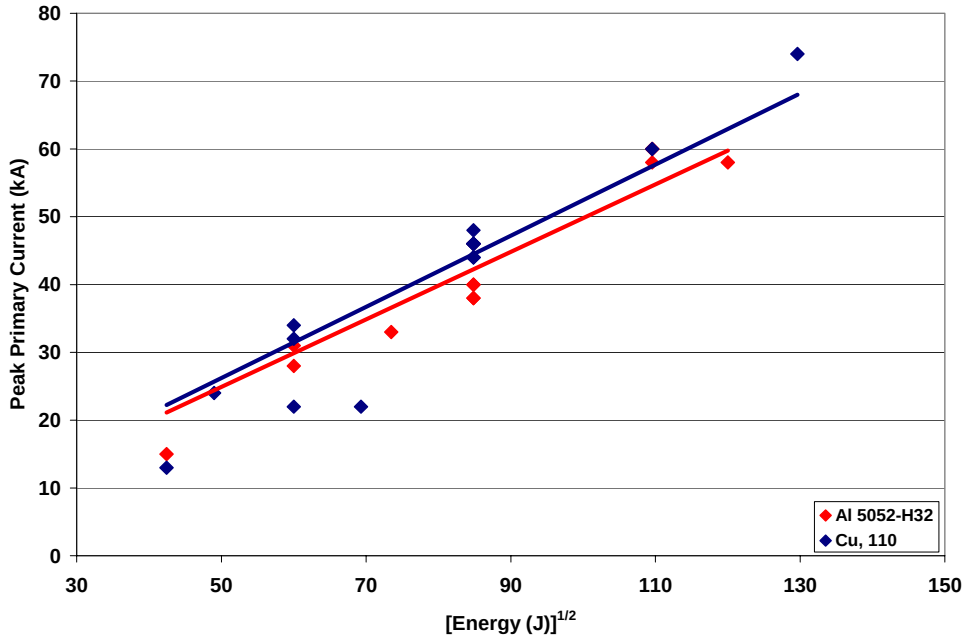

Figure 6.46: Variation of peak primary current with energy for Actuator 3, Die E3.

The variation is similar to what was seen earlier in Chapter 4 for Actuators 1 and 2. There is a linear variation in the peak primary current with energy and the higher conductivity sheet material is more efficient. However, the peak currents in this case are not as high for the same energy as with the other two actuators. A comparison is shown in Fig. 6.47 for the peak current variation with energy for all three actuators.

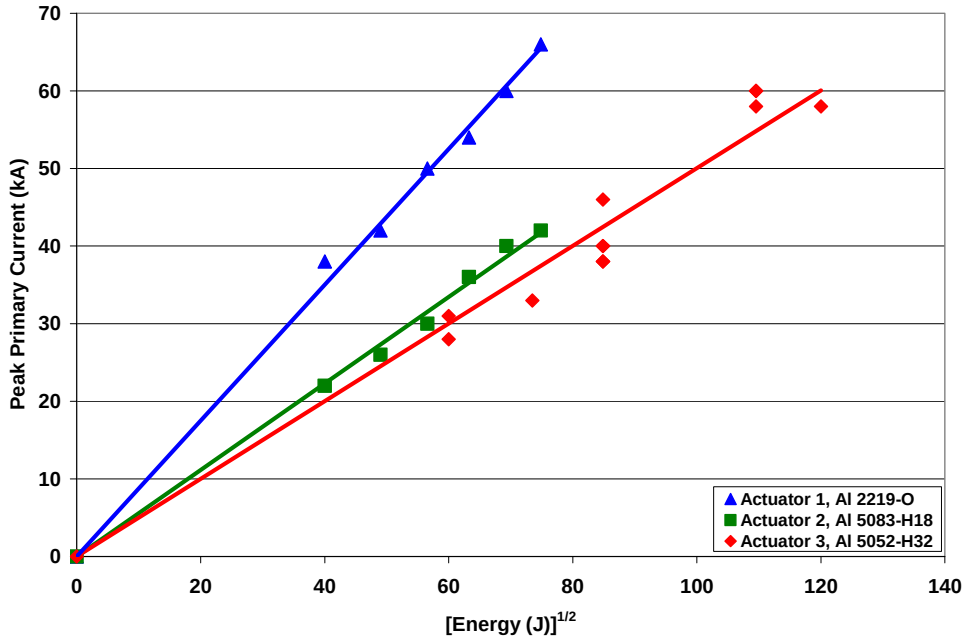

Figure 6.47: The variation of peak current with energy for all the actuators using Al alloys for comparison.

The above figure points out that higher inductance coils may be less efficient. Typical inductance values for the actuators were as follows: Actuator 1- 1.40 μH, Actuator 2- 3.68 μH and Actuator 3- 4.20 μH. Clearly the inductance is higher with a larger actuator. As mentioned earlier the inductance varies to the first order roughly with the volume over which the magnetic field exists. Thus a larger actuator has a higher inductance. Also the peak currents are inversely proportional to the root of the inductance of the system. Thus larger coils in general are less efficient and low inductance coils are needed for higher

efficiency. The best approach is to use the analysis in Chapter 4 to predict the optimal coil design.

6.2.1.2.2. Issue of Coil Movement

An important issue in this phase was the issue of registry. Does moving the coil for successive shots make a difference? No registry issues were observed with the movement of the coil for the second and third shots. This result was very significant for the successful application of the technique. An example is shown in Fig. 6.48.

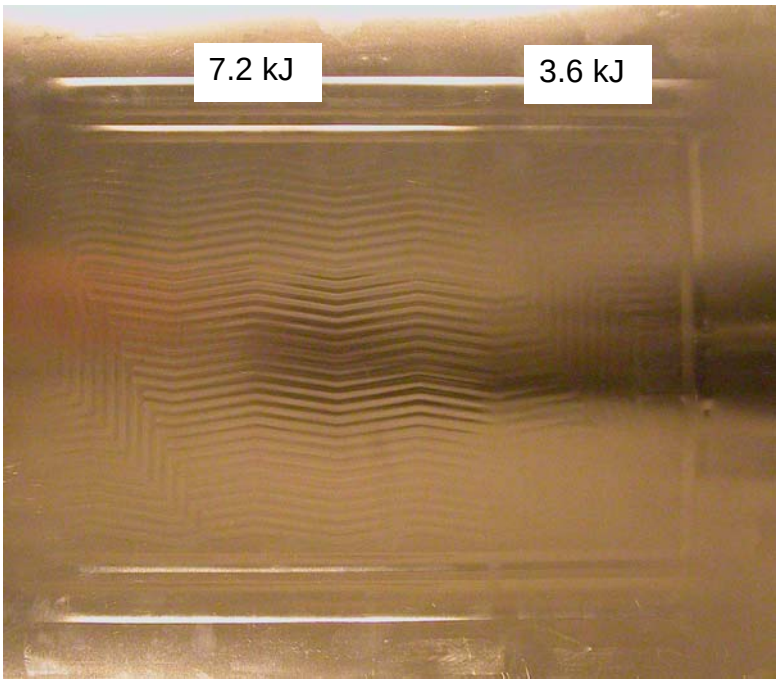

Figure 6.48: Formed Al 5052-H32, 0.25 mm thick sheet showing that there are no registry issues, with the use of subsequent horizontal motion of Actuator 3.

6.2.1.2.3 Multiple Discharges

As discussed earlier it can lead to a better definition of the geometry. The same was tried in this setup with successful results. An example is shown in Fig. 6.49.

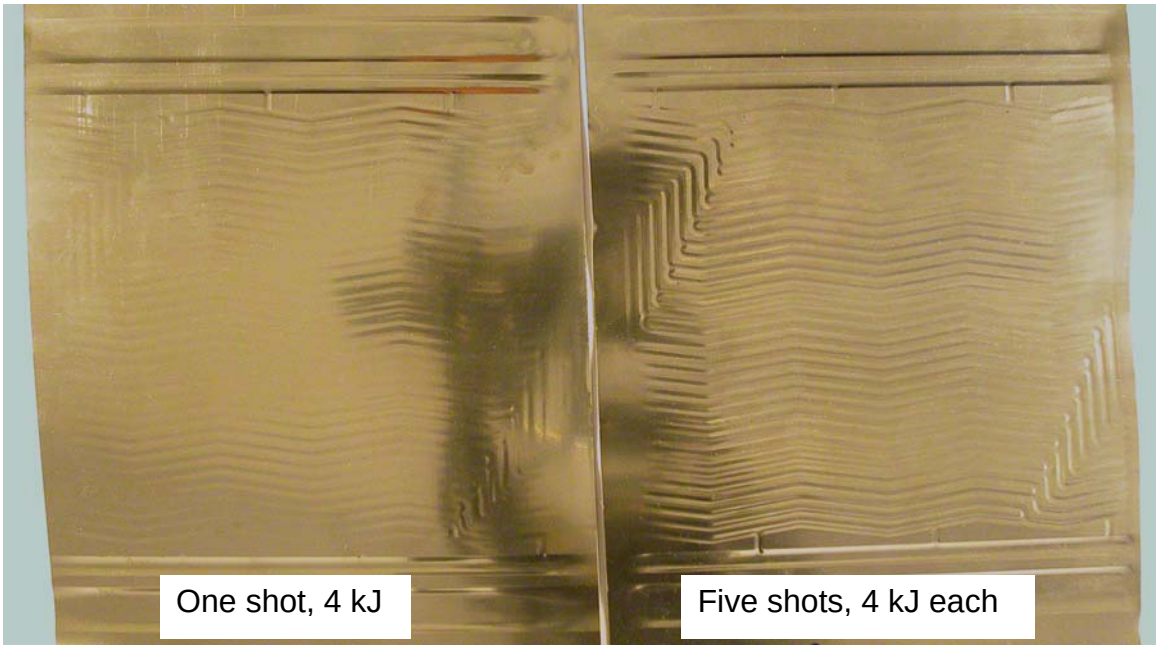

Figure 6.49: The effect of multiple discharges. Stainless Steel (SS 301), 0.13 mm thick EM formed with 0.13 mm copper driver sheet.

6.2.1.2.4 Promising Results

EM forming was successfully able to form the fuel cell panel in full length. Some results are shown below in Fig. 6.50 and Fig. 6.51. The details in the formed sheets are clear. However, still higher energies would be needed to fully form the sheets.

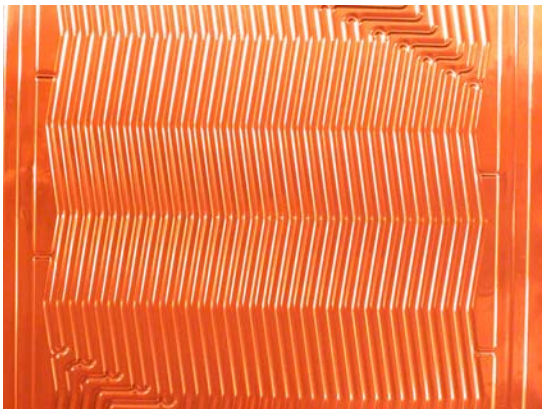

0.13 mm Cu at 12.0 kJ

0.13 mm formed stainless steel at 16.8 kJ

Figure 6.50: Parts formed with Actuator 3 on a full scale fuel cell die. Both are 15 x 22.5 cm^2 in area.

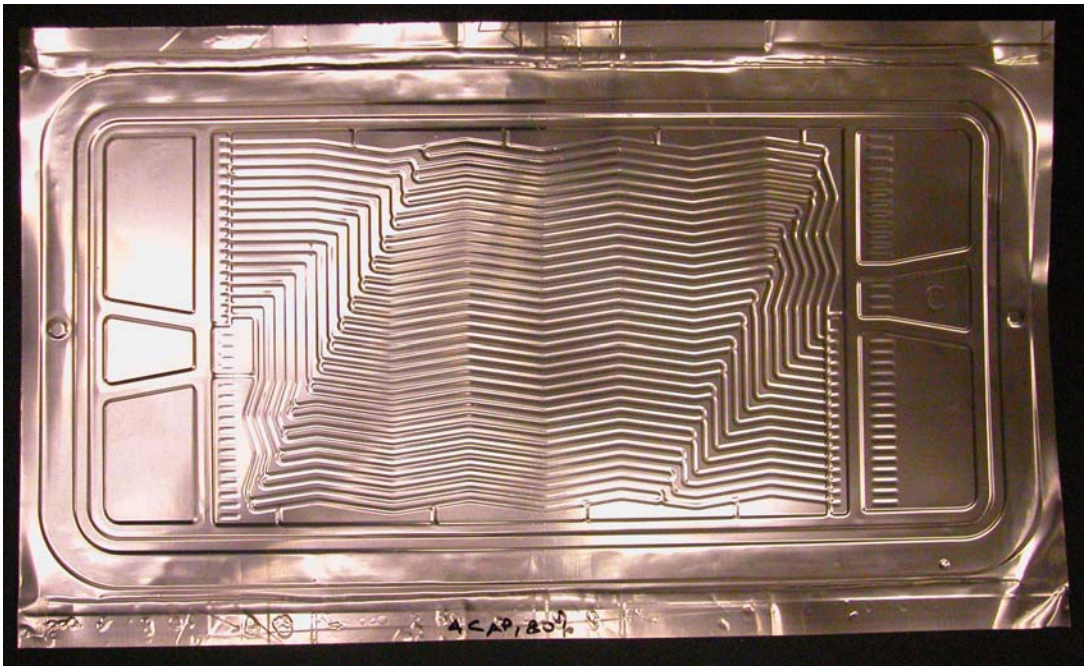

Figure 6.51: A full section (22.5 x 35 cm^2) fuel cell plate formed using three shots of 19.2 kJ with Actuator 3 on 0.13 mm SS 301. A 0.13 mm Cu sheet was used as a driver.

6.2.1.2.5 Summary

The following can be concluded from the experiments on the fuel cell plates:

1) Electromagnetic forming using the uniform pressure coil does seem to basically show the attributes of a robust process for forming fuel cell bipolar plates. The process works well and good levels of formability and shape fidelity are indicated. Good electrical connections between the sheet and return path are possible with good engineering. Despite this, some further improvements to the design are necessary.

2) Impact is required to fully form the features in the bipolar plates. In order to impact with a significant sheet velocity the sheet must have a standoff from the die surface.

3) At least rough vacuum is needed between the sheet and die to allow good fidelity of the die shape in the sheet. In order to do this while maintaining a gap between the die and sheet, vacuum must exist on both sides. This will require tool redesign.

4) We have shown the utility of coupled differential equation modeling to understand system performance.

The investigation also points out that a low inductance coil can be beneficial. This can be achieved for the current setup by using two coils in parallel with one outer channel to reduce the inductance and have better efficiency. An example of a coil made for the system is shown in Fig. 6.52.

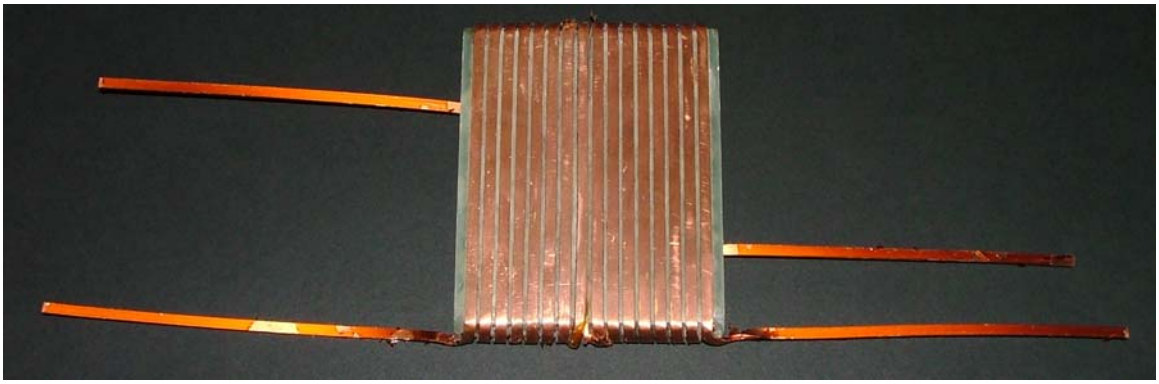

Figure 6.52: Two coils in parallel that can be used to have a lower inductance actuator for forming fuel cell plates.

6.2.2 Holograms

A hologram is usually recorded on a photographic plate or a flat piece of film, but produces a three dimensional image. The unique characteristic of the hologram is the idea of recording both the phase and the amplitude of the light waves from an object.

Holograms can be copied by embossing and are widely used as a security feature on credit cards and quality merchandise. However there is no feasible conventional technique to emboss on metallic sheets to form holograms. The high impact pressures generated by the uniform pressure actuator may be used to get micron level surface relief and thus the holographic features onto the sheet metal.

An embossing die E4 (Fig. 3.23) was used to evaluate this effect. A 0.5 mm thick, commercially available hologram (electroless nickel plated) from MIRDC were taped onto a stainless steel block to serve as a die. Figure 6.53 shows the SEM micrograph of this hologram. The micrographs at increasing resolution show the presence of micron level ridges which lead to the light interference effect in a hologram.

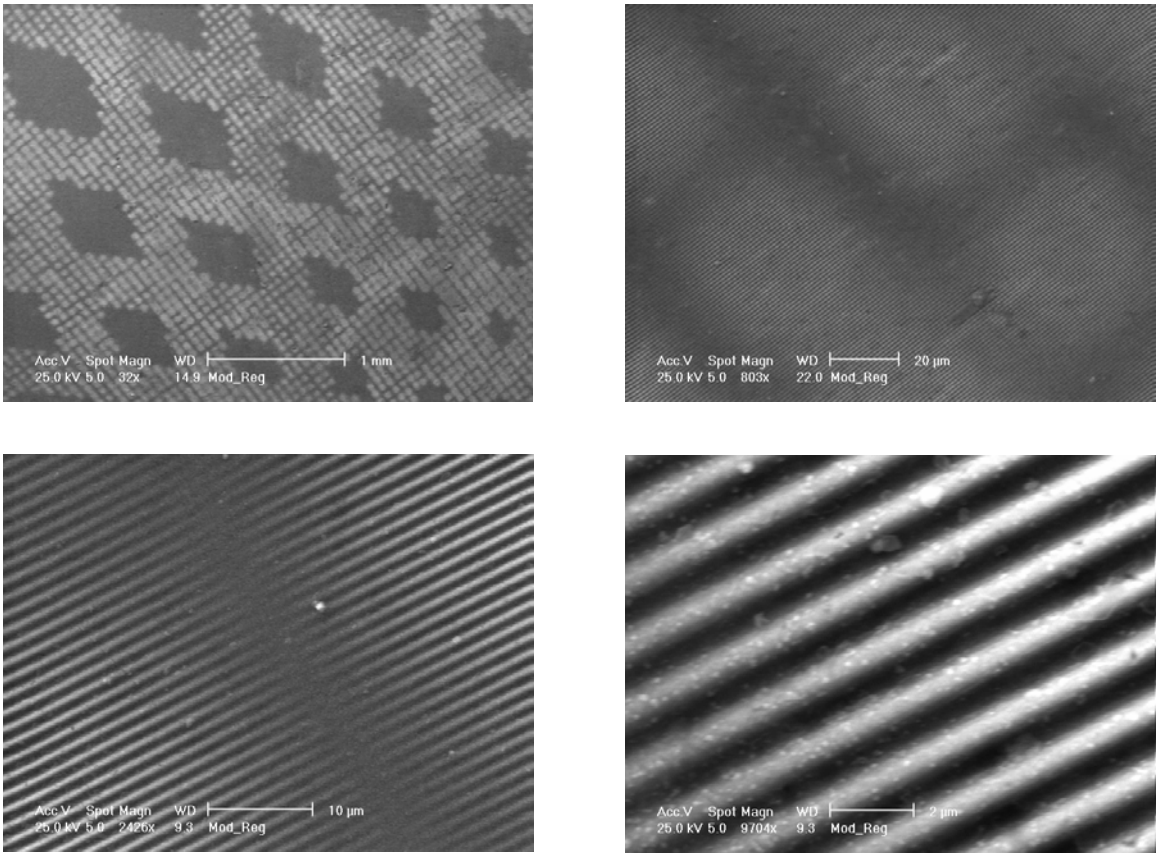

Figure 6.53: SEM micrographs of the original hologram, Die E4.

Copper and aluminum sheets were formed onto the die using Actuator 1. A standoff of 2 mm was used between the sheet and the die. No vacuum was used. The results from the experiments are shown in Fig. 6.54. Both sheet materials are able to form holograms. The use of a commercially manufactured die and vacuum in the setup will enhance the ability of the sheet material to properly copy the features of the die.

Cu 110 alloy, 0.13 mm thick, 75 mm by 100 mm formed at 2.4 kJ (4 Cap., 30%)

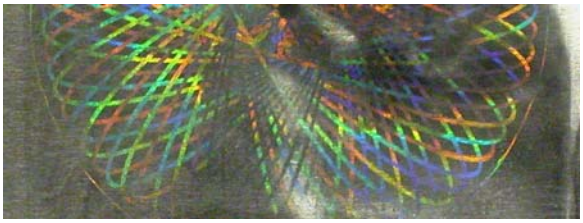

Al 5052-H32, 0.25 mm thick, 75 mm by 100 mm formed at 3.2 kJ (4 Cap., 40%)

Figure 6.54: Hologram embossing trials using Cu and Al sheets with Actuator 1.

Figure 6.55 shows the comparison between the SEM micrographs of the hologram and the formed copper sheet at 2.4 kJ. It shows that the EM forming process is able to replicate micron level features in the formed sheet. This ability of the process can be used to form holograms on metal sheets effectively.

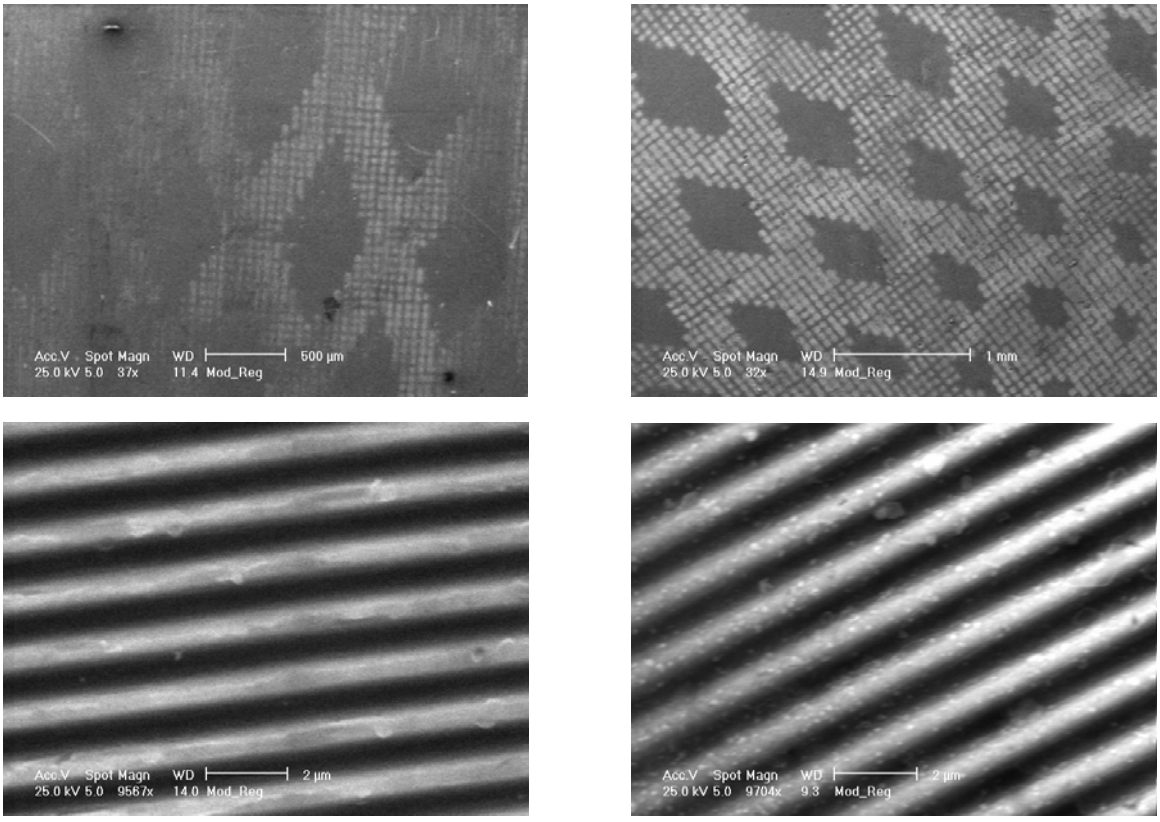

Formed Cu sheet Hologram used as a die

Figure 6.55: SEM micrograph comparisons of the formed Cu sheet and the die.

6.3 Shearing

The high velocity impact with the die can also be used for shearing if the die corners are sharp. Actuator 1 was used in some shearing experiments with 0.25 mm thick Al 5052-H32. The actuator was used to push the aluminum over a three hole with an entry radius provided by drilling a hole in mild steel. A cut sample is shown in Fig. 6.56. It shows that the cutting technique can work quite well. Also the tooling for this cutting method is simple and flexible.

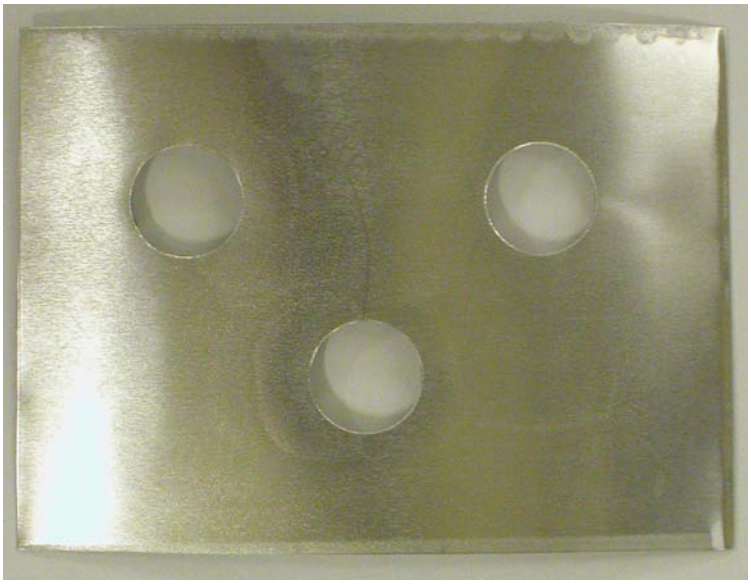

Figure 6.56: Al 5052-H32 with three cut holes using Actuator 1 at energy of 2.4 kJ (4 Cap. and 30% energy) and no standoff between the sheet metal and the die.

Shearing by EM forming can be very useful in coated materials, e.g., washing machine panels. Here the coated sheet needs to have circular openings along which the control knobs are attached to the machine. Typically cutting is done using a punch and a die where the sheet is in contact on both sides. Since EM forming is a non contact technique, only single sided contact is necessary for cutting. This is very important for coated materials especially if the coating needs to be retained in a good condition after the cutting operation. Also, the gap between the punch and the die needs to be carefully controlled in standard cutting as it controls the quality of the sheared edge. Typically a clearance of around 2 to 10% of sheet thickness is used [69]. This leads to burrs along the edges if not carefully controlled. Using EM forces, there is no need for this control.

To demonstrate the effect on coated materials, some shearing experiments were performed with 0.9 mm printed aluminum material. Actuator 1 was used to push the aluminum over a very simple die - basically just a ring with an internal hole of about 25.4 mm in diameter and an outer diameter of about 50.8 mm. There is some space around the outside of the ring that is not flat and this causes some further deformation (this is removed by using a 'real' tool).

As expected, the two sides of the sheet are quite different. The side that is against the tool is quite flat and has a good quality cut. The side that is pushed by the coil does get a nice curved surface going into the hole, as we expected, but the local stretching of the sheet causes the paint to crack. Figures 6.57 and 6.58 show this with the printed sheet cut at 4 kJ (4 Cap., 50% energy) using Actuator 1. In Fig. 6.57 the coated surface is facing the

coil. A good cut is achieved, but the coating has some rupture along the cut. In Fig. 6.58 the coated surface is against the cutting steel. The edges are sharply defined with no indications of coating rupture.

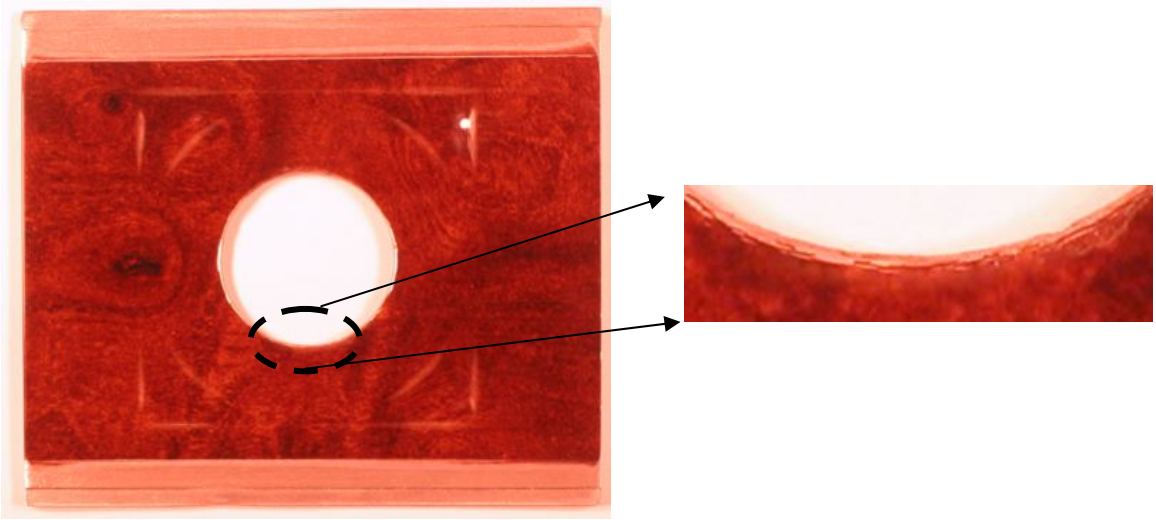

Figure 6.57: Overview of part with paint on side next to coil, away from cutting steel. It also shows the detail of surface which is curved nicely, but has some coating rupture.

There are a few decent conclusions from this:

1) The cutting technique can work quite well.
2) The tooling for this cutting method is very simple and very flexible (can change layouts or even hole shapes easily).

3) The effect of standoff was studied and it seems there is no great advantage in having a gap between the sheet and cutting form. This is good news from the point of view of being able to use the process practically.

Top surface with the paint facing the cutting steel

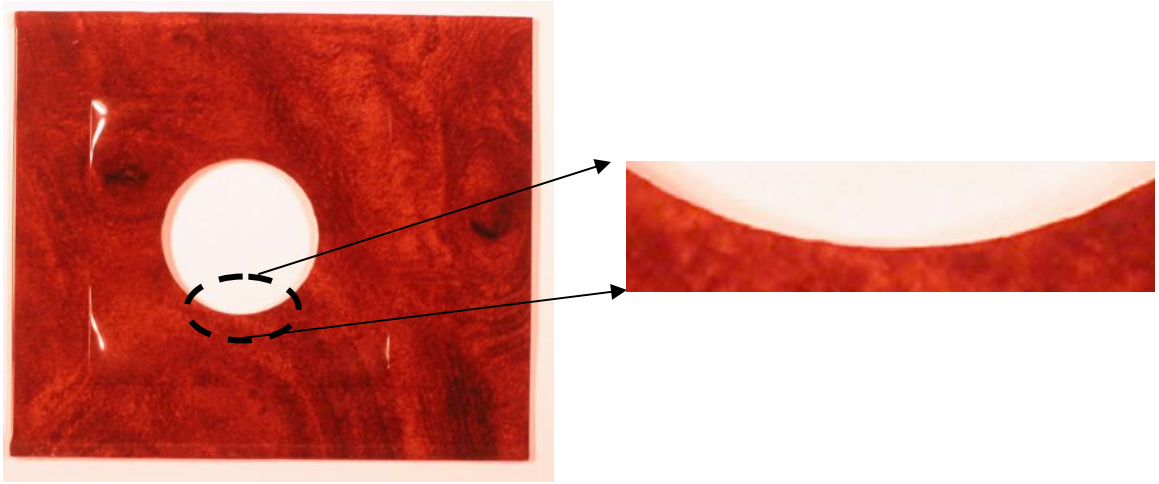

Bottom surface facing the cutting steel Details of the cut surface

Figure 6.58: Overview of part when paint faces cutting steel. It also shows the detail of details of cut edge which is very flat with no disruption of the coating.

CHAPTER 7

PRACTICAL CHALLENGES

There are some practical issues that need consideration for a successful application of this actuator. This chapter will deal with four such issues.

7.1 Uniformity of the Pressure Distribution

7.1.1 Round vs Square vs Flat Wire for Flat Distribution

A primary goal of this new actuator is to achieve a flat pressure distribution by the actuator. The *B* field (magnetic field intensity) produced by a wire may be dependent on the geometry of the wire. Since the B field determines the pressure distribution, the cross-section of the wire used maybe important.

This was investigated by 2D simulations in Maxwell 2D®. Rectangular (5 mm by 1.8 mm), square (3 mm by 3 mm) and circular (1.7 mm radius) wires, all 9 mm^2 in area were used. Each wire carried a current of 50 kA at 5 kHz, typical of our system. A spacing of 2 mm between the wire edges was chosen for our simulations (this is a typical practical gap governed by our insulation needs). A 1 mm thick Al sheet was placed at 2 mm and 5 mm below the coil (again typical of our system). The current density was measured and

compared along the width of the sheet, at a thickness of 0.2 mm below the surface, as shown in the schematic in Fig. 7.1.

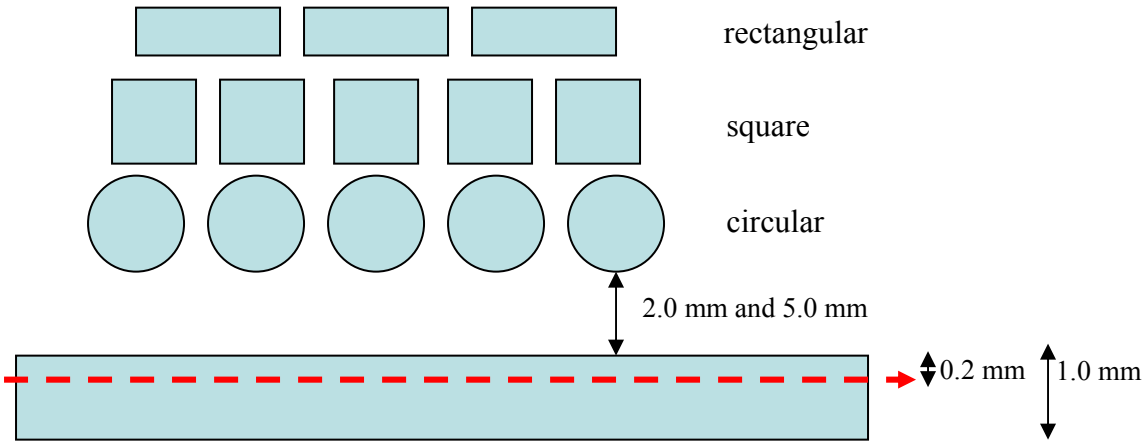

Figure 7.1: Schematic of the simulation in Maxwell 2D for effect of section of wires on the pressure distribution.

Figure 7.2 shows the current density distribution when the sheet is 5 mm from the wires. All the wires seem to have a uniform current distribution but the efficiency is the highest in the case of the square wire and least in the case of rectangular wires. Figure 7.3 shows the current density distribution for the case when the sheet is 2 mm from the wires. Even here the same pattern in the efficiency can be observed; however the rectangular wire does not have a uniform current distribution in this case. Figure 7.4 shows the contour plots of the current density in the rectangular and circular section wires.

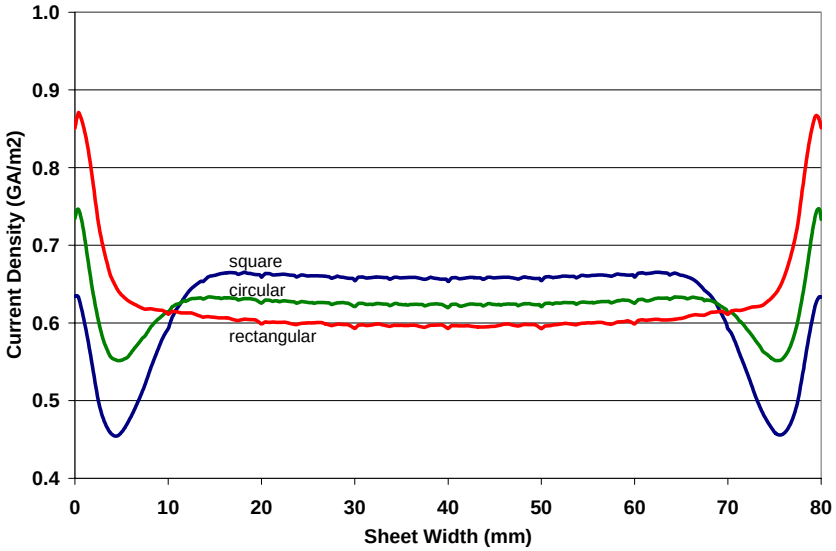

Figure 7.2: Current density distribution along the width of the sheet at 0.2 mm depth from the surface with wires of different sections. Sheet is at a distance of 5 mm from the coil.

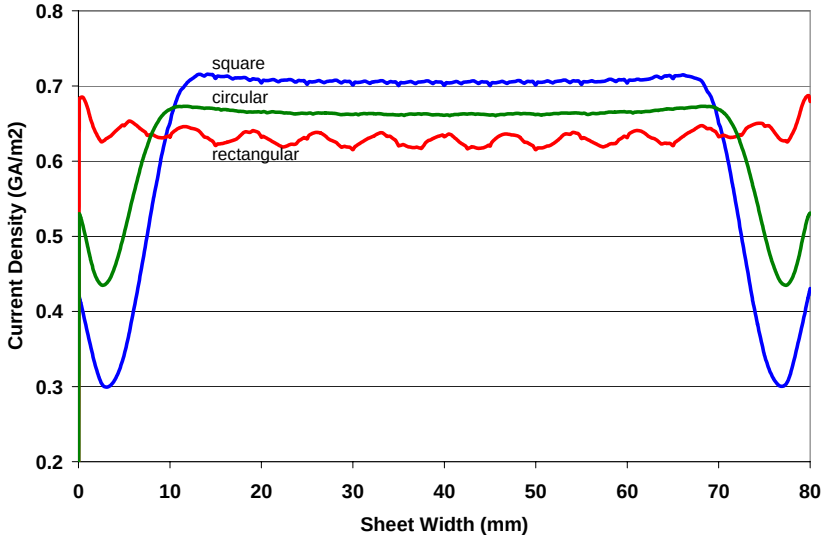

Figure 7.3: Current density distribution along the width of the sheet at 0.2 mm depth from the surface with wires of different sections. Sheet is at a distance of 2 mm from the coil.

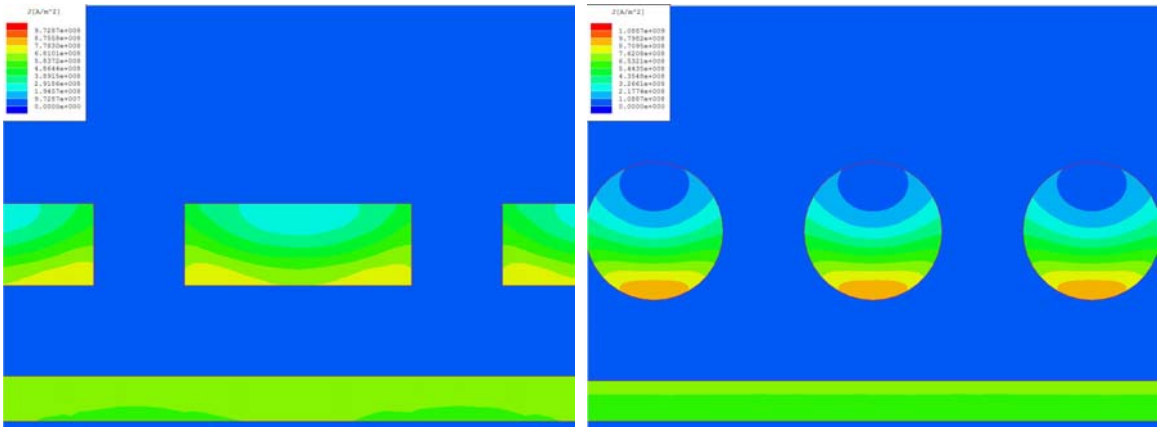

Rectangular Circular

Figure 7.4: Current density plots for the rectangular and circular section wires when the sheet is 2 mm away from the coil.

The flux lines for a rectangular wire do not differ significantly from that of the circular wire. They emanate as roughly concentric circles with the center in the wire as shown in Fig. 7.5. With multiple wires in the vicinity the flux lines interact in a resultant field. Therefore the pitch is more important for the uniform pressure distribution, not the shape. The square wires are more efficient because they have a lower pitch.

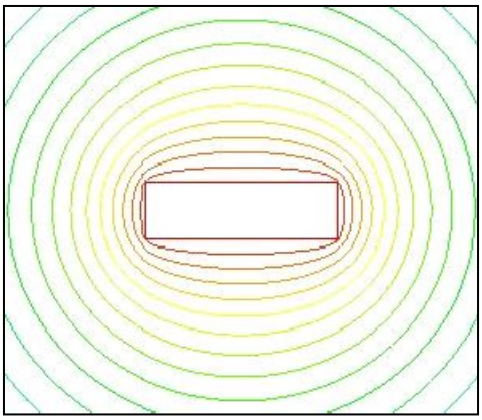

Figure 7.5: Typical flux lines for a single rectangular section wire.

These results are also verified by our experiments. If gaps between wires are too large the sheet can take a corrugated appearance - square wires mitigate this. An example of the comparison between the square and circular sectioned wires is shown in Fig. 7.6. Here 0.25 mm, Al 5052-H32 was formed at energy of 4.8 kJ (6 Cap., 40% energy). The figure shows that at the same energies the circular sectioned wires give a ridgy appearance on the formed part (left), whereas the square sectioned wires give a more uniform pressure distribution.

circular section wire

square section wire

Figure 7.6: Comparison between square and circular sectioned wires using Al 5052-H32 formed at 4.8 kJ (6 Cap., 40%).

7.1.2 Variation in Coil Pitch to vary Pressure Distribution

The correspondence between electromagnetic field intensity and magnetic pressure can be exploited in the design of electromagnetic forming coils. In regions where the current paths are closely packed there will be a much higher pressure than in regions where the coil has thick and /or sparse conductors. This ultimately determines the launch velocity distribution for the sheet and the free-form shape the sheet metal would take.

It is important to keep the gaps between the conductors to a minimum to get a uniform pressure distribution. Two wires conducting the current in the actuator should ideally be

as close to each other as possible so that the pressure distribution is uniform with no dead regions (the regions where no current is flowing and hence which does not experience any forming pressure). Windings that are too tight have thin insulation between the wires. This thin insulation needs to be strong enough to support electrical and mechanical loads, without any issues of breakdown, for the entire life of the actuator.

The pressure distribution can be varied by using the coil pitch. Here a 2D steady state simulation was carried out in Maxwell 2D®. Circular sectioned copper wires with radius of 1.7 mm, area 9 mm^2, and each carrying a current of 50 kA at 5 kHz was used. A 1 mm thick Al sheet was placed 5 mm below the coil. A spacing of 5.4 mm between the wire centers (2 mm between ends of two wires in the first case) and 10.8 mm (7.4 mm between ends of two wires) was chosen for our simulations. The current density was measured and compared along the width of the sheet, at a thickness of 0.2 mm below the surface, as shown in the schematic in Fig. 7.1. Since the pressure developed is directly proportional to the product of the current density and the magnetic field intensity developed, this plot gives an indication of the pressure distribution obtained.

Figure 7.7 shows the flux lines for the two cases, which is not uniform near the sheet in the case of the higher pitch. The current density distribution is shown in Fig. 7.8 which shows that uniform pressure distribution is not possible with a high spacing of wires. Figure 7.9 shows the current density contour plots for the two cases which emphasize the results observed. These results are also verified by our experiments.

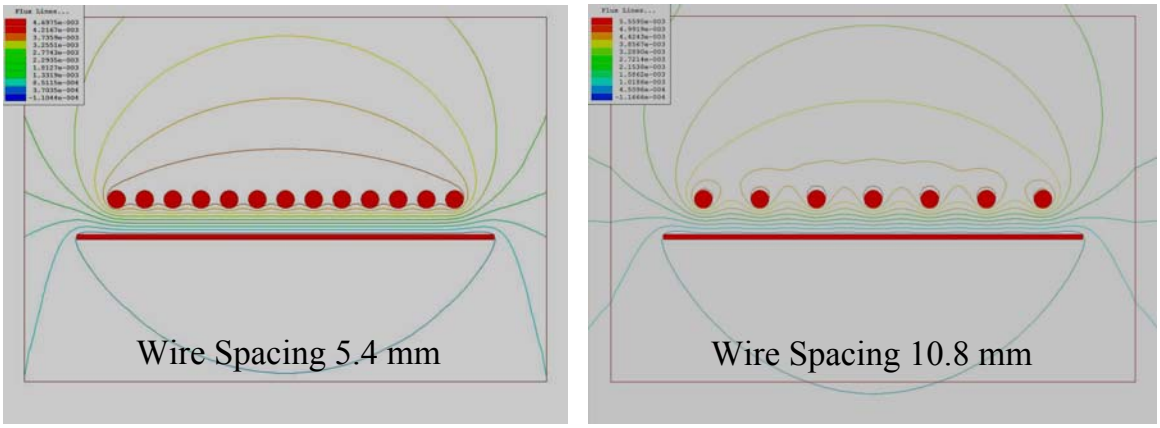

Figure 7.7: Flux lines plot for wire spacing of 5.4 mm and 10.8 mm showing the effect of variation of pitch on pressure distribution.

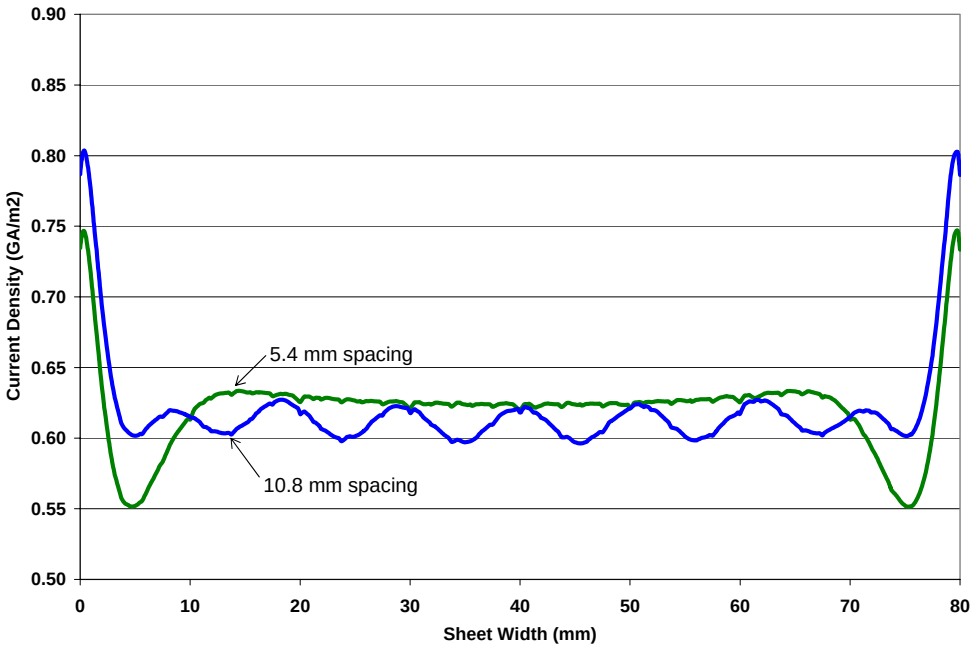

Figure 7.8: Current density distribution along the width of the sheet at 0.2 mm depth from the surface with different wire spacing.

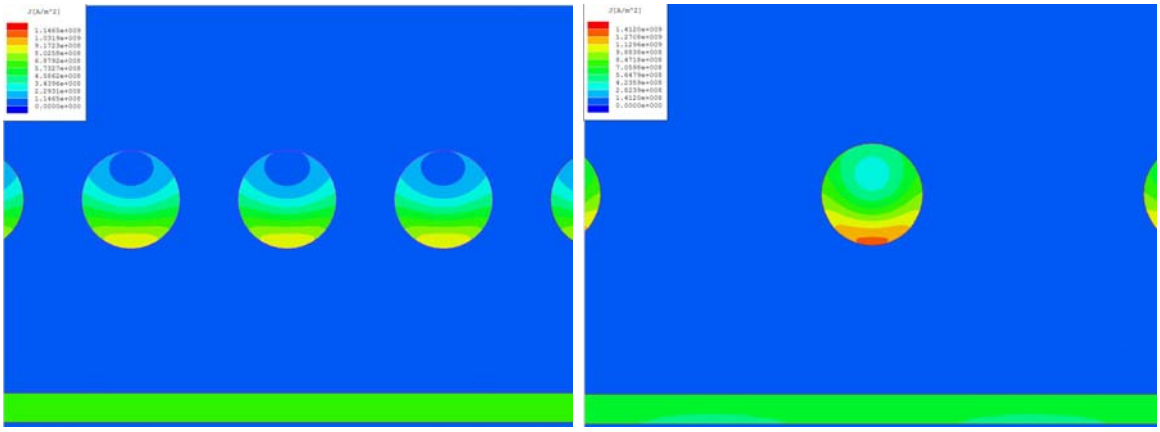

Wire Spacing 5.4 mm Wire Spacing 10.8 mm

Figure 7.9: Current density plots for circular section wires with different pitch when the sheet is 2 mm away from the coil.

7.2 Electrical Contacts

In conventional electromagnetic forming methods, the induced current flows through one continuous material. On the other hand, in a uniform pressure coil, the sheet metal forms a closed circuit together with an outer conductive channel to provide a return path for the induced eddy currents (Fig. 3.3). When the capacitor bank is discharged the primary current flows through the coil. The forming coil is well insulated from the outer conductive channel. The outer channel and the sheet metal form a closed circuit through which the induced current flows. Since the induced current path completely encircles the coil, there is a smaller loss of the magnetic flux energy and hence better efficiency. However, the contact can be a cause of concern since very high currents (typically around 10^4 -10^6 A) flow through it at high circuit voltages (typically a few kilo Volts). Arcing

can occur at the contacts. There are two possibilities for the formation of an arc: (i) arcing occurs during the forming process when the contacts try to open, or (ii) arcing occurs at a critical current density even if we hold the contacts shut. Proper design of the contact is therefore very important to avoid arcing issues. An inefficient contact may lead to arcing at the interface, which may be critical for surface sensitive parts. In addition to that the outer channel needs to be replaced frequently as it gets damaged for further use.

This section will begin with a review of the origin of electrical contact resistance at solid-solid interfaces and the major factors that affect the fundamental properties of the contacts. With the background information on electrical contacts in place, the occurrence of an electric arc at contact opening and the issues of contact erosion and welding will be described. A scaling analysis will be carried out to predict the parameters that are important in arc initiation and, in the end, issues that are worthy of further study for electrical contacts in our system will be discussed.

7.2.1 Background

The term ‘electrical contact’ means a releasable junction between two conductors which is apt to carry electric current. These conductors may be called contact members, or simply contacts [70].

All solid surfaces are rough on the microscale [71]. Surface microroughness consists of peaks and valleys whose shape, height variations, average separation and other

geometrical characteristics depend on the fine details of the surface generation process [70-72]. Contact between two engineering bodies thus occurs at discrete spots produced by the mechanical contact of asperities on the two surfaces as illustrated in Fig. 7.10.

For all solid materials the true area of contact is thus a small fraction of the apparent contact area for a wide range of loads. Under most engineering loads, the area of real contact between the surfaces is likely to be less than 1% of their nominal area [70]. In a bulk electrical interface where the mating components are metals, the contacting surfaces are often covered with oxides of other electrically insulative layers. Generally, the interface becomes electrically conductive only when metal-to-metal contact spots are produced, i.e., where electrically insulative films are ruptured or displaced along the contacting asperities.

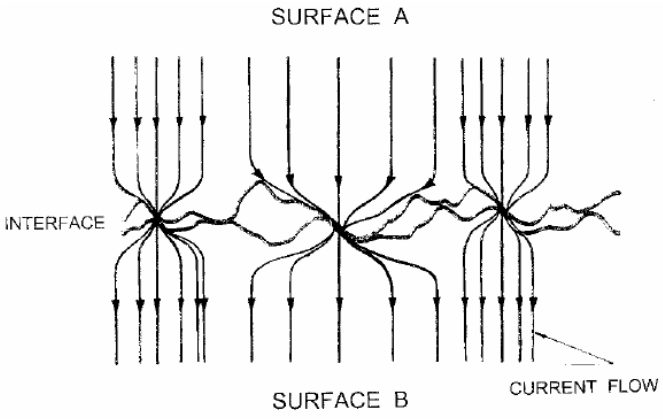

Figure 7.10: Schematic diagram of a bulk interface [73].

In a bulk electrical junction the electrical current lines become increasingly distorted as the contact spot is approached and the flow lines bundle together to pass through separate contact spots, called "*a*-spots" as illustrated in Fig. 7.10 [73]. Constriction of the electrical currents by the *a*-spots reduces the volume of the material used for electrical conduction and thus increases the electrical resistance. This increase in the resistance is called the constriction resistance of the interface. The presence of contaminant films of relatively large electrical resistivity on the contacting surfaces increases the resistance of *a*-spots beyond the value given by the constriction resistance. The total interfacial resistance provided by the constriction and the film resistance determine the contact resistance of the interface [71, 72].

7.2.1.1 Electrical Constriction Resistance

For the sake of simplicity the evaluation of constriction resistance generally assumes *a*-spots to be circular. This description is valid on an average for most general cases where the mating surfaces are characterized by isotropic roughness topographies. The assumption is invalid in the case where the surfaces are characterized by directional roughness as in rolled sheets or extruded rods.

7.2.1.1.1 Circular a-spots

For a circular constriction located between two semi-infinite solids, the equipotential surfaces in contact members consist of ellipsoids [72, 74]. The resistance between the equipotential surfaces can be calculated using normal resistance equations. Sufficiently

far away from the constriction, the constriction resistance for each contact member, is given as

$$R_s = \rho / 4a \qquad \text{..... (7.1)}$$

where a is the contact radius and ρ is the resistivity of the conductor. The total constriction resistance for the entire contact is thus twice this or

$$R_c = \rho / 2a \qquad \text{..... (7.2)}$$

Equations (7.1) and (7.2) are widely used in the design of electrical contacts. Holm [70] has experimentally verified this formula within error limits of observation of ± 1.5%. In case the upper and lower half of the contact interface consist of materials of resistivity ρ_1 and ρ_2 respectively, the electrical constriction resistance is given by

$$R_c = (\rho_1 + \rho_2) / 4a \qquad \text{..... (7.3)}$$

Timsit [75, 76] and Rosenfeld [77] have used solutions of Laplace equations with appropriate boundary conditions to find the constriction resistance for circular *a*-spots in a cylindrical conductor. Their results are identical to eqn. (7.2) when the constriction diameter is small compared to the diameter of the cylinder. Nakamura has used the boundary element method [78] and finite element methods [79] to arrive at the same result as that of Holm in eqn. (7.2).

Thus for a copper-copper interface (ρ=1.75x10^{-8} Ω m) and *a*-spot radius of 100 μm, the constriction resistance is approximately 1 mΩ [72]. Therefore the electrical contact between two surfaces need not be large to generate an electrical contact of low resistance.

7.2.1.1.2 Non circular and ring a-spots

Rigorous numerical evaluation of the spreading resistance of square and ring shaped *a*-spots has been done by Nakamura [78, 79]. He showed that the spreading resistance (resistance on one side of the contacts) of a square constriction with the side length of 2L and located between two semi-infinite conductors is given as

$$R_s = 0.434\rho / L \qquad \text{..... (7.4)}$$

He showed that the conductance of a square and circular ring shaped constriction does not decrease until the thickness becomes very close to zero. This suggests that the constriction resistance is proportional to the perimeter of the conducting spots and not to the area.

Table 7.1 gives an indication of the significance of the constriction shape on the constriction resistance. The expressions for constriction resistance for various geometries find application where the contacting surfaces are especially textured.

Constriction type	Radius (μm)	Length (μm)	Width (μm)	Ring Thickness (μm)	Resistance (Ω)
circular disk	5.64	–	–	–	1.55×10^{-3}
square	–	10	10	–	3.04×10^{-3}
rectangle	–	50	2	–	0.43×10^{-3}
ring	16.41	–	–	1	0.71×10^{-3}

Table 7.1: Resistance of constrictions of the same area (100 μm^2) and different shapes at a copper-copper interface [72] .

7.2.1.1.3 Multiple contact spots

In practice, an electrical junction consists of a number of contact *a*-spots through which electrical current passes from one connector component to the other. The *a*-spots are formed from the contact of asperities and the number of these increases with normal load [72, 80].

The contact resistance is determined by the number and dimensions of the *a*-spots and the grouping and dimensions of the clusters. The actual number of metal-to-metal *a*-spots is difficult to predict as it depends on the deformation mode of the asperities, i.e., elastic or plastic deformation but it will be appreciably smaller than the number of asperities in mechanical contact.

In the simplest case of a large number, *n*, of *a*-spots situated within a single cluster, it was shown by Greenwood [81] that the contact resistance can be approximated as,

$$R_c = \rho(1/2na + 1/2\alpha) \qquad \text{..... (7.5)}$$

where *a* is the mean *a*-spot radius defined as $\sum a_i / n$ (a_i is the radius of the ith spot) and α is the radius of the cluster defined as the Holm radius. Greenwood showed that the contact radius of a single spot of the same resistance is given to a reasonable approximation by the Holm radius α.

The results are significant because it suggests that the details of the number and spatial distribution of the *a*-spots are unimportant to the evaluation of the contact resistance in many practical applications where electrical contact occurs reasonably over the nominal contact area, i.e., in the absence of electrically insulating films. This conclusion is supported by Nakamura and Minowa [79] and Minowa *et al.* [82] who used finite element techniques to examine the effect of *a*-spot distribution on electrical resistance.

This suggests that for many engineering purposes knowledge of the Holm radius may be sufficient to estimate contact resistance. As a first approximation, the Holm radius may be estimated from the true contact area A as $[A/\pi]^{1/2}$ [72]. Because the true area of contact is smaller than the apparent area of contact, *a*-spots must support the local pressures that are comparable with the strengths of the materials of the contacting bodies. Greenwood and Williamson [72, 83] have shown that the asperity deformation is plastic in most practical applications. Bowden and Tabor [84] have proposed that the contact pressure on the contacting asperities is equal to the flow pressures of the softer of the two contacting materials. Therefore the area of mechanical contact (A_c) is related to the load applied (F) and the localized plastic flow stress (or hardness) H of the softer material as

$$F = A_c H \qquad \text{..... (7.6)}$$

If the electrical interface does not carry electrically insulative films and is characterized by a sufficiently large number of *a*-spots distributed within a Holm radius the contact resistance may be expressed as [72]

$$R_c = \{\rho^2 \eta \pi H / 4F\}^{1/2} \qquad \text{..... (7.7)}$$

where η is a constant equal to unity for clean interfaces.

Mathematical models by several other workers [83, 85] confirm that details of asperity deformation are relatively unimportant and the assumptions in the derivation of the above equation are not overly simplistic. The above equation is widely used by engineers to estimate the constriction resistance for selected values of hardness and contact force in an electrical contact. This estimate generally agrees to 20% or better with the actually measured values [72].

Some work has been done in identifying dimensionless parameters in electrical contact resistance [85-88]. Kogut *et al.* [86] have defined the dimensionless contact resistance as $R^* = R_c A_c^{1/2} \Big/ \rho_1 + \rho_2$ and dimensionless contact load as $F^* = F \Big/ A_c Y$, where Y is the elastic modulus. Similar non-dimensionalizing approach has been used by other authors [87, 88]. Park and Na [85] have used another approach of non-dimensionalizing the contact pressure by the hardness, i.e., P_n / H, where P_n is the nominal contact pressure and H is the hardness.

7.2.1.2 Effect of surface films on contact resistance

The presence of a film at the interface of an electrical junction affects contact resistance in a variety of ways as described below.

7.2.1.2.1 Electrically conductive layers and thin contaminant films

Electrically conductive coatings (electroplates) are often used to minimize electrical contact resistance. Contact resistance may be reduced through the action of several mechanisms such as a decrease in surface hardness, a large electrical conductivity of the electroplate relative to the substrate and the elimination of electrically insulating surface oxide films. Conductive coatings are also used to protect contact surfaces against tarnishing and oxidation [72, 89].

To a first approximation for the case where the film is sufficiently thin, the total resistance R_t with the film becomes

$$R_t = R_s + \rho_f d / \pi a^2 \qquad \text{..... (7.8)}$$

where R_s is the spreading resistance, ρ_f is the resistivity of the film and d is the thickness of the film.

Equation (7.8) demonstrates that the effect of constriction resistance is overshadowed by the film resistance whenever the ratio $(\rho_f / \rho)(d / a)$ is much larger than unity. This is confirmed by Nakamura and Minowa [90] who used finite element techniques to study the same. In this case, the contact resistance varies with the applied load as F^{-1}. This is generally taken as an evidence of the presence of contaminant material on the surface [72, 91, and 92].

7.2.1.2.2 Intermetallics

Contacts are often plated to lower the contact resistance and improve upon other characteristics like corrosion resistance. However, formation of intermetallics due to

plated materials at the electrical interfaces during the normal life cycle of a contact is an issue that needs to be addressed. This formation arises from the interdiffusion of materials across the bimetallic interface. This might occur due to higher operating temperature of the interface or the increase in the *a*-spot temperature well above the ambient conditions due to high current flow through the interface [72]. The formation of intermetallics is generally deleterious to the electrical stability and mechanical integrity of the bimetallic joint because the intermetallics are characterized by low mechanical strength and high electrical resistivity [72, 93-100].

Studies indicate that the growth of an intermetallic layer to a thickness of more than 2 μm greatly reduces the strength of aluminum-to-copper joints [95, 98 and 99]. At this thickness the interface becomes highly porous and more susceptible to environmental effects due to the generation of numerous fissures in the interdiffusion layer.

Aluminum-copper and tin-plated copper are commonly found in many electrical devices and systems. Braunovis *et al.* [93, 94] did a study over a temperature range of 250 to 515°C on friction welded aluminum-copper and tin-plated copper conductors. Over the entire temperature range investigated, the interdiffusion layer consisted of five major bands. The important characteristics of these are listed in the table below.

Phase	Symbol	Compsn	Cu (wt %)	Al (wt %)	Hardness (kg/mm^2)	Resistivity ($\mu\Omega cm$)
Phase 1	γ_2	Cu_2Al	80	20	35	14.2
Phase 2	δ	Cu_3Al_2	78	22	180	13.4
Phase 3	ζ_2	Cu_4Al_3	75	25	624	12.2
Phase 4	η_2	CuAl	70	30	648	11.4
Phase 5	θ	$CuAl_2$	55	45	413	8.0

Table 7.2: Important characteristics of intermetallic phases in bimetallic Al-Cu system [93, 98].

As can be seen in the table the microhardness of the intermetallic phase is significantly higher than that of aluminum (38 kg/mm^2) or copper (42 kg/mm^2) as is the resistivity (compared to 2.67 μΩcm for Al and 1.69 μΩcm for Cu). Extensive cracking was observed not only within the intermetallic layer but also at the neighboring interface.

The growth of the intermetallic layer with time has been shown in Fig. 7.11. Figure 7.12 shows the growth of contact resistance with the thickness of the intermetallic phases formed at the Al- Cu bimetallic joints after heat treatment by an electrical current at different temperatures and time [93].

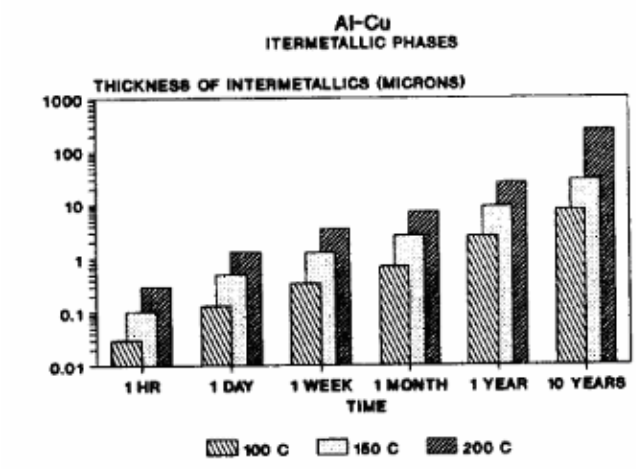

Figure 7.11: Thickness of intermetallic phases formed at different times and temperatures in Al-Cu bimetallic joints [93].

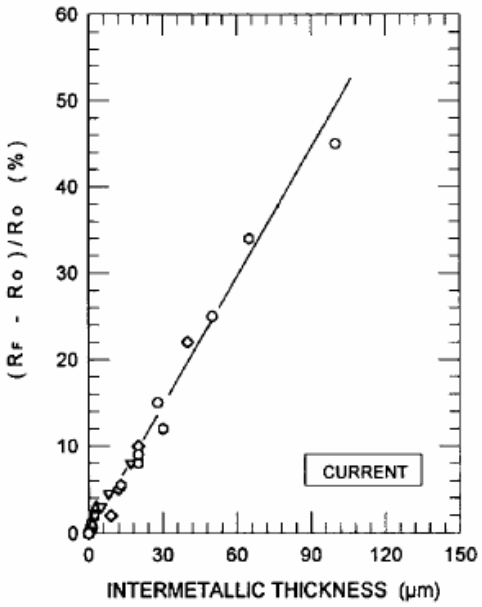

Figure 7.12: Growth of interface resistance with the thickness of the intermetallic phases formed at the Al- Cu bimetallic joints [93].

A direct consequence of increased resistance is the heating of the contact, which will result in increased rate of formation of intermetallic phases and other degradation processes such as creep, corrosion, etc. Although the discussion above has been made with respect to Al-Cu, the effects are not really limited to these types of interfaces and apply generally to a wide number of bimetallic couples including Cu-Sn, zinc coatings and plated layers of brass [72].

Electromigration, which is the current induced transport of the conducting material, needs consideration here. Electromigration is important in microelectronics; it can potentially lead to circuit failure [101-103]. Electromigration has been studied in bulk electrical contacts also [93, 99] but Timsit [72] has shown that in the case of intermetallics its effect is negligible as compared to the band growth thermally under those conditions. Even if we move aside from intermetallics and just consider the effects of electromigration in our system the effect will be negligible. In the overall time scales involved, the contact may have to be removed due to normal wear or corrosion.

7.2.1.2.3 Electrically insulating or weakly conducting film

The origin of a electrically insulating or weakly conducting surface usually lies in the formation of oxide or corrosion products on the contact surfaces. Most often, these types of films are mechanically brittle, as in the case of Al_2O_3 films on aluminum. In such a case electrical contact is established only after the rupture of the film and the establishment of metal-to-metal contact. Therefore the shape of the *a*-spots and the constriction resistance is dependent upon the fracture mode of the insulating layers [104].

A highly resistive film has a deleterious effect on the contact resistance as can be seen by comparing Figs. 7.13 and 7.14. In Fig. 7.13, a load of about 1N is required to fracture the insulative oxide layers in the interface. It can be seen that the behavior is much better in ultra high vacuum, where the oxide layer was removed by ion-beam etching. Here a lower contact resistance is achieved at much lesser applied load [105].

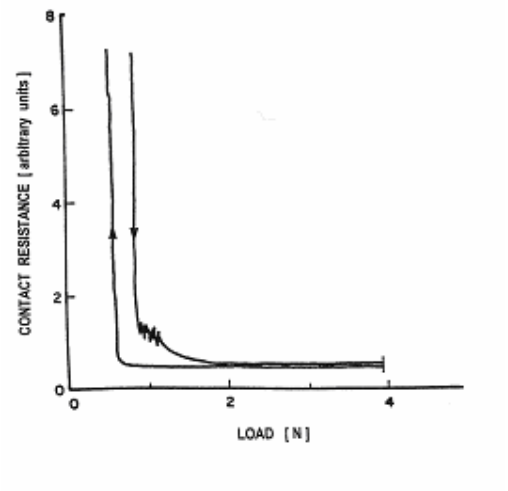

Figure 7.13: Contact resistance in an Al-Al contact with oxide film on the contact surfaces [105].

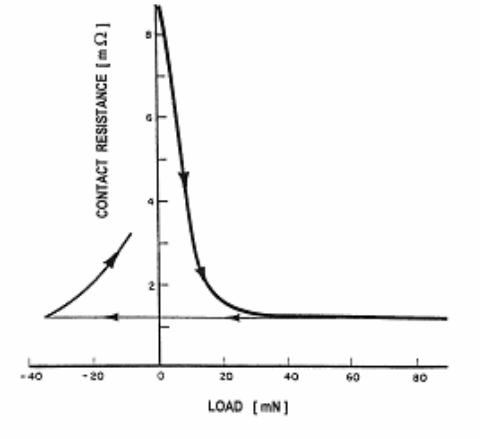

Figure 7.14: Contact resistance in an Al-Al contact with oxide films removed from the contact surfaces [105].

As an example, in the case of aluminum the oxidation rate in air at temperatures ranging from room temperature to about 400ºC is very rapid. In air or dry oxygen the growth rate is self-limiting with a maximum thickness of 2-4 nm over a wide temperature range. At temperatures as high as 300ºC the Al_2O_3 film seldom exceeds 20 nm in thickness even on surfaces originally subjected to extensive mechanical deformation [106, 107]. The electrical resistivity of Al_2O_3 is so large (~10^{14}-10^{16} Ω cm) at 100ºC that the film is a perfect insulator for all intensive purposes. Mathematical calculations by Timsit [72] suggest that in practical electrical contacts the current flow through the metal oxide film can be ignored in comparison to the current flow through the metal-to-metal contacts.

7.2.1.3 Effect of Temperature on an *a*-spot

The constriction resistance of $\rho/2a$ according to eqn. (7.2) was based on the assumption that the heat generation at the contact is negligible. The effect of a thermal gradient complicates the relationship between voltage drop across the contact, the electric current and the *a*-spot dimension. Kohlrausch [70] derived a simple relationship between the voltage drop V across the contact and the maximum temperature T_m in the contact interface based on the condition that the electrical and thermal current flow lines follow the same paths. In this case the electrical potential and the isothermal surfaces within the conductor coincide [72, 107 and 108].

Over a temperature range where ρ, the electrical resistivity and λ, the thermal conductivity varies little with temperature and for a monometallic contact, the voltage temperature relationship can be reduced to

$$(T_m - T_1) = V^2 / 8\lambda\rho \qquad \text{..... (7.9)}$$

where T_1 is the temperature in the conductor far away from the contact. Equation (7.9) finds usage in designing electrical contacts in making sure that the contact supertemperature, (T_m-T_1), does not exceed 1-3ºC under extreme operating conditions. Under conditions where the super temperature is large, eqn. (7.9) loses validity. However this *V*-*T* relationship is valid for electrical contacts of any shape or dimensions [72].

Usually the dependence of thermal conductivity and electric resistivity on temperature, can be expressed as $\lambda = \lambda_0(1 - \beta t)$ and $\rho = \rho_0(1 + \alpha t)$ over a wide temperature range [70, 109]. Here α and β refer to the temperature coefficients of electrical resistivity and

thermal conductivity respectively and the subscript *0* refers to the value at 0ºC. The calculated dependence of T_m on V using this temperature dependence has been shown in Fig. 7.14 for some common contacts. It is important to note that the generation of potential drops in excess of 0.1 V produces contact temperatures which easily lead to the softening or melting of the contact material.

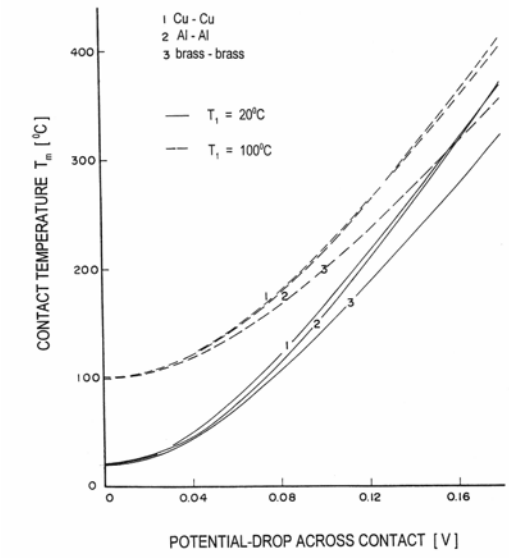

Figure 7.15: Voltage temperature relationship for some common materials [72].

The Wiedemann-Franz law [70, 110] is used sometimes to simplify the temperature dependence of thermal conductivity and electrical resistivity. It states that the variations of thermal conductivity and electrical resistivity with temperature, can be related by the expression,

$$\lambda\rho = LT \qquad \text{..... (7.10)}$$

where L is the Lorentz constant (2.45 x 10^{-8} V^2K^{-2}) and T is the absolute temperature. This implies that the V-T relationship can be written as

$$V^2 = 4L(T_m^2 - T_1^2) \qquad \text{..... (7.11)}$$

which is clearly independent of the materials in contact. Although this relationship provides a reasonable description over the temperature range of interest for ordinary electrical contacts, it is not universally valid.

The increased thermal dissipation by the larger current causes an increase in temperature which in turn increases resistivity and further increases the ohmic heating. Also the increased temperature decreases thermal conductivity, which reduces the ability of the junction to dissipate heat by thermal conduction. With good electrical conductors like copper, copper alloys and aluminum, the rise in electrical resistivity and the decrease in thermal conductivity are such that the *a*-spot reaches an equilibrium temperature. However in contacts such as those of Fe or Ni, this effect is relatively very rapid. In contacts made of these materials there exists a critical voltage at which heat is no longer dissipated at a rate compatible with the requirements of thermal equilibrium which leads to contact melting. The increase in temperature at frequent operations has to be carefully investigated in our experimental setup since very high current densities (as much as 10^9 A/m^2) may be involved.

With a good background in electrical contacts in general, we will now consider how this leads to an explanation of the arcing phenomenon in our experimental setup.

7.2.2 The Electric Arc

Ideally the opening and closing of contacts should produce an instantaneous electrical change of state. But since nature tends to resist a discontinuity, a number of transition effects are likely to occur. Most prominent among these is the formation of an arc in the gap [111]. An electric arc is formed due to an ionization process. If an impacting electron accelerated by the voltage difference between the cathode and the anode has enough energy, it can knock out a weakly bound electron from the atom of a gas or metal vapor in the contact gap. If the electric field in the contact gap increases, the current increases. There is a sudden transition from a "dark discharge" to another form of sustained discharge. This transition sometimes called a spark, consists of a sudden increase of current in the gap and is accompanied by a sudden increase in the light visible between the contacts. It is this spark that initiates the arc. Details of the breakdown process can be found elsewhere [70, 72 and 111].

The formation of an electric arc during contact opening has been extensively studied [70, 72, 111] and is similar to what is occurring in our experimental setup. If the circuit current is greater than a certain value and the voltage between the contacts is above a minimum value an arc will always form between them. The arc formation depends entirely upon the properties of the contact material and the arc always initiates in the metal vapor from the contacts themselves [72]. From eqn. (7.7) it is clear that as the contacts begin to open $F \rightarrow 0$ and so R_c will increase. As R_c increases, V_c, the voltage drop across the contacts given by $V_c = IR_c$ also increases. Following eqn. (7.11) the temperature of the contact spots increase.

A stage is reached when the temperature reaches T_m, the melting temperature of the metal. Once the contact spot has melted and the contacts continue to separate, a molten bridge is formed between them. This molten bridge forms between them even at low currents [70], even when contacts open at high acceleration [112, 113] and in vacuum [114]. The molten bridge lengthens, becomes unstable and finally ruptures releasing metal vapor in the contact gap. If the electrical field at the gap is above a critical value an arc is initiated. The parameters required to form and sustain an arc is summarized in Table 7.3 [111].

Condition	Voltage across the contacts, V	Circuit current, I
To initiate breakdown		
Gas breakdown:		
nonconduction to glow	V_B gas $> 329 + 7 \times 10^6 d$ for air (d in m)	$I \approx 0.01$–0.6 A
nonconduction to arc		$I > 0.6$–1.0 A
To sustain breakdown		
Glow (gas dependent)	$V_G = 280 + 10^3 d$ for air	$I_{G\,min}$ 0.01–0.6 A
Arc (contact material dependent)	$U_A = U_{min} + 10^4 d$, where $U_{min} \approx V_i + U_\phi = 11$–$15$ V	$I_{min} \approx 0.05$–1.0 A depends upon metal surface and condition

Table 7.3: Parameters required to form and sustain an arc [111].

Once an arc is established it requires a continuous supply of electrons from the cathode to sustain it. The electrons will be liberated only if the cathode temperature is high enough for release of thermionic electrons for refractory contacts or release of electrons by thermionic field emission for low melting point contacts. Therefore if the current is below

a minimum, I_{min}, the energy losses will exceed the energy input to the cathode and the electron production will cease. Also the arc would require a minimum voltage, U_{min} that corresponds to the work function voltage, U_{φ}, of the cathode contact and the ionization potential of the gas, V_i. Thus

$$U_{\min} \approx V_i + U_{\varphi} \qquad \text{..... (7.12)}$$

It is also important to note that if a metal gets contaminated with carbon deposits then the I_{min} decreases to a value associated with carbon contacts.

	V_i (volts)	U_{ϕ} (volts)	$V_i + U_{\phi}$ (volts)	$U_{\min}$ (volts)	$I_{\min}$ (clean) (amperes)
Al	5.98	4.10	10.08	11.2	0.4
Ag	7.57	4.74	12.31	12	0.4
Au	9.22	4.90	14.12	12.5	0.35
Cu	7.72	4.47	12.19	13	0.4
Fe	7.90	4.63	12.53	12.5	0.45
Ni	7.63	5.05	12.68	13.5	0.5
C	11.27	4.60	15.87	20	0.01

Table 7.4: Minimum arc current and minimum voltages for some common contacts [71]

Arcing has only been dealt with in regards to opening or closing of contacts or at a gap. The author is not aware of a work in which arcing has been described for two metallic conductors in intimate contact.

7.2.2.1 Contact erosion and material transfer

Contact erosion can be electrical or mechanical. We will deal with arc erosion here. Arc erosion is a result of the high temperatures near or over the boiling points of the contact materials at the cathode and anode face. The amount of erosion per operation is dependent on the arcing time [72, 111], circuit parameters [115, 116], surrounding gas [117, 118], and contact shape, size and contact material [115, 118] among a multitude of other factors. However some broad guidelines can be made on the erosion behavior.

Higher arc currents lead to excessive heating of the contact spots leading to higher erosion rates. To give a quantitative picture, studies done by Turner *et al.* [119] for AgCdO contacts found the erosion rate to be given by $6I^{1.6}$ μgs^{-1} for currents more than 1000 A, where I is the arc current. Yoshida [120] has reported that increased system inductance and voltage also leads to higher arcing time and hence higher erosion.

Contact size is an important factor for erosion as it decides the contact volume that conducts the heat away from the contact surface. For example, Slade [72] suggests a rule of thumb for currents lower than 50 A. He suggests that the contact diameter should be three times the arc root diameter and that its thickness should be greater than the arc depth. Various authors have developed models for explaining materials transfer in erosion but the PSD model (particle sputtering and deposition) by Chen *et. al.* [121] is commonly used. It says that the material transfer depends not only on the metallic arc formation but also on the gaseous arc formation. Usually it is difficult to compare the material transfer for different contact materials because no standards exist. Thus most of

the design information on erosion is more of a qualitative guideline and individual parameters need to be considered before designing for a system.

7.2.2.2 Contact Welding

Contact welding can occur if high enough currents pass through the closed contacts and cause the contact spot to melt. It can also occur after an arc. Welding is typically characterized by welding current, which is the current above which the contacts weld; and welding force, which is the force needed to separate the contacts after they have welded [122]. It is only when the strength of the weld prevents the proper functioning of the contacts that it is a problem [72, 122].

7.2.2.3 Scaling Issues in Arcing

The author is not aware of any work done in the area connecting the scaling issues in arcing with electromagnetic forming. Similarity issues in arcs have predominantly been studied for sustained arcs, as in electric arc furnaces, but not for the initiation of arcs [123, 124]. The application of similarity methods to electrical discharges is confronted by a number of difficulties. Although the number of controlled parameters is small, they act on a multitude of closely interrelated processes of different physical natures - electric, magnetic, optical, etc. Determining what parameters are important is complicated by the dependence of the basic processes on the discharge conditions [123].

The concern in our case is in determining what parameters are important in characterizing the initiation of arcs in our system. Based on the review of literature [70, 72, 111, 123-125], the following model is proposed.

7.2.2.3.1 Assumptions

1. A critical electrical field is required above which the breakdown occurs. This field is typically in the range of 5 x 10^7 V/m to 10^9 V/m, depending on contact activation or cleanliness [111].
2. The arc formation depends entirely upon the properties of the contact material and the arc always initiates in the metal vapor from the contact material. Circuit operating voltages are important. According to Table 7.4, all materials possess a characteristic arcing voltage in the 10-20 volt range. If the maximum voltage is below this range, arcing will not occur. Above this voltage, arcing and subsequent material loss must be expected [127]. Gas pressure might be important but we assume working is under atmospheric pressure. The ionization potential of the metal vapors and work function of the cathode contact are important for efficient liberation of electrons but these requirements are taken care of in the requirement for sufficient electrical field.
3. The arcing occurs during the forming process when the separation force between the sheet metal and the outer conductive channel tries to open the electrical contact between them.
4. Arcing, as proposed by Holm [70], occurs at the asperities making contact. The cathode temperature needs to be high enough to sustain the arc by a continuous

supply of electrons. Thus heating of the contact is important for a sustained arc. This can be due to resistive heating during arcing.

5. Welding occurs at the contacts when the temperature of the contacts reaches the melting temperature [72]. Since the contact sees high current pulses for short durations, the heating is adiabatic at the contacts [128]. However we assume steady state conditions which give us a lower limit on contact welding.

7.2.2.3.2 Analysis

For arcing the first and foremost requirement is the presence of a critical electrical field, E, in the gap of length d.

$$E = V_c / d \qquad \text{..... (7.13)}$$

where V_c is the potential drop across the contacts.

Also as noted above, heating is important. Using eqn. (7.11) and assuming the ambient temperature is negligible compared to the melting temperature of the contact material, the voltage across the contacts when it melts (V_m) is given by

$$V_m = 2L^{1/2}T_m \qquad \text{..... (7.14)}$$

where T_m is the melting point of the contact material and L is the Lorentz constant. Clearly, above a critical voltage, which is material dependent, the contacts melt. Equation (7.14) is thus the criteria for welding of contacts. Also, the initiation of arcing is just defined by the voltage drop across the contacts. Since the voltage given by eqn. (7.14) is less than 1 V for most common contact materials the voltage defined by eqn. (7.13) becomes the critical voltage for arc initiation. The voltage across the contacts can be

further simplified as IR_c where I is the current and R_c is the contact resistance. Taking another look at R_c, and using similarity analysis,

$$\sigma \propto (R_c l)^{-1} \qquad \text{..... (7.15)}$$

where l is a length parameter and σ is the electrical conductivity due to the constriction. A direct expression for the dependence of resistance on conductivity of the form $R = Length / \sigma A$, is not applicable here as we are talking about constriction resistance. Here A is the area. The choice of the length parameter is critical. It should be a parameter which is perpendicular to the direction of current flow. Although the *a*-spots are formed over a larger area, the skin depth lowers the actual area through which the current passes as shown in Fig. 7.16. Since the skin depth is more or less constant for a particular operation the other length parameter (l in this case) might be important. Based on (7.15) now,

$$E = JR_c l \qquad \text{..... (7.16)}$$

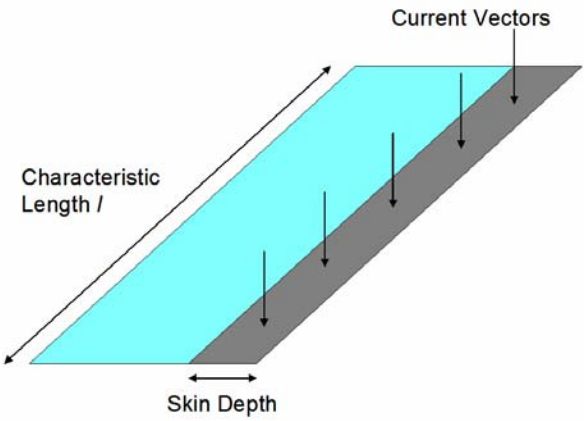

Figure 7.16: Schematic of the nominal area of electrical contact.

Given a particular system design, the parameter l is a constant. Thus the critical parameters that determine the initiation of an arc are the current density J and the contact resistance R_c. Based on this we can determine the ranges where we can operate our forming system. Typical calculations are attached in Appendix B.

It is worthwhile to refer to the work of Henselek *et al.* [129] who used current per unit length to define the initiation of welding in contacts. This is only true if we assume R_c to be a constant which in his case was true due to the nature of his experimental setup.

7.2.2.3.3 Design Recommendations based on the Analysis

1. Intrinsic in the above analysis is the need to select a proper material for the contacts. To lower the R_c, the material should be soft and have a high electrical conductivity. Its work function should be high so that it is difficult for it to emit electrons and its

vapors should have a high ionization potential. The contact surfaces should be clean and especially be free of any organic impurities to avoid activation. Higher thermal conductivity is preferred for better heat dissipation along with higher boiling and melting points to lower chances of arcing.

2. Higher contact loads help by lowering R_c. The only question is how high is high? The recommendation by Holm [70] is to keep the load around ten times more than the one required to give a desired contact resistance. This takes into account improper contact and other effects like film formation. With specific regards to our experimental setup, the force should also be enough to take care of the electromagnetic repulsive force that cause contact opening. The force employed on the contacts should be the maximum the material can withstand without excessive wear or deformation [127].

   Another important requirement is the uniform contact of the sheet metal with the outer channel. A pressure sensitive film was used in-between the metal sheet and the die with Actuator 1 to see the actual pressure distribution achieved. The usage of the film has been shown in Fig. 7.17. The left side of the figure shows the way the film was attached to the metal sheet. The right side shows the strip that has been taken out from the sheet after the experiment. The color-coding obtained after the experiment on the film can be interpreted in terms of the pressure. Here it can be seen that the C channel contact the metal sheet uniformly (uniform dark red coloration along the contact with Al C channel, indicating pressure > 127 MPa) and hence no arcing was observed in the sample.

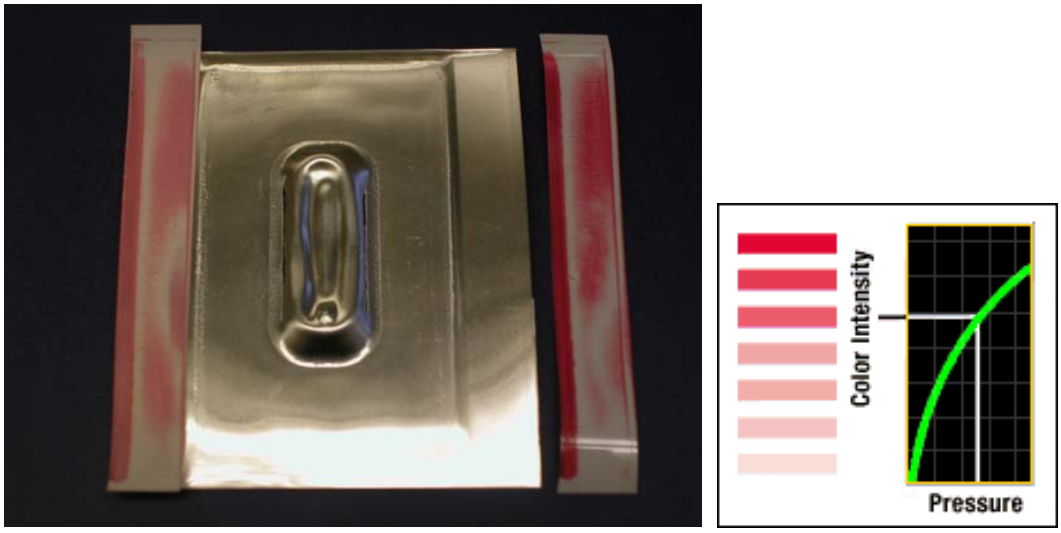

Figure 7.17: The formed metal sheet along with the pressure sensitive film using Actuator 1. The color coding can be interpreted in terms of pressure [138].

The above approach was carefully maintained in all experiments to confirm the uniformity of pressure distribution. Figure 7.17 clearly shows the effect of pressure distribution on arcing using Actuator 1 on 0.25 mm, Al 5052-H32. Sparking does not occur in the left hand side due to the uniform pressure distribution and the C channel contacting the whole surface. In the right had side it can be seen that the C channel does not contact the surface at all the points along the length of the sheet. In the area marked there is no contact with the C channel and arcing occurs at that location.

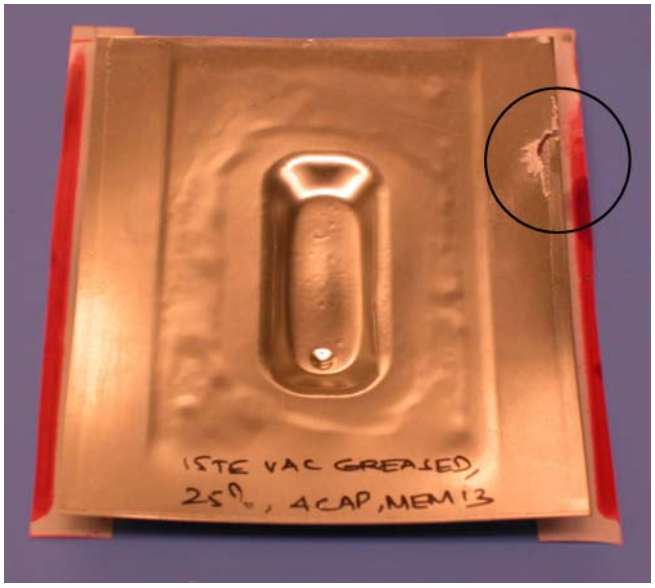

Figure 7.18: Formed Al 5052-H32 using Actuator 1 at 2 kJ (4 Cap. and 25% energy) showing the effect of pressure distribution on arcing.

3. Design to mitigate the drawbacks at the contacts due to the skin effect. Higher frequencies are important for higher forming efficiency but that leads to small skin depths. The skin effect reduces the area through which the current flows. Some asperities contact points may not come in use as the current is confined to flow through a narrow region due to the frequency effect. Commercial finite element modeling packages like MAXWELL® can be used in the design process.

4. Effective cooling of the outer conductive channel or doing the experiment at lower temperatures. This follows from cooling electrodes in spot welding [130-133] that

carry high current densities in the order of 10^9 A/m^2. The probability of arcing is reduced as the plasma needs more energy to form prior to arc generation.

5. Use of clamped capacitor bank [134] which delivers only the first half of the current pulse. Since a major part of the work in deforming the material is done in the first cycle of the pulse, the later parts of the pulse can therefore be eliminated, which only lead to enhanced probability of arcing as the electrodes get heated up. The latter part of the pulse also gives more time for the contacts to open.

   A clamped capacitor bank has a diode in the circuit to cut off the current after the first half of the pulse. The capacitor banks used in this study are of the ringing type where the entire pulse of current is obtained. This is demonstrated in Fig. 7.19 where two Al 5052-H32 samples were formed at 2 kJ (4 capacitors and 25% energy). Arcs were intentionally produced in one by using the pressure distribution and the current plots with time were compared for the two cases.

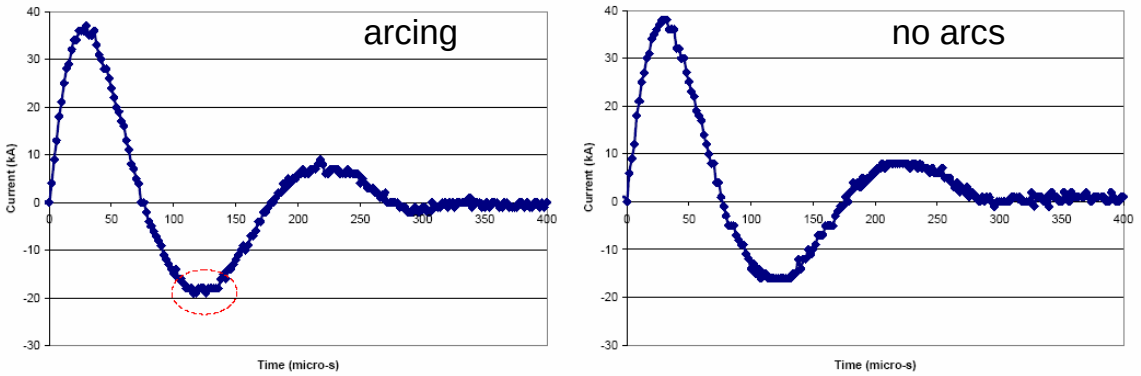

Figure 7.19: Comparison of the plots for case with and without arcing in Al 5052-H32 formed at 2 kJ (4 Cap. and 25%) using Actuator 1.

It can be seen that in the case of arcing there is a peak in the lower part of the current time plot, which is absent in the case with no arcs. This shows that the arcing event occurs after the first half of the current pulse.

6. Usage of a compliant layer, like automotive gasket material, between the sheet metal and the die. This helps by reducing the chances of contact opening.

This concept was used in the fuel cell plate forming using Actuator 3. Here a 1.6 mm cork rubber gasket (automotive gasket) was used as shown in Fig. 7.20.

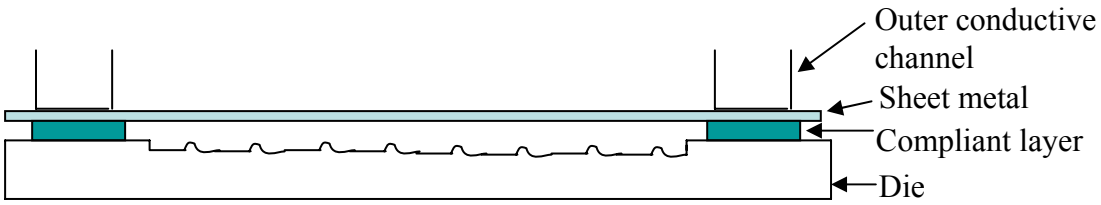

Figure 7.20: Schematic of the gasket setup for control of arcing in Actuator 3 setup.

The results from the use of this gasket are shown in Fig. 7.21. It can be seen that with the use of the gasket the contact surface is better in appearance with lower chances of arcing.

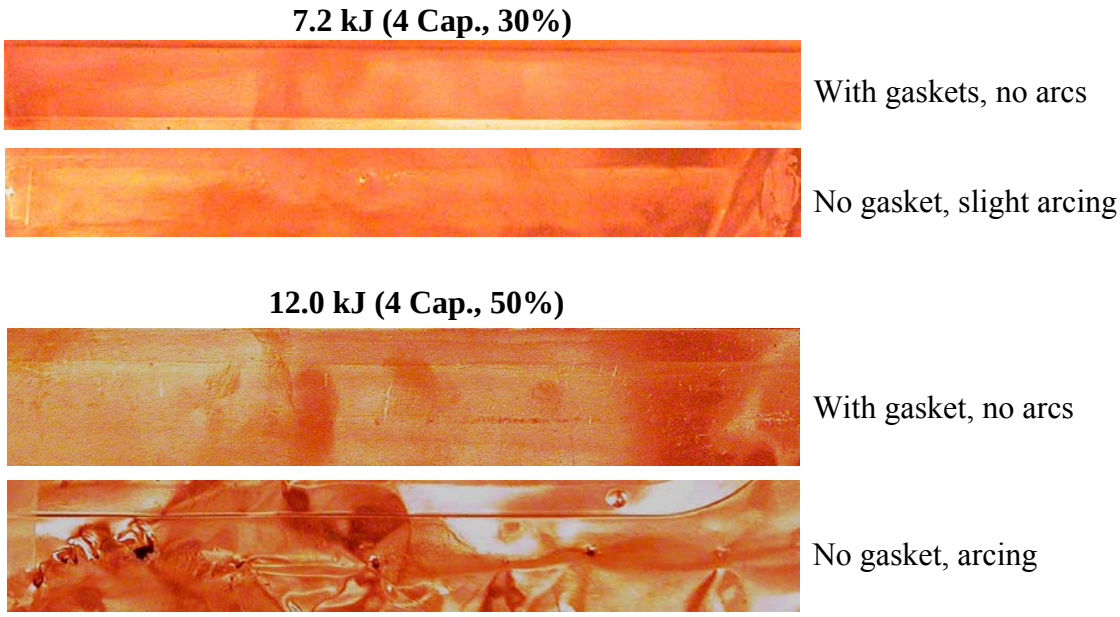

Figure 7.21: The contact surface of 0.13 mm Cu formed onto the fuel cell die using the 48 kJ Capacitor bank. A 1.6 mm cork rubber gasket (automotive gasket) was used.

7.2.3 Summary

Electrical contacts are a very extensively studied subject with published research dating back to 1835, but the basics of the field are not very different from those established by Holm [70] decades ago. Optimization of the contact resistance is obtained by optimizing or eliminating the physical factors like hardness and contact force as they control the dimensions and distribution of the *a*-spots. The independence of true contact area with the nominal contact area and details of the surface micro-topography lead to the dependence of contact resistance on the inverse root of the load.

Based on the literature survey the following missing elements can be identified:

(i) Arcing issues have been primarily studied for opening and closing of contacts and for electrodes at a gap. The issue of whether electrodes in intimate contact (close to the asperities) arc at a particular current density has not been addressed.

(ii) Microelectronics and spot welding are close to our experimental regime in terms of the current density but they have no problem with arcing as the voltages used for most practical purposes are below 10 V. Also in both cases there is no opening of contacts.

(iii) The universal parameter determining the *a*-spot temperature is the voltage drop across the interface and not the magnitude of electrical current [72]. This is based on contacts at steady state which is not applicable in our case. The author is not aware of a model that can predict welding under these situations. There is some similarity with spot welding in this case. Though the current densities are the same ($\sim 10^9$ A/m^2), generally 0.1 seconds or more of current time is required for a proper weld [130-133]. In our experiments the current pulse lasts for a maximum of 0.5 milliseconds, so welding should not be a problem.

(iv) The critical electrical field at which arcing occurs is difficult to predict and is dependent on the circuit conditions, contact configuration and the ambient surroundings. No models exist to accurately predict the onset of arcing.

(v) Similarity studies have been carried out predominantly for sustained arcs and the author is not aware of work using it to describe the initiation of arcs.

(vi) Although, the effect of different materials has been investigated by many researchers, a unified model describing the complex processes in the contact zone is lacking.

7.2.4 Unresolved Issues

The principal goal of this project is to exploit the advantages of electromagnetic sheet metal forming using a uniform pressure actuator. Our previous work has proven the feasibility of electromagnetic forming. However a successful application of the coil industrially will require a good understanding and control of arcing at the interface between the sheet metal and the outer conductive channel. The limited information of the process (both electromagnetic forming and arcing) brings some difficulties into the numerical study. Firstly, the calculation of the current density at which the system will arc is not a straightforward process. A lot depends on the surface conditions. However experience shows that the increase in current density does lead to arcing. Higher energy from the capacitor banks means two things: higher operating voltages leading to higher voltage across the contacts, and higher current density, resulting in more heating. The analyses of the governing equations give some design variables, which can serve as broad guidelines while designing a contact. However, very specific design methodology to accurately predict when arcing occurs is too complex and dependent on too many parameters. The author is not aware of any unified model which can predict the onset of arcing in a particular system. The common design philosophy is to use the above principles as guidelines to make a contact and carry out actual testing to validate the suitability of the contact in a particular application [70, 72 and 111].

Scaling analysis and the study of the initiation of arcs leads us to look at the design of the forming actuator from a different view. One of the important things to note from the analysis is that we should be able to push the high currents without arcing if the contacts

do not open. Two issues are worthy of study over here. The first one is the effect of skin depth. Is there a design of the contacts that can lead to a more uniform current flow through the entire contact area? Another issue is the location of the contacts. Calculations (Appendix B) show that the opening force at contact opening is ten times higher than the applied loads. This means that rethinking the location and design of the contacts might lead to a better solution to the problem. On a broader scale a different design of the capacitor banks is another option with operation at low voltages. One of the things that remain to be seen is how well we can predict the arcing using the analysis developed.

What has become imperative from our study is the need for materials selection. Developing the best contact solution for an application is complex since many factors and their relationships must be considered. Low hardness is required to lower the constriction resistance but this increases the wear. Thus design requirements are not often compatible and a materials selection process is required. This entails basically defining the constraints, the formulation of a value function and a search procedure to explore the solution space and rank the materials by their ability to meet the requirements [135, 136]. The process is still in its early stages of development and the more immediate need now is to avoid the formation of arcs. A long term perspective here is to look at the lifetime of the coils where mechanical wear and corrosion come into picture. The key to success in improving the efficiency of the process is in getting better with each step in the learning curve.

7.3 Maximum Available Pressure/ Velocities

There are two important limitations of this type of coil. First, the forces on the workpiece and coil are equal and opposite (in addition to other magnetic interactions within the coil). Therefore, the coil construction materials determine the pressure the coil can withstand. For this reason coils of this construction are often limited to pressures on the order of 7,000 psi, if they are to be used for many operations [1]. Second, it is usually difficult to use a very fine winding pitch to increase local field intensity. This also limits the local pressures that can be generated from this kind of coil. Both these issues can be partly treated in short-run production by using inexpensive coils that are essentially replaced. Also high velocities can be used to generate the high impact pressures. The velocity can be developed without extreme pressures, as discussed earlier.

7.4 Coil Life

Development of long life coils is an important challenge. Robust coils are needed for high-volume industrial production. Moving from the design in Actuator 1 to Actuators 2 and 3 did provide much more robust coils. Actuator 2 saw more than 200 shots up to a maximum energy of 8 kJ and no failure was observed. Actuator 3 saw more than a 100 shots up to a maximum of 19.6 kJ and did not observe sufficient damage. Actuator 1 was used up to 7 kJ and also saw more than 200 shots in operation before it failed.

Figure 7.22 shows the failures observed in Actuator 1 and another actuator of the same generation. Actuator 1 failed by arcing between the coil and the outer channel. The insulation provided by the urethane potting was damaged in the course of use of the coil.

Another failure for a first generation actuator is shown. This actuator was similar to actuator 1 but had circular sectioned wires. This actuator also failed by insulation failure. The insulation layer between the sheet metal and the actuator was destroyed over time which resulted in the failure as a result of arcing.

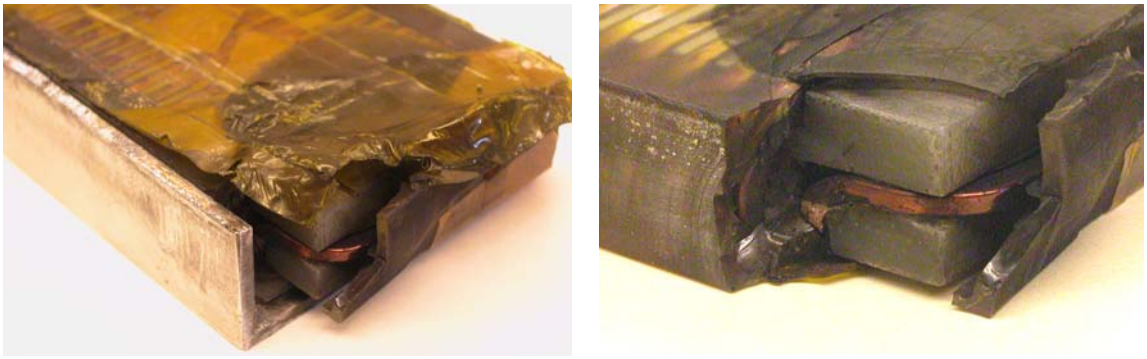

Arcing between the coil and the outer channel

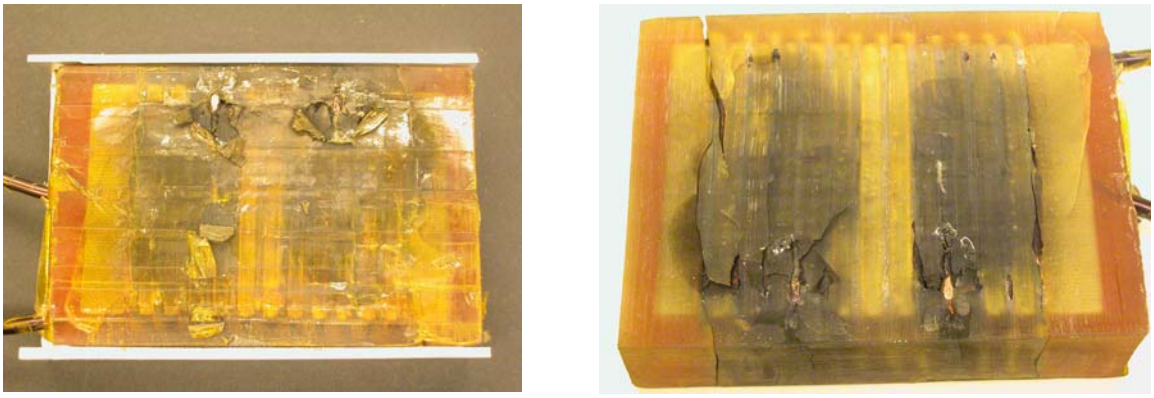

Arcing between the coil and the sheet metal

Figure 7.22: Failures observed in first generation actuators.

There are a few design rules that should be taken into account while designing the coils.

1. The coil system should be self supporting. One should not count on the urethane or the insulation to provide mechanical strength. This idea is seen in third generation actuators where machined copper and brass are being used.
2. Eddy currents should be avoided in the structural parts. In experiments with Actuator 1 we have seen some issues with this. This can be done better by using G-10 or an insulating structural part. This has also been incorporated in the vacuum chamber design for the third generation actuators.
3. Corners should be rounded to avoid high electrical potential (can be seen in Fig. 7.4).
4. Lead lengths should be kept to a minimum to lower the inductance. Also these leads should be restrained.
5. The insulation should be sufficient to avoid arcing. It should also be periodically evaluated to see if there is any significant damage. This problem can also be solved in short run production by using disposable coils.

CHAPTER 8

CONCLUSIONS

Based on the experiments carried out and previous experiences with electromagnetic forming the following can be concluded:

1. Design methods for dynamic forming can solve many troublesome issues in metal forming.
2. The new concept gives a uniform pressure distribution and is very efficient. Electromagnetic forming can be used to form car door pockets, cell phone cases, fuel cell panels, etc., very efficiently.
3. The occurrence of arcing in the system can be predicted and the system designed to avoid its occurrence.
4. Multiple capacitor discharges may lead to a better-formed geometry.
5. Effective engineering design can be carried out using the uniform pressure coil.

High velocity forming methods have a long and significant history. However these techniques have never quite achieved a clear place among mainstream manufacturing methods. This might be attributed to the fact that there is little intersection between the

communities that understand capacitor bank discharge or explosive engineering with the metal forming community [1]. However the uniform pressure actuator gives the designer and the engineer a new and hopefully useful tool for manufacturing.

CHAPTER 9

FUTURE WORK

The work in this study has shown that an actuator can be used for flat sheet forming. The following areas need more study.

1. Coil Life and Durability: This is one of the most important factors that will govern the viability of usage of this coil industrially. The current study has focused on a limited set of materials for the coil, urethane and the outer conductive channel. A material selection process is needed along with experimentation to design a robust actuator.
2. Coil Design: There is a need for innovation in coil design. Contacts can be designed differently to mitigate the skin effect and reduce arcing possibilities. Coils that need less time to manufacture need to be studied. Both the coil and setup design should be aligned with the ultimate idea of industrial feasibility.
3. Repeatability: The current work focused on developing the new actuator and showing some of its capabilities. The ability to repeat the forming needs to be evaluated to show the feasibility of the process. Since the currents and hence the

forming pressure can be precisely controlled, the process is amenable to automation. Also precise control of the process is possible and is one of the reasons the process is favored in assembly operations.

4. Predictive Capability: This study has focused more on the experimental part. This is true for the development stage of most new technologies. However the further growth and adoption of the process will depend upon predictive tools for the process. The analytical model discussed in Chapter 4 provides a good tool for the predictability of the process. The model needs to be refined to incorporate the effect of resistance, change of frequency during the duration of the process and material deformation with time. These will help in sharpening the predictability of the process. Also FEM codes like LS DYNA which is currently incorporating EM forming capability in its material deformation model will be a valuable tool for design. The arcing criterion also needs further development.
5. Dimensional Accuracy: This needs to be evaluated to check the conformity with the die. The effect of vacuum level needs to be evaluated to set the limits required in the process. The effect of standoff between the sheet and the die needs careful study.

REFERENCES

1. G.S. Daehn, *High Velocity Metal Forming*, Draft for publication in ASM Handbook (2003/2004), "Forming and Forging", (2003)

2. G.S. Daehn, *Electromagnetically Assisted Stamping- A vision of a future for Metal Forming*, www.hyperplasticity.com, April, (2005)

3. D. Risch, C. Beerwald, A. Brosius, M. Kleiner, *On the Significance of the Die Design for Electromagnetic Sheet Metal Forming*, Proceedings of the First International Conference on High Speed Forming, pp. 191-200, (2004)

4. L. V. Belyy, S. M. Fertik and L. T. Khimenko, *Electromagnetic Metal Forming Handbook, (A Translation of the Russian Book: Sprvochnik Po Magnitno-impul' Snoy Obrabotke Metallov),* Translated by M. M. Altynova and Glenn S. Daehn, Columbus, OH, (1996)

5. Yuri V. Batygin and Glenn S. Daehn, *The Pulse Magnetic Fields for Progressive Technologies*, Kharkov, Columbus, (1999)

6. S.T.S. Al Hassani, J.L. Duncan and W. Johnson, *Techniques for Designing Electromagnetic Forming Coils*, Proc. Second International Conference on High Rate Forming, Colorado, USA, pp. 5.1.2 -5.1.16, (1969)

7. R. Davis and E.R. Austin, *Developments in High Speed Metal Forming*, Industrial Press Inc., (1970)

8. N. Takatsu, M. Kato, K. Soto, T. Tobe, *High-Speed Forming of Metal Sheets by Electromagnetic Force*, JSME International Journal, Series III, Vol. 31, No. 1, pp. 142-148, (1988)

9. G.K. Fenton, M.S. Thesis, The Ohio State University, (1996)

10. M. A. Meyers, *Dynamic Behavior of Materials,* published by John Wiley and Sons, (1994)

11. www.afterimagegallery.com/dledgerton.htm, July, (2005)

12. www.hyperplasticity.com, July, (2005)

13. DARPA Technology Transition Report (www.darpa.mil/body/pdf/transition.pdf), (2002)

14. A.A. Ezra, *Principles and Practices of Explosive Metallurgy*, Metal Working, Industrial Newspapers Ltd., London, (1973)

15. J.S. Rinehart and J. Pearson, *Explosive Working of Metals*, Mac Million, New York, (1963)

16. Glenn S. Daehn, *Electromagnetically Assisted Sheet Forming: Enabling Difficult Shapes and Materials by Controlled Energy Distribution*, Research Proposal to NSF, (2002)

17. Frank W. Wilson, *High-velocity Forming of Metals*, American Society of Tool and Manufacturing Engineers, Prentice-Hall Inc., Englewood Cliffs, N. J., (1964)

18. Glenn S. Daehn, Vincent J. Vohnout and Larry DuBois, *Improved Formability with Electromagnetic Forming: Fundamentals and a Practical Example*, Sheet Metal Forming Technology, Edited by Mahmoud Y. Demeri, The Minerals, Metals & Materials Society, pp.105-116, (1999)

19. R.P. Feynman, R.B. Leightman and M.L. Sands, *The Feynman Lectures on Physics*, Addison-Wesley, Chapter 17, (1989)

20. F. W. Grover, *Inductance Calculations: Working Formulas and Tables*, D. Van Nostrand Co., New York, NY, (1946)

21. J. Jablonski and R. Winkler, *Analysis of the Electromagnetic Forming Process*, Int. J. Mech. Sci., Vol. 20(5), pp. 315-325, (1978)

22. W.H. Gourdin, *Analysis and Assessment of Electromagnetic Ring Expansion as a High-Strain-Rate Test*, J. Applied Physics, Vol. 65(2), pp. 411-422, (1989)

23. S.T.S Al-Hassani, J. L. Duncan and W. Johnson, *On The Parameters of The Magnetic Forming Process*, J. of Mech. Engg. Science, Vol. 16 (1), pp. 1-9, (1974)

24. Francis C. Moon, *Magneto-Solid Mechanics*, John Wiley & Sons, Inc., (1984)

25. Vincent J. Vohnout, *A Hybrid Quasi-static/Dynamic Process for Forming Large Sheet Metal Parts From Aluminum Alloys*, Ph.D. Dissertation, the Ohio State University, Columbus, OH, (1998)

26. L. Du Bois, Personal Communication with Vincent J. Vohnout, General Motors Corp., North American Operations, Die Systems Engineering, Flint, MI, (1996)

27. A.K. Henry, Personal Communication with Vincent J. Vohnout, General Motors Corp., North American Operations, Engineering, Flint, MI, (1995)

28. William F. Hosford and Robert M. Caddell, *Metal Forming: Mechanics and Metallurgy*, Second Edition, Englewood Cliffs, N.J., Prentice Hall, (1993)

29. J. L. Duncan, Jack Hu, Z. Marciniak, *Mechanics of Sheet Metal Forming*, Second Edition, Butterworth-Heinemann, (2002)

30. G.S. Daehn, *Electromagnetically Assisted Stamping- A vision of a future for Metal Forming*, www.hyperplasticity.com, October, (2003)

31. Amit A. Tamhane, Marina M. Altynova and Glenn S. Daehn, *Effect of Sample Size on Ductility in Electromagnetic Ring Expansion*, Scripta Materialia, Vol. 34, 8, pp. 1345-1350, (1996)

32. V. S. Balanethiram and G. S. Daehn, *Hyperplasticity-Increased Forming Limits at High Workpiece Velocities*, Scripta Metallurgica, Vol.31, pp. 515-520, (1994)

33. X. Hu and G. S. Daehn, *Effect of Velocity on Localization in Uniaxial Tension*, Acta Materialia, Vol. 44, pp.1021-1033, (1996)

34. C. Fressengeas and A. Molinari, *Inertia and Thermal Effects on the Localization of Plastic Flow*, Acta Metallurgica Materialia, Vol.33, 3, pp.387-396, (1985)

35. I. M. Fyfe and A. M. Rajendran, *Dynamic Pre-strain and Inertia effects on the Fracture of Metals*, Journal of the Mechanics and Physics of Solids, Vol. 28, pp.17-26, (1980)

36. G. Regazzoni, J. N. Johnson and P. S. Follanbsbee, *Theoretical study of the dynamic tensile test*, Journal of Applied Mechanic, Vol. 53, September, pp. 519-528, (1986)

37. A Needleman and V. Tevergaard, *Analyses of Plastic Flow Localization in Metals*, Applied Mechanics Reviews, Vol.45, pp. S3-S15, (1992)

38. P. S. Follansbee and U. F. Kocks, *A Constitutive Description of the Deformation of Cooper Based on the Use of the Mechanical Threshold Stress as an Internal State Variable*, Acta Metallurgica Materialia, Vol.36, 1, pp. 81-93, (1988)

39. M. Padmanabhan, *Wrinkling and Springback in Electromagnetic Sheet Metal Forming and Electromagnetic Ring Compression*, MS Thesis, The Ohio State University (1997)

40. John A. Waller, *Press Tools and Presswork*, The Graphic Group, Burgess Hill, W. Sussex, (1978)

41. Paul B. Schubert, *Die Methods: Design, Fabrication, Maintenance, and Application, Book One*, Industrial Press Inc., New York, N. Y., (1966)

42. E. J. Bruno, Editor, *High-velocity forming of metals*, American Society of Tool and Manufacturing Engineers, Dearborn, MI, (1968)

43. http://www.rocoil.cwc.net, April, (2005)

44. Mala Seth, *High Velocity Formability of High Strength Steel Sheet*, M.S. Thesis, The Ohio State University, (2003)

45. Mala Seth, Glenn Daehn, *Effect of Aspect Ratio on High Velocity Formability of Aluminum Alloy*, Trends in Materials and Manufacturing Technologies for Transportation Industries, TMS, (2005)

46. Peihui Zhang, *Joining Enabled by High Velocity Deformation*, Ph.D. Thesis, The Ohio State University, (2003)

47. Autodyn Manual, Century Dynamics, (2005)

48. G.I. Taylor, *The Use of Flat Ended Projectiles for Determining Yield Stress. I: Theoretical Considerations*, Proceedings of Royal Society, A 194, 289, (1948)

49. M.L. Wilkins and M.W. Guinan, *Impact of Cylinders on a Rigid Boundary*, Journal of Applied Physics, Vol. 44, No. 3, March, (1973)

50. G.R. Johnson and W.H. Cook, *Fracture Characteristics of Three Metals Subjected to Various Strains, Strain Rates, Temperatures and Pressures*, Engineering Fracture Mechanics, Vol. 21, No. 1, pp. 31-48, (1985)

51. Maxwell Manual, Ansoft Corporation, (2005)

52. C.S. Park, T.W.Ku, B.S. Kang and S.M. Hwang Park, *Process Design And Blank Modification In The Multistage Rectangular Deep Drawing Of An Extreme Aspect Ratio*, Journal of Materials Processing Technology, 153–154, pp. 778–784, (2004)

53. E. Sato, T. Shimizu, T. Sano, S. Fuchizawa, *Square Cup Deep Drawing Of Thick Plate By Multi-Axial Loading. Part 1. Finite Element Analysis*, J. Mater. Process. Technol. 48, 69–74, (1995)

54. S.K. Esche, M.A. Ahmetoglu, L.G. Kinzel, T. Altan, *Numerical And Experimental Investigation Of Redrawing Of Sheet Metals*, J. Mater. Process. Technol. 98, 17–24, (2000)

55. L.P. Lei, S.M. Hwang, B.S. Kang, *Finite Element Analysis And Design In Stainless Steel Sheet Forming And Experimental Comparison*, J. Mater. Process. Technol. 110, 70–77, (2001)

56. N.S. Kim, S. Kobayashi, *Blank Design In Rectangular Cup Drawing By An Approximate Method*, Int. J. Mach. Tool Des. Res. 26, 125–135, (1986)

57. D.K. Min, B.Y. Jeon, H.J. Kim, N.S. Kim, *A Study On Process Improvements Of Multi-Stage Deep-Drawing By The finite Element Method*, J. Mater. Process. Technol. 54, 230–238, (1995)

58. N. Kishor, D.R. Kumar, *Optimization Of Initial Blank Shape To Minimize Earing In Deep Drawing Using finite Element Method*, J. Mater. Process. Technol. 130–131, 20–30, (2002)

59. T. Broek, M.S Thesis, *Deep Drawing Aluminum Alloy 2008-T4 Sheet Into Rectangular Pans Using Different Blank Shapes And Grain Orientations*, The Ohio State University, (1995)

60. J. D'sa, M.S Thesis, *Deep Drawing of Rectangular Cups: Analysis and Tool Design*, The Ohio State University, (1993)

61. T.L. Hursman, *Development of Forming Limit Curves for Aerospace Aluminum Alloys*, Formability Topics- Metallic Materials, ASTM STP 647, B.A. Niemeier, A.K. Schmieder, and J.R. Newby, Eds., American Society for Testing and Materials, pp. 122-149, (1978)

62. G.S. Daehn, Manish Kamal, Mala Seth, Jianhui Shang, *Strategies for Sheet Metal Forming Using Mechanical Impulse*, 6th Global Innovations Symposium: Trends in Materials and Manufacturing Technologies for Transportation Industries: Sheet Metal Forming, TMS Annual Meeting, California, (2005)

63. G.S. Daehn, Edurne Iriondo, Manish Kamal, Mala Seth, Jianhui Shang, *Electromagnetic and High Velocity Forming: Opportunities for Reduced Cost and Extended Capability in Sheet Metal Forming*, Society of Manufacturing Engineers Summit Conference, August, Wisconsin, (2005)

64. E. Doege, K. Droder, *Sheet Metal Forming Of Magnesium Wrought Alloys-Formability And Process Technology*, JMPT, 115, pp. 14-19, (2001)

65. F.K. Chen, T.B. Huang, C.K. Chang, *Deep Drawing Of Square Cups With Magnesium Alloy AZ31 Sheets*, IJMTM, 43, pp. 1553-1559, (2003)

66. E. Uhlmann, R. Hahn, D. Jurgasch, *Pulsed Magnetic Hot Joining- New Solutions For Modern Lightweight Structures*, Steel Research International, 76 (2-3), pp. 245-250, Feb., (2005)

67. Hiroshi Ike, Surface Deformation Vs. Bulk Plastic Deformation- A Key For Microscopic Control Of Surfaces In Metal Forming, Journal of Materials Processing Technology 138, pp. 250–255, (2003)

68. Personal Communication, Dr. J.R. Bradley, General Motors R&D Center, Michigan, December 9, (2004)

69. G.E. Dieter, *Mechanical Metallurgy*, McGraw-Hill Book Company, (2001)

70. R. Holm, *Electrical Contacts- Theory and Applications*, Springer-Verlag New York, (1967)

71. T.R. Thomas, *Rough surfaces*, Imperial College Press, pp. 1-10 and 247-250, (1999)

72. P.G. Slade, *Electrical Contacts*, Principles and Applications, Marcel Dekker, (1999)

73. R.S. Timsit, *Electrical Contact Resistance: Properties of Stationary Interfaces*, IEEE Transactions on Components and Packaging Technology, Vol. 22, No. 1, March (1999)

74. W.R. Smythe, *Static and Dynamic Electricity*, New York, McGraw-Hill, (1968)

75. R.S. Timsit, *The potential distribution in a constricted cylinder*, J. Phys. D, Appl. Phys. 19, pg. 2011, (1977)

76. R.S. Timsit, *The potential distribution in a constricted cylinder*, Proceedings of the 14th International Conference on Electrical Contacts, Paris, p. 21, (1988)

77. A.M. Rosenfeld, R.S. Timsit, *The potential distribution in a constricted cylinder: An exact Solution*, Quart. Appl. Math, 39, pg. 405, (1981)

78. M. Nakamura, *Constriction resistance of Conducting Spots by the Boundary Element Method*, IEEE Transactions on Components and Packaging Technology, Vol. 16, No. 3, May (1993)

79. M. Nakamura, I. Minowa, *Computer Simulation for the Conductance of a Contact Interface*, IEEE Transactions on Components, Hybrids and Manufacturing Technology, Vol. CHMT-9, No. 2, pp. 150-155, June (1986)

80. T.R. Thomas, S.D. Probert, *Establishment of Contact Parameters from Surface Profiles,* J. Phys. D: Appl. Phys., Vol. 3, pp. 277, (1970)

81. J.A. Greenwood, *Constriction Resistance and the Real Area of Contact*, Brit. J. Appl. Phys. , Vol. 17, pp. 1621, (1966)

82. I.Minowa, M. Nakamura, M Kanno, *Conductance of a Contact Interface depending on Location and Distribution of Conducting Spots*, Proceedings of Electrical Conference on Contacts, Electromechanical Components and their Applications, p. 19, (1986)

83. J.A. Greenwood, and J.B.P. Williamson, *Contact of nominally flat surfaces*, Proc. Roy. Soc. A, Vol. 295, pp. 300, (1966)

84. F.P. Bowden, D. Tabor, *Friction and Lubrication of Solids, Vol. II*, Oxford: Oxford University Press, (1964)

85. S.W. Park, S.J. Na, *Contact Pressure and Current Density Distribution in a Circular Contact Surface*, IEEE Transactions on Components, Hybrids and Manufacturing Technology, Vol. CHMT-13, No. 2, pp. 320-325, June (1990)

86. L. Kogut and K. Komvopoulos, *Electrical Contact Resistance theory for conductive rough surfaces*, Journal of Applied Physics, Vol. 94, Number 5, pp. 3153-3162, (2003)

87. M.D. Bryant, *Resistance buildup in Electrical Connectors due to fretting corrosion of rough surfaces*, IEEE Transactions on Components, Packaging, and Manufacturing Technology, Part A, Vol. 17, No. 1, March, pp. 86-95, (1994)

88. H.N. Wagar, *Impact of the Contact on Electrical Systems*, IEEE Transactions on Parts, Hybrids, and Packaging, Vol. PHP-13, No. 1, pp. 3-13, March, (1997)

89. M. Antler, *Connector Contact Materials: Effect of Environment on Clad Palladium, Palladium-Silver Alloys and Gold Electrodeposits,* IEEE Trans. on Comp., Pack., and Manufacturing Tech., Vol. CHMT-4, No. 4, pp. 482-492, December (1981)

90. M. Nakamura, I. Minowa, *Film Resistance and Constriction Effect of Current in a Contact Interface*, IEEE Transactions on Components, Hybrids and Manufacturing Technology, Vol. -12, No. 1, pp. 109-113, March (1989)

91. G. Horn, *Test Method for Cleanliness of Technical Contact Surfaces by an Automatic Measurement Device for Contact Resistance*, Proc. 8th International Conference on Electrical Contact Phenomena, Tokyo, Japan, p. 449 , (1976)

92. M.P. Asar, F.G. Sheeler, H.L. Maddox, *Measuring Contact Contamination Automatically*, Western Electric Engineer, 23, p. 32, (1979)

93. M. Braunovic, N. Alexandrov, *Intermetallic Compounds at Aluminum-To-Copper Electrical Interfaces: Effect Of Temperature and Electrical Current*, IEEE Trans. on Comp., Pack., and Manufacturing Tech., Part A, Vol. 17, No. 1, pp. 78-85, March (1994)

94. M. Braunovic, N. Alexandrov, *Intermetallic Compounds at Aluminum-To-Copper Electrical Interfaces: Effect of Temperature and Electrical Current*, Proceedings of the 38th Holm conference on Electrical Contacts, pp. 25-32, (1992)

95. J.A. Rayne, M.P. Shearer, C.L. Bauer, *Investigation of Interfacial Reactions in Thin Film Couples of Aluminum and Copper by Measurement of Low Temperature Contact Resistance*, Thin Solid Films, Vol. 65, pp. 381-391, (1980)

96. E.R. Wallach and G.J. Davis, *Mechanical Properties of Aluminum-Copper Solid Phase Welds*, Metals Tech., pp. 183-190, April, (1977)

97. D.M. Rabkin, V.R. Ryabov, A.V. Lozosvkaya, and V.A. Dovzhenko, *Preparation and Properties of Copper- Aluminum Intermetallic Compounds*, Sov. Powder Mettal. Ceram., No. 8, (92), pp. 695-700, (1970)

98. J.A. Rayne and C.L. Bauer, *Effect of Intermetallic Phase Formation on Electrical and Mechanical Properties of Flash Welded Al-Cu Couples*, Proc. 5th Bolton Landing Conf. Weldments, General Electric, pp. 353-363, (1979)

99. R.S. Timsit, The *Connectibility Properties of Aluminum: Contact Fundamentals*, Canadian Electrical Association Report, 76-19, (1976)

100. R.S. Timsit, *Some Fundamental Properties of Aluminum-Aluminum Electrical Contacts*, IEEE Transactions on Components, Hybrids and Manufacturing Technology, Vol. CHMT-3, No. 1, , pp. 71-79, March (1980)

101. B.T. Reagor, *Interconnection Reliability*, IEEE Trans. on Comp., Pack., and Manufacturing Tech., Vol. 2, No. 4, pp. 390-392, December (1998)

102. A.S. Holland and G.K. Reeves, *New Challenges to the Modeling and Electrical Characterization of Ohmic Contacts for ULSI Devices*, Microelectronics Reliability 40, pp. 965-971, (2000)

103. B.G. Streetman and S. Banerjee, *Solid State Electronics Devices*, Fifth Edition, Prentice Hall New Jersey, (2000)

104. R.J. Osias, J.H. Tripp, *Mechanical Disruption of Surface Films on Metals*, Wear 9, p. 388, (1966)

105. W.D. Treadwell, *Obrist. Uber Die Bestimmung Und Bildung Von Oxydischen Deckschichten Auf Aluminum*, Helv. Chim. Acta 26, (1943)

106. S.J. Bushby, B.W. Callen, K. Griffiths, R.S. Timsit and P.R. Norton, *Associative Versus Dissociative Adsorption of Water on Al(100)*, Surf. Sci. 298, L181, (1993)

107. F. Kohlrausch, *Uber Den Statioaren Temperaturzustand Eines Elektrisch Geheizten Leiters*, Ann. Phys., Leipzig 1: 132, (1900)

108. H. Diesselhorst, *Uber Das Problem Eines Elektrisch Erwarmten Leiters*, Ann. Phys., Leipzig 1: 312, (1900)

109. J.A. Greenwood and J.B.P Williamson, *Electrical Conduction in Solids II, Theory of Temperature Dependent Conductors*, Proc. Roy. Soc., A246, p. 13, (1958)

110. R.S. Timsit, *On the Evaluation of Contact Temperature from Potential Drop Measurements*, IEEE Transactions on Components, Hybrids and Manufacturing Technology, Vol. CHMT-6, , pp. 115-121, (1983)

111. H.N. Wagar, *Contact and Connection Technology in "Integrated Device and Connection Technology"*, Prentice Hall Inc., Englewood Cliffs, pp. 439-595, (1971)

112. T. Utsumi, *Theoretical and Experimental Investigations of the Dynamic Molten Bridge*, IEEE Transactions on Parts, Materials and Packaging, Vol. PMP-5, No. 1, , pp. 62-68, March (1969)

113. P.P. Koren, M.D. Nahemow, P.G. Slade, *The Molten Metal Bridge State of Opening Electric Contacts*, IEEE Transactions on Parts, Hybrids and Packaging, Vol. PHP-11, No. 1, pp. 4-10, March (1975)

114. P.G. Slade, M.F. Hoyaux, *The Effect of Electrode Material on the Initial Expansion of an Arc in Vacuum*, IEEE Transactions on Parts, Hybrids and Packaging, Vol. PHP-8, pp. 35-47, (1972)

115. C.H. Leung and A. Lee, *Contact Erosion in Automotive DC relays*, Proceedings of the 36th IEEE Conference on Electrical Contacts, Montreal, pp. 85-93, (1990)

116. C.H. Leung and A. Lee, *Electrical Contact Materials and their Erosion in Automotive DC relays*, Proceedings of the 37th IEEE Conference on Electrical Contacts, Chicago, pp. 114-121, (1991)

117. T. Takagi and H. Inoue, *Distribution of Arc Duration and Material Wear due to Arc for Ag, Cu, And Pd Contacts*, IEEE Transactions on Comp., Hybrids and Manufacturing Tech., Vol. 2, pp. 20-24, (1979)

118. Z.K. Chen and K. Sawa, *Effects of Oxide Films and Arc Duration Characteristics on Ag Contact Resistance Behaviors*, IEEE Trans. CPMT., Part A, Vol. 18, pp. 409-416, (1995)

119. H.W. Turner, C. Turner, *Discontinuous Contact Erosion*, Proceedings of the 3rd International Research Symposium on Electrical Contact Phenomena, University of Maine, pp. 309-320, June, (1966)

120. K. Yoshida, *Studies of Maintaining Mechanism of Contact Arc Discharge and Spectrum Measurement System*, Doctoral Thesis, Nippon Institute of Technology, Saitama, Japan, pp. 74-89, (1995)

121. Z.K. Chen, K. Sawa, *Effect of Arc Behavior on Material Transfer: A Review*, IEEE Transactions on Components, Hybrids, and Manufacturing Technology, Vol. 21 , Issue 2, pp. 310-322, June (1998)

122. A. Tslaf, *A Thermophysical Criterion for the Weldability of Electric Contact Material in a Steady State Regime*, IEEE Transactions on Components, Packaging, and Manufacturing Technology, Vol. 5, Issue 1, pp. 147-152, March, (1982)

123. O.I. Yas'ko, *Problems of Physical Modeling of Electric Arc Discharges*, Journal of Engineering Physics and Thermophysics, Vol. 70, No. 4, (1997)

124. R.E. Blundell, M.T.C Fang, *The Similarity and Scaling of Radiating Arcs Burning in a Turbulent, Axially Accelerating Gas Flow*, J. Phys. D: Appl. Phys. 30, pp. 628-635, (1997)

125. G.I. Barenblatt, Scaling, *Self Similarity and Intermediate Asymptotics*, Cambridge University Press, (1996)

126. A.C. Snowdon, *Studies of Electrodynamic Forces occurring at Electrical Contacts*, AIEE Transactions 80, pp. 24-28, (1961)

127. www.deringer.com, May, (2004)

128. J.P. Thurmond, J.P. Barber, *Electrical Contacts for Pulsed Power Systems*, Pulsed Power Conference, pp. 160-162, June, (1989)

129. A. Henselek, M. Beerwald, C. Beerwald, *Design and Adaptation of EMF Equipment – From Direct Acting Multi-turn Coils to Separable Tool Coils for*

Electromagnetic Tube Crimping, Proceedings of the First International Conference on High Speed Forming, pp. 275-284, (2004)

130. Dorn, Lutz, Baker, Shawqi, *Extending the Electrode Life in the Spot Welding of Aluminium Alloys by using composite electrodes,* Welding Research Abroad, Vol. 48, No. 5, p.39-43, (2002)

131. P. H. Thornton, A.R. Krause, R.G. Davies, *Contact resistances in Spot Welding,* Welding Journal (Miami, Fla), Vol. 75, No. 12, pp.402-412, (1996)

132. T. Dupuy, S. Ferrassee, *Influence of the Type of Current and Materials Properties on Resistance Spot Welding, Using a Finite Element Model*, ASM Proceedings of the International Conference, Trends in Welding Research, pp.610-615, (1998)

133. S. Fukumoto, I. Lum, E. Biro, D.R. Boomer, Y. Zhou, *Effects of Electrode Degradation on Electrode Life in Resistance Spot Welding of Aluminum Alloy 5182*, Welding Journal (Miami, Fla), Vol. 82, No. 11, pp.307-312, (2003)

134. Personal Communication, G.S. Daehn with Exploform BV, Netherland, March, (2003)

135. M.F. Ashby, Y.J.M Brechet, D. Cebon, L. Salvo, *Selection strategies for materials and processes,* Materials and Design, 25, pp. 51-67, (2004)

136. J.T. Wood, J.D. Embury and M.F. Ashby, *An Approach to Materials Processing and Selection for High Field Magnet Design*, Acta Mater., Vol. 45, No. 3, pp. 1099-1104, (1997)

137. www.matweb.com, August, (2005)

138. http://sensorprod.com/pressurex/, August, (2005)

139. Personal Communication, Jianhui Shang, Graduate Research Associate, Dept. of Materials Science and Engineering, September 12, (2005)

APPENDIX A

Parameters of the 48 kJ Maxwell Magneform Capacitor Bank [139]

The 48 KJ capacitor bank is composed of 8 capacitors. Each of them has a capacitance of 125μF. Any number of capacitors can be included in the LRC circuit. They can be schematically modeled as shown in Figure A.1.

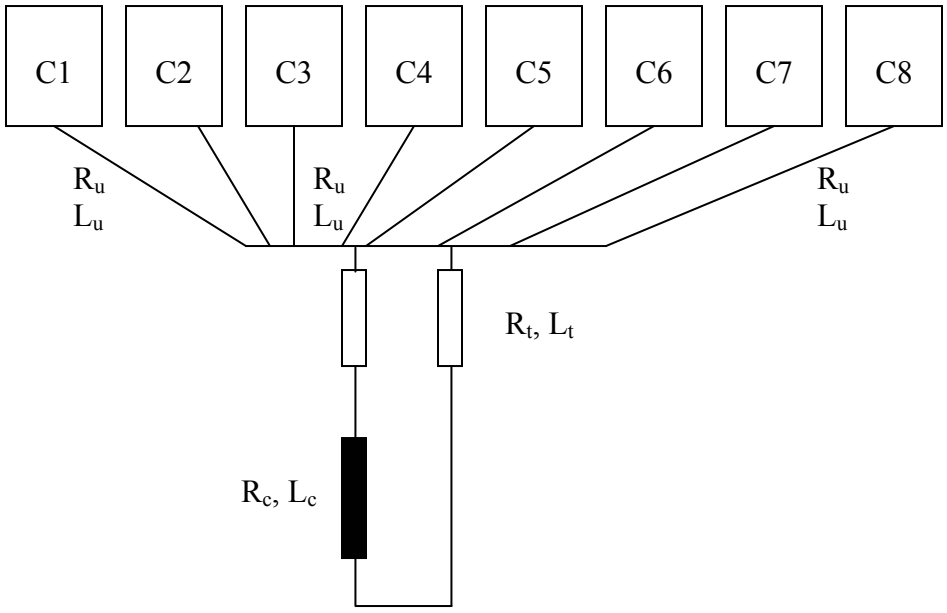

Figure A.1: Schematic model of 48 KJ capacitor bank.

The system inductance L_s and resistance R_s can be modeled based on the inductance and resistance of the coil (L_c and R_c) as well as that for each unit connection between the capacitor module and coil (L_u and R_u) and the system resistance and inductance at the terminal (L_t and R_t). Based on elements in series and parallel, they can be modeled based on the number of units, n, as:

$$L_s = L_c + L_t + \frac{L_u}{n} \qquad \text{..... (A.1)}$$

$$R_s = R_c + R_t + \frac{R_u}{n} \qquad \text{..... (A.2)}$$

The capacitance of the system C is:

$$C = nC_{unit} \qquad \text{..... (A.3)}$$

The parameters are determined by curve fitting to current traces from experiments. From this, we can estimate the modeling parameters as shown in Table A.1.

Parameter	48 KJ System
C_{unit}	125 μF
R_u	0.013 Ω
L_u	0.28 μH
R_t	~0
L_t	~0
R_c	0.01 Ω
V_{max}	10 KV
n_{max}	8

Table A.1: Estimated parameters of the 48 kJ capacitor bank

APPENDIX B

Arcing calculations for Actuator 3 using a copper sheet

Quantity	**Source**	**Value**
Hardness of Cu (H)	[137]	880×10^{6} Nm^{-2}
Resistivity of Cu (ρ)	[137]	1.7×10^{-8} Ωm
Applied Load (F)	Expt. Data	120400 N
Contact Resistance (R_c) assuming clean interfaces	Eqn. [7.7]	1.288 μΩ
Peak Primary Current (I_p)	Expt. Data	65×10^{3}A @ 4 Cap., 70% energy
Peak Induced Current (I_i)	Expt. Data	683×10^{3}A
Peak Potential Drop Across the Contact	V=IR	0.880 V
Potential Drop Required for melting based on Wiedemann- Franz Law	Eqn. [7.11]	0.416 V **The voltage may lead to melting of the contacts**
Required Contact Resistance based on 65 kA primary current	Eqn. [7.7] and [7.11]	0.609 μΩ
Max.. Practical Design Contact Resistance	**Eqn. [7.7] and Holm [70]**	**0.193 μΩ we may be in the trouble region**
Load required to avoid contact melting	**Eqn. [7.7] and [7.11]**	**311032 N**
Peak Opening Load	$P = \mu_0 I_1 I_2 / 2$	**1625800 N more than ten times our current load levels**
Maximum load recommended based on yield strength	**[70] and [137]**	**754845 N around six times more than our current levels**
Frequency	Expt. Data	4 kHz
Skin Depth	Expt. Data	1.04 mm
Yield Strength of Cu outer channel	[137]	195 MPa
Ultimate Strength of Cu outer channel	[137]	250 MPa
Apparent Contact Area (one contact side)	Expt. Data	19.35×10^{-4} m^2
Actual contact Area , ~10% Apparent Contact Area and the skin depth (A_p)	[70], [72]	15.85×10^{-6} m^2
Current Density at the contacts	**$J=I_i/A_p$**	**4.309×10^{10} Am^{-2}**
Characteristic Length, λ	Expt. Data	0.152 m
Electric Field at the contacts	**[72]**	**8.434×10^{3} V/m , no arcs**

Table B.1: Arcing calculations for Actuator 3 using a 0.13 mm thick Cu sheet.

The following analysis is based on the scaling analysis for our system and Cu- Cu contact using Actuator 3. The design process is as follows:

Estimate the current density taking a conservative estimate of breakdown of an activated surface, i.e., 5 x 10^7 V/m.

In this setup λ= 0.152 m.

JR_c= 3.289 x 10^8 V/m^2.

Assuming we have a particular value of R_c and it does not change during the forming process (which is not the case in our present design and we will discuss that later) we have 27,000 lbs of load at Cu-Cu contacts. Following the above table ,

R_c= 1.288 $\mu\Omega$

Therefore, J=2.554 x 10^{14} A/m^2

Now taking the skin depth into account the actual area through which the current flows is

A_p= 15.85 x 10^{-6} m^2

Maximum induced current that can flow

I_i= 4.032 x 10^9 A.

Peak Primary Current I_p= 3.840 x 10^8 A

We can calculate the pressure based on this by using $P = \mu_0 I_1 I_2 / 2$, where I_1 and I_2 are the primary and induced currents densities.

The peak primary current that we obtain from the above analysis is very high. Typically for our system with 48 KJ energy the peak primary current will not be more than 200 kA, which means that the peak induced current will never be more than 3000 kA, assuming

perfect coupling. So where is the flaw? The flaw is in assuming that the value of R_c is consistently low. During the pulse the contacts try to open and hence R_c increases. The final value at the peak of the pulse is difficult to estimate. The peak opening load is 1.62 x 10^6 N which is more than ten times the applied load of 0.12 x 10^6 N. Thus the contacts will try to open.

We can actually calculate the opening distance.

The forming area (A_f) = 2.710 x 10^{-2} m^2.

Mass of the copper block (m) = 15.76 Kgs

Acceleration to the first peak of current = (1.72 x 10^9 /6) t^3 where t is the time based on a rise time of 60 micro-seconds.

Therefore the distance traveled in one complete pulse is 0.25 mm, which is the amount by which the contacts open. Gasket compliance can be used to mitigate this.

This implies that the voltage required for breakdown is 12500 V. But even with peak charging the applied voltage is 10,000 V and hence the circuit voltage cannot be over this. This leads to two conclusions:

(i) Arcing should not occur in this system and the occurrence can be avoided if the opening of contacts is prevented.

(ii) Welding is a possibility (above table). It can be avoided by using higher loads.